

# **Microscopic theory of the linear and nonlinear optical properties of TMDCs**

Dissertation  
zur  
Erlangung des Doktorgrades  
der Naturwissenschaften  
(Dr. rer. nat.)

dem Fachbereich Physik  
der Philipps-Universität Marburg  
vorgelegt

von  
**Lars Meckbach**

aus Marburg (Lahn)

Marburg (Lahn), 2020

Vom Fachbereich Physik der Philipps-Universität Marburg  
als Dissertation angenommen am: 04.05.2020

Hochschulkenziffer: 1180

Erstgutachter: Prof. Dr. Stephan W. Koch  
Zweitgutachter: Prof. Dr. Wolfgang Stolz

Tag der mündlichen Prüfung: 14.07.2020

## Abstract

Since the discovery of graphene, the research interest in two-dimensional materials has drastically increased. Among them, semiconducting transition-metal dichalcogenides promise great potential for future applications in optoelectronics and photonics as they combine atomic-scale thickness with pronounced light-matter coupling and sizable band gaps in the visible to near-infrared range. In this context, a quantitative and predictive description of the optical properties is of great importance. For the results summarized in this thesis, a self-consistent scheme was established to provide such a quantitative and predictive description for various semiconducting transition-metal dichalcogenide systems in the vicinity of the  $K/K'$  points. The theoretical framework combines an anisotropic dielectric model for the Coulomb potential in layered materials with gap equations for the ground-state renormalization, Dirac-Wannier equation to determine the excitonic properties, and Dirac-Bloch equations to access linear and nonlinear optical properties. The latter are formally equivalent to the semiconductor Bloch equations, that have proven to be reliable to compute the optical properties of various semiconductor systems for many years. Detailed differences arise from the relativistic framework, the massive Dirac Fermion model, that applies to transition-metal dichalcogenides. To account for the finite out-of-plane extension of the individual layers, a form factor was introduced in the Coulomb potential.

The theoretical framework described above was applied in investigations on the ground-state and excitonic properties of monolayer and homogeneous-multilayer structures. For the case of an unspecified monolayer, the dielectric tuning of the renormalized bands and excitonic resonances was simulated by variation of the Coulomb coupling showing characteristics that are observed in experiments on real monolayer systems. Encouraged by the initial results, realistic monolayers were considered, i.e. MoS<sub>2</sub>, MoSe<sub>2</sub>, WS<sub>2</sub>, WSe<sub>2</sub>, whose material parameters were taken from external density-functional-theory calculations. The procedure to determine the effective-thickness parameter, entering the form factor to account for finite-thickness effects, was illustrated for a SiO<sub>2</sub>-supported MoS<sub>2</sub> monolayer. Once this parameter was fixed for a given material, the advantage of this approach was demonstrated for MoS<sub>2</sub>, again, by predicting

the  $K/K'$ -point interband transition energies and excitonic resonances for various dielectric environments and layer numbers, including the bulk limit. Comparisons to experimental findings and similar theoretical approaches were drawn for all of the stated material systems yielding almost excellent overall agreement. In particular, the results suggest a reinterpretation of the bulk exciton series of  $\text{MoS}_2$  as a combined two-dimensional intra- and interlayer exciton series. The results strongly indicate that the applied approach captures the essential physics around the  $K/K'$  points.

Stacking two materials with different band gaps adds a new element to the band-gap engineering of transition-metal dichalcogenides. Heterostructures such as bilayers  $\text{WSe}_2/\text{MoS}_2$  and  $\text{WSe}_2/\text{MoSe}_2$  display type-II band alignment enabling highly efficient charge transfer which is promising for applications in photovoltaics. In a theoretical study on the stated bilayer systems, it was demonstrated that the established theoretical framework could also be applied to investigate intra- and interlayer excitons in transition-metal dichalcogenide heterostructures. For this purpose the anisotropic dielectric model for the Coulomb potential was adjusted to the hetero-bilayer environment. Based on the material parameters provided by internal density-functional-theory calculations, linear optical absorption spectra were computed revealing tightly bound interlayer excitons with binding energies comparable to those of the intralayer excitons. Computing the oscillator strength of the respective resonances yielded relatively long radiative lifetimes for the interlayer excitons, two orders of magnitude larger than that of the intralayer excitons. The artificial strain in  $\text{WSe}_2/\text{MoS}_2$  bilayer resulted in heavily misaligned spectra which is why theory-experiment comparisons were avoided for this system. For the rather unstrained  $\text{WSe}_2/\text{MoSe}_2$  bilayer, intra- and interlayer excitonic resonances as well as the ratio of the intra- and interlayer exciton lifetimes compared reasonably well to experimental and theoretical findings.

Among the semiconducting transition-metal dichalcogenides, monolayer  $\text{MoS}_2$  has drawn the most attention from researchers, not least because it was the first representative that displayed experimental evidence of a direct band gap. Combining the direct band gap with pronounced light-matter coupling, monolayer systems hold promise for laser applications on the atomic scale. In this context, the optical properties of suspended and  $\text{SiO}_2$ -supported  $\text{MoS}_2$  monolayers were investigated in the nonlinear excitation regime for the case of initial thermal charge carriers located in the  $K/K'$  valleys. In particular, it was demonstrated that excited carriers lead to an enormous reduction of the band gap. In the range of comparable carrier densities, the computed optical spectra, excitation-induced band-gap renormalization and exciton binding energies were found to be in good agreement with earlier theoretical investigations on  $\text{MoS}_2$ , as was the predicted Mott-density. For densities beyond the Mott-transition, broadband plasma-induced optical gain energetically below the exciton resonance was observed, which has yet to be realized in experimental setups.

Besides the canonical representatives discussed so far, the optical properties of a  $\text{SiO}_2$ -supported  $\text{MoTe}_2$  monolayer were studied. This material system became of particular interest since room-temperature lasing had already been observed. A numerical experiment in the nonlinear excitation regime was performed. In particular, excitation conditions for achieving plasma gain in  $\text{MoTe}_2$  monolayers were identified. Within

the scope of this investigation, the theoretical framework was extended beyond the quasiequilibrium regime by including Boltzmann-like carrier- and phonon-scattering rates. Whereas a Markovian treatment was sufficient within the simulation of the  $K/K'$ -point carrier-relaxation dynamics, the excitation-induced dephasing of the microscopic polarizations was treated dynamically in order to avoid unphysical behavior within the optical spectra. It was demonstrated that pump-injected charge carriers induce a huge reduction of the band gap on the timescale of the optical pulse. This observation including the magnitude of the band-gap renormalization compared well with experimental findings on monolayer MoS<sub>2</sub>. Probing the strongly excited system at distinct time delays yielded ultrafast gain build-up on a few-picosecond timescale as a result of efficient carrier thermalization. Allowing the carriers to equilibrate within the entire Brillouin zone, even larger output was predicted. This numerical experiment represents the first study proposing monolayer MoTe<sub>2</sub> as a promising candidate to achieve plasma-induced optical gain.



## Zusammenfassung

Mit der Entdeckung von Graphen ist das Forschungsinteresse an zweidimensionalen Materialien immens gestiegen. Unter ihnen verheißen speziell die halbleitenden Übergangsmetall-Dichalkogenide großes Potential für künftige Anwendungen in Bereichen wie Optoelektronik und Photonik, da sie atomare Dicke mit starker Licht-Materie-Wechselwirkung und beeinflussbaren Bandlücken im sichtbaren und nahen-Infrarot Spektralbereich vereinen. Vor diesem Hintergrund ist eine quantitative und vorhersagende theoretische Beschreibung der optischen Eigenschaften von zentraler Bedeutung. Zur Erzielung der Resultate, die in dieser Arbeit zusammengefasst werden, kam eine selbstkonsistente Methode zum Einsatz, die eine quantitative Modellierung von diversen halbleitenden Vertretern der Übergangsmetall-Dichalkogenide in der Umgebung der  $K/K'$ -Punkte ermöglicht. Das theoretische Konzept vereint ein anisotropes dielektrisches Modell für das Coulomb-Potential in Schichtmaterialien mit Lückengleichungen (engl. *gap equations*) zur Renormierung des Grundzustands, der Dirac-Wannier-Gleichung zur Bestimmung der exzitonischen Eigenschaften und Dirac-Bloch-Gleichungen zur Beschreibung der linearen und nichtlinearen optischen Eigenschaften. Letztere sind formal identisch mit den Halbleiter-Bloch-Gleichungen, welche sich für Beschreibung der optischen Eigenschaften einer Vielzahl an Halbleitersystemen über die Jahre hinweg als zuverlässig erwiesen haben. Unterschiede ergeben sich aus dem relativistischen Konzept, dem Modell der massiven Dirac-Fermionen, dass in der Beschreibung der Übergangsmetall-Dichalkogenide Anwendung findet. Zu guter Letzt wurde ein Formfaktor im Coulomb-Potential eingeführt, um die endliche Ausdehnung der einzelnen Schichten zu berücksichtigen.

Das oben beschriebene theoretische Konzept fand zunächst in der Untersuchung der Grundzustands- und exzitonischen Eigenschaften von Mono- und Multischichtstrukturen Anwendung. Für eine nicht-näher spezifizierte Monolage wurde der Einfluss der dielektrischen Umgebung auf die renormierten Bänder und exzitonische Resonanzen durch Variation der Coulomb-Kopplung simuliert. Dabei zeigten sich charakteristische Eigenschaften, die auch in Experimenten an realen Schichten beobachtet werden. Darauf aufbauend wurden folglich reale Monolagen betrachtet, explizit die der

Materialien  $\text{MoS}_2$ ,  $\text{MoSe}_2$ ,  $\text{WS}_2$  und  $\text{WSe}_2$ . Deren Materialparameter basierten auf externen Dichtefunktionaltheorie-Berechnungen. Die Vorgehensweise zur Bestimmung des Parameters der effektiven Dicke, die über den Formfaktor die endliche Ausdehnung der Schichten berücksichtigt, wurde am Beispiel einer Monolage  $\text{MoS}_2$  auf einem  $\text{SiO}_2$ -Substrat illustriert. Nachdem dieser Parameter festgelegt war, wurde die Stärke dieses Ansatzes am Beispiel von  $\text{MoS}_2$  demonstriert, indem sowohl die Energien der Interbandübergänge am  $K/K'$ -Punkt als auch die exzitonischen Resonanzen für diverse dielektrische Umgebungen und Anzahl an Schichten prognostiziert wurden, den Grenzfall des Volumenmaterials eingeschlossen. Es wurden Vergleiche mit experimentell bestimmten Werten gezogen, als auch mit den Ergebnissen anderer theoretischer Herangehensweisen, mit dem Resultat, dass nahezu exzellente Übereinstimmung gefunden wurde. Hervorzuheben ist das Resultat, dass die Berechnungen zu einer Neuinterpretation der Exzitonserie im Volumenmaterial führten, die als eine Zusammensetzung einer zweidimensionalen Intra- und Interschicht-Exzitonserie aufzufassen ist. Die erzielten Resultate weisen stark daraufhin, dass der verwendete Ansatz die wesentliche Physik um die  $K/K'$ -Punkte erfasst.

Das Stapeln zweier Materialien mit verschiedenen Bandlücken stellt eine weitere Möglichkeit zur Manipulation der Bandlücke in Übergangsmetall-Dichalkogeniden dar. Manche Heterostrukturen, wie die Bilagen  $\text{WSe}_2/\text{MoS}_2$  und  $\text{WSe}_2/\text{MoSe}_2$ , weisen eine Typ-II-Ausrichtung der Bänder auf, die effizienten Ladungstransfer ermöglicht. Dieser ist vielversprechend für Anwendungen in Solarzellen. In einer theoretischen Studie der genannten Bilagen wurde demonstriert, dass das zuvor etablierte theoretische Konzept gleichermaßen das Modellieren von Intra- und Interschicht-Exzitonen in Heterostrukturen von Übergangsmetall-Dichalkogeniden umfasst. Vor diesem Hintergrund wurde das Coulomb-Potential an die dielektrische Umgebung der heterogenen Bilage angepasst. Basierend auf internen Dichtefunktionaltheorie-Berechnungen, die wichtige Materialparameter lieferten, wurden lineare Absorptionsspektren berechnet. Diese enthüllten stark gebundene Interschicht-Exzitonen, mit Bindungsenergien vergleichbar zu denen der Intraschicht-Exzitonen. Die zugehörigen Oszillatorstärken äußerten sich in verhältnismäßig langen strahlenden Lebenszeiten für erstere, die um zwei Größenordnungen länger waren als die der Intraschicht-Exzitonen. Die künstlich induzierte Verspannung in der  $\text{WSe}_2/\text{MoS}_2$ -Bilage lies keinen vernünftigen Vergleich mit experimentellen Beobachtungen zu. Im Gegensatz dazu führten Vergleiche der unverspannten  $\text{WSe}_2/\text{MoSe}_2$ -Bilage hinsichtlich der Resonanzen von Intra- und Interschicht-Exziton sowie dem Verhältnis der Lebenszeiten zu guter Übereinstimmung mit experimentellen und theoretischen Beobachtungen.

Unter den halbleitenden Übergangsmetall-Dichalkogeniden hat die  $\text{MoS}_2$ -Monolage bislang die meiste Aufmerksamkeit der Wissenschaftler erlangt, nicht zuletzt aufgrund der Tatsache, dass für sie die direkte Bandlücke zuerst nachgewiesen wurde. Vereint man die direkte Bandlücke mit der ausgeprägten Licht-Materie-Wechselwirkung, liegt das Potential für Laseranwendungen auf atomarer Skala auf der Hand. Vor diesem Hintergrund wurden die optischen Eigenschaften freistehender und auf  $\text{SiO}_2$  montierter  $\text{MoS}_2$ -Monolagen im nichtlinearen Anregungsregime für thermische Ladungsträgerverteilungen in den  $K/K'$ -Tälern untersucht. Es wurde gezeigt, dass die Anwe-

senheit angeregter Ladungsträger zu einer enormen Verringerung der Bandlücke führt. Im Bereich vergleichbarer Dichten wurde gute Übereinstimmung mit vorigen theoretischen Untersuchungen hinsichtlich berechneter optischer Spektren, Plasma-induzierter Bandlückenverringerng, Exziton-Bindungsenergien und Mott-Dichte gefunden. Für Dichten jenseits des Mott-Übergangs wurde Plasma-induzierte optische Verstärkung beobachtet, was bisher noch nicht experimentell realisiert wurde.

Neben den bisher betrachteten kanonischen Vertretern wurden schließlich die optischen Eigenschaften von MoTe<sub>2</sub>-Monolagen auf einem SiO<sub>2</sub> Substrat untersucht. Dieses Materialsystem weckte das Interesse nachdem darin bereits Laseremission bei Raumtemperatur nachgewiesen wurde. Es wurde ein numerisches Experiment im nichtlinearen Anregungsregime verfolgt. Speziell wurden Anregungsbedingungen identifiziert, die zu Plasma-induzierter optischer Verstärkung in MoTe<sub>2</sub>-Monolagen führen. Im Rahmen dieser Untersuchungen wurde das theoretische Konzept jenseits der Beschreibung von Gleichgewichtssituationen erweitert, indem Boltzmann-artige Ladungsträger- und Phononenstreuraten ergänzt wurden. Während die Markov-Näherung verlässliche Ergebnisse für die  $K/K'$ -Ladungsträger-Relaxationsdynamik lieferte, war eine dynamische Behandlung der durch die Anregung induzierten Dephasierung (engl. *excitation-induced dephasing*) der mikroskopischen Polarisierung erforderlich. Dadurch konnte unphysikalisches Verhalten in den optischen Spektren vermieden werden. Es wurde demonstriert, dass durch die Anregung induzierte Ladungsträger eine enorme Verringerung der Bandlücke auf der Zeitskala des optischen Pulses bewirken. Dieses Phänomen sowie die Größenordnung der Bandlückenrenormierung sind im Einklang mit den Befunden von Experimenten an MoS<sub>2</sub>-Monolagen. Durch Abfragen des stark angeregten Systems zu bestimmten Verzögerungszeiten konnte ein ultraschnelles Aufbauen der optischen Verstärkung innerhalb weniger Pikosekunden nachgewiesen werden. Dieses ist effizienter Ladungsträger-Thermalisierung geschuldet. Die Betrachtung einer Gleichgewichtssituation, die die gesamte Brillouin-Zone einschließt, führte sogar zu einer erhöhten optischen Verstärkung. Dieses numerische Experiment stellt die erste Studie dar, in der MoTe<sub>2</sub>-Monolagen als verheißungsvolle Kandidaten für Plasma-induzierte optische Verstärkung vorgeschlagen werden.



## Danksagung

An dieser Stelle möchte ich mich herzlich bei allen bedanken, die zum Gelingen dieser Arbeit beigetragen haben. Allen voran danke ich Prof. Dr. Stephan W. Koch für die hervorragende Betreuung während meiner Zeit als Master- und Promotionsstudent, sowie für die Gelegenheit an spannenden Projekten auf dem Gebiet neuartiger, quasi-zweidimensionaler Materialien mitzuarbeiten und diese auf Seminaren und Workshops zu präsentieren. Darüber hinaus bedanke ich mich bei dir und Prof. Dr. Jerome V. Moloney für die Ermöglichung der beiden Forschungsaufenthalte am College of Optical Sciences der University of Arizona. Die beiden Aufenthalte in Tucson kristallisierten sich als besondere Höhenpunkte während meiner Zeit als Doktorand heraus.

Prof. Dr. Wolfgang Stolz danke ich für die Übernahme des Zweitgutachtens, sowie Prof. Dr. Peter Lenz für die Bereitschaft in meiner Prüfungskommission mitzuwirken.

Ich danke der DFG für die finanzielle Unterstützung unserer Projekte im Rahmen des SFBs 1083, sowie den Koordinatoren/innen und Organisatoren/innen des SFBs für die Planung und Ausrichtung von Kolloquien, Seminaren und Workshops.

Besonders hervorzuheben ist Dr. Tineke Stroucken. Tineke, bei dir möchte ich mich umfangreich bedanken. Einerseits für die hervorragende Zusammenarbeit und lehrreiche Betreuung auf einem spannenden und zugleich hart umkämpften Themengebiet. Bei jeglichen Fragen hattest du, genau wie Stephan, stets ein offenes Ohr und Rat für mich. Du warst es auch, die mich als Tutorin auf die Möglichkeit einer Masterarbeit mit anschließender Promotion in der AG Halbleitertheorie aufmerksam gemacht hat. Gerade in der Phase wo Isas Transplantation bevorstand, trugen Stephans Vorlesungen zur *QM II* – die einzige Lehrveranstaltung, die ich zu der Zeit besuchte – zusammen mit den von dir geleiteten Tutorien zu einer gewissen Ablenkung von den Ängsten des Alltags bei. Dafür bin ich euch beiden für immer dankbar!

Dr. Jörg Hader danke ich ausdrücklich für die Zusammenarbeit hinsichtlich der Programmentwicklung der Streuterme. Ich habe in den letzten beiden Jahren sehr viel von dir gelernt und danke dir auch dafür, dass du dir stets die Zeit für meine Fragen genommen hast. Gleichmaßen gilt mein Dank Josefine Neuhaus, Dr. Ulrich Huttner und Dr. Johannes Steiner für die fruchtbare interne Zusammenarbeit. Fine und Uli,

eure DFT-basierten Rechnungen versorgten uns stets mit grundlegendem Verständnis und darüber hinaus mit den nötigen Modellparametern. Hanno, dir danke ich für die Aufklärung rund um das Thema *Excitation-induced dephasing*. Bei Dr. Philipp Springer möchte ich mich für die hervorragende Einarbeitung in die Arbeitsweise mit der Programmiersprache Fortran bedanken. Dadurch gelang es mir zügig Programme zu schreiben, die für die Untersuchungen im Rahmen dieser Arbeit zum Einsatz kamen.

Ein besonderer Dank gilt Dr. Lars Bannow und Sven Christian Liebscher für die Bereitschaft sich um die EDV der AG zu kümmern, sowie Stefanie Kramer und Linda Grigat für die organisatorische Unterstützung. Bei Dr. Colm Dineen und Lacey Singh bedanke ich mich für Unterstützung am College of Optical Sciences und bei Dr. Phil Rosenow für das herzliche Willkommen und die Ausflüge in und um Tucson. Danke auch an alle aktuellen und ehemaligen Mitglieder der AG Halbleiterteorie für die tolle Arbeitsatmosphäre: Maria W., Lars B., Uli, Tineke, Sven Christian, Fine, Maria H., Ada, Hanno, Oli, Osmo, Peter H., Christian, Philipp, Markus, Peter T., Steffi, Linda und Gaurav. Darüber hinaus gilt Fine, Sven Christian und meiner Schwester Stefanie ein ganz besonderer Dank für das Korrekturlesen von Teilen dieser Arbeit. Ihr habt mir sehr geholfen!

Unseren Familien und Freunden, insbesondere meinen Eltern, meiner Oma, Renate und Peter, danke ich von Herzen für die unermüdliche und vielfältige Unterstützung in allen Lebenslagen. Ihr seid immer für uns da und das bedeutet uns die Welt!

Mein letzter und größter Dank gilt dem wichtigsten Menschen in meinem Leben, meiner großen Liebe Isa: dafür, dass du mich stets unterstützt und mir zur Seite stehst, mich ermutigst und aufbaust. DANKE, dass du einfach immer für mich da bist!

## Author's contributions

In this thesis an introductory summary of the results obtained during my doctoral studies is given. This work was presented in detail in the publications, posters and talks that are listed below. Besides, this list contains one publication which is not part of the cumulative framework but also originates from the time of my doctoral studies.

### Publications in peer-reviewed journals

- [I] L. Meckbach, T. Stroucken, and S. W. Koch, “Influence of the effective layer thickness on the ground-state and excitonic properties of transition-metal dichalcogenide systems”, *Phys. Rev. B* **97**, 035425 (2018).
- [II] L. Meckbach, T. Stroucken, and S. W. Koch, “Giant excitation induced bandgap renormalization in TMDC monolayers”, *Appl. Phys. Lett.* **112**, 061104 (2018).
- [III] L. Meckbach, U. Huttner, L. C. Bannow, T. Stroucken, and S. W. Koch, “Inter-layer excitons in transition-metal dichalcogenide heterostructures with type-II band alignment”, *J. Phys.: Condens. Matter* **30**, 374002 (2018).
- [IV] L. Meckbach, J. Hader, U. Huttner, J. Neuhaus, J. T. Steiner, T. Stroucken, J. V. Moloney, and S. W. Koch, “Ultrafast band-gap renormalization and build-up of optical gain in monolayer MoTe<sub>2</sub>”, *Phys. Rev. B* **101**, 075401 (2020).

### Publications not part of the cumulative framework

- [V] L. M. Schneider, J. Kuhnert, S. Schmitt, W. Heimbrod, U. Huttner, L. Meckbach, T. Stroucken, S. W. Koch, S. Fu, X. Wang, K. Kang, E.-H. Yang, and A. Rahimi-Iman, “Spin-Layer and Spin-Valley Locking in CVD-Grown AA'- and AB-Stacked Tungsten-Disulfide Bilayers”, *J. Phys. Chem. C* **123**, 21813–21821 (2019).

## Talks and posters

- **L. Meckbach**, T. Stroucken, U. Huttner, J. Hader, J. V. Moloney, S. W. Koch, *Excitation-induced band-gap renormalization and optical gain in TMDC monolayers*, Contributed Talk, SFB 1083 Workshop on TMDCs in Münster, Germany (2018)
- **L. Meckbach**, T. Stroucken, U. Huttner, J. Hader, J. V. Moloney, S. W. Koch, *Optical gain in TMDC monolayers*, Contributed Talk, Joint GRK 1782 & SFB 1083 Seminary in Volkenroda, Germany (2018)
- **L. Meckbach**, T. Stroucken, U. Huttner, J. Hader, J. V. Moloney, S. W. Koch, *Linear and nonlinear optical properties of TMDCs*, Contributed Talk, ACMS Group Meeting at the University of Arizona in Tucson, AZ, USA (2019).
- **L. Meckbach**, T. Stroucken, S. W. Koch, *Excitonic properties of transition metal dichalcogenides*, Poster presented at the “Materialforschungstag Mittelhessen 2017” in Gießen, Germany (2017).
- **L. Meckbach**, T. Stroucken, S. W. Koch, *Excitons in TMDCs: From monolayer to bulk*, Poster presented by T. Stroucken, Fundamental Optical Processes in Semiconductors (FOPS) conference in Stevenson, WA, USA (2017).
- **L. Meckbach**, L. C. Bannow, U. Huttner, J. T. Steiner, T. Stroucken, and S. W. Koch, *Optical excitations in transition-metal dichalcogenides*, Poster presented at the “Materialforschungstag Mittelhessen 2018” in Marburg, Germany (2018).
- **L. Meckbach**, J. Hader, T. Stroucken, U. Huttner, J. T. Steiner, J. V. Moloney, S. W. Koch, *Ultrafast band-gap renormalization and build-up of optical gain in TMDC monolayers*, Poster presented at the “Materialforschungstag Mittelhessen 2018” in Gießen, Germany (2019).

## Original Contributions

All studies presented in this thesis have been frequently discussed in meetings and other forms of correspondence with my supervisor Prof. Dr. Stephan W. Koch, my primary research colleagues Dr. Tineke Stroucken and Dr. Jörg Hader, and our research partners. This aided in planning the next steps and advancing the results which are published in references [I–IV].

The first project built the foundation of the theoretical investigations on the linear and nonlinear optical properties of the various TMDC systems. The results have been published in ref. [I] and are summarized in chapter 3. Therein, a self-consistent scheme to calculate the ground-state renormalization and optical properties in the vicinity of the  $K/K'$  points of mono- and multilayer TMDCs is presented. In the following, it is referred to as gap and Dirac-Bloch equation scheme.

Based on the presented theoretical framework developed in our research group by Tineke Stroucken, I contributed by performing the majority of numerical simulations. While the optical spectra that are displayed in ref. [I] were based on the calculations of Tineke Stroucken, I confirmed the presented results in own calculations. Within the scope of this project, I extended my numerical code – which I started writing during my master thesis – to the modeling of the aforementioned properties of mono- and multilayer TMDCs within arbitrary dielectric environments. The resulting program enabled efficient calculations for structures of very high numbers of layers. Furthermore, I contributed to writing the main text of the manuscript. Since this paper was selected by the editors of Phys. Rev. B to be an “Editors’ Suggestion”, a teaser page was required where I contributed by designing the image of the teaser. Prior to publication, preliminary results contributed to a poster I designed for the Fundamental Optical Processes in Semiconductors (FOPS) - 2017 Conference in Stevenson, WA, USA (presented by Tineke Stroucken) where I was unfortunately unable to attend.

The second project initialized our investigations in the nonlinear excitation regime. In particular, the influence of thermal carrier distributions on the band-gap renormalization and optical absorption spectra was investigated for monolayer MoS<sub>2</sub>. In this context, the recently established gap and Dirac-Bloch equation scheme was extended to describe excited quasiequilibrium situations. After extending the numerical code for this project, I provided the entire numerical calculations and contributed to writing the manuscript. The results have been published in ref. [II] and are summarized in the first part of chapter 4. After publication, I presented parts of the results in talks I gave at the SFB 1083 Workshop on TMDCs (Münster, Germany) and the joint SFB 1083/GRK 1782 Seminary (Volkenroda, Germany) in 2018.

In a third project intra- and interlayer excitons in spatially indirect TMDC heterostructures were investigated. Here, density-functional-theory calculations, performed in our research group by Ulrich Huttner, were combined with the gap and Dirac-Bloch equation scheme to compute the ground-state and excitonic properties of WSe<sub>2</sub>/MoS<sub>2</sub> and WSe<sub>2</sub>/MoSe<sub>2</sub> hetero-bilayers. As part of “J. Phys.: Condens. Matter Special Issue on Internal Interfaces”, the results have been published in ref. [III] and are summarized at the end of chapter 3. For this purpose, the dielectric model for

the Coulomb potential had to be adjusted to the hetero-bilayer environment, which I provided. Based on my developed code, I conducted the entire gap and Dirac-Bloch equation related calculations to obtain the ground-state renormalizations, excitonic properties and optical spectra. Consequently, I contributed to writing the manuscript parts concerning these subjects. After submission, I presented parts of the results in a poster session at the “Materialforschungstag Mittelhessen 2018” (Marburg, Germany). I also gave a talk summarizing the results of our investigations during an ACMS Group Meeting at the University of Arizona (Tucson, AZ, USA) in 2019.

Ultimately, the theoretical framework was extended beyond the description of the low-excitation and quasiequilibrium regimes. By the example of monolayer MoTe<sub>2</sub>, microscopic calculations of the carrier dynamics and optical gain development after nonresonant optical excitation were performed. This project was a collaboration of our research group with Jörg Hader and Jerome Moloney (both University of Arizona, Tucson, USA). Jörg Hader kindly provided the initial numerical code of the carrier- and phonon-scattering terms and was heavily involved in the program development from then on. My research stays at the University of Arizona in spring 2018 and 2019 intensified our collaboration. Together, we developed the numerical code that led to the results published in ref. [IV] and are summarized in the second part of chapter 4. However, a dynamic treatment of the polarization-carrier and polarization-phonon scattering turned out to be crucial to avoid unphysical results. Based on the theory development concerning screening and Coulomb scattering, contributed by Tineke Stroucken, I extended the numerical code by the dynamic screening and scattering contributions. Subsequently, I performed the entire optical simulations yielding the published results and contributed to writing the manuscript. Density functional theory calculations, providing material parameters and form factors, were performed by Ulrich Huttner and Josefine Neuhaus. I presented intermediate results in a talk at the joint SFB 1083/GRK 1782 Seminary (Volkenroda, Germany) in 2018 and in a poster session at the “Materialforschungstag Mittelhessen 2019” (Gießen, Germany).

## List of abbreviations

<b>BZ</b>	Brillouin zone
<b>DBEs</b>	Dirac-Bloch equations
<b>DFT</b>	density functional theory
<b>DWE</b>	Dirac-Wannier equation
<b>EID</b>	excitation-induced dephasing
<b>EOM</b>	equation(s) of motion
<b>GEs</b>	gap equations
<b>LO</b>	longitudinal optical
<b>MDFs</b>	massive Dirac fermions
<b>RPA</b>	random-phase approximation
<b>TMDCs</b>	transition-metal dichalcogenides
<b>2D/3D</b>	two-/three-dimensional
<b>SBEs</b>	semiconductor Bloch equations



# Contents

<b>Zusammenfassung</b>	<b>III</b>
<b>Danksagung</b>	<b>XI</b>
<b>Author's contributions</b>	<b>XIII</b>
<b>1. Introduction</b>	<b>1</b>
<b>2. Theoretical background</b>	<b>5</b>
2.1. The massive Dirac Fermion model . . . . .	5
2.1.1. Massive Dirac Fermions in TMDCs . . . . .	5
2.1.2. Model Hamiltonian . . . . .	6
2.2. Coulomb interaction in layered TMDC structures . . . . .	9
2.2.1. Anisotropic dielectric model . . . . .	10
2.2.2. Finite-thickness effects – Form factor . . . . .	13
2.3. Equation of motion approach . . . . .	14
2.3.1. Band-gap renormalization – Gap equations . . . . .	15
2.3.2. Dirac-Bloch equations . . . . .	16
2.3.3. Screening and Coulomb scattering . . . . .	19
2.3.4. Phonon scattering . . . . .	22
<b>3. Excitonic properties of TMDC mono- and multilayers</b>	<b>23</b>
3.1. Numerically solving gap and Dirac-Wannier equations . . . . .	24
3.2. TMDC monolayers: Theory-experiment comparison . . . . .	28
3.3. Monolayer-to-bulk transition . . . . .	31
3.4. Intra- and interlayer excitons in TMDC hetero-bilayers . . . . .	33
<b>4. Nonlinear optical properties of TMDC monolayers</b>	<b>39</b>
4.1. Quasiequilibrium investigations of MoS <sub>2</sub> . . . . .	39

*Contents*

4.2. Pump-probe simulations of MoTe <sub>2</sub> . . . . .	44
4.2.1. Excitation dynamics and ultrafast band-gap renormalization . .	45
4.2.2. Build-up of the optical gain . . . . .	49
4.2.3. Influence of side-valley effects on the optical gain . . . . .	53
<b>5. Conclusion and outlook</b>	<b>57</b>
<b>A. List of material parameters</b>	<b>59</b>
<b>Appendix</b>	
<b>Bibliography</b>	<b>63</b>
<b>Publications</b>	<b>71</b>
Paper I . . . . .	73
Paper II . . . . .	91
Paper III . . . . .	99
Paper IV . . . . .	113

## Introduction

The worldwide research interest in two-dimensional (2D) materials has drastically increased after K. S. Novoselov, A. K. Geim and coworkers reported the first isolation of graphene – a planar carbon sheet with hexagonal lattice structure – in 2004 [1]. Before then, 2D crystals were believed to be thermodynamically unstable at finite temperatures for many decades. Ironically, the approach that led to the isolation of the first few-to-single-layer samples turned out to be rather simple. Weak van der Waals forces between adjacent layers enable mechanical exfoliation from its three-dimensional (3D) counterpart graphite by repeatedly peeling small surface areas using adhesive tape. Combining unmatched transport [2] and mechanical [3] properties with atomic thickness provides the basis for ultrafast, flexible and transparent electronics. However, a major drawback of graphene lies in its lacking band gap which makes it unsuitable for logic applications. In search for graphene-related materials with sizable band gaps, monolayer transition-metal dichalcogenides (TMDCs) and their heterostructures emerged among the rapidly growing family of 2D materials [4, 5].

In the following, I focus on the group-VI semiconducting representatives  $MX_2$  with transition metal  $M = \text{Mo, W}$  and chalcogen  $X = \text{S, Se, Te}$  that have been investigated within the scope of this thesis<sup>1</sup>. In their bulk form, they had already been studied over 40 years ago with respect to their electronic and optical properties [6–11]. The research interest in TMDCs has been revived with the ability to fabricate single- and few-layer samples. However, it took until 2010 for experimentalists [12, 13] to confirm that TMDCs undergo a transition from an indirect to a direct semiconductor when the number of layers is reduced to a single layer. Unlike many III-V semiconductors with direct band gaps in the center of the Brillouin zone (BZ), the direct gap occurs at the BZ boundaries, denoted as  $K/K'$  points. As a consequence of a lacking inversion center in the monolayer crystal structure,  $K$  and  $K'$  points are nonequivalent, enabling valley-selective excitation via light of opposite circular polarization. The large spin-splitting of the valence bands additionally allows for integrated spin-selective excitation [14]. Encoding and processing information through spin and valley degrees of freedom rather than electric current is explored in the fields called spin- and valleytronics.

---

<sup>1</sup>The studied TMDCs were considered in their trigonal prismatic (hexagonal) phase.

## 1. Introduction

Combining the direct band gap with strong light-matter coupling and transition energies in the visible to near-infrared range, the potential for TMDC monolayers as atomic-scale active material in optoelectronic and photonic devices becomes evident. Indeed, many prototypical monolayer-based devices including logic circuits [15], light-emitting diodes [16], solar cells [17] and low-threshold lasers [18–20], to name only a few, have already been demonstrated. Despite the steadily increasing number of promising applications, the realization of efficient TMDC-based devices on an industrial scale is still in its infancy. Therefore, further research is required in order to get a better understanding of this promising class of materials. The goal of this thesis is to contribute by systematically investigating the  $K/K'$ -point linear and nonlinear optical properties of various TMDC systems via the combined gap and Dirac-Bloch equation approach. The corresponding theoretical framework is presented in chapter 2.

Beginning with the linear optical properties, monolayer TMDCs provide an intriguing platform for fundamental research on excitons in quasi-2D systems. Described as Coulomb-bound electron-hole pairs, excitons govern the  $K/K'$ -point optical properties at low excitation levels and show a remarkable absorbance of up to 20 % of the incident light [21]. Enhanced quantum confinement and reduced intrinsic screening result in binding energies of several hundred meV, revealing an entire exciton series even at room temperature [22, 23]. Observed resonances show strong non-hydrogenic behavior which has been attributed to non-local screening effects of the material [22], however, ignoring the finite out-of-plane extension of the monolayer.

Since monolayers are exposed to the dielectric surrounding, exciton binding energies and band-gap renormalization are extremely susceptible to environmental influences. This enables Coulomb-engineering of the excitonic properties and electronic band gap by attaching them to different substrates [24]. In this context, one may also consider the case where a monolayer is placed between many dielectric sheets of its own material which recovers the bulk limit. Beyond monolayers, the picture of strongly confined quasiparticles in the vicinity of the  $K/K'$  points also applies for bulk TMDCs [25], providing the rare opportunity to observe quasi-2D excitons in 3D systems.

Considering more exotic van der Waals materials, hetero-bilayers with type-II band alignment have emerged as prototypical heterostructures among TMDCs. They consist of two different vertically stacked monolayers, such as  $\text{WSe}_2/\text{MoS}_2$  and  $\text{WSe}_2/\text{MoSe}_2$ , where the relative band alignment of the constituent layers results in a fundamental  $K/K'$ -point transition that is spatially indirect. This represents an ideal situation to investigate interlayer excitons. As a consequence of electrons and holes being confined in different layers, they exhibit an enhanced radiative lifetime compared to the respective intralayer excitons. Strong absorbance at the intralayer-exciton resonances combined with ultrafast charge separation [26, 27] and long-lived interlayer excitons is appealing to applications in photodetection and photovoltaics [28, 29].

In simplified terms, exciting a semiconductor by an intense optical field with photon energies above the electronic band gap eventually generates electron and hole populations in its conduction and valence bands, respectively. This is considered a nonlinear optical process since the photoexcitation of the charge carriers is effectively quadratic in the amplitude of the optical field. In the regime where high carrier densities are

generated, excitons can no longer exist as bound states so that electrons and holes are more precisely described by a Coulomb-correlated plasma. Furthermore, if electron and hole densities are high enough, population inversion can be achieved which in case of a direct transition leads to efficient stimulated emission and optical gain. As direct-gap semiconductors featuring strong light-matter coupling, monolayer TMDCs have potential for efficient gain materials at the atomic scale. First prototypical lasers based on monolayers of  $\text{WS}_2$  [18],  $\text{WSe}_2$  [19] and  $\text{MoTe}_2$  [20] have been realized. While the reported low lasing thresholds cannot be attributed to plasma lasing, population inversion at elevated densities has been achieved in few-layer  $\text{WS}_2$  [30].

Finding new ways to tune a material's electronic and optical band gap is always intriguing since both are key properties when it comes to the engineering of optoelectronic and photonic devices. Injecting significant amounts of excited charge carriers into a TMDC enables Coulomb-engineering of the electronic band gap beyond the static approach of mounting different substrates. Applying high-intensity optical pulses leads to photo-induced band-gap renormalizations of up to several hundred meV on ultrashort timescales [30–32].

In the context of the phenomena highlighted above, chapter 3 summarizes the investigations on the ground-state and linear optical properties of suspended and substrate-supported monolayers of  $\text{MoS}_2$ ,  $\text{MoSe}_2$ ,  $\text{WS}_2$  and  $\text{WSe}_2$ , multilayer structures consisting of single van der Waals bonded  $\text{MoS}_2$  layers, as well as spatially indirect  $\text{WSe}_2/\text{MoS}_2$  and  $\text{WSe}_2/\text{MoSe}_2$  hetero-bilayers. Thereafter, chapter 4 contains a summary of the studies where the optical properties of direct-gap  $\text{MoS}_2$  and  $\text{MoTe}_2$  monolayers were explored in the nonlinear excitation regime. Finally, this work is concluded with an outlook given in chapter 5.



## Theoretical background

Phenomena like the band-gap renormalization, excitonic properties or excitation dynamics of the various TMDC systems, investigated within the scope of this thesis, were calculated within a microscopic many-body quantum theory based on an equation-of-motion (EOM) approach. A summary of the theoretical framework for the near- $K/K'$ -point modeling of linear and nonlinear optical properties of TMDC mono- and multilayer structures is provided within this chapter.

Firstly, the concept of massive Dirac Fermions (MDFs) in TMDCs and the corresponding model Hamiltonian are briefly introduced. Thereafter, a brief description of the applied anisotropic dielectric model for the Coulomb interaction in layered two-dimensional (2D) materials is provided. Finally, the EOM-based gap and Dirac-Bloch equations (GEs and DBEs) [33–36], [I–IV] are presented. Further information beyond this overview can be found in the supplied references.

### 2.1. The massive Dirac Fermion model

The material systems investigated were a stack of  $N$  van der Waals bonded  $\text{MoS}_2$  monolayers [I], suspended and substrate-supported TMDC monolayers ( $N = 1$ ) [I, II, IV] and TMDC hetero-bilayers ( $N = 2$ ) [III]. Major parts of the underlying theory are provided for the more general multilayer case and the mono- and bilayer cases can be deduced by explicitly setting  $N = 1$  and  $N = 2$ , respectively. Furthermore, whenever the monolayer case is considered, layer indices ( $m = n = 1$ ) are automatically dropped throughout this thesis.

#### 2.1.1. Massive Dirac Fermions in TMDCs

Graphene has drawn interest from researchers for many years because of its unique electronic band structure. Within a tight-binding approach [37] it can be shown that the two carbon sublattices, which shape the hexagonal lattice, lead to a description of the graphene band structure by a Dirac-like Hamiltonian [38]. Displaying the same

## 2. Theoretical background

hexagonal symmetry as the crystal lattice, valence and conduction bands intersect at the nonequivalent  $K/K'$  Dirac points that are related by the parity transformation. In the vicinity of these points of high symmetry quasiparticles are formally described as massless Dirac Fermions resulting from their spinor-like operators and linear dispersion. Within the relativistic framework the speed of light is replaced by the Fermi velocity which is about two orders of magnitude smaller [38].

In group-VI TMDCs with the structural formula  $MX_2$  the transition-metal ( $M$ ) and chalcogenide ( $X$ ) atoms form a quasi-2D hexagonal lattice. There, the  $M$  atoms (Mo, W)  $s$ - $p$ -bond with the neighboring  $X$  atoms (S, Se, Te), while the conduction and valence-band states are characterized by the  $d$  orbitals of the  $M$  atoms [39–44]. In TMDCs its not the contributions of the two real-space sublattices but the  $d$  orbitals of the  $M$  atoms that span the pseudospinors [14]. The resulting minimal four-band Hamiltonian describing the single-particle properties in the vicinity of the  $K/K'$  points is given by [14]

$$\hat{H}_0 = \sum_{s,\tau,\mathbf{k}} \hat{\Psi}_{s\tau\mathbf{k}}^\dagger \left( at\mathbf{k} \cdot \hat{\boldsymbol{\sigma}}_\tau + \frac{\Delta}{2}\hat{\sigma}_z - s\tau\lambda\frac{\hat{\sigma}_z - 1}{2} \right) \hat{\Psi}_{s\tau\mathbf{k}}. \quad (2.1)$$

However, the different atomic species cause an on-site energy difference between the two sublattices in these materials which results in an opening of a band gap  $\Delta$  at the  $K/K'$  points. Within the relativistic framework the band gap is understood as the rest energy of MDFs [14]. The quasiparticles – formally described by the two-component pseudospinors  $\hat{\Psi}_{s\tau\mathbf{k}}^{(\dagger)}$  – are characterized by the pseudo quantum number  $\tau$  and true quantum numbers of crystal momentum  $\mathbf{k}$  and spin  $s$ . In particular,  $\tau$  denotes the valley index yielding a combined description for the two nonequivalent  $K$  and  $K'$  points within a single model Hamiltonian. Furthermore,  $2\lambda$ ,  $a$  and  $t$  denote the spin-splitting of the valence bands by spin-orbit coupling, in-plane lattice constant and effective hopping integral, respectively. The Fermi velocity is given by  $v_F = at/\hbar$  and the Pauli matrices  $\hat{\boldsymbol{\sigma}}_\tau = (\tau\hat{\sigma}_x, \hat{\sigma}_y)$  and  $\hat{\sigma}_z$  act on the pseudospinors.

Throughout this thesis, bands with spin-valley combination of  $s\tau = +1$  are referred to as A bands, whereas  $s\tau = -1$  corresponds to the spin-split B bands.

### 2.1.2. Model Hamiltonian

For the TMDC structure of  $N$  electronically independent layers interacting with light we apply the Hamiltonian

$$\hat{H} = \sum_{n=1}^N \hat{H}_0^n + \hat{H}_I + \hat{H}_C, \quad (2.2)$$

where  $\hat{H}_0^n$  contains the single-particle band structure of layer  $n$ ,  $\hat{H}_I$  is the light-matter-interaction Hamiltonian and  $\hat{H}_C$  describes the Coulomb interaction between the quasiparticles. Even in bulk TMDCs one finds that the out-of-plane effective masses are much larger than the in-plane effective masses at the  $K/K'$  points [12]. Therefore,

the out-of-plane kinetic energy becomes negligible supporting the picture of quasiparticles that are well confined within each layer. This observation is essential to model the ground-state and excitonic properties of multilayer TMDC structures based on eq. (2.2). It justifies a quasi-2D description of electronically independent layers, even in the bulk limit.

### Single-particle band structure

To describe the single-particle band structure in the vicinity of the  $K/K'$  points of the individual layers, we adapt the MDF-model Hamiltonian (2.1) introduced above:

$$\hat{H}_0^n = \sum_{\bar{\mathbf{k}}} \hat{\Psi}_{n\bar{\mathbf{k}}}^\dagger \left( \hbar v_{F,n\sigma\tau} \mathbf{k} \cdot \hat{\boldsymbol{\sigma}}_{\tau_n} + \frac{\Delta_{n\sigma\tau}}{2} \hat{\sigma}_z + E_{F,n\sigma\tau} \mathcal{I}_2 \right) \hat{\Psi}_{n\bar{\mathbf{k}}}. \quad (2.3)$$

$\Delta_{n\sigma\tau}$  and  $v_{F,n\sigma\tau}$  now denote the layer, spin and valley-dependent intralayer band-gap energy and Fermi velocity, respectively. To improve readability, the shorthand notation  $\bar{\mathbf{k}} = \{s, \tau, \mathbf{k}\}$  is introduced. While  $\tau$  is understood as the valley index of the joint BZ of the multilayer structure,  $\tau_n$  denotes the valley index of the BZ of the single layer  $n$ . The relation between  $\tau_n$  and  $\tau$  is determined by the stacking of the individual layers. Besides, it is crucial to regard the correct band alignment. Therefore, we include the Fermi levels  $E_{F,n\sigma\tau}$  within the model Hamiltonian. The diagonalization of the Hamiltonian (2.3) within different layers reveals the relativistic band dispersion

$$\epsilon_{n\bar{\mathbf{k}}}^{c/v} = E_{F,n\sigma\tau} \pm \epsilon_{n\bar{\mathbf{k}}} \quad , \quad \epsilon_{n\bar{\mathbf{k}}} = \sqrt{(\Delta_{n\sigma\tau}/2)^2 + (\hbar v_{F,n\sigma\tau} \mathbf{k})^2} \quad (2.4)$$

for the conduction and valence-band states in the vicinity of the  $K/K'$  points.

### Light-matter interaction

With the aid of the minimal substitution principle,  $\hbar \mathbf{k} \rightarrow \hbar \mathbf{k} - \frac{e}{c} \mathbf{A}(t)$ , one obtains the semi-classical light-matter-interaction Hamiltonian as

$$\hat{H}_I = -\frac{e}{c} \sum_{n,\bar{\mathbf{k}}} v_{F,n\sigma\tau} \hat{\Psi}_{n\bar{\mathbf{k}}}^\dagger \mathbf{A}(t) \cdot \hat{\boldsymbol{\sigma}}_{\tau_n} \hat{\Psi}_{n\bar{\mathbf{k}}}, \quad (2.5a)$$

$$= -\frac{e}{c} \sum_{n,\bar{\mathbf{k}}} \sum_{\lambda,\lambda'} v_{F,n\sigma\tau} \langle n\lambda\bar{\mathbf{k}} | \mathbf{A}(t) \cdot \hat{\boldsymbol{\sigma}}_{\tau_n} | n\lambda'\bar{\mathbf{k}} \rangle \hat{a}_{n\lambda\bar{\mathbf{k}}}^\dagger \hat{a}_{n\lambda'\bar{\mathbf{k}}}, \quad (2.5b)$$

where  $\mathbf{A}(t)$  is the classical vector potential. Equation (2.5b) follows from expanding the pseudospinors,  $\hat{\Psi}_{n\bar{\mathbf{k}}} = \sum_{\lambda} |n\lambda\bar{\mathbf{k}}\rangle \hat{a}_{n\lambda\bar{\mathbf{k}}}$ , in terms of the eigenstates of  $\hat{H}_0^n$  and therefore only contains the light-matter coupling to intralayer transitions. Here,  $\hat{a}_{n\lambda\bar{\mathbf{k}}}^{(\dagger)}$  is the annihilation (creation) operator for an electronic state in band  $\lambda$  of layer  $n$  with quantum numbers  $\bar{\mathbf{k}}$ . The product  $\mathbf{A}(t) \cdot \hat{\boldsymbol{\sigma}}_{\tau_n}$  describes the well-known optical selection rules for TMDCs where s-type states with valley index  $\tau_n = \pm 1$  couple to left and

## 2. Theoretical background

right-handed circular polarized light, respectively. However, it also contains the much weaker coupling to d-type states with inverted valley index that has been generally neglected within the numerical simulations.

For the study of interlayer excitons in ref. [III] we employed the more general form

$$\hat{H}_I = -\frac{e}{m_0 c} \sum_{n,m} \sum_{\lambda,\lambda'} \sum_{\bar{\mathbf{k}}} \mathbf{p}_{\lambda\lambda'}^{nm}(\bar{\mathbf{k}}) \mathbf{A}(t) \hat{a}_{n\lambda\bar{\mathbf{k}}}^\dagger \hat{a}_{m\lambda'\bar{\mathbf{k}}}, \quad (2.6)$$

that additionally includes the coupling to interlayer transitions. Here,  $\mathbf{p}_{\lambda\lambda'}^{nm}(\bar{\mathbf{k}})$  represents the matrix elements of the momentum operator related to the transition dipole matrix elements  $\mathbf{d}_{\lambda\lambda'}^{nm}(\bar{\mathbf{k}})$  via

$$\frac{e\hbar}{m_0} \mathbf{p}_{\lambda\lambda'}^{nm}(\bar{\mathbf{k}}) = (\epsilon_{m\bar{\mathbf{k}}}^{\lambda'} - \epsilon_{n\bar{\mathbf{k}}}^{\lambda}) \mathbf{d}_{\lambda\lambda'}^{nm}(\bar{\mathbf{k}}), \quad (2.7)$$

where we generally neglected the contribution of intraband currents. Comparing the intralayer contributions of eq. (2.6) with expression (2.5b) suggests the relation

$$\mathbf{p}_{\lambda\lambda'}^{nn}(\bar{\mathbf{k}}) \cdot \mathbf{A}(t) = m_0 v_{F,n\sigma\tau} \langle n\lambda\bar{\mathbf{k}} | \mathbf{A}(t) \cdot \hat{\boldsymbol{\sigma}}_{\tau_n} | n\lambda'\bar{\mathbf{k}} \rangle \quad (2.8)$$

for intraband light-matter coupling. The validity of relation (2.8) was verified in the vicinity of the  $K/K'$  points, further supporting the applicability of the MDF-model. See ref. [III] for further details. Relation (2.8) had been employed within the numerical simulations contributing to refs. [I, II, IV].

### Coulomb interaction

As pointed out previously, we assume quasiparticles strongly localized within the individual layers. Thus, the Coulomb-interaction Hamiltonian  $\hat{H}_C$  coupling the electronically independent layers is given by

$$\hat{H}_C = \frac{1}{2} \sum_{n,m} \sum_{\mathbf{q} \neq 0} : \hat{\rho}_{\mathbf{q}}^n V_{\mathbf{q}}^{nm} \hat{\rho}_{-\mathbf{q}}^m :, \quad (2.9)$$

where  $\hat{\rho}_{\mathbf{q}}^n$  is the charge-density operator in the  $n$ -th layer and  $: \cdot :$  denotes the normal ordering of operators. Expressing the charge-density operator

$$\hat{\rho}_{\mathbf{q}}^n = \sum_{\bar{\mathbf{k}}} \hat{\Psi}_{n\bar{\mathbf{k}}-\mathbf{q}}^\dagger \hat{\Psi}_{n\bar{\mathbf{k}}} = \sum_{\bar{\mathbf{k}}} \sum_{\lambda,\lambda'} \langle n\lambda\bar{\mathbf{k}} - \mathbf{q} | n\lambda'\bar{\mathbf{k}} \rangle \hat{a}_{n\lambda\bar{\mathbf{k}}-\mathbf{q}}^\dagger \hat{a}_{n\lambda'\bar{\mathbf{k}}} \quad (2.10)$$

with respect to the pseudospinors and transitioning into the conduction and valence-band picture yields

$$\hat{H}_C = \frac{1}{2} \sum_{n,m} \sum_{\bar{\mathbf{k}},\bar{\mathbf{k}}',\mathbf{q} \neq 0} : \hat{\Psi}_{n\bar{\mathbf{k}}-\mathbf{q}}^\dagger \hat{\Psi}_{n\bar{\mathbf{k}}} V_{\mathbf{q}}^{nm} \hat{\Psi}_{m\bar{\mathbf{k}}'+\mathbf{q}}^\dagger \hat{\Psi}_{m\bar{\mathbf{k}}}' : \quad (2.11a)$$

$$= \frac{1}{2} \sum_{n,m} \sum_{\lambda,\lambda',\mu,\mu'} \sum_{\bar{\mathbf{k}},\bar{\mathbf{k}}',\mathbf{q} \neq 0} V_{\mathbf{q},\bar{\mathbf{k}}',\bar{\mathbf{k}}}^{nm,\lambda\mu\mu'\lambda'} \hat{a}_{n\lambda\bar{\mathbf{k}}-\mathbf{q}}^\dagger \hat{a}_{m\mu\bar{\mathbf{k}}'+\mathbf{q}}^\dagger \hat{a}_{m\mu'\bar{\mathbf{k}}}' \hat{a}_{n\lambda'\bar{\mathbf{k}}} \quad (2.11b)$$

where the shorthand notation

$$V_{\mathbf{q}, \bar{\mathbf{k}}', \bar{\mathbf{k}}}^{nm, \lambda \mu \mu' \lambda'} = V_{\mathbf{q}}^{nm} \langle n \lambda \bar{\mathbf{k}} - \mathbf{q} | n \lambda' \bar{\mathbf{k}} \rangle \langle m \mu \bar{\mathbf{k}}' + \mathbf{q} | m \mu' \bar{\mathbf{k}}' \rangle \quad (2.12)$$

for the Coulomb matrix elements is introduced. Besides intraband Coulomb scattering,  $\hat{H}_C$  also contains Auger scattering as well as pair-creation and -annihilation processes [36]. Whereas the former contributions are dominant in wide-gap semiconductors, the latter are a priori not negligible in TMDCs because of the pronounced Coulomb interaction.

### Phonon interaction

At finite temperatures the quasiparticles additionally interact with phonons. The interaction with phonons was included for the first time in our investigations on monolayer MoTe<sub>2</sub> [IV]. In ref. [45], Sohler *et al.* could show that the interaction with longitudinal optical (LO) phonons is the most effective phonon-coupling contribution in monolayer MoTe<sub>2</sub>. Phonon-assisted intraband transitions  $\hat{a}_{\lambda \bar{\mathbf{k}} + \mathbf{q}}^\dagger \hat{a}_{\lambda \bar{\mathbf{k}}}$  were described by the well-established Fröhlich Hamiltonian

$$\hat{H}_{\text{e-LO}} = \sum_{\lambda} \sum_{\bar{\mathbf{k}}, \mathbf{q} \neq 0} g_{\mathbf{q}}^0 \hat{a}_{\lambda \bar{\mathbf{k}} + \mathbf{q}}^\dagger \hat{a}_{\lambda \bar{\mathbf{k}}} (\hat{b}_{\mathbf{q}} + \hat{b}_{-\mathbf{q}}^\dagger), \quad (2.13)$$

where  $\hat{b}_{\mathbf{q}}$  ( $\hat{b}_{-\mathbf{q}}^\dagger$ ) denotes the absorption (emission) of a phonon with momentum  $\pm \mathbf{q}$ . Based on linear response theory, the approach of Sohler *et al.* to derive an analytical expression for the bare Fröhlich interaction  $g_{\mathbf{q}}^0$  in a monolayer surrounded by two dielectrics,  $\epsilon_1$  and  $\epsilon_2$ , is similar to the anisotropic dielectric model for the Coulomb interaction that is presented in the following section. Within the numerical simulations, the proposed analytical expression  $g_{\mathbf{q}}^0 = \frac{C_{\mathcal{Z}}}{\epsilon_{\text{eff}}(\mathbf{q})}$  with  $\epsilon_{\text{eff}}(\mathbf{q}) = \epsilon_{\text{eff}}^0 + r_{\text{eff}}|\mathbf{q}|$  was employed. There,  $\epsilon_{\text{eff}}^0 \approx \frac{\epsilon_1 + \epsilon_2}{2}$  accounts for the background screening of the surrounding dielectrics and  $r_{\text{eff}}|\mathbf{q}|$  introduces non-local screening effects to the unscreened interaction  $C_{\mathcal{Z}}$ . The respective parameters for monolayer MoTe<sub>2</sub> are explicitly stated in ref. [45].

## 2.2. Coulomb interaction in layered TMDC structures

In the following, an overview of our approach to model the Coulomb potential in a stack of  $N$  identical TMDC layers, sandwiched between two dielectrics that are characterized by their background dielectric constants  $\epsilon_1$  and  $\epsilon_2$ , is given. A sketch of the model system is depicted in the left panel of figure 2.1. Differences in the modeling for the hetero-bilayers [III], schematically shown in the right panel of fig. 2.1, are added at the end of sec. 2.2.1. This part closes with a summary on the inclusion of finite-thickness effects in theory and how they have been treated numerically.

## 2. Theoretical background

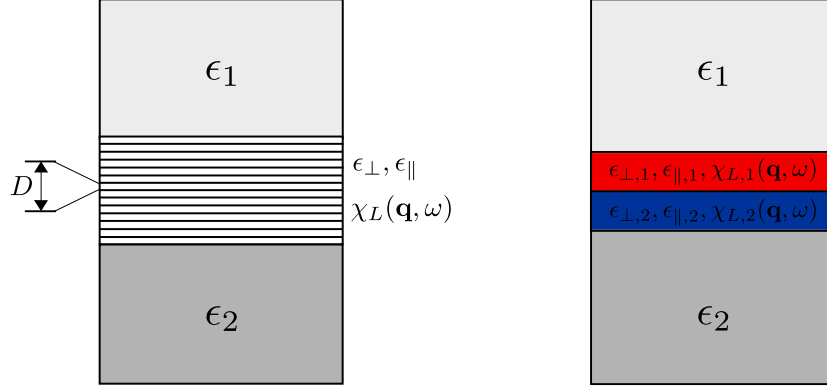


Figure 2.1.: Schematics of the model systems. Left: Slab geometry for the stack of  $N$  identical van der Waals bonded monolayers. The distance between the layers is denoted by  $D$ . (According to ref. [I].) Right: Slab geometry for the TMDC hetero-bilayers investigated in ref. [III].

### 2.2.1. Anisotropic dielectric model

The derivation, following the description of ref. [I], is based on the solution of Maxwell's equations where the anisotropic ansatz

$$\mathbf{D}(\mathbf{r}, \omega) = \epsilon_{\parallel}(z)\mathbf{E}_{\parallel}(\mathbf{r}, \omega) + \epsilon_z(z)E_z(\mathbf{r}, \omega)\mathbf{e}_z + 4\pi\mathbf{P}(\mathbf{r}, \omega) \quad (2.14)$$

is made for the electric displacement field. Here,  $\epsilon_{\parallel}(z)$  and  $\epsilon_z(z)$  contain the non-resonant background contributions of the anisotropic dielectric tensor. The explicit expressions are given by

$$\epsilon_{\parallel}(z) = \begin{cases} \epsilon_1, & z < 0, \\ \epsilon_{\parallel}, & 0 \leq z \leq L, \\ \epsilon_2, & L < z \end{cases} \quad \epsilon_z(z) = \begin{cases} \epsilon_1, & z < 0, \\ \epsilon_{\perp}, & 0 \leq z \leq L, \\ \epsilon_2, & L < z \end{cases}$$

for the multilayer structure of thickness  $L = ND$  that is encapsulated by two dielectrics. The monolayer thickness  $D$  is given by the out-of-plane lattice constant of the van der Waals bonded layers.

Within this approach, the induced polarization  $\mathbf{P}(\mathbf{r}, \omega)$  contains the entirety of non-local, frequency-dependent resonant contributions. Here, it is crucial to distinguish between longitudinal and transverse parts of the in-plane polarization. While the longitudinal part introduces non-local screening effects, the transverse part leads to the radiative coupling of the individual layers. The effects of radiative coupling were not studied within the scope of this thesis and will therefore be ignored in the following. We refer the interested reader to ref. [46] concerning radiative coupling effects in few-layer TMDCs.

Inserting the anisotropic ansatz in Maxwell's equation  $\nabla \cdot \mathbf{D}(\mathbf{r}, \omega) = 4\pi\rho_{\text{ext}}(\mathbf{r}, \omega)$  yields the differential equation

$$\left(\epsilon_{\parallel}\nabla_{\parallel} \cdot \mathbf{E}_{\parallel}(\mathbf{r}, \omega) + \epsilon_{\perp}\partial_z E_z(\mathbf{r}, \omega)\right) = 4\pi\left(\rho_{\text{ext}}(\mathbf{r}, \omega) - \nabla_{\parallel} \cdot \mathbf{P}_{\parallel}^L(\mathbf{r}, \omega)\right), \quad (2.15)$$

for the region  $0 \leq z \leq L$ , wherein resonant out-of-plane contributions are already neglected. After introducing scalar and vector potentials of the electric and magnetic fields, applying the generalized Coulomb gauge and performing a Fourier transform with respect to the in-plane coordinates, Poisson's equation

$$\left(-\epsilon_{\perp}\partial_z^2 + \epsilon_{\parallel}\mathbf{q}_{\parallel}^2\right)\phi(\mathbf{q}_{\parallel}, z, \omega) = 4\pi\left(\rho_{ext}(\mathbf{q}_{\parallel}, z, \omega) - i\mathbf{q}_{\parallel} \cdot \mathbf{P}_{\parallel}^L(\mathbf{q}_{\parallel}, z, \omega)\right) \quad (2.16)$$

for the scalar potential  $\phi(\mathbf{q}_{\parallel}, z, \omega)$  is obtained in the mixed  $(\mathbf{q}_{\parallel}, z)$  representation. In order to avoid confusion based on mixed  $(\mathbf{q}_{\parallel}, z)$  and  $(\mathbf{q}_{\parallel}, q_z)$  representations, the subscript “ $\parallel$ ” labeling in-plane wave and position vectors is included in this section.

The resonant contributions  $\mathbf{P}_{\parallel}^L(\mathbf{q}_{\parallel}, z, \omega)$  were treated within linear response theory. On the length scale of the optical wavelength it is appropriate to decompose

$$\mathbf{P}_{\parallel}^L(\mathbf{q}_{\parallel}, z, \omega) = -ie^2\mathbf{q}_{\parallel} \sum_{n=1}^N \chi_L(\mathbf{q}_{\parallel}, \omega)\phi(\mathbf{q}_{\parallel}, z_n, \omega)\delta(z - z_n) \quad (2.17)$$

into resonant 2D contributions, where  $\chi_L(\mathbf{q}_{\parallel}, \omega)$  is the longitudinal susceptibility of a single layer within the structure and  $z_n = (n - 1/2)D$  denotes the central position of the  $n$ -th layer.

The solution of eq. (2.16) for  $\rho_{ext}(\mathbf{q}_{\parallel}, z, \omega) = \delta(z - z')$  and without resonant contributions yields the bare 2D Coulomb potential  $\phi_0^{2D}(\mathbf{q}_{\parallel}, z, z')$  for the considered slab geometry. There, the homogeneous Poisson equations for the dielectrics outside of the multilayer structure provide additional boundary conditions yielding the explicit analytical expression that is stated for  $\epsilon_1 = 1$  (vacuum) and  $\epsilon_2 = \epsilon_S$  (substrate) in the appendix of ref. [1]. Once  $\phi_0^{2D}(\mathbf{q}_{\parallel}, z, z')$  is known, the non-locally screened Coulomb potential  $\phi^{2D}(\mathbf{q}_{\parallel}, z, z', \omega)$  is determined by inserting eq. (2.17) in eq. (2.16) employing the concept of Green functions.

The numerical calculation of the non-locally screened Coulomb potential becomes particularly efficient assuming point charges localized at the center of the individual layers,  $\rho_{ext}(\mathbf{q}_{\parallel}, z, \omega) = \delta(z - z_m)$ , finally yielding

$$\phi^{2D}(\mathbf{q}_{\parallel}, z_n, z_m, \omega) = \sum_{l=1}^N \epsilon_{res}^{-1}(\mathbf{q}_{\parallel}, z_n, z_l, \omega)\phi_0^{2D}(\mathbf{q}_{\parallel}, z_l, z_m), \quad (2.18)$$

$$\epsilon_{res}(\mathbf{q}_{\parallel}, z_n, z_l, \omega) = \delta_{nl} + e^2\mathbf{q}_{\parallel}^2\chi_L(\mathbf{q}_{\parallel}, \omega)\phi_0^{2D}(\mathbf{q}_{\parallel}, z_n, z_l). \quad (2.19)$$

Here, the matrix  $\epsilon_{res}(\mathbf{q}_{\parallel}, z_n, z_l, \omega)$  contains the non-local, frequency-dependent resonant screening contributions induced by the point charges within the layered structure. Solved via matrix inversion<sup>1</sup> at low numerical cost, eqs. (2.18) and (2.19) provide an efficient method to model non-local screening effects in layered TMDCs. Related treatments for the modeling of the Coulomb potential and non-local screening effects in

<sup>1</sup>For the numerical solution of linear-algebra-related problems, e.g. matrix inversions and diagonalizations, the routines of the LAPACK library [47] were used.

## 2. Theoretical background

low-dimensional materials can be found in refs. [48–52]. From eq. (2.19) the relation  $\chi_L(\mathbf{q}_{\parallel}, \omega) = -\Pi(\mathbf{q}_{\parallel}, \omega)/\mathbf{q}_{\parallel}^2$  between the longitudinal susceptibility and the ground-state polarization function  $\Pi(\mathbf{q}_{\parallel}, \omega)$  of the single layer can be deduced. Within the numerical simulations the long-wavelength limit  $\Pi_{s\tau}(\mathbf{q}_{\parallel}, 0) = -\frac{1}{6\pi} \frac{q_{\parallel}^2}{\Delta_{s\tau}}$  [53] has been applied. The summation over both indices then yields  $\Pi(\mathbf{q}_{\parallel}, 0)$ .

For the calculations contributing to the results presented within this thesis, the parameters for the nonresonant background dielectric constants  $\epsilon_{\parallel}^{\text{B}}$  and  $\epsilon_{\perp}^{\text{B}}$  were taken from bulk density functional theory (DFT) calculations. However, the DFT dielectric tensor contains both resonant and nonresonant contributions. Therefore, the resonant screening contributions arising from the bands under consideration had to be separated from the nonresonant background contributions of all other bands in order to avoid double counting. This succeeded by solving Poisson's equation within the bulk limit ( $N \gg 1$ ). Here, one obtains for the Coulomb potential by Fourier transform of eq. (2.16) with respect to the out-of-plane coordinate

$$\phi^{3\text{D}}(\mathbf{q}_{\parallel}, q_z) = \frac{4\pi}{\epsilon_{\perp} q_z^2 + \mathbf{q}_{\parallel}^2 (\epsilon_{\parallel} + 4\pi e^2 \chi_L(\mathbf{q}_{\parallel}, 0)/D)} \quad (2.20)$$

in the static limit. Comparing eq. (2.20) with the 3D anisotropic Coulomb potential,  $4\pi/(\epsilon_{\perp}^{\text{B}} q_z^2 + \epsilon_{\parallel}^{\text{B}} \mathbf{q}_{\parallel}^2)$ , suggests the connection

$$\epsilon_{\parallel}^{\text{B}} = \epsilon_{\parallel} + \lim_{\mathbf{q}_{\parallel} \rightarrow 0} 4\pi e^2 \chi_L(\mathbf{q}_{\parallel}, 0)/D \quad (2.21)$$

between the bulk ( $\epsilon_{\parallel}^{\text{B}}$ ) and 2D nonresonant ( $\epsilon_{\parallel}$ ) in-plane dielectric constants. Relation (2.21) had been employed for the deduction of all 2D nonresonant in-plane dielectric constants from their bulk counterparts contributing to the results presented within this work. They are listed in app. A. Since resonant out-of-plane contributions were neglected, the nonresonant out-of-plane dielectric constants  $\epsilon_{\perp}$  were directly given by the bulk values  $\epsilon_{\perp}^{\text{B}}$ .

### Hetero-bilayer environment

The modeling of the Coulomb potential for the hetero-bilayer environment contributing to results achieved in ref. [III] is accordingly. Differences occur in the solution  $\phi_0^{2\text{D}}(\mathbf{q}_{\parallel}, z, z')$  of Poisson's equation because of the deviating slab geometry (right panel of fig. 2.1). It is parameterized by

$$\epsilon_{\parallel}(z) = \begin{cases} \epsilon_1, & z < 0, \\ \epsilon_{\parallel,1}, & 0 \leq z \leq D_1, \\ \epsilon_{\parallel,2}, & D_1 < z \leq L, \\ \epsilon_2, & L < z \end{cases}, \quad \epsilon_z(z) = \begin{cases} \epsilon_1, & z < 0, \\ \epsilon_{\perp,1}, & 0 \leq z \leq D_1, \\ \epsilon_{\perp,2}, & D_1 < z \leq L, \\ \epsilon_2, & L < z \end{cases},$$

where  $L = D_1 + D_2$  is the thickness of the bilayer structure. See app. A for a compact analytical expression of  $\phi_0^{2\text{D}}(\mathbf{q}_{\parallel}, z_n, z_m)$  at the layer centers, i.e. the numerically relevant cases  $z_1 = D_1/2$  and  $z_2 = D_1 + D_2/2$ . Note that in this case the resonant contributions to the longitudinal susceptibility  $\chi_{L,n}(\mathbf{q}_{\parallel}, \omega)$  also become layer dependent.

### 2.2.2. Finite-thickness effects – Form factor

The assumption of point charges localized in the center of the respective layers ignores the finite extension of the layers in  $z$ -direction. This is corrected by substituting  $\delta(z - z_n)$  with a more general expression  $\rho_{\mathbf{q}_{\parallel}}(z - z_n)$  for the distribution of the external charges in eq. (2.16) which allows for a finite out-of-plane extension,  $|z - z_n| \lesssim D$ , of the charges within the layers. Likewise, one obtains

$$\mathbf{P}_{\parallel}^L(\mathbf{q}_{\parallel}, z, \omega) = -ie^2 \mathbf{q}_{\parallel} \sum_{n=1}^N \chi_L(\mathbf{q}_{\parallel}, \omega) \rho_{\mathbf{q}_{\parallel}}(z - z_n) \int_{z_n - D/2}^{z_n + D/2} dz' \phi(\mathbf{q}_{\parallel}, z', \omega) \rho_{-\mathbf{q}_{\parallel}}(z' - z_n) \quad (2.22)$$

for the resonant contributions to the longitudinal polarization. Defining the bare quasi-2D Coulomb potential between charges within layers  $n$  and  $m$  as

$$\phi_0^{\text{q2D}}(\mathbf{q}_{\parallel}, z_n, z_m) \equiv \int_{z_m - D/2}^{z_m + D/2} dz \int_{z_n - D/2}^{z_n + D/2} dz' \rho_{-\mathbf{q}_{\parallel}}(z' - z_n) \phi_0^{2\text{D}}(\mathbf{q}_{\parallel}, z, z') \rho_{\mathbf{q}_{\parallel}}(z - z_m), \quad (2.23)$$

the previously introduced matrix-inversion scheme remains applicable for the quasi-2D treatment. Within the numerical simulations the relation

$$\phi_0^{\text{q2D}}(\mathbf{q}_{\parallel}, z_n, z_m) = \phi_0^{2\text{D}}(\mathbf{q}_{\parallel}, z_n, z_m) F(\mathbf{q}_{\parallel}) \quad (2.24)$$

was employed, where finite-thickness effects are projected into the form factor  $F(\mathbf{q}_{\parallel})$ .

The non-locally screened quasi-2D Coulomb interaction  $V_{\mathbf{q}_{\parallel}}^{nm} \equiv \frac{e^2}{\mathcal{A}} \phi^{\text{q2D}}(\mathbf{q}_{\parallel}, z_n, z_m, \omega)$  that enters the Coulomb-interaction Hamiltonian (2.9) is then obtained by matrix inversion, where  $\phi_0^{\text{q2D}}(\mathbf{q}_{\parallel}, z_n, z_m)$  replaces the strict-2D Coulomb potential  $\phi_0^{2\text{D}}(\mathbf{q}_{\parallel}, z_n, z_m)$  in eqs. (2.18) and (2.19). Here,  $\mathcal{A}$  denotes the normalization area. The projection of finite-thickness effects into the form factor has the numerical advantage that two-fold out-of-plane integration can be avoided during matrix inversion, leading to a highly efficient scheme to model the Coulomb interaction in layered quasi-2D materials.

For the results achieved in refs. [I–III], the form factor had been approximated by  $F(\mathbf{q}_{\parallel}) \approx e^{-|\mathbf{q}_{\parallel}|d}$  corresponding to the 2D Ohno potential. Therein, the effective thickness parameter  $d$  was introduced in order to reproduce and predict experimentally observable features. In contrast to the distance  $D$  of the van der Waals bonded layers, the effective thickness parameter  $d$  is a free parameter.

*Ab-initio* based form factors have been employed for the first time in our numerical simulations on monolayer MoTe<sub>2</sub> contributing to the results presented in ref. [IV]. Their derivation shall be sketched briefly in the following. We refer to refs. [54, 55] for detailed descriptions. Starting point is the second-quantized Coulomb-interaction Hamiltonian

$$\hat{H}_C = \frac{1}{2} \int_{\mathcal{V}} d^3r \int_{\mathcal{V}} d^3r' \hat{\Psi}^\dagger(\mathbf{r}) \hat{\Psi}^\dagger(\mathbf{r}') V(\mathbf{r}, \mathbf{r}') \hat{\Psi}(\mathbf{r}') \hat{\Psi}(\mathbf{r}) \quad (2.25)$$

## 2. Theoretical background

in real-space representation, where

$$V(\mathbf{r}, \mathbf{r}') = \frac{e^2}{\sqrt{\epsilon_{\parallel}^2 \epsilon_{\perp}}} \frac{1}{\sqrt{(\mathbf{r}_{\parallel} - \mathbf{r}'_{\parallel})^2 / \epsilon_{\parallel} + (z - z')^2 / \epsilon_{\perp}}} \quad (2.26)$$

is the out-of-plane anisotropic Coulomb interaction [56],  $\hat{\Psi}(\mathbf{r})$  is the fermionic field operator and  $\mathcal{V}$  denotes the normalization volume. By applying the in-plane Bloch ansatz  $\hat{\Psi}(\mathbf{r}) = \sum_{\lambda, \mathbf{k}_{\parallel}} e^{i\mathbf{k}_{\parallel} \cdot \mathbf{r}} u_{\lambda \mathbf{k}_{\parallel}}(\mathbf{r}) \hat{a}_{\lambda \mathbf{k}_{\parallel}}$ , where  $u_{\lambda \mathbf{k}_{\parallel}}(\mathbf{r})$  is a lattice periodic function, and by in-plane Fourier expansion  $V(\mathbf{r}, \mathbf{r}') = \sum_{\mathbf{q}_{\parallel} \neq 0} V_{\mathbf{q}_{\parallel}}(z, z') e^{i\mathbf{q}_{\parallel} \cdot (\mathbf{r}_{\parallel} - \mathbf{r}'_{\parallel})}$  of the Coulomb interaction, one obtains the momentum-space representation

$$\hat{H}_C = \frac{1}{2} \sum_{\lambda, \lambda', \mu, \mu'} \sum_{\mathbf{k}_{\parallel}, \mathbf{k}'_{\parallel}, \mathbf{q}_{\parallel} \neq 0} V_{\mathbf{q}_{\parallel}, \mathbf{k}'_{\parallel}, \mathbf{k}_{\parallel}}^{\lambda \mu \mu' \lambda'} \hat{a}_{\lambda \mathbf{k}_{\parallel} - \mathbf{q}_{\parallel}}^{\dagger} \hat{a}_{\mu \mathbf{k}'_{\parallel} + \mathbf{q}_{\parallel}}^{\dagger} \hat{a}_{\mu' \mathbf{k}'_{\parallel}} \hat{a}_{\lambda' \mathbf{k}_{\parallel}}. \quad (2.27)$$

Through the course of the calculation, the Coulomb-interaction matrix elements reveal themselves as

$$V_{\mathbf{q}_{\parallel}, \mathbf{k}'_{\parallel}, \mathbf{k}_{\parallel}}^{\lambda \mu \mu' \lambda'} = V_{\mathbf{q}_{\parallel}}^{2D} F_{\mathbf{q}_{\parallel}, \mathbf{k}'_{\parallel}, \mathbf{k}_{\parallel}}^{\lambda \mu \mu' \lambda'} \quad , \quad V_{\mathbf{q}_{\parallel}}^{2D} = \frac{2\pi e^2}{\sqrt{\epsilon_{\parallel} \epsilon_{\perp}} \mathcal{A}} \frac{1}{|\mathbf{q}_{\parallel}|}, \quad (2.28)$$

$$F_{\mathbf{q}_{\parallel}, \mathbf{k}'_{\parallel}, \mathbf{k}_{\parallel}}^{\lambda \mu \mu' \lambda'} = \int_{\mathcal{V}_{\text{uc}}} d^3 r \int_{\mathcal{V}_{\text{uc}}} d^3 r' u_{\lambda \mathbf{k}_{\parallel} - \mathbf{q}_{\parallel}}^*(\mathbf{r}) u_{\mu \mathbf{k}'_{\parallel} + \mathbf{q}_{\parallel}}^*(\mathbf{r}') e^{-\sqrt{\frac{\epsilon_{\parallel}}{\epsilon_{\perp}}} |\mathbf{q}_{\parallel}| |z - z'|} u_{\mu' \mathbf{k}'_{\parallel}}(\mathbf{r}') u_{\lambda' \mathbf{k}_{\parallel}}(\mathbf{r}), \quad (2.29)$$

where  $\mathcal{V}_{\text{uc}}$  denotes the unit-cell volume. Comparing eqs. (2.28) and (2.24), one easily identifies  $F_{\mathbf{q}_{\parallel}, \mathbf{k}'_{\parallel}, \mathbf{k}_{\parallel}}^{\lambda \mu \mu' \lambda'}$  as the generalized form factors.

The investigations of refs. [54, 55] have shown that  $F_{\mathbf{q}_{\parallel}, \mathbf{k}'_{\parallel}, \mathbf{k}_{\parallel}}^{\lambda \mu \mu' \lambda'}$  is of minor angular dependence for wave vectors  $\mathbf{q}_{\parallel}$  with  $|\mathbf{q}_{\parallel}| = |\mathbf{k}_{\parallel} - \mathbf{k}'_{\parallel}|$  in the vicinity of the  $K/K'$  points. Thus, it was appropriate to employ isotropic form factors  $F^{\lambda \mu \mu' \lambda'}(\mathbf{q}_{\parallel})$  for the modeling of the  $K/K'$ -point optical properties. The form factors were approximated using the explicit expression  $F^{\lambda \mu \mu' \lambda'}(\mathbf{q}_{\parallel}) \approx e^{-\sum_{j=1}^2 b_j |\mathbf{q}_{\parallel}|^j}$  yielding a very good approximation for wave vectors  $|\mathbf{q}_{\parallel}| \lesssim 0.6 \text{ \AA}^{-1}$  [55]. Further details on the numerical treatment of the generalized form factors as well as their fit parameters  $b_j$  are provided within app. A.

## 2.3. Equation of motion approach

Analog to the semiconductor-Bloch-equation (SBE) approach [57–59] – that is a widely used method to describe the optical properties of semiconductors and semiconductor heterostructures – the GEs and DBEs are based on the EOM concept for the microscopic polarizations and the occupation probabilities. Hence, the EOM concept is introduced briefly in the following.

The time dynamics of an observable  $\langle \hat{O} \rangle$  of a quantum-mechanical system are determined by its Hamiltonian  $\hat{H}$  via the Heisenberg EOM

$$\frac{d}{dt}\langle \hat{O} \rangle = \frac{i}{\hbar}\langle [\hat{H}, \hat{O}] \rangle + \frac{\partial}{\partial t}\langle \hat{O} \rangle, \quad (2.30)$$

where  $[\cdot, \cdot]$  indicates the commutator of the two operators. Even though not stated explicitly,  $\hat{O} = \hat{O}(t)$  is a time-dependent operator.

### 2.3.1. Band-gap renormalization – Gap equations

In ref. [36] the ground-state renormalization in TMDC systems via the GEs is motivated as follows: The solution of the EOM for the interband polarization in absence of an external field is not stationary, if one assumes an unexcited semiconductor described by the unrenormalized bands as initial state. Therefore, the unrenormalized state cannot be the true ground state of the TMDC system.

For derivation of the TMDC multilayer-structure GEs we consider the system Hamiltonian  $\hat{H}$  of eq. (2.2) in the pseudospinor basis, i.e. by including the explicit expressions (2.3), (2.5a) and (2.11a) for the single-particle, light-matter, and Coulomb-interaction Hamiltonians, respectively. The following summary is according to ref. [1] that follows the original refs. [33, 36]. Initially, one defines the dynamical variables  $\Gamma_{n\bar{k}} \equiv \langle \hat{b}_{n\bar{k}}^\dagger \hat{b}_{n\bar{k}} \rangle - \langle \hat{a}_{n\bar{k}}^\dagger \hat{a}_{n\bar{k}} \rangle$  and  $\Pi_{n\bar{k}} \equiv \langle \hat{b}_{n\bar{k}}^\dagger \hat{a}_{n\bar{k}} \rangle$ , where  $\hat{a}_{n\bar{k}}^{(\dagger)}$  and  $\hat{b}_{n\bar{k}}^{(\dagger)}$  are Fermi operators annihilating (creating) a particle in the basis states of the pseudospinor of layer  $n$ . Subsequently, the derivation of the EOM for  $\Gamma_{n\bar{k}}$  and  $\Pi_{n\bar{k}}$  in the absence of an external optical field yields

$$i\hbar \frac{d}{dt} \Pi_{n\bar{k}} = \tilde{\Delta}_{n\bar{k}} \Pi_{n\bar{k}} + \tau_n \hbar \tilde{v}_{F,n\bar{k}} k e^{i\tau_n \theta_k} \Gamma_{n\bar{k}}, \quad (2.31)$$

$$\frac{\hbar}{2} \frac{d}{dt} \Gamma_{n\bar{k}} = \Im \left[ \Pi_{n\bar{k}} \tau_n \hbar \tilde{v}_{F,n\bar{k}} k e^{-i\tau_n \theta_k} \right], \quad (2.32)$$

on the Hartree-Fock (HF) level. There, the renormalized Fermi-velocity and band-gap energy of layer  $n$  reveal themselves as

$$\tilde{\Delta}_{n\bar{k}} = \Delta_{n\sigma\tau} + \hat{V}^n[\Gamma_{n\sigma\tau}], \quad (2.33)$$

$$\tau \hbar \tilde{v}_{F,n\bar{k}} k e^{i\tau_n \theta_k} = \tau \hbar v_{F,n\sigma\tau} k e^{i\tau_n \theta_k} - \hat{V}^n[\Pi_{n\sigma\tau}], \quad (2.34)$$

respectively, where  $\hat{V}^n[f] \equiv \sum_{\mathbf{k}' \neq \mathbf{k}} V_{|\mathbf{k}-\mathbf{k}'|}^{nn} f_{\mathbf{k}'}$  is introduced to shorten the notation. In order to determine the ground-state renormalization in the vicinity of the  $K/K'$  points for each layer, the static solutions of the coupled equations (2.31) and (2.32) are required. Applying the relation,  $1 = \Gamma_{n\bar{k}}^2 + 4|\Pi_{n\bar{k}}|^2$  for the coherent state then leads to the linking of the variables  $\Gamma_{n\bar{k}}$  with  $\tilde{\Delta}_{n\bar{k}}$  and  $\Pi_{n\bar{k}}$  with  $\tilde{v}_{F,n\bar{k}}$ , and finally yields the

## 2. Theoretical background

coupled set of integral equations

$$\tilde{\Delta}_{n\bar{k}} = \Delta_{ns\tau} + \sum'_{\bar{k}' \neq \bar{k}} V_{|k-k'|}^{nn} \frac{\tilde{\Delta}_{n\bar{k}'}}{\sqrt{\tilde{\Delta}_{n\bar{k}'}^2 + (2\hbar\tilde{v}_{F,n\bar{k}'}k')^2}}, \quad (2.35)$$

$$\tilde{v}_{F,n\bar{k}} = v_{F,ns\tau} + \sum'_{\bar{k}' \neq \bar{k}} V_{|k-k'|}^{nn} \frac{k'}{k} \frac{\tilde{v}_{F,n\bar{k}'}}{\sqrt{\tilde{\Delta}_{n\bar{k}'}^2 + (2\hbar\tilde{v}_{F,n\bar{k}'}k')^2}} \cos(\theta_k - \theta_{k'}), \quad (2.36)$$

namely the GEs. Here, the notation  $\sum'_{\bar{k}' \neq \bar{k}} \equiv \sum_{\bar{k}' \neq \bar{k}} \delta_{s,s'} \delta_{\tau,\tau'}$  is introduced to clarify that the Coulomb interaction is assumed to conserve spin and valley indices.

The GEs determine the mean-field Hamiltonian

$$\hat{H}_0^{MF} = \sum_{n,\bar{k}} \hat{\Psi}_{n\bar{k}}^\dagger \left( \hbar\tilde{v}_{F,n\bar{k}} \mathbf{k} \cdot \hat{\sigma}_{\tau_n} + \frac{\tilde{\Delta}_{n\bar{k}}}{2} \hat{\sigma}_z + E_{F,ns\tau} \mathcal{I}_2 \right) \hat{\Psi}_{n\bar{k}} \quad (2.37)$$

for renormalized ground state of the multilayer TMDC structure in the vicinity of the  $K/K'$  points. Expanding the two-component pseudospinors

$$\hat{\Psi}_{n\bar{k}}^{(\dagger)} = \sum_{\lambda} |n\lambda\bar{k}\rangle \hat{a}_{n\lambda\bar{k}}^{(\dagger)} \quad (2.38)$$

in terms of the eigenstates,  $|nc\bar{k}\rangle = (u_{n\bar{k}}, v_{n\bar{k}} e^{-i\tau_n\theta_k})^T$  and  $|nv\bar{k}\rangle = (v_{n\bar{k}} e^{i\tau_n\theta_k}, -u_{n\bar{k}})^T$ , of the mean-field Hamiltonian yields the renormalized conduction and valence bands

$$\Sigma_{n\bar{k}}^{c/v,0} = E_{F,ns\tau} \pm \tilde{\epsilon}_{n\bar{k}} \quad , \quad \tilde{\epsilon}_{n\bar{k}} = \frac{1}{2} \sqrt{\tilde{\Delta}_{n\bar{k}}^2 + (2\hbar\tilde{v}_{F,n\bar{k}}k)^2} \quad (2.39)$$

of the individual layers. Here, the MDF-model prefactors,  $u_{n\bar{k}} = \sqrt{(\tilde{\epsilon}_{n\bar{k}} + \tilde{\Delta}_{n\bar{k}}/2)/2\tilde{\epsilon}_{n\bar{k}}}$  and  $v_{n\bar{k}} = \sqrt{(\tilde{\epsilon}_{n\bar{k}} - \tilde{\Delta}_{n\bar{k}}/2)/2\tilde{\epsilon}_{n\bar{k}}}$ , are given with respect to the renormalized ground state. The superscript “0” marks the zero-density limit.

### 2.3.2. Dirac-Bloch equations

The linear and nonlinear optical properties of the different TMDC systems investigated within the scope of this thesis were calculated based on the DBEs. Analog to the SBEs, they describe the coupled dynamics of conduction and valence-band occupations, and interband polarizations in the vicinity of the  $K/K'$  points of semiconducting TMDC systems via first-order integro-differential equations. Based on the solution of these microscopic equations for various excitation conditions the macroscopic response of the material can be computed.

Firstly, the DBEs in the linear excitation regime, that have been employed for the investigations on the linear optical properties of various TMDC mono- and multilayer systems [I, III], will be presented. Thereafter, the DBEs in the nonlinear excitation regime are introduced. In the nonlinear excitation regime we restricted ourselves to the investigation of TMDC monolayers, i.e. monolayer MoS<sub>2</sub> [II] and MoTe<sub>2</sub> [IV], as they are direct-gap semiconductors and thus candidates for 2D gain materials.

### Linear excitation regime

For the derivation of the DBEs we considered the system Hamiltonian (2.2) in the conduction and valence-band picture employing the renormalized ground state based on the solution of the GEs. Defining the time-dependent interband polarizations  $P_{\bar{\mathbf{k}}}^{mn} \equiv \langle \hat{a}_{m\nu\bar{\mathbf{k}}}^\dagger \hat{a}_{n\lambda\bar{\mathbf{k}}} \rangle$  and occupation numbers  $f_{\lambda\bar{\mathbf{k}}}^n \equiv \langle \hat{a}_{n\lambda\bar{\mathbf{k}}}^\dagger \hat{a}_{n\lambda\bar{\mathbf{k}}} \rangle$ , the DBE in the linear excitation regime ( $f_{c\bar{\mathbf{k}}}^n = 1 - f_{v\bar{\mathbf{k}}}^n = 0$ ) is given by

$$i\hbar \frac{d}{dt} P_{\bar{\mathbf{k}}}^{mn} = \left( \Sigma_{n\bar{\mathbf{k}}}^{c,0} - \Sigma_{m\bar{\mathbf{k}}}^{v,0} \right) P_{\bar{\mathbf{k}}}^{mn} - \sum'_{\bar{\mathbf{k}}' \neq \bar{\mathbf{k}}} \left[ V_{\bar{\mathbf{k}}-\bar{\mathbf{k}}', \bar{\mathbf{k}}', \bar{\mathbf{k}}}^{mn, cvvc} P_{\bar{\mathbf{k}}'}^{mn} + V_{\bar{\mathbf{k}}-\bar{\mathbf{k}}', \bar{\mathbf{k}}', \bar{\mathbf{k}}}^{mn, ccvv} P_{\bar{\mathbf{k}}'}^{nm*} \right] - \frac{e}{m_0 c} \mathbf{p}_{cv}^{nm}(\bar{\mathbf{k}}) \cdot \mathbf{A}(t) + i\hbar \frac{d}{dt} P_{\bar{\mathbf{k}}}^{mn} \Big|_{\text{corr.}}. \quad (2.40)$$

Therein, the microscopic polarizations correspond to interlayer transitions for  $m \neq n$  and to intralayer transitions for  $m = n$ . Furthermore,  $\frac{d}{dt} P_{\bar{\mathbf{k}}}^{mn} \Big|_{\text{corr.}}$  contains all many-body correlations beyond HF approximation. For the simulations contributing to refs. [I, III], the latter were treated by a phenomenological dephasing  $\hbar\gamma$ .

By Fourier-transforming  $P_{\bar{\mathbf{k}}}^{mn}(t)$  and  $\mathbf{A}(t)$  into frequency space, the linear optical susceptibility is obtained by

$$\chi(\omega) = \frac{ec}{m_0 \omega^2} \frac{\delta}{\delta \mathbf{A}(\omega)} \sum_{m,n,\bar{\mathbf{k}}} \mathbf{p}_{cv}^{nm}(\bar{\mathbf{k}}) P_{\bar{\mathbf{k}}}^{mn}(\omega), \quad (2.41)$$

where  $P_{\bar{\mathbf{k}}}^{mn}(\omega)$  and  $\mathbf{A}(\omega)$  denote the frequency spectra of the microscopic polarizations and vector potential, respectively.

Expanding the microscopic polarizations in terms of the eigenstates of the Dirac-Wannier equation (DWE)

$$\left( \Sigma_{n\bar{\mathbf{k}}}^{c,0} - \Sigma_{m\bar{\mathbf{k}}}^{v,0} \right) \psi_{\nu}^{mn}(\bar{\mathbf{k}}) - \sum'_{\bar{\mathbf{k}}' \neq \bar{\mathbf{k}}} \left[ V_{\bar{\mathbf{k}}-\bar{\mathbf{k}}', \bar{\mathbf{k}}', \bar{\mathbf{k}}}^{mn, cvvc} \psi_{\nu}^{mn}(\bar{\mathbf{k}}') + V_{\bar{\mathbf{k}}-\bar{\mathbf{k}}', \bar{\mathbf{k}}', \bar{\mathbf{k}}}^{mn, ccvv} \psi_{\nu}^{nm*}(\bar{\mathbf{k}}') \right] = E_{s\tau\nu}^{mn} \psi_{\nu}^{mn}(\bar{\mathbf{k}}), \quad (2.42)$$

## 2. Theoretical background

the susceptibility can alternatively be expressed through Elliott's formula [60]

$$\chi(\omega) = -\frac{e^2}{m_0^2 \omega^2} \sum_{m,n} \sum_{s,\tau,\nu} \left( \frac{\mathcal{F}_{s\tau\nu}^{mn}}{\hbar(\omega + i\gamma) - E_{s\tau\nu}^{mn}} - \frac{\mathcal{F}_{s\tau\nu}^{mn}}{\hbar(\omega + i\gamma) + E_{s\tau\nu}^{mn}} \right), \quad (2.43)$$

where the eigenvalues  $E_{s\tau\nu}^{mn}$  and eigenstates  $\psi_{\nu}^{mn}(\bar{\mathbf{k}})$  are the resonance energies and  $\mathbf{k}$ -space wavefunctions of the respective intra- and interlayer excitons. Furthermore,  $\mathcal{F}_{s\tau\nu}^{mn} = \left| \sum_{\mathbf{k}} \mathbf{p}_{cv}^{nm}(\bar{\mathbf{k}}) \psi_{\nu}^{mn}(\bar{\mathbf{k}}) \right|^2$  correlates to the oscillator strength of the transition. The entirety of excitonic resonance energies contributing to the work presented in this thesis were calculated with the aid of the DWE (2.42). Additionally, radiative decay rates of the respective excitonic transitions, stated in ref. [III], were calculated via  $\Gamma_{s\tau\nu}^{mn} = \frac{4\pi}{n_1+n_2} \frac{e^2}{c} \frac{\mathcal{F}_{s\tau\nu}^{mn}}{m_0^2 E_{s\tau\nu}^{mn}}$  [61]. Here,  $n_1$  and  $n_2$  denote the refractive indices of the bottom and top dielectric sheets, respectively. The optical absorption spectrum is computed from the linear optical susceptibility via

$$\alpha(\omega) = \frac{4\pi n_1 \frac{\omega}{c} \Im[\chi(\omega)]}{\left| (n_1 + n_2)/2 - 2\pi i \frac{\omega}{c} \chi(\omega) \right|^2}. \quad (2.44)$$

### Nonlinear excitation regime

In the nonlinear excitation regime nontrivial conduction and valence-band occupations are generated within the considered monolayers. The DBEs in their more general form,

$$i\hbar \frac{d}{dt} P_{\bar{\mathbf{k}}} = (\Sigma_{\bar{\mathbf{k}}}^c - \Sigma_{\bar{\mathbf{k}}}^v) P_{\bar{\mathbf{k}}} - (f_{\bar{\mathbf{k}}}^v - f_{\bar{\mathbf{k}}}^c) \Omega_{\bar{\mathbf{k}}} + i\hbar \frac{d}{dt} P_{\bar{\mathbf{k}}} \Big|_{\text{corr.}}, \quad (2.45)$$

$$\frac{\hbar}{2} \frac{d}{dt} f_{\bar{\mathbf{k}}}^{c/v} = \pm \Im [P_{\bar{\mathbf{k}}} \Omega_{\bar{\mathbf{k}}}^*] + \frac{\hbar}{2} \frac{d}{dt} f_{\bar{\mathbf{k}}}^{c/v} \Big|_{\text{corr.}}, \quad (2.46)$$

are formally equivalent to the widely used SBEs. The major difference arises from the fact that the MDF-model Hamiltonian already provides a detailed description of the Coulomb and momentum matrix elements in the vicinity of the  $K/K'$  points. This results in rather complex expressions for the renormalized single-particle energies,  $\Sigma_{\bar{\mathbf{k}}}^c$  and  $\Sigma_{\bar{\mathbf{k}}}^v$ , and the generalized Rabi energy  $\Omega_{\bar{\mathbf{k}}}$ . We refer to ref. [IV] for the detailed expressions where the same notation is employed. Many-body correlations beyond HF approximation are again contained within  $\frac{d}{dt} P_{\bar{\mathbf{k}}} \Big|_{\text{corr.}}$  and  $\frac{d}{dt} f_{\bar{\mathbf{k}}}^{c/v} \Big|_{\text{corr.}}$ .

As already shown in ref. [62], the ground-state renormalization before excitation is very well contained within  $\Sigma_{\bar{\mathbf{k}}}^c$  and  $\Sigma_{\bar{\mathbf{k}}}^v$ , whereas the contribution of  $\Omega_{\bar{\mathbf{k}}}$  to the ground-state renormalization is negligibly small for the investigated wide-gap TMDC systems. Therefore, contributions from Auger-recombination processes – corresponding

to  $V_{\bar{\mathbf{k}}-\bar{\mathbf{k}}',\bar{\mathbf{k}}',\bar{\mathbf{k}}}^{\text{cvcc}}$  and related matrix elements – could be neglected, effectively yielding

$$\Sigma_{\bar{\mathbf{k}}}^{\text{c}} = \epsilon_{\bar{\mathbf{k}}}^{\text{c}} - \sum'_{\bar{\mathbf{k}}' \neq \bar{\mathbf{k}}} \left[ V_{\bar{\mathbf{k}}-\bar{\mathbf{k}}',\bar{\mathbf{k}}',\bar{\mathbf{k}}}^{\text{cccc}} - V_{\bar{\mathbf{k}}-\bar{\mathbf{k}}',\bar{\mathbf{k}}',\bar{\mathbf{k}}}^{\text{cvcv}} \right] f_{\bar{\mathbf{k}}}'^{\text{c}}, \quad (2.47)$$

$$\Sigma_{\bar{\mathbf{k}}}^{\text{v}} = \epsilon_{\bar{\mathbf{k}}}^{\text{v}} - \sum'_{\bar{\mathbf{k}}' \neq \bar{\mathbf{k}}} \left[ V_{\bar{\mathbf{k}}-\bar{\mathbf{k}}',\bar{\mathbf{k}}',\bar{\mathbf{k}}}^{\text{vvvv}} - V_{\bar{\mathbf{k}}-\bar{\mathbf{k}}',\bar{\mathbf{k}}',\bar{\mathbf{k}}}^{\text{vcvc}} \right] f_{\bar{\mathbf{k}}}'^{\text{v}}, \quad (2.48)$$

$$\Omega_{\bar{\mathbf{k}}} = \frac{e}{m_0 c} \mathbf{p}_{\text{cv}}(\bar{\mathbf{k}}) \cdot \mathbf{A}(t) + \sum'_{\bar{\mathbf{k}}' \neq \bar{\mathbf{k}}} \left[ V_{\bar{\mathbf{k}}-\bar{\mathbf{k}}',\bar{\mathbf{k}}',\bar{\mathbf{k}}}^{\text{cvvc}} P_{\bar{\mathbf{k}}}' + V_{\bar{\mathbf{k}}-\bar{\mathbf{k}}',\bar{\mathbf{k}}',\bar{\mathbf{k}}}^{\text{ccvv}} P_{\bar{\mathbf{k}}}'^* \right]. \quad (2.49)$$

It is important to point out that here  $\Sigma_{\bar{\mathbf{k}}}^{\text{c}}$  and  $\Sigma_{\bar{\mathbf{k}}}^{\text{v}}$  are expressed in terms of the unrenormalized bands,  $\epsilon_{\bar{\mathbf{k}}}^{\text{c}}$  and  $\epsilon_{\bar{\mathbf{k}}}^{\text{v}}$ . Considering a TMDC monolayer in its ground state before excitation ( $f_{\bar{\mathbf{k}}}^{\text{c}} = 1 - f_{\bar{\mathbf{k}}}^{\text{v}} = 0$ ), the second term in eq. (2.48) leads to a ground-state renormalization of the valence bands. Numerically verified, this so-called Coulomb-hole contribution precisely accounts for the ground-state renormalization that is expected from the solution of the previously introduced GEs (2.35) and (2.36) on the HF level. Whereas contributions from Auger-recombination processes are negligible, pair-creation and -annihilation processes,  $\propto V_{\bar{\mathbf{k}}-\bar{\mathbf{k}}',\bar{\mathbf{k}}',\bar{\mathbf{k}}}^{\text{vcvc}}$ , provide a small contribution to the ground-state renormalization of the valence bands.

It is equally common to formulate equations (2.45) and (2.46) as well as the renormalized single-particle and generalized Rabi energies in the electron-hole picture. Described as a lacking valence-band electron, the hole is consequently of opposite charge, energy, momentum and spin. The transition from the conduction and valence-band to the electron-hole picture is introduced by

$$\begin{aligned} \epsilon_{\bar{\mathbf{k}}}^{\text{c}} &\rightarrow \epsilon_{\bar{\mathbf{k}}}^{\text{e}} \quad , \quad \epsilon_{\bar{\mathbf{k}}}^{\text{v}} \rightarrow -\epsilon_{-\bar{\mathbf{k}}}^{\text{h}}, \\ f_{\bar{\mathbf{k}}}^{\text{c}} &\rightarrow f_{\bar{\mathbf{k}}}^{\text{e}} \quad , \quad f_{\bar{\mathbf{k}}}^{\text{v}} \rightarrow (1 - f_{-\bar{\mathbf{k}}}^{\text{h}}), \end{aligned}$$

and equivalently for the renormalized single-particle energies.

### 2.3.3. Screening and Coulomb scattering

Recalling the EOM approach, the two-particle nature of the Coulomb interaction couples the dynamics of the stated single-particle expectation values,  $P_{\bar{\mathbf{k}}}$  and  $f_{\bar{\mathbf{k}}}^{\text{c/v}}$ , to two-particle quantities, marking the first step of an infinite hierarchy of equations [63]. However, the cluster expansion [59, 63–65] provides a systematic scheme to truncate this hierarchy on a desired level of approximation.

A truncation at the singlet level yields the previously introduced EOM in HF approximation. In order to describe phenomena like plasma screening, the excitation-induced dephasing (EID) of the microscopic polarizations and the relaxation dynamics of the conduction and valence-band occupations, next-level clusters need to be included. In the following an overview of the dynamic treatment of screening and Coulomb scattering is given which is based on the theory provided by refs. [59, 63–65] and follows the description of ref. [IV]. For simplicity, spin and valley indices are dropped. Specifics on the numerical implementation will be provided in sec. 4.2.

## 2. Theoretical background

The second level of the cluster expansion includes the dynamics of the occurring two-particle correlations (doublets)

$$\Delta C_{q,p,k}^{\lambda\mu\mu'\lambda'} = C_{q,p,k}^{\lambda\mu\mu'\lambda'} - C_{q,p,k}^{\lambda\mu\mu'\lambda'} \Big|_{\text{S}} \quad , \quad C_{q,p,k}^{\lambda\mu\mu'\lambda'} = \langle \hat{a}_{\lambda\mathbf{k}}^\dagger \hat{a}_{\mu\mathbf{p}-\mathbf{q}}^\dagger \hat{a}_{\mu'\mathbf{k}'} \hat{a}_{\lambda\mathbf{k}-\mathbf{q}} \rangle. \quad (2.50)$$

They are formally defined as the difference between the two-particle expectation values  $C_{q,p,k}^{\lambda\mu\mu'\lambda'}$  and their respective singlet contributions  $C_{q,p,k}^{\lambda\mu\mu'\lambda'} \Big|_{\text{S}}$ . Since the dynamics of two-particle expectation values couple to three-particle quantities, a hierarchy truncation at the doublet level requires a factorization of occurring three-particle expectation values into singlet and doublet contributions [63]. Effects of three-particle correlations (triplets) are then reduced to the inclusion of a phenomenological dephasing  $\hbar\gamma_{\text{T}}$ .

Based on the system Hamiltonian, the EOM for the two-particle correlations of interest read

$$i\hbar \frac{d}{dt} \Delta C_{q,p,k}^{\lambda\mu\mu\lambda'} = \left( \Delta \Sigma_{q,p,k}^{\lambda\mu\mu\lambda'} - i\hbar\gamma_{\text{T}} \right) \Delta C_{q,p,k}^{\lambda\mu\mu\lambda'} + \left( f_{\mathbf{p}-\mathbf{q}}^\mu - f_{\mathbf{p}}^\mu \right) I_{q,k}^{\lambda\lambda'} + S_{q,p,k}^{\lambda\mu\mu\lambda'} + \text{remaining doublets}, \quad (2.51)$$

where the shorthand notation  $\Delta \Sigma_{q,p,k}^{\lambda\mu\mu\lambda'} = \Sigma_{\mathbf{k}-\mathbf{q}}^{\lambda'} + \Sigma_{\mathbf{p}}^\mu - \Sigma_{\mathbf{p}-\mathbf{q}}^\mu - \Sigma_{\mathbf{k}}^\lambda$  for the renormalized single-particle energies is introduced. Originating from the singlet factorization, the non-screening related source terms read

$$S_{q,p,k}^{\lambda\mu\mu\lambda'} = V_q \left( P_{\mathbf{k}}^{\lambda\lambda'} f_{\mathbf{p}-\mathbf{q}}^\mu \bar{f}_{\mathbf{p}}^\mu - P_{\mathbf{k}-\mathbf{q}}^{\lambda\lambda'} \bar{f}_{\mathbf{p}-\mathbf{q}}^\mu f_{\mathbf{p}}^\mu \right) + V_{\mathbf{k}-\mathbf{p}} P_{\mathbf{k}}^{\lambda\mu} \sum_{\gamma} P_{\mathbf{p}-\mathbf{q}}^{\mu\gamma} \left( P_{\mathbf{k}-\mathbf{q}}^{\gamma\lambda'} - \delta_{\gamma\lambda'} \right) - V_{\mathbf{k}-\mathbf{p}} P_{\mathbf{p}}^{\lambda\mu} \sum_{\gamma} P_{\mathbf{k}-\mathbf{q}}^{\gamma\lambda'} \left( P_{\mathbf{p}-\mathbf{q}}^{\mu\gamma} - \delta_{\gamma\mu} \right) + V_{\mathbf{k}-\mathbf{p}} \left( P_{\mathbf{p}-\mathbf{q}}^{\mu\lambda'} - P_{\mathbf{k}-\mathbf{q}}^{\mu\lambda'} \right) \sum_{\gamma} P_{\mathbf{k}}^{\lambda\gamma} P_{\mathbf{p}}^{\gamma\mu}, \quad (2.52)$$

where  $\bar{f}_{\mathbf{k}}^\lambda = 1 - f_{\mathbf{k}}^\lambda$  is used to shorten the notation. They represent in- and out-scattering contributions of the different single-particle quantities [63]. Depending on the index combinations, we identify carrier-carrier ( $\lambda = \lambda'$ ) and polarization-carrier ( $\lambda \neq \lambda'$ ) scattering. Within this description contributions from Auger recombinations as well as pair-creation and -annihilation processes, whose timescales were numerically found to be several orders of magnitude longer, are already neglected. Furthermore, the weak angular and  $\mathbf{k}, \mathbf{k}'$ -dependence of the remaining intraband Coulomb matrix elements is also negligible.

Assuming that plasma screening is the dominant correlation effect at elevated charge-carrier densities, it is useful to separate the screening contribution  $\left( f_{\mathbf{p}-\mathbf{q}}^\mu - f_{\mathbf{p}}^\mu \right) I_{q,k}^{\lambda\lambda'}$  from the singlet-doublet factorization. Therein,

$$I_{q,k}^{\lambda\lambda'} = V_q \sum_{\mu,p} C_{q,p,k}^{\lambda\mu\mu\lambda'} \quad (2.53)$$

denote the density-assisted transition ( $\lambda \neq \lambda'$ ) and occupation ( $\lambda = \lambda'$ ) probabilities. Its singlet contribution  $I_{q,k}^{\lambda\mu\mu\lambda'} \Big|_{\text{S}}$  describes the renormalization of the single-particle and

Rabi energies, whereas the fully correlated part  $\Delta I_{q,k}^{\lambda\mu\mu\lambda'}$  couples to the dynamics of the microscopic polarizations and the conduction and valence-band occupations via

$$i\hbar \frac{d}{dt} P_{\mathbf{k}}^{\lambda\lambda'} \Big|_{\text{el.}} = \sum_{\mathbf{q} \neq 0} \left[ \Delta I_{q,\mathbf{k}}^{\lambda\lambda'} - \Delta I_{q,\mathbf{k}+\mathbf{q}}^{\lambda\lambda'} \right], \quad (2.54)$$

where the notation  $P_{\mathbf{k}}^{\lambda\lambda'} = \langle a_{\lambda\mathbf{k}}^\dagger a_{\lambda'\mathbf{k}} \rangle$ ,  $f_{\mathbf{k}}^\lambda = P_{\mathbf{k}}^{\lambda\lambda}$  is used.

Neglecting remaining doublet contributions – marking the second-Born approximation – an analytical solution of eq. (2.51) is possible in frequency space under the assumption of quasistatic occupations  $f_{\mathbf{k}}^\lambda$ . Executing summations over  $\mu$  and  $\mathbf{p}$  yields

$$I_{q,\mathbf{k}}^{\lambda\lambda'}(\omega) = W_{q,\mathbf{k}}^{\lambda\lambda'}(\omega) \left[ \sum_{\mu\mathbf{p}} C_{q,\mathbf{p},\mathbf{k}}^{\lambda\mu\mu\lambda'}(\omega) \Big|_{\text{S}} + T_{q,\mathbf{k}}^{\lambda\lambda'}(\omega) \right], \quad (2.55)$$

$$\Delta I_{q,\mathbf{k}}^{\lambda\lambda'}(\omega) = W_{q,\mathbf{k}}^{\lambda\lambda'}(\omega) \left[ \Pi_{q,\mathbf{k}}^{\lambda\lambda'}(\omega) I_{q,\mathbf{k}}^{\lambda\mu\mu\lambda'} \Big|_{\text{S}} + T_{q,\mathbf{k}}^{\lambda\lambda'}(\omega) \right], \quad (2.56)$$

where the dynamically screened Coulomb matrix elements are explicitly given by

$$W_{q,\mathbf{k}}^{\lambda\lambda'}(\omega) = V_{\mathbf{q}} + V_{\mathbf{q}} \Pi_{q,\mathbf{k}}^{\lambda\lambda'}(\omega) W_{q,\mathbf{k}}^{\lambda\lambda'}(\omega) = \frac{V_{\mathbf{q}}}{1 - \Pi_{q,\mathbf{k}}^{\lambda\lambda'}(\omega) V_{\mathbf{q}}}. \quad (2.57)$$

Therein,

$$\Pi_{q,\mathbf{k}}^{\lambda\lambda'}(\omega) = \Pi_{\mathbf{q}}(\omega + (\Sigma_{\mathbf{k}}^\lambda - \Sigma_{\mathbf{k}-\mathbf{q}}^{\lambda'})/\hbar + i\gamma_{\text{T}}), \quad (2.58)$$

$$\Pi_{\mathbf{q}}(\omega) = \sum_{\mu\mathbf{p}} \frac{f_{\mathbf{p}-\mathbf{q}}^\mu - f_{\mathbf{p}}^\mu}{\hbar\omega + \Sigma_{\mathbf{p}-\mathbf{q}}^\mu - \Sigma_{\mathbf{p}}^\mu} \quad (2.59)$$

denotes the dynamic Lindhard polarization function. Note that the bare Coulomb interaction  $V_{\mathbf{q}}$  already contains local and non-local contributions to the background screening based on the solution of Poisson's equation, eqs. (2.18) and (2.19) including finite-thickness effects, for  $m = n = 1$  and  $z_1 = D/2$ . Furthermore, the remaining single-particle sources are contained within

$$T_{q,\mathbf{k}}^{\lambda\lambda'}(\omega) = \sum_{\mu\mathbf{p}} \frac{S_{q,\mathbf{p},\mathbf{k}}^{\lambda\mu\mu\lambda'}(\omega)}{\hbar\omega - \Delta\Sigma_{q,\mathbf{p},\mathbf{k}}^{\lambda\mu\mu\lambda'} + i\hbar\gamma_{\text{T}}}. \quad (2.60)$$

Evidently, the contribution  $(f_{\mathbf{p}-\mathbf{q}}^\mu - f_{\mathbf{p}}^\mu) I_{q,\mathbf{k}}^{\lambda\lambda'}$  induces screening of the Coulomb matrix elements within the singlet and remaining scattering contributions. Noticeably, the unscreened HF renormalizations  $\Delta\Sigma_{q,\mathbf{p},\mathbf{k}}^{\lambda\mu\mu\lambda'}$  enter the energy denominators of  $\Pi_{q,\mathbf{k}}^{\lambda\lambda'}(\omega)$  and  $T_{q,\mathbf{k}}^{\lambda\lambda'}(\omega)$  at this point. They should be replaced by their screened counterparts,  $\tilde{\Delta\Sigma}_{q,\mathbf{p},\mathbf{k}}^{\lambda\mu\mu\lambda'}$ , when including next-level clusters. Additionally neglecting the scattering contributions  $T_{q,\mathbf{k}}^{\lambda\lambda'}(\omega)$  within eqs. (2.55) and (2.56) yields the screened HF approximation. There, the bare Coulomb matrix elements are replaced by their screened counterparts within the renormalized single-particle and generalized Rabi energies.

### 2.3.4. Phonon scattering

The inclusion of the Fröhlich Hamiltonian (2.13) yields a coupling of the microscopic polarizations and conduction and valence-band occupations to the phonon-assisted density matrices  $G_{q,k}^{\lambda\lambda',+} = \langle \hat{a}_{\lambda k}^\dagger \hat{a}_{\lambda' k-q} \hat{b}_{-q}^\dagger \rangle$  and  $G_{q,k}^{\lambda\lambda',-} = \langle \hat{a}_{\lambda k}^\dagger \hat{a}_{\lambda' k-q} \hat{b}_q \rangle$  via

$$i\hbar \frac{d}{dt} P_k^{\lambda\lambda'} \Big|_{\text{ph.}} = \sum_{q \neq 0} g_q^0 \left[ G_{q,k}^{\lambda\lambda',+} + G_{q,k}^{\lambda\lambda',-} - G_{q,k+q}^{\lambda\lambda',+} - G_{q,k+q}^{\lambda\lambda',-} \right]. \quad (2.61)$$

These are quantities that are formed by two electron operators and one phonon operator, resulting in the first step of an infinite hierarchy on their own. Following the description of ref. [58], the EOM for the phonon-assisted density matrices are then computed with respect to the mean-field Hamiltonian of the system that is coupled to a phonon bath. In order to form a closed set of equations for the respective phonon-scattering contributions, the phonon-assisted density matrices are factorized into electronic single-particle expectation values and phonon occupation numbers  $n_q$ . In terms of the phonon-scattering of the conduction and valence-band occupations, a formal integration in the long-time regime (Markov approximation) yields the quantum-Boltzmann-like scattering rates [58] that were employed to compute the intraband carrier thermalization in monolayer MoTe<sub>2</sub>.

Within the phonon-scattering of the microscopy polarizations, where  $G_{q,k}^{v,c,-}$  and related matrices enter, a Markovian treatment needed to be avoided. Based on the description of ref. [58], the time evolution of the former is given by

$$\begin{aligned} i\hbar \frac{d}{dt} G_{q,k}^{v,c,-} = & - \left( \Sigma_k^v - \Sigma_{k-q}^c - \hbar\omega_q + i\hbar\eta \right) G_{q,k}^{v,c,-} \\ & + g_q^0 \left( n_q f_{k-q}^c + (1+n_q) \bar{f}_{k-q}^c \right) P_k \\ & - g_q^0 \left( n_q \bar{f}_k^v + (1+n_q) f_k^v \right) P_{k-q}, \end{aligned} \quad (2.62)$$

where  $\hbar\omega_q$  is the LO-phonon energy and  $\hbar\eta$  denotes a phenomenological dephasing. Motivated by the approach described in the previous section, the analytical solution

$$G_{q,k}^{v,c,-}(\omega) = g_q^0 \frac{\left( n_q f_{k-q}^c + (1+n_q) \bar{f}_{k-q}^c \right) P_k(\omega) - \left( n_q \bar{f}_k^v + (1+n_q) f_k^v \right) P_{k-q}(\omega)}{\hbar\omega + \Sigma_k^v - \Sigma_{k-q}^c - \hbar\omega_q + i\hbar\eta} \quad (2.63)$$

is obtained by Fourier transform assuming quasistatic occupations. By the example of eq. (2.63) it becomes evident that the phonon-assisted density matrices still contain the unscreened renormalized single-particle energies and Fröhlich interaction. In order to treat carrier and phonon-scattering on the same level of approximation, both were replaced by their respective screened counterparts in all phonon-scattering contributions.

## Excitonic properties of TMDC mono- and multilayers

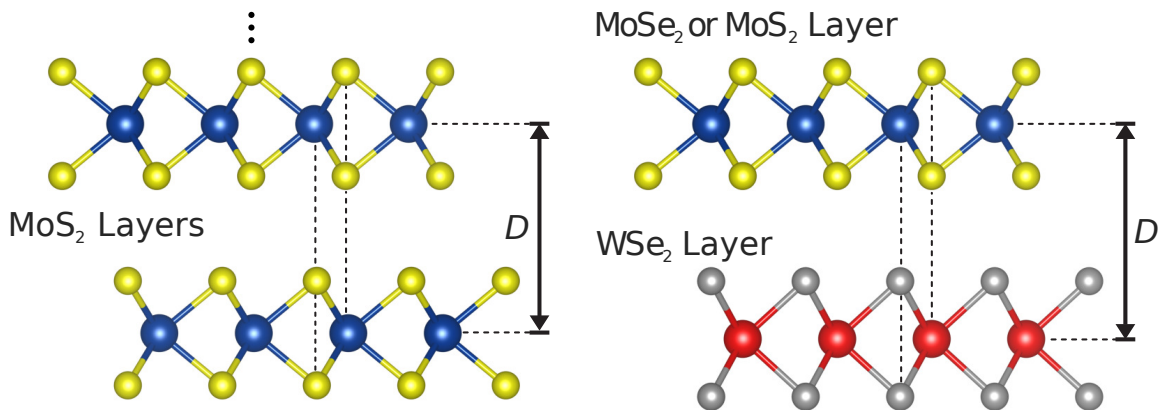


Figure 3.1.: Left: AA'-stacked MoS<sub>2</sub> monolayers with interlayer spacing  $D$  considered in ref. [I]. The Mo atoms are depicted in blue, whereas the S atoms are shown in yellow. Right: A MoSe<sub>2</sub> or MoS<sub>2</sub> monolayer is stacked on top of a WSe<sub>2</sub> monolayer in AA'-stacking, where the S/Se (yellow) or Se (grey) atoms of the one layer are placed on top of a W (red) or Mo (blue) atom in the other layer. (Adapted from ref. [III].)

This chapter contains a summary of our research on the linear optical properties of monolayer, homogeneous-multilayer and hetero-bilayer TMDC structures, complemented by details concerning the numerical implementation. The results presented in the following contributed to refs. [I] and [III].

Firstly, the approach of numerically solving the GEs and DWE, in order to compute the ground-state and excitonic properties of the stated TMDC systems, is introduced. Based on the determination of the effective-thickness parameter that accounted for the finite out-of-plane extension of the layers, theory-experiment comparisons for concrete monolayer TMDC systems are drawn. Next, the monolayer-to-bulk transition and

### 3. Excitonic properties of TMDC mono- and multilayers

its influence on band-gap renormalization and excitonic resonances was investigated for the case of AA'-stacked MoS<sub>2</sub> monolayers. In this configuration, schematically shown in the left part of fig. 3.1, neighboring layers are mirror-identical copies of each other, related by parity transformation. Thus, the sign of the valley index  $\tau_n = -\tau_{n+1}$  alternates for neighboring layers  $n$  and  $n + 1$ . Allowing for a finite overlap of the localized electron and hole distributions of neighboring layers, a pronounced interlayer-exciton resonance emerged in the optical spectra leading to a reinterpretation of the A-exciton series in bulk MoS<sub>2</sub>.

In ref. [III] we investigated AA'-stacked strained and unstrained TMDC heterostructures, WSe<sub>2</sub>/MoS<sub>2</sub> and WSe<sub>2</sub>/MoSe<sub>2</sub>, schematically depicted in the right part of fig. 3.1. In the final section of this chapter details of the numerical implementation of the DBE (2.40), that built the foundation for the calculation of the optical spectra of the investigated hetero-bilayers, are provided along with the results.

## 3.1. Numerically solving gap and Dirac-Wannier equations

In order to approach the problem of solving the GEs (2.35) and (2.36) and DWE (2.42), unspecified TMDC monolayers ( $n = m = 1$ ) were considered initially, whereby the Coulomb interaction between electrons and holes was generalized. In ref. [I], the Ohno potential  $V_{\mathbf{q}} = 2\pi e^2 e^{-q\bar{d}}/(\kappa q)$  was motivated to describe a monolayer embedded in bulk,  $\kappa = \sqrt{\epsilon_{\parallel}^B \epsilon_{\perp}^B}$ , or the long-wavelength limit of a monolayer encapsulated by two dielectrics,  $\kappa = (\epsilon_1 + \epsilon_2)/2$ . In this context it is advantageous to introduce scaled units. We expressed energies, velocities and lengths in terms of single-particle band gap  $\Delta \equiv \Delta_{s\tau}$ , Fermi velocity  $v_F \equiv v_{F,s\tau}$  and Compton wavelength of the electrons and holes  $\lambda_C = 2\hbar v_F/\Delta$ , respectively, where spin and valley indices are dropped for simplicity. For the non-interacting single-particle dispersion one then finds  $\bar{\epsilon}_{\mathbf{k}}^{c/v} = \pm \bar{\epsilon}_{\mathbf{k}}$ , with  $\bar{\epsilon}_{\mathbf{k}} = \epsilon_{\mathbf{k}}/\Delta = \frac{1}{2}\sqrt{1 + \bar{k}^2}$  and  $\bar{k} = \lambda_C k$ , where the Fermi level is set to zero.

The inclusion of non-local resonant screening contributions from the bands under consideration then yields

$$\bar{V}_{\bar{\mathbf{q}}} = \frac{\pi}{\mathcal{A}} \frac{\alpha}{\epsilon_{\text{res}}(\bar{\mathbf{q}}) \bar{q}} e^{-\bar{q}\bar{d}} \quad , \quad \epsilon_{\text{res}}(\bar{\mathbf{q}}) = 1 + \frac{2}{3} \alpha \bar{q} e^{-\bar{q}\bar{d}} \quad (3.1)$$

the for scaled quasi-2D Coulomb potential. Therein,  $\alpha = e^2/\kappa\hbar v_F$  is the effective fine-structure constant. It is a measure of the relative strength of the Coulomb interaction, which is in the range of  $3/\kappa$  to  $5/\kappa$  for the material parameters stated in tab. A.1.

Evidently, the solutions of the GEs and DWE are characterized by the parameters  $\alpha$  and  $\bar{d}$ . The 2D limit,  $\bar{d} = 0$ , of the scaled Coulomb potential (3.1) is given by the Rytova-Keldysh potential [66, 67] for a point charge in a thin film. It has been widely applied to investigate the excitonic properties of TMDC systems [22, 48, 68–71], but lacks the influence of finite-thickness effects.

### 3.1. Numerically solving gap and Dirac-Wannier equations

The numerical implementation of the GEs (2.35) and (2.36) had been thoroughly discussed in ref. [62], thereby only a condensed version shall be provided here. Since the GEs are nonlinear coupled integral equations, they must be solved self-consistently. Experience has shown that this succeeds within a few ten iterations, even for rather large values of the Coulomb coupling, by entering the non-interacting ground-state properties

$$\tilde{\Delta}_k^{[0]} = \Delta \quad , \quad \tilde{v}_{F,k}^{[0]} = v_F \quad , \quad \tilde{\epsilon}_k^{[0]} = \sqrt{(\Delta/2)^2 + (2\hbar v_F k)^2} \quad (3.2)$$

within the first iteration step. The numerical solution of the  $n$ -th iteration step is then given by

$$\begin{aligned} \tilde{\Delta}_k^{[n]} &= \Delta + \frac{1}{2} \sum_{k'} dk' k' V_{kk'}^0 \frac{\tilde{\Delta}_{k'}^{[n-1]}}{\tilde{\epsilon}_{k'}^{[n-1]}} \quad , \quad \tilde{v}_{F,k}^{[n]} = v_F + \frac{1}{2} \sum_{k'} dk' \frac{(k')^2}{k} V_{kk'}^1 \frac{\tilde{v}_{F,k'}^{[n-1]}}{\tilde{\epsilon}_{k'}^{[n-1]}} \quad , \\ \tilde{\epsilon}_k^{[n]} &= \frac{1}{2} \sqrt{(\tilde{\Delta}_k^{[n]})^2 + (2\hbar \tilde{v}_{F,k}^{[n]} k)^2} \quad , \quad V_{kk'}^l = \frac{\mathcal{A}}{2\pi^2} \int_0^\pi d\theta V_{|k-k'|} \cos(l\theta) \quad , \end{aligned}$$

where  $V_{kk'}^l$  are the angular-averaged Coulomb matrix elements for angular-momentum quantum number  $l$  and  $\theta \equiv \theta_k - \theta_{k'}$  denotes the angle between  $\mathbf{k}$  and  $\mathbf{k}'$ . The angular integration was generally performed by using a Gauss-Chebyshev quadrature [72]. Furthermore,  $dk$  is the step size of the equidistant  $|\mathbf{k}|$ -grid.

The numerical solution of the GEs is depicted in fig. 3.2 for values of the effective fine-structure constant of  $\alpha = 1.0, 3.0, 5.0$  and a representative thickness parameter of  $d = \lambda_C$ . In particular, the renormalized band gap  $\tilde{\Delta}_k$  and Fermi velocity  $\tilde{v}_{F,k}$  (inset)

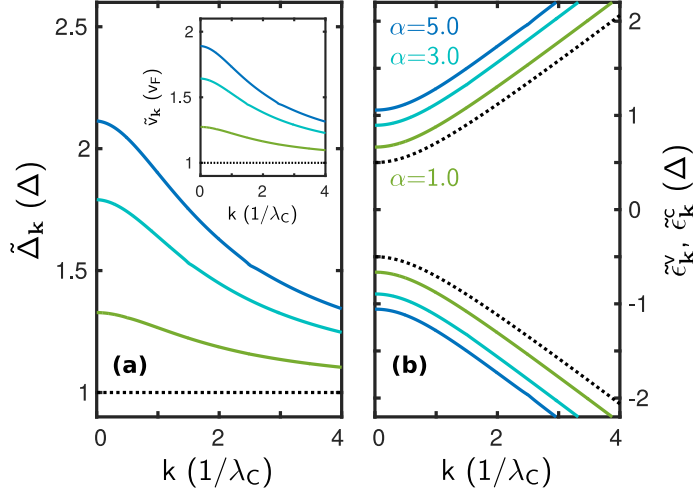


Figure 3.2.: (a) Renormalized band-gap energy and Fermi-velocity (inset) distributions for  $d = \lambda_C$  and  $\alpha = 1.0$  (green),  $3.0$  (cyan), and  $5.0$  (blue). The resulting renormalized single-particle dispersion is shown in (b). The black dotted lines represent the non-interacting ground state properties. (According to ref. [1].)

### 3. Excitonic properties of TMDC mono- and multilayers

are shown in (a), whereas the resulting renormalized single-particle bands  $\Sigma_{\mathbf{k}}^{c/v,0}$  are depicted in (b). Despite the strong  $|\mathbf{k}|$ -dependence of  $\tilde{\Delta}_{\mathbf{k}}$  and  $\tilde{v}_{F,\mathbf{k}}$ , the resulting renormalized single-particle bands  $\Sigma_{\mathbf{k}}^{c/v,0}$  experience predominantly a rigid shift towards higher band gaps for increasing Coulomb couplings.

Entering the self-consistently determined renormalized conduction and valence bands in the DWE

$$\left(\Sigma_{\mathbf{k}}^{c,0} - \Sigma_{\mathbf{k}}^{v,0}\right) \psi_{\nu}(\mathbf{k}) - \sum_{\mathbf{k}' \neq \mathbf{k}} \left[ V_{\mathbf{k}-\mathbf{k}',\mathbf{k}',\mathbf{k}}^{\text{cvvc}} \psi_{\nu}(\mathbf{k}') + V_{\mathbf{k}-\mathbf{k}',\mathbf{k}',\mathbf{k}}^{\text{ccvv}} \psi_{\nu}^*(\mathbf{k}') \right] = E_{\nu} \psi_{\nu}(\mathbf{k}) \quad (3.3)$$

yields the excitonic resonance energies and momentum-space wave functions. Noticeably, the coupling of  $\psi_{\nu}$  and  $\psi_{\nu}^*$  via the Coulomb matrix element  $V_{\mathbf{k}-\mathbf{k}',\mathbf{k}',\mathbf{k}}^{\text{ccvv}}$  makes this a non-trivial problem to solve. According to eq. (2.12) with

$$\langle c\mathbf{k}|v\mathbf{k}'\rangle \langle c\mathbf{k}'|v\mathbf{k}\rangle = e^{2i\tau\theta_{\mathbf{k}}} \left[ 2u_{\mathbf{k}}u_{\mathbf{k}'}v_{\mathbf{k}}v_{\mathbf{k}'}e^{-i\tau(\theta_{\mathbf{k}}-\theta_{\mathbf{k}'})} - u_{\mathbf{k}'}^2v_{\mathbf{k}}^2 - u_{\mathbf{k}}^2v_{\mathbf{k}'}^2e^{-2i\tau(\theta_{\mathbf{k}}-\theta_{\mathbf{k}'})} \right], \quad (3.4)$$

this contribution induces – among others – a coupling between  $s$ - and  $d$ -type states because of the remaining phase factor  $e^{2i\tau\theta_{\mathbf{k}}}$ . Theoretically, the angular momentum is no longer a good quantum number potentially causing problems when pursuing an isotropic description for the microscopic polarizations. However, knowing that the investigated TMDCs have rather large band gaps, these contributions are expected to be small suggesting a perturbative treatment. Considering

$$\left(\Sigma_{\mathbf{k}}^{c,0} - \Sigma_{\mathbf{k}}^{v,0}\right) \psi_{\nu}^{[0]}(\mathbf{k}) - \sum_{\mathbf{k}' \neq \mathbf{k}} V_{\mathbf{k}-\mathbf{k}',\mathbf{k}',\mathbf{k}}^{\text{cvvc}} \psi_{\nu}^{[0]}(\mathbf{k}') = E_{\nu}^{[0]} \psi_{\nu}^{[0]}(\mathbf{k}) \quad (3.5)$$

as the unperturbed DWE where the angular momentum remains a good quantum number, energy corrections to the bound excitonic states can be estimated by

$$\Delta E_{\nu}^{[1]} = \langle \psi_{\nu}^{[0]} | \hat{V}^{\text{ccvv}} | \psi_{\nu}^{[0]} \rangle, \quad \Delta E_{\nu}^{[2]} = \sum_{\nu' \neq \nu} \frac{|\langle \psi_{\nu'}^{[0]} | \hat{V}^{\text{ccvv}} | \psi_{\nu}^{[0]} \rangle|^2}{E_{\nu}^{[0]} - E_{\nu'}^{[0]}}, \quad (3.6a)$$

$$\langle \psi_{\nu'}^{[0]} | \hat{V}^{\text{ccvv}} | \psi_{\nu}^{[0]} \rangle \equiv - \sum_{\mathbf{k}} \psi_{\nu'}^{[0],*}(\mathbf{k}) \sum_{\mathbf{k}'} V_{\mathbf{k}-\mathbf{k}',\mathbf{k}',\mathbf{k}}^{\text{ccvv}} \psi_{\nu}^{[0],*}(\mathbf{k}') \quad (3.6b)$$

in first and second-order non-degenerate, time-independent perturbation theory [73].

In order to apply the latter, it is crucial that the degeneracy is already lifted in the initial states  $E_{\nu}^{[0]}$ . This is assured since

$$\langle c\mathbf{k}|c\mathbf{k}'\rangle \langle v\mathbf{k}'|v\mathbf{k}\rangle = u_{\mathbf{k}}^2u_{\mathbf{k}'}^2 + 2u_{\mathbf{k}}u_{\mathbf{k}'}v_{\mathbf{k}}v_{\mathbf{k}'}e^{i\tau(\theta_{\mathbf{k}}-\theta_{\mathbf{k}'})} + v_{\mathbf{k}}^2v_{\mathbf{k}'}^2e^{2i\tau(\theta_{\mathbf{k}}-\theta_{\mathbf{k}'})}, \quad (3.7)$$

contributing to the Coulomb matrix element  $V_{\mathbf{k}-\mathbf{k}',\mathbf{k}',\mathbf{k}}^{\text{cvvc}}$ , already induces a splitting of states that are degenerate in the wide-gap approximation. Applying the separation ansatz

$$\psi_{\nu}^{[0]}(\mathbf{k}) = \psi_{n,l}^{[0]}(\mathbf{k}) = R_{n,l}(k) \frac{e^{il\theta_{\mathbf{k}}}}{\sqrt{2\pi}} \quad (3.8)$$

### 3.1. Numerically solving gap and Dirac-Wannier equations

and defining the angular-averaged Coulomb matrix elements

$$e^{i\tau\Phi(\theta_{\mathbf{k}})} V_{kk'}^{\lambda\mu\mu'\lambda',l} = \frac{\mathcal{A}}{(2\pi)^2} \int_0^{2\pi} d(\theta_{\mathbf{k}} - \theta_{\mathbf{k}'}) V_{\mathbf{k}-\mathbf{k}',\mathbf{k}',\mathbf{k}}^{\lambda\mu\mu'\lambda'} e^{il(\theta_{\mathbf{k}} - \theta_{\mathbf{k}'})}, \quad (3.9)$$

enabled us to solve the eigenvalue problem for the radial wave function  $R_{n,l}(k)$  via numerical matrix diagonalization in momentum space. Here,  $n$  and  $l$  denote the main and angular-momentum quantum numbers. In general, the phase  $\Phi(\theta_{\mathbf{k}})$  is given by integer multiples of  $\theta_{\mathbf{k}}$ , as becomes evident in eq. (3.4). It is only zero for all intraband and the real-valued pair-creation and -annihilation Coulomb matrix elements. The numerical implementation of eq. (3.5) had been thoroughly described in ref. [62] for its wide-gap-approximated form ( $u_{\mathbf{k}} \approx 1$ ,  $v_{\mathbf{k}} \approx 0$ ) and is therefore not repeated here.

Knowing the momentum-space radial wave functions, first and second-order energy corrections are explicitly given by

$$\Delta E_{n,l}^{[1]} = \langle n, l | \hat{V}^{\text{ccvv}} | n, l \rangle, \quad \Delta E_{n,l}^{[2]} = \sum_{n'} \frac{|\langle n', 2\tau - l | \hat{V}^{\text{ccvv}} | n, l \rangle|^2}{E_{n,l}^{[0]} - E_{n',2\tau-l}^{[0]}}, \quad (3.10a)$$

$$\langle n', l' | \hat{V}^{\text{ccvv}} | n, l \rangle \equiv -\delta_{l',2\tau-l} \sum_{\mathbf{k}} d\mathbf{k} k R_{n',l'}(k) \sum_{\mathbf{k}'} d\mathbf{k}' k' V_{\mathbf{k}\mathbf{k}'}^{\text{ccvv},l} R_{n,l}(k'), \quad (3.10b)$$

where  $n' = n$  needs to be excluded from the sum for the case  $l = \tau$ . Evidently, first-order corrections only affect the  $p$ -type states  $l = \tau$  at the corresponding valley  $\tau$  contributing to the splitting of  $p$ -type states with  $l = \pm 1$ . Note that for the  $l = \tau$  states the separation ansatz (3.8) succeeds in solving the full DWE non-perturbatively. As indicated previously,  $s$ -type states at valley  $\tau$  experience second-order corrections from  $d$ -type contributions  $l' = 2\tau$ , whereas  $p$ -type states  $l = -\tau$  are shifted by  $f$ -type contributions  $l' = 3\tau$ . These corrections were found to be negligible for typical TMDC parameters conserving the angular-momentum quantum number within a very good approximation. Beyond sec. 3.2, only  $s$ -type properties are considered. Therefore, the negligible contribution  $\propto V_{\mathbf{k}-\mathbf{k}',\mathbf{k}',\mathbf{k}}^{\text{ccvv}}$  is dropped from then on without further notice.

Finally, the results from numerically solving the combined GEs and DWE are depicted in fig. 3.3. In particular, fig. 3.3 (a) shows the five lowest  $s$ -type excitonic resonances and renormalized band gap (black dashed-dotted line) in dependence of the Coulomb coupling  $\alpha$  for an effective-thickness parameter of  $d = \lambda_{\text{C}}$ . The respective exciton binding energies increase with increasing Coulomb coupling resulting in a blue shift of the resonance positions that is least pronounced for the  $1s$  exciton. More specifically, for particularly large Coulomb couplings the increase of the  $1s$ -exciton binding energy and band-gap renormalization almost perfectly cancel [I].

The numerical solution of the full DWE reveals a fine structure of the excitonic resonances that is not observable in the wide-gap approximation. Based on previous considerations, the lifting of the degeneracy of  $p$ -type states is particularly pronounced. Therefore, the splitting between the lowest  $p$ -type states with opposite orbital angular momentum is plotted as a function of  $\alpha$  in fig 3.3 (b). The splitting starts increasing quadratically in the limit of small Coulomb couplings, but turns into a linear increase

### 3. Excitonic properties of TMDC mono- and multilayers

for moderate to high values of  $\alpha$ . We reported splittings of the  $2p$  states that should be measurable for suspended and substrate-supported monolayers in experimental setups.

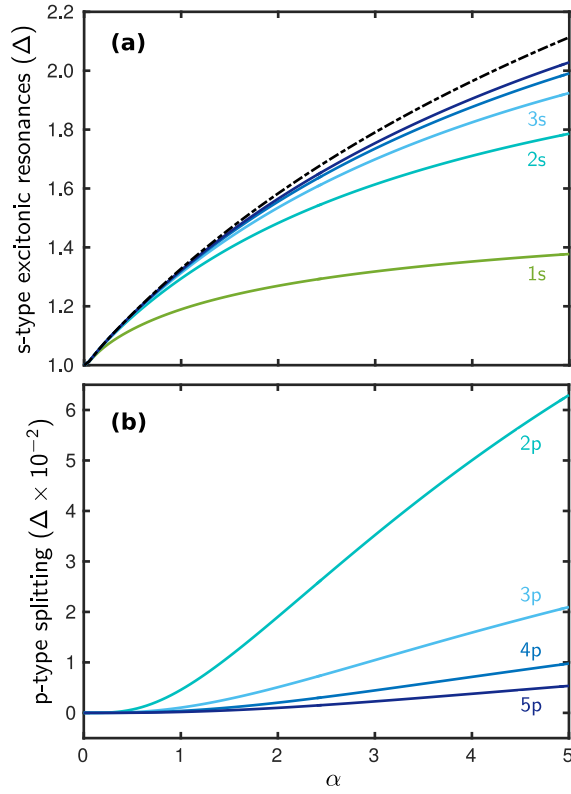


Figure 3.3.: (a) Lowest  $s$ -type energy eigenvalues of the DWE as a function of  $\alpha$  with respect to the renormalized single-particle dispersion. The black dashed-dotted line indicates the renormalized band gap. (b) Fine structure of the excitonic spectra, illustrated by the splitting of the lowest  $p$ -type excitonic states. For both the effective thickness parameter was set to  $d = 1.0 \lambda_C$ . (Adapted from ref. [I].)

## 3.2. TMDC monolayers: Theory-experiment comparison

In the previous section, the numerical solutions of the GEs and DWE were demonstrated using a simplified expression for the Coulomb interaction to investigate more general aspects of these equations. In order to perform quantitative calculations on the ground-state and excitonic properties of mono- and multilayer TMDC structures, the Coulomb interaction based on the full solution of Poisson's equation for the slab geometry (see chapter 2.2) is required. For the results that contributed to ref. [I] and

are summarized in the following, finite-thickness effects were included via the Ohno-potential form factor. Corresponding material parameters of the investigated TMDC systems are summarized in tab. A.1 of the appendix.

Unlike all other material parameters, the effective-thickness parameter  $d$  is the only free parameter in our theory that needed to be determined by variation. This was done by varying  $d$  over a reasonable range, demonstrated by the example of a SiO<sub>2</sub>-supported ( $\epsilon_{\text{SiO}_2} = 2.1$ ) MoS<sub>2</sub> monolayer within fig. 3.4. Since increasing  $d$  effectively weakens the Coulomb interaction, renormalized band gaps and excitonic resonances evolve to lower energies. In particular, the material-specific effective-thickness parameter was defined as the value for  $d$  where the combined solution of GEs and DWE reproduced the A<sub>1s</sub>-exciton resonance of experimentally available data. This was the preferable choice over a comparison with experimental band gaps since documented values of the latter are rather sparse. For the SiO<sub>2</sub>-supported MoS<sub>2</sub> monolayer we found an effective-thickness parameter of  $d = 4.47$  Å, yielding  $E_{1s}^A = 1.94$  eV which is in the range of experimental findings [74–77]. Combined with a renormalized single-particle band gap of  $E_g^A \equiv \Sigma_{A,k=0}^{c,0} - \Sigma_{A,k=0}^{v,0} = 2.39$  eV, an A<sub>1s</sub>-exciton binding energy of about  $E_{b,1s}^A = 450$  meV was predicted.

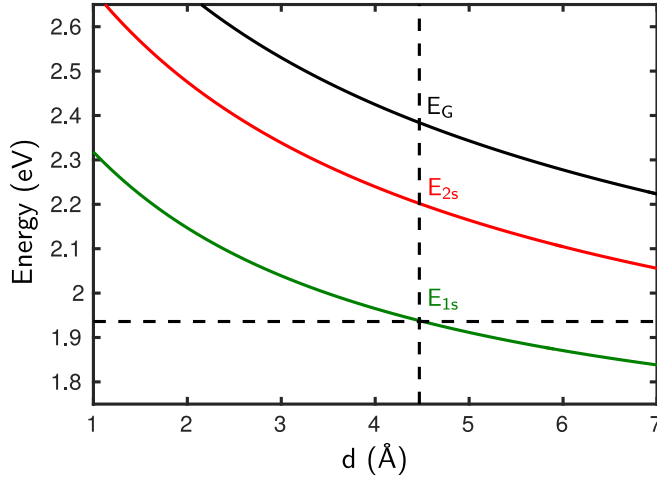


Figure 3.4.: Theoretical A-exciton resonances for MoS<sub>2</sub> on SiO<sub>2</sub> as function of effective-thickness parameter. The solid lines show the theoretical position of the A<sub>1s</sub> (green), A<sub>2s</sub> (red) resonance and the gap (black), the dashed lines mark the target energy value for the A<sub>1s</sub>-exciton resonance  $E_{1s}^A$  and the best fit for the thickness parameter. (Adapted from ref. [I].)

After the effective-thickness parameter is determined once for a given monolayer TMDC, the advantage of this approach lies within predicting the environmental influence on the renormalized band gaps and exciton resonances. Fig. 3.5 (a) displays the resulting excitonic spectra of monolayer MoS<sub>2</sub> for different dielectric environments that were computed for the lowest excitonic resonances from Elliott’s formula (2.43). For the chosen dielectric environments, hBN-encapsulation, SiO<sub>2</sub> substrate, freely

### 3. Excitonic properties of TMDC mono- and multilayers

suspended, the environmental background screening decreases within the presented spectra from top to bottom. As a result, we observed a large decrease in the renormalized band gap  $E_g^A$  from 2.55 eV of the suspended monolayer to 2.18 eV of the hBN-encapsulated monolayer. The simultaneous reduction of the  $A_{1s}$ -exciton binding energy leaves the optical band gap rather unchanged. This behavior was found not only for monolayer MoS<sub>2</sub>, but for all monolayer TMDCs investigated. Nevertheless, our calculations generally predict a small net red shift of the  $A_{1s}$ -exciton resonance of a few ten meV when increasing the environmental screening which is in agreement with experimental findings, e.g. of ref. [24] where WS<sub>2</sub> monolayers were investigated.

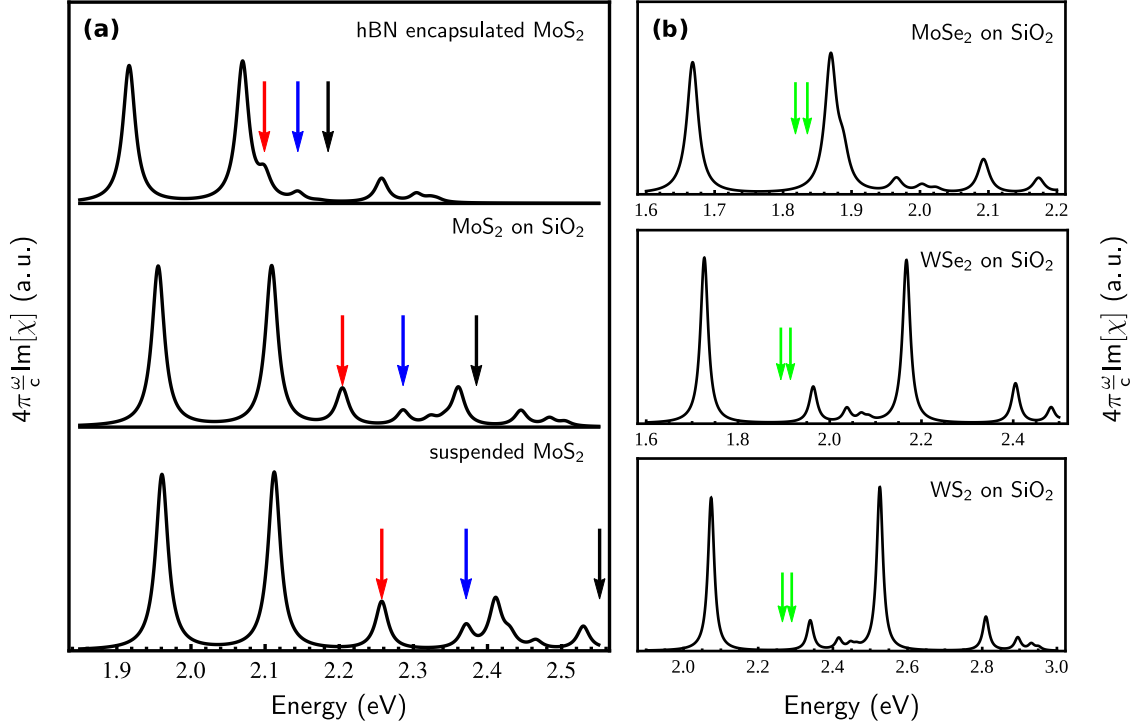


Figure 3.5.: (a) Calculated excitonic spectra for MoS<sub>2</sub> within different dielectric environments using the same thickness parameter  $d = 4.47$  Å. Top: hBN-encapsulated ( $\epsilon_{\text{hBN}} = 2.89$ ), center: SiO<sub>2</sub>-supported ( $\epsilon_{\text{SiO}_2} = 2.1$ ), bottom: Freely suspended. The red and blue arrows highlight the spectral positions of the  $A_{2s}$ - and  $A_{3s}$ -exciton resonances, respectively, to make them distinguishable from the resonances of the B-exciton series. The black arrows mark the renormalized band gap  $E_g^A$ . (b) Calculated excitonic spectra for different SiO<sub>2</sub>-supported TMDC monolayers. Top: MoSe<sub>2</sub> ( $d = 4.96$  Å), center: WSe<sub>2</sub> ( $d = 5.17$  Å), bottom: WS<sub>2</sub> ( $d = 2.78$  Å). The green arrows show the spectral positions of the split  $A_{2p}$ -exciton resonances. (Adapted from ref. [I].)

Particularly, we found an  $A_{1s}$ -exciton binding energy of about 600 meV for suspended monolayer MoS<sub>2</sub>, in very good agreement with experimental findings of ref. [78], wherein a binding energy of  $E_{b,1s}^A \geq 570$  meV was reported. For the hBN-encapsulated MoS<sub>2</sub> layer we computed the lowest three A-exciton resonances,  $E_{1s}^A = 1.92$  eV,  $E_{2s}^A = 2.10$  eV and  $E_{3s}^A = 2.14$  eV, and ground-state B-exciton resonance  $E_{1s}^B = 2.07$  eV in almost perfect agreement with the experimentally reported values of 1.926 eV, 2.10 eV, 2.12 eV and 2.08 eV of ref. [79].

Accordingly, we determined the effective-thickness parameters of 4.96 Å, 5.17 Å and 2.78 Å for monolayer MoSe<sub>2</sub> [77, 80], WSe<sub>2</sub> [81] and WS<sub>2</sub> [22], respectively, by comparing with the  $A_{1s}$ -exciton resonances of the stated references. A detailed comparison for the complete exciton series of monolayer WSe<sub>2</sub> [81] and WS<sub>2</sub> [22] is found in ref. [I]. The excitonic spectra of the respective SiO<sub>2</sub>-supported monolayers are depicted in fig. 3.5 (b). The green arrows highlight the resonance positions of the  $A_{2p}$  states that lie several 10 meV below the  $A_{2s}$  resonance and are split by about 20-25 meV, depending on the specific material. This behavior was also observed in an earlier theoretical study on suspended monolayer MoS<sub>2</sub> [51].

### 3.3. Monolayer-to-bulk transition

Besides predicting environmental influences on the renormalized bands and positions of excitonic resonances of monolayer TMDCs, the anisotropic dielectric model for the Coulomb interaction enabled us to investigate the aforementioned properties for homogeneous structures of arbitrary numbers of layers. In fact, our numerically efficient matrix-inversion scheme – computing the non-locally screened Coulomb interaction at the center of the respective layers – proved to be capable of performing calculations for multilayer structures of up to 50 layers [I] on the timescale of several ten minutes without requiring high-performance computing<sup>1</sup>.

To revisit sec. 2.1.2, the out-of-plane kinetic energy becomes negligible in the vicinity of the  $K/K'$  points, even in the bulk limit, leading to quasiparticles well confined within the layers. As a consequence, the single-particle bands, whose number increases proportionally with the number of layers, are almost degenerate in this region of the BZ [39, 83]. This observation justified us to assign the unrenormalized properties of the monolayer, stated in tab. A.1, to each layer of the multilayer structure. Note that this approach is only valid since we are exclusively interested in the ground-state and excitonic properties in the vicinity of the  $K/K'$  points. Logically, the calculation of the renormalized bands based on the GEs is not capable of predicting a direct-to-indirect transition of the band gap when increasing the number of layers. Hence, in the following we speak of renormalized single-particle transition energies since they might not correspond to the true fundamental band gap.

By the example of suspended MoS<sub>2</sub> fig. 3.6 (a) displays the renormalized single-particle transition energies  $E_g^A(n, m) \equiv \sum_{n,A,k=0}^{c,0} - \sum_{m,A,k=0}^{v,0}$  for  $m = n$  and correspond-

<sup>1</sup>Nevertheless, these computation timescales required OpenMP-based shared memory parallelism to extend Fortran [82].

### 3. Excitonic properties of TMDC mono- and multilayers

ing  $A_{1s}$ -intralayer-exciton resonances  $E_{1s}^A(n, n)$  in dependence of the total number  $N$  of the stacked monolayers. Here, the combined GEs and DWE were solved for each transition separately, electron and hole assumed to be located within layers  $n = 1$  to  $n = N$ , producing the tuples  $\{E_g^A(n, n), E_{1s}^A(n, n)\}$  for a given number of layers. Thus, the numerical implementation is analog to the monolayer case with the difference of requiring the respective electron and hole locations and total number of layers as additional input.

Induced by the change in the dielectric surrounding when transitioning from layer to layer, degeneracy is lifted in  $E_g^A(n, n)$  and  $E_{1s}^A(n, n)$  for multilayer structures with  $N \geq 3$ . Note that degeneracy is still present for layer tuples  $\{n, N - n + 1\}$  of the suspended structure because of a lacking substrate to break the environmental symmetry. Evidently, increasing the number of layers increases the screening of the Coulomb interaction between quasiparticles within a given layer in the presence of all layers [I]. As a result, we observed a simultaneous decrease of the renormalized single-particle transition and exciton binding energies leading to a net redshift of a few ten meV of the corresponding excitonic resonances. The bulk limit was computed by considering a single MoS<sub>2</sub> layer embedded in bulk ( $\epsilon_1 = \epsilon_2 = \sqrt{\epsilon_{\parallel}^B \epsilon_{\perp}^B}$ ) resulting in  $E_{1s}^{A, \infty} = 1.88$  meV and  $E_g^{A, \infty} = 2.03$  meV. The corresponding binding energy of 150 meV was found to be in good agreement with the theoretical findings of ref. [84] where the authors predicted a binding energy of 130 meV.

Considering neighboring layers as electronically completely independent, i.e. a vanishing overlap

$$\left| \int_{-\infty}^{\infty} dz \phi_e(z - z_n) \phi_h(z - z_m) \right|^2 = 0 \quad (3.11)$$

for  $n \neq m$  between the localized electron ( $\phi_e$ ) and hole ( $\phi_h$ ) distributions, interlayer excitons are optically dark. While the calculation of the layer-dependent Coulomb matrix elements via matrix inversion technically requires strongly localized distributions for the sake of bijectivity, we relaxed this condition and applied normalized Gaussian distributions of a finite width to compute the interlayer light-matter coupling as fraction of the intralayer coupling estimated by the electron-hole overlap.

The resulting optical spectrum for the A-exciton series of bulk MoS<sub>2</sub> is depicted in fig. 3.6 (b). In order to account for interlayer excitons in nearest and next-nearest neighboring layers, we considered a trilayer MoS<sub>2</sub> embedded in bulk. As can be seen, we found a pronounced resonance around 1.93 eV, between the  $A_{1s}$ - and  $A_{2s}$ -intralayer-exciton resonances, resulting from the nearest-neighbor  $A_{1s}$  interlayer exciton.

Here, the theory-experiment comparison was particularly interesting. In bulk-MoS<sub>2</sub> measurements already performed in the early to mid 1970s, the authors of refs. [6–8] observed pronounced resonances at energies of about 1.92 eV, 1.96 eV and 1.99 eV, which they believed to be part of a single 3D A-exciton Rydberg series. Nowadays, the 2D nature of  $K/K'$ -point excitons in bulk TMDCs is widely accepted. However, an association of the second-lowest resonance to the  $A_{1s}$  interlayer exciton was missing. Despite a small shift of a few 10 meV in the absolute resonance positions, the pronounced resonances in Fig 3.6 (b) can be quite precisely assigned to the measured

resonances. Consequently, we proposed a reinterpretation of the bulk exciton series as a combined 2D intra- and interlayer exciton series. More recent measurements on bulk MoTe<sub>2</sub> [25] further supported our proposed reinterpretation.

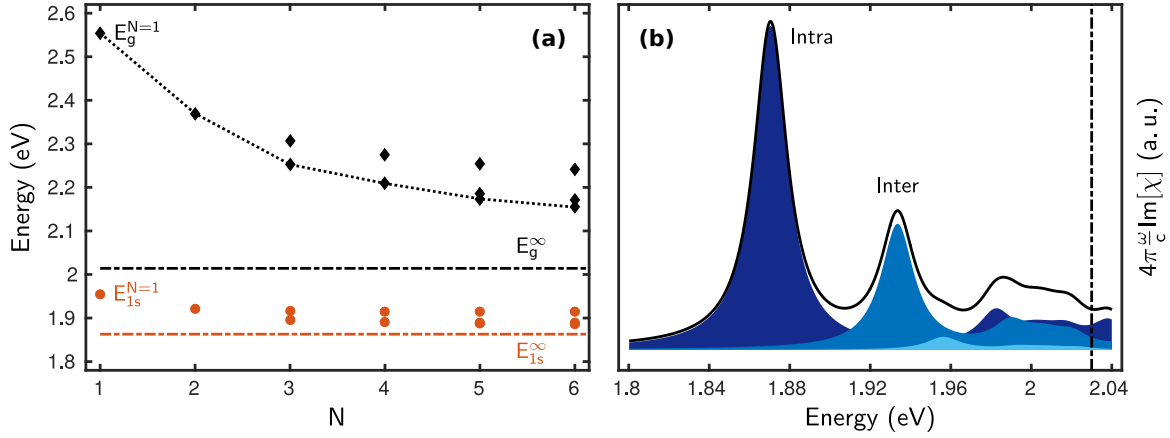


Figure 3.6.: (a) Renormalized single-particle transition energies  $E_g^A(n, n)$  (black diamonds) and excitonic resonance positions  $E_{1s}^A(n, n)$  (orange dots) of layers  $n = 1, \dots, N$  in dependence of the total layer number  $N$  for suspended MoS<sub>2</sub>. The black dotted line indicates the fundamental transition energy for a given  $N$  while the dashed-dotted lines show the bulk limit  $N \rightarrow \infty$ . (b) Excitonic spectrum in the bulk limit. The black line shows the total optical spectrum, whereas the dark blue shaded area shows the intralayer contributions. The interlayer contribution of the nearest (next-next) neighboring layers is depicted in (light) blue. The dashed-dotted line around 2.03 eV indicates  $E_g^A$  in the bulk limit. (Adapted from ref. [I].)

### 3.4. Intra- and interlayer excitons in TMDC hetero-bilayers

In ref. [III] we combined the framework of GEs, DWE and DBE with DFT calculations to theoretically study intra- and interlayer excitons in freely suspended AA'-stacked WSe<sub>2</sub>/MoS<sub>2</sub> and WSe<sub>2</sub>/MoSe<sub>2</sub> hetero-bilayers. In terms of the DFT calculations, equilibrium lattice constants for the respective hetero-bilayer structures were assumed. Hence, bilayer WSe<sub>2</sub>/MoS<sub>2</sub> emerged as artificially strained system because of the slight deviation in the lattice constants of the constituent MoS<sub>2</sub> and WSe<sub>2</sub> layers compared to their respective monolayer value [85]. On the contrary, bilayer WSe<sub>2</sub>/MoSe<sub>2</sub> is a negligibly strained system since the lattice constants of the stacked monolayers are almost identical.

The DFT-based analysis of the ion contribution of the W (red) and Mo (blue) atoms to the bands of interest, e.g. depicted for bilayer WSe<sub>2</sub>/MoS<sub>2</sub> in fig. 3.7 (a) and (b),

### 3. Excitonic properties of TMDC mono- and multilayers

helped us to relate the bands to the respective layers. While both layers were found to contribute rather equally to the valence-band states of bilayer  $\text{WSe}_2/\text{MoS}_2$  at the  $\Gamma$  point, conduction and valence-band states are dominated by either W or Mo at the  $K$  point, as expected. Similar observations were made for bilayer  $\text{WSe}_2/\text{MoSe}_2$ . Hence, the fundamental  $K$ -point transition in both hetero-bilayer structures was found to be of interlayer nature. Despite strong confinement within the layers, the small but finite contribution of the opposite layer is crucial for non-vanishing dipole matrix elements, and thus for the possibility to observe optically bright interlayer excitons.

Already assigned to the layers of dominating ion contributions, the single-particle band structure was approximated by the relativistic bands in the vicinity of the  $K$  point. Thus, necessary material parameters of the MDF-model Hamiltonian, i.e. the single-particle transition energies and Fermi-velocities, were extracted. The “full” (dotted lines) and approximated (solid lines) single-particle band structures are shown for bilayer  $\text{WSe}_2/\text{MoS}_2$  in fig. 3.7 (c). For the complete list of material parameters see tab. A.2 of the appendix.

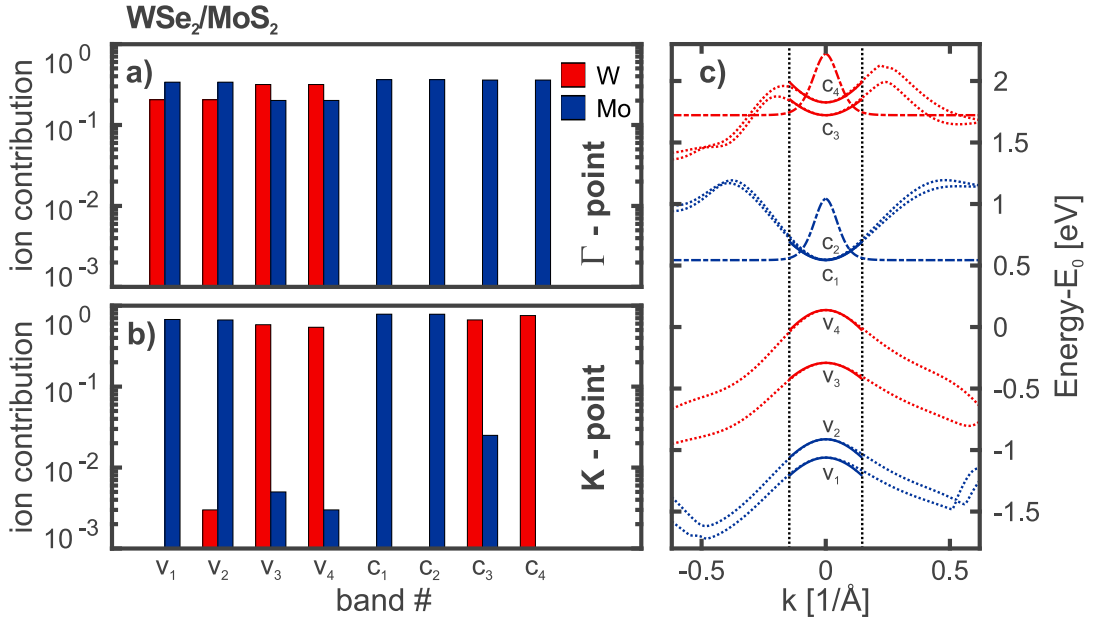


Figure 3.7.: Relative contributions of W (red) and M (blue) atoms to the first four valence and conduction bands at the  $\Gamma$  (a) and  $K$  (b) points for the example of the  $\text{WSe}_2/\text{MoS}_2$  hetero-bilayer on a logarithmic scale. The contributions of the S and Se atoms are not shown. (c) The corresponding single-particle band structure (dotted lines) is approximated by the relativistic dispersion (solid lines) in the vicinity of the  $K$  point. The W (Mo) dominated bands are plotted in red (blue). The probability densities of the respective intralayer excitonic ground states are shown in dashed-dotted lines. (Adapted from ref. [III].)

### 3.4. Intra- and interlayer excitons in TMDC hetero-bilayers

Equipped with a complete set of parameters, GEs, DWE and DBE were solved to compute the renormalized ground-state and linear optical properties. Since the numerical procedure to determine the renormalized bands and resulting intra- and interlayer excitonic resonances is according to the description of previous sections, in the following we focus on the numerical solution of the DBE.

Considering a single transition between a conduction band of layer  $n$  and a valence band of layer  $m$ , the Fourier transform of the DBE (2.40) reads

$$\left[ \hbar(\omega + i\gamma) - (\Sigma_{nk}^{c,0} - \Sigma_{mk}^{v,0}) \right] P_k^{mn}(\omega) + \sum_{k' \neq k} V_{k-k',k',k}^{cvvc} P_{k'}^{mn}(\omega) = -\frac{e}{m_0 c} \mathbf{p}_{cv}^{nm}(\mathbf{k}) \cdot \mathbf{A}(\omega), \quad (3.12)$$

where spin and valley indices are dropped for simplicity. Correlation effects beyond HF approximation were included via a phenomenological dephasing of  $\hbar\gamma = 15$  meV. Noticeably, eq. (3.12) has the form of a matrix equation

$$\sum_{k'} \underbrace{\left[ \left( \hbar(\omega + i\gamma) - \Sigma_{nk}^{c,0} + \Sigma_{mk}^{v,0} \right) \delta_{k,k'} + dk' k' V_{kk'}^{mn,cvvc} \right]}_{= M_{kk'}^{mn}(\omega)} P_{k'}^{mn}(\omega) = -\underbrace{\frac{e p_{cv}^{nm}(k)}{\sqrt{2} m_0 c} A(\omega)}_{= I_k^{mn}(\omega)} \quad (3.13)$$

for the optically bright  $s$ -type polarizations,  $P_k^{mn}(\omega) = P_k^{mn}(\omega)$ , with matrix elements  $M_{kk'}^{mn}(\omega)$  and inhomogeneity  $I_k^{mn}(\omega)$ . The latter contains the light-matter coupling. Furthermore,  $V_{kk'}^{mn,cvvc}$  denote the  $s$ -type angular-averaged Coulomb matrix elements according to eq. (3.9). Within the numerical simulations, we assumed weak excitation by a linear-polarized optical field,  $\mathbf{A}(\omega) = A(\omega) \mathbf{e}_x$ , effectively reducing the light-matter coupling of a given transition by a factor of  $\sqrt{2}$ . The momentum matrix elements  $p_{cv}^{nm}(k) = p_{cv,K}^{nm} u_{nk} u_{mk}$  were computed from the  $K$ -point dipoles  $d_{cv,K}^{nm}$  that are stated tab. A.2 by employing relation (2.7) for each of the transitions considered. We took the  $k$ -dependence of the light-matter coupling in the vicinity of the  $K/K'$  points into account by including the MDF-model prefactors of the respective layers.

Numerically solved via matrix inversion, eq. (3.13) yields the microscopic polarizations for a single transition and frequency. Repeating this scheme for all  $K$ -point transitions over the frequency range of interest, the total optical susceptibility and absorption spectra as well as their respective intra- and interlayer contributions were obtained with the aid of eqs. (2.41) and (2.44). In order to account for the equally contributing  $K'$ -point transitions of the joint BZ, a degeneracy factor of 2 was included within the calculation of the optical susceptibility.

The resulting spectra for the WSe<sub>2</sub>/MoS<sub>2</sub> (left panel) and WSe<sub>2</sub>/MoSe<sub>2</sub> (right panel) hetero-bilayers are depicted in fig. 3.8. Retaining the initial color code, the intralayer contributions of the Mo and W dominated bands to the respective total absorption spectra (bottom, black) are plotted in blue and red, whereas the contributions of the interlayer transitions are shown in green. The shaded areas highlight the respective renormalized single-particle transitions.

In case of the WSe<sub>2</sub>/MoS<sub>2</sub> structure, the pronounced strain in the constituent layers led to huge shifts of the non-interacting single-particle transition energies. As a direct

### 3. Excitonic properties of TMDC mono- and multilayers

consequence, the resonance positions of the  $\text{MoS}_2$  ( $E_{1s}^A = 1.73$  eV) and  $\text{WSe}_2$  ( $E_{1s}^A = 2.01$  eV) intralayer excitons were found to be heavily misaligned compared to their respective monolayer values of about 1.94 eV ( $\text{MoS}_2$ ) and 1.74 eV ( $\text{WSe}_2$ ). On the contrary, real TMDC heterostructures are basically unstrained because of the weak van der Waals interaction between adjacent layers. Therefore, comparing calculated intra- and interlayer excitonic resonance positions with experimental findings, e.g. of ref. [86], is not productive. Binding energies, however, can be considered rather independent of these artificially induced shifts. Here, the calculations revealed interlayer excitons with large binding energies of about 350 meV, comparable to those of the respective

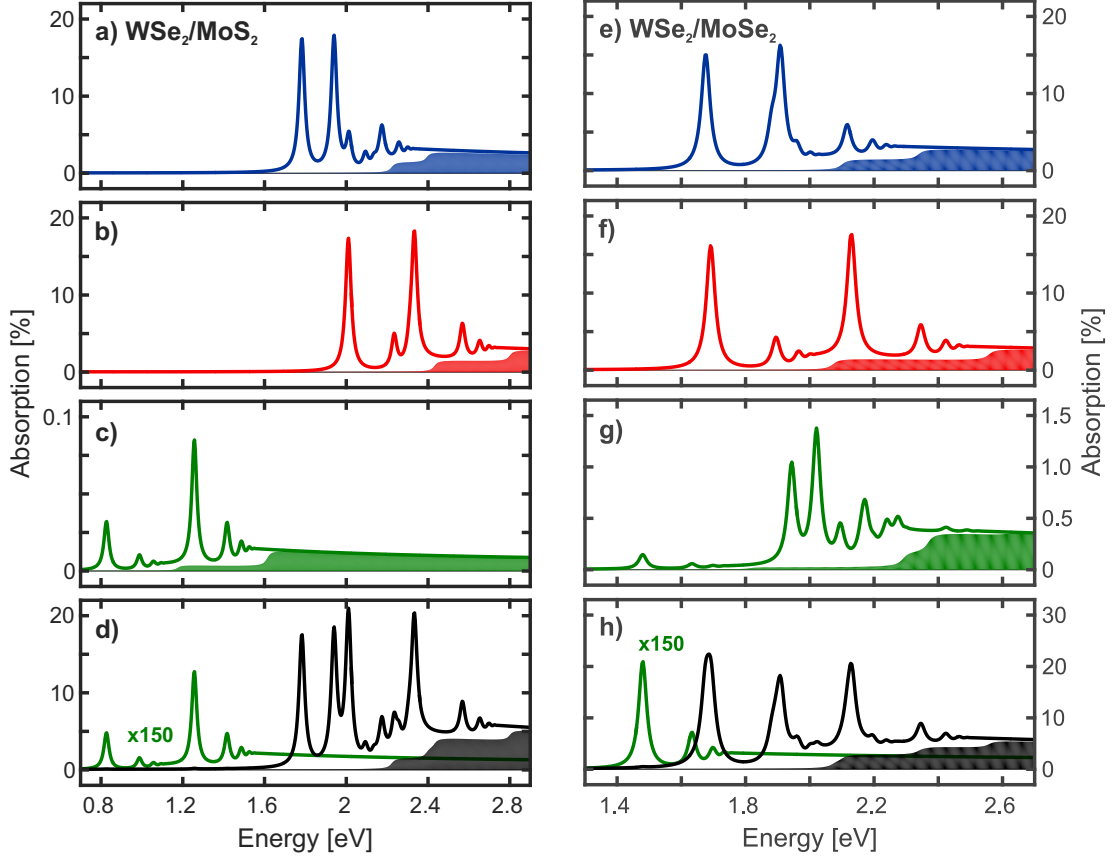


Figure 3.8.: Absorption spectra of the  $\text{WSe}_2/\text{MoS}_2$  (a)-(d) and  $\text{WSe}_2/\text{MoSe}_2$  (e)-(h) hetero-bilayers: Contributions of intralayer transitions between Mo (a,e) and W (b,f) dominated bands to the respective absorption spectra (blue and red solid lines). (c,g) Contributions of the interlayer transitions (green solid lines). (d,h) Total absorption spectra of the  $\text{WSe}_2/\text{MoS}_2$  and  $\text{WSe}_2/\text{MoSe}_2$  hetero-bilayers in black solid lines, respectively. The contribution of the lowest interlayer transition is magnified by a factor of 150 (green solid lines). The shaded areas show the respective free particle transitions. (Adapted from ref. [III].)

intralayer excitons.

Focusing on  $\text{WSe}_2/\text{MoSe}_2$  hetero-bilayer, we found almost degenerate  $A_{1s}$ -intralayer-exciton resonances of the constituent layers at around 1.69 eV, whereas the fundamental interlayer-exciton transition was observed at 1.48 eV. Due to the small strain, theoretical and experimental conditions were much more comparable. Based on the accuracy estimated in ref. [III], the calculated intra- and interlayer exciton resonances were found to be in good agreement with the experimental findings of refs. [87–90], where the authors investigated  $\text{SiO}_2$ - [87, 88], graphite- [89] and hBN-supported [90] bilayers. In good agreement with the observation of ref. [90], the oscillator strength of the interlayer exciton was predicted to be about 150 times smaller than those of the respective intralayer excitons. This resulted in a radiative lifetime of the former that is two orders of magnitude larger than those of the intralayer excitons confirming the existence of long-lived interlayer excitons in bilayer  $\text{WSe}_2/\text{MoSe}_2$ .



## Nonlinear optical properties of TMDC monolayers

This chapter contains a summary of our research on the  $K/K'$ -point nonlinear optical properties of the TMDC monolayers MoS<sub>2</sub> [II] and MoTe<sub>2</sub> [IV]. The presentation of the results is supported by details concerning the numerical implementation.

Firstly, the results of the investigations on monolayer MoS<sub>2</sub>, that was assumed to be in an excited quasiequilibrium state after strong optical excitation, are presented. Among them are the observation of excitation-induced band-gap renormalization and occurrence of broadband optical gain.

Subject of the second part of this chapter is the study of the nonlinear optical properties of monolayer MoTe<sub>2</sub> beyond the quasiequilibrium regime. Here, the inclusion of incoherent carrier-carrier and carrier-phonon scattering processes within the DBEs enabled us to explore the  $K/K'$ -point charge-carrier dynamics, excitation-induced band-gap renormalization and gain build-up on an ultrashort time scale. While an isotropic description is not capable of exploring the dynamics of intervalley scattering, the influence of side-valley occupations on the optical spectra was investigated for true equilibrium conditions.

### 4.1. Quasiequilibrium investigations of MoS<sub>2</sub>

In this numerical experiment we considered a situation where a single MoS<sub>2</sub> layer has initially been excited by a high-intensity optical pulse. Incoherent scattering processes lead among others to the relaxation of the optically excited charge carriers within their respective bands until a quasiequilibrium is reached. In this configuration excited electrons and holes in bands  $i = \{s, \tau\}$  are described by thermal states

$$f_{i\mathbf{k}}^{e/h}(\mu_i^{e/h}, T) = \frac{1}{e^{\beta(\tilde{\Sigma}_{i\mathbf{k}}^{e/h} - \mu_i^{e/h})} + 1}, \quad \beta = \frac{1}{k_B T}, \quad (4.1)$$

with temperature  $T$  and chemical potential  $\mu_i^{e/h}$ . At this point, we considered separate chemical potentials for A- and B-band carriers describing completely decoupled valleys.

#### 4. Nonlinear optical properties of TMDC monolayers

For chosen carrier density  $n_i^{e/h}$  the corresponding chemical potential  $\mu_i^{e/h}$  to set up  $f_{i\mathbf{k}}^{e/h}(\mu_i^{e/h}, T)$  was obtained from the numerical solution of

$$0 = n_i^{e/h} - \frac{1}{\mathcal{A}} \sum_{\mathbf{k}} f_{i\mathbf{k}}^{e/h}(\mu_i^{e/h}, T), \quad (4.2)$$

wherein  $n_i^e = n_i^h$  assured charge-carrier neutrality.

At elevated densities, screening of the excited charge carriers is assumed to be the dominant correlation effect. Hence, many-body correlations contained within  $\left. \frac{d}{dt} P_{i\mathbf{k}} \right|_{\text{corr.}}$  of eq. (2.45) were treated on the level of the screened HF approximation. Furthermore, non-radiative decay processes were described by a phenomenological dephasing  $\hbar\gamma$ , yielding the frequency-space representation

$$\begin{aligned} & \left[ \hbar(\omega + i\gamma) - (\tilde{\Sigma}_{i\mathbf{k}}^h + \tilde{\Sigma}_{i\mathbf{k}}^e) \right] P_{i\mathbf{k}}(\omega) + (1 - f_{i\mathbf{k}}^h - f_{i\mathbf{k}}^e) \sum_{\mathbf{k}' \neq \mathbf{k}} W_{\mathbf{k}-\mathbf{k}', i\mathbf{k}', i\mathbf{k}}^{\text{cvvc}} P_{i\mathbf{k}'}(\omega) \\ & = -(1 - f_{i\mathbf{k}}^h - f_{i\mathbf{k}}^e) \frac{e}{m_0 c} \mathbf{p}_{i,\text{cv}}(\mathbf{k}) \cdot \mathbf{A}(\omega) \end{aligned} \quad (4.3)$$

of the DBE in screened HF approximation. Inserting the static limit of the screened Coulomb interaction  $W_{\mathbf{q}}(\omega) = V_{\mathbf{q}}/(1 - \Pi_{\mathbf{q}}(\omega)V_{\mathbf{q}})$  into eq. (2.12) provided the relevant screened Coulomb matrix elements  $W_{\mathbf{k}-\mathbf{k}', i\mathbf{k}', i\mathbf{k}}^{\text{cvvc}}$ , wherein  $\mathbf{q} = \mathbf{k} - \mathbf{k}'$  is already implied. The former was computed with the aid of the Lindhard polarization function in the static, long-wavelength limit

$$\Pi_{\mathbf{q}} \approx \Pi_{\mathbf{q} \rightarrow 0}(\omega \rightarrow 0) = - \sum_{\lambda, i, \mathbf{k}} \frac{\partial f_{i\mathbf{k}}^\lambda}{\partial \mu_i^\lambda} = - \frac{\beta}{2} \sum_{\lambda, i, \mathbf{k}} \frac{1}{\cosh[\beta(\tilde{\Sigma}_{i\mathbf{k}}^\lambda - \mu_i^\lambda)] + 1}. \quad (4.4)$$

Referred to as generalized DWE, the homogeneous solution of eq. (4.3) contains pronounced resonances at energies  $\hbar\omega = E_{i\nu}$  that are given by

$$(\tilde{\Sigma}_{i\mathbf{k}}^h + \tilde{\Sigma}_{i\mathbf{k}}^e) \psi_{i\nu}^R(\mathbf{k}) - (1 - f_{i\mathbf{k}}^h - f_{i\mathbf{k}}^e) \sum_{\mathbf{k}' \neq \mathbf{k}} W_{\mathbf{k}-\mathbf{k}', i\mathbf{k}', i\mathbf{k}}^{\text{cvvc}} \psi_{i\nu}^R(\mathbf{k}') = E_{i\nu} \psi_{i\nu}^R(\mathbf{k}). \quad (4.5)$$

The generalized DWE is non-Hermitian consequently having left- ( $\psi_\nu^L$ ) and right-handed ( $\psi_\nu^R$ ) solutions that are related via  $\psi_\nu^L(\mathbf{k}) = \psi_\nu^R(\mathbf{k})/(1 - f_{i\mathbf{k}}^h - f_{i\mathbf{k}}^e)$  and obey the orthogonalization and completeness relations [59, 91]

$$\sum_{\mathbf{k}} [\psi_{i\nu}^L(\mathbf{k})]^* \psi_{i\nu'}^R(\mathbf{k}) = \delta_{\nu, \nu'}, \quad \sum_{\nu} [\psi_{i\nu}^L(\mathbf{k})]^* \psi_{i\nu}^R(\mathbf{k}') = \delta_{\mathbf{k}, \mathbf{k}'}. \quad (4.6)$$

Renormalized single-particle energies  $\tilde{\Sigma}_{i\mathbf{k}}^{e/h}$  entering Fermi-Dirac distributions, DBE and generalized DWE followed from the solution of the GEs that are given by

$$\tilde{\Delta}_{i\mathbf{k}} = \Delta_i + \frac{1}{2} \sum_{\mathbf{k}' \neq \mathbf{k}} W_{|\mathbf{k}-\mathbf{k}'|} \frac{\tilde{\Delta}_{i\mathbf{k}'}}{\tilde{\epsilon}_{i\mathbf{k}'}} (1 - f_{i\mathbf{k}'}^h - f_{i\mathbf{k}'}^e), \quad (4.7)$$

$$\tilde{v}_{F, i\mathbf{k}} = v_{F, i} + \frac{1}{2} \sum_{\mathbf{k}' \neq \mathbf{k}} W_{|\mathbf{k}-\mathbf{k}'|} \frac{k'}{k} \frac{\tilde{v}_{F, i\mathbf{k}'}}{\tilde{\epsilon}_{i\mathbf{k}'}} \cos(\theta_{\mathbf{k}} - \theta_{\mathbf{k}'}) (1 - f_{i\mathbf{k}'}^h - f_{i\mathbf{k}'}^e) \quad (4.8)$$

in the presence of excited charge-carrier distributions. Employing eq. (2.39), the renormalized quasiparticle dispersion  $\tilde{\epsilon}_{i\mathbf{k}}$  finally yields  $\tilde{\Sigma}_{i\mathbf{k}}^{e/h} = \tilde{\epsilon}_{i\mathbf{k}} \pm E_{F,i}$ .

Evidently, eqs. (4.2), (4.4), (4.7) and (4.8) are non-trivially coupled equations. In particular, the calculation of  $\tilde{\Sigma}_{i\mathbf{k}}^{e/h}$  requires the Fermi-Dirac distributions  $f_{i\mathbf{k}}^{e/h}$  as well as the screened Coulomb interaction  $W_{\mathbf{q}}$  which relates to the Lindhard polarization function  $\Pi_{\mathbf{q}}$ . In turn,  $f_{i\mathbf{k}}^{e/h}$  and  $\Pi_{\mathbf{q}}$  depend on  $\tilde{\Sigma}_{i\mathbf{k}}^{e/h}$  themselves. In general, this quartet of equations has to be solved self-consistently. Learning that the GEs predominantly introduce a constant energy shift, it turned out to be sufficient to set up  $f_{i\mathbf{k}}^{e/h}$  and  $\Pi_{\mathbf{q}}$  onetime with respect to the unrenormalized single-particle energies. Once the stated quantities are determined for given electron and hole densities  $n_i^{e/h}$ , all ingredients are provided to compute the optical properties via the generalized DWE and DBE.

To begin with, let us focus on the excitation-induced band-gap renormalization and Mott transition in suspended MoS<sub>2</sub> monolayers. The Mott-transition was quantified by the critical density where the binding energy of the respective 1s excitons vanishes, or equivalently, A<sub>1s</sub>- and B<sub>1s</sub>-exciton resonances coincide with the renormalized A and B band gaps  $E_g^{A/B} \equiv \tilde{\Sigma}_{A/B,k=0}^h + \tilde{\Sigma}_{A/B,k=0}^e$ , respectively. In this context the generalized DWE was solved providing the density-dependent A<sub>1s</sub>- and B<sub>1s</sub>-exciton resonances and binding energies, as well as the left- and right-handed momentum-space radial wave functions. The numerical procedure is analog to its counterpart (3.5) in the zero-density limit. Corresponding left- and right-handed real-space radial wave functions followed from the Fourier-Bessel transform. Subsequently, A<sub>1s</sub>- and B<sub>1s</sub>-exciton Bohr radii  $a_0^{A/B} \equiv \langle 1s|r|1s \rangle$  were computed in real-space representation and in the zero-density limit where left- and right-handed wave functions are identical. The numerical results according to ref. [II] are shown in fig. 4.1.

Fig. 4.1 (a) displays  $E_g^{A(B)}$  in light (dark) green solid lines as function of the total carrier density for the suspended MoS<sub>2</sub> monolayer at room temperature ( $T = 300$  K). Equal A- and B-band carrier densities were assumed, reflecting the spin-forbidden relaxation between B and A bands in a given valley. The dashed lines represent the energetic position of the corresponding 1s-exciton resonances. The inset schematically shows the momentum-space Fermi-Dirac distributions of the renormalized A and B bands in the vicinity of the  $K/K'$  points. Relative to the renormalized band gap in the zero-density limit, an enormous excitation-induced band-gap shrinkage as large as 800 meV was observed for carrier densities up to  $10^{14}$  cm<sup>-2</sup>.

Phase-space filling via the factor  $(1 - f_{i\mathbf{k}'}^h - f_{i\mathbf{k}'}^e)$  and plasma screening of the Coulomb interaction were identified as the two distinct mechanisms contributing to the excitation-induced band-gap shrinkage. By solving the GEs excluding the stated phase-space-filling factor, it became evident that plasma screening is the dominant contribution to the band-gap reduction. Consequently, the renormalized single-particle energies  $\tilde{\Sigma}_{i\mathbf{k}}^{e/h}$  converge towards the unrenormalized band structure in the high-density limit of the screened HF approximation.

A<sub>1s</sub>- (solid lines) and B<sub>1s</sub>-exciton (dashed lines) binding energies are depicted in fig. 4.1 (b) as functions of the total charge-carrier density for decreasing temperatures from red to yellow. Evidently, the critical densities shift to higher densities for de-

#### 4. Nonlinear optical properties of TMDC monolayers

creasing temperatures. This can be explained by the fact that hotter quasiequilibrium distributions shift to larger crystal momenta for a given density consequently reducing screening and phase-space filling. The slightly larger Mott-densities of the B exciton are due to its smaller exciton Bohr radius,  $a_0^B = 8.9 \text{ \AA}$  compared to  $a_0^A = 9.3 \text{ \AA}$ , and thus tighter binding [II]. A Mott-transition was predicted for a total charge-carrier density of close to  $10^{13} \text{ cm}^{-2}$  at room temperature.

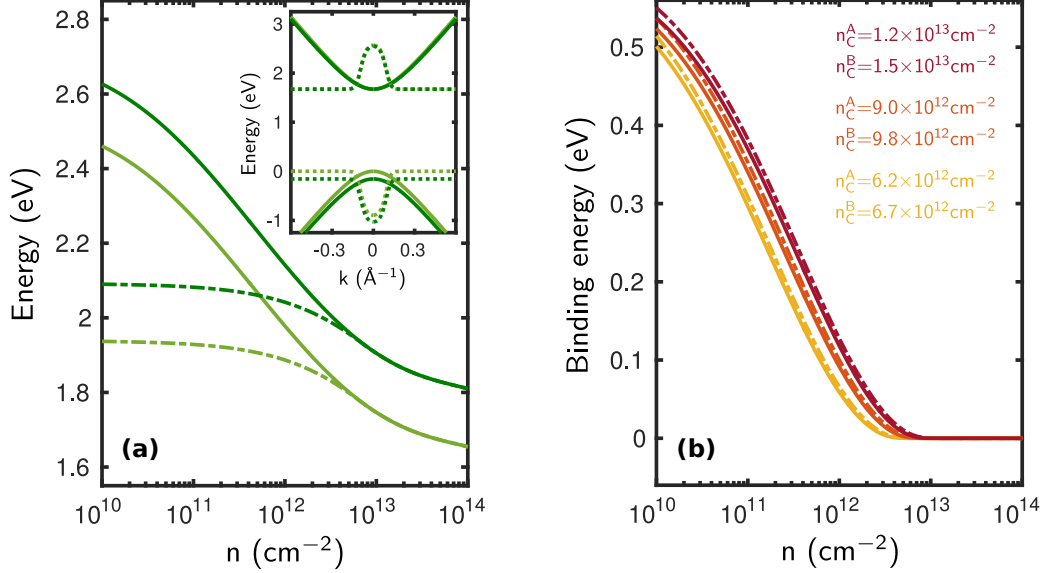


Figure 4.1.: (a) Renormalized band gap (solid lines) and 1s-exciton resonance energy (dashed lines) as function of total carrier density for the A (light green) and B (dark green) exciton of MoS<sub>2</sub> at  $T = 300 \text{ K}$ . The inset schematically shows the occupation of the A and B bands as a function of  $|\mathbf{k}|$ . (b) A<sub>1s</sub>- (solid lines) and B<sub>1s</sub>-exciton (dashed lines) binding energies as functions of carrier density for  $T = 200, 300$  and  $400 \text{ K}$ , respectively. The numbers refer to the critical density at which the 1s exciton merges with the continuum states. (Adapted from ref. [II]<sup>1</sup>.)

Finally, room-temperature optical absorption spectra, depicted in fig. 4.2, were computed employing the matrix-inversion approach described previously. Focusing on the left panel, fig. 4.2 (a) displays the optical absorption spectra for increasing carrier densities  $n = \sum_{i,\lambda} n_i^\lambda$  from top to bottom. Again, carrier densities were equally distributed between the A and B bands. The solid (dashed) lines represent the spectra for a freely suspended (SiO<sub>2</sub>-supported) monolayer. While pronounced for low carrier densities ( $n < 10^{12} \text{ cm}^{-2}$ ), the environmental influence on both band-gap and exciton binding energies becomes negligible for moderate to high densities ( $n \gtrsim 10^{12} \text{ cm}^{-2}$ ) because screening of the Coulomb interaction becomes dominated by the intrinsic screening of

<sup>1</sup>The highlighted typing error in  $n_B^C = 6.7 \times 10^{13} \text{ cm}^{-2}$  which is present in the original figure of ref. [II] was corrected to  $n_B^C = 6.7 \times 10^{12} \text{ cm}^{-2}$  in fig. 4.1(b).

the excited carriers. The simultaneous reduction of the band gap and exciton binding energy with increasing carrier densities led to a few-10-meV red shift of the respective 1s-exciton resonances. Beyond the Mott-transition the optical spectra displayed a broad gain region above  $E_g^A$  over a spectral range of a few 100 meV.

Fig. 4.2 (b) shows the optical spectra exclusively in the regime where gain is already observed<sup>2</sup>. Explicitly, the B-band density was increased from top to bottom for a fixed A-band density of  $n_A = 5.0 \times 10^{13} \text{ cm}^{-2}$ . The dominant plasma screening of the A-band carriers led to the ionization of the B-band electron-hole pairs well below the projected Mott-density of the B band. Consequently, free-carrier absorption was observed above the B-band edge while optical gain is present in the spectral region between  $E_g^A$  and  $E_g^B$ . Increasing the B-band density into the regime where inversion occurred, optical gain was observed from both bands.

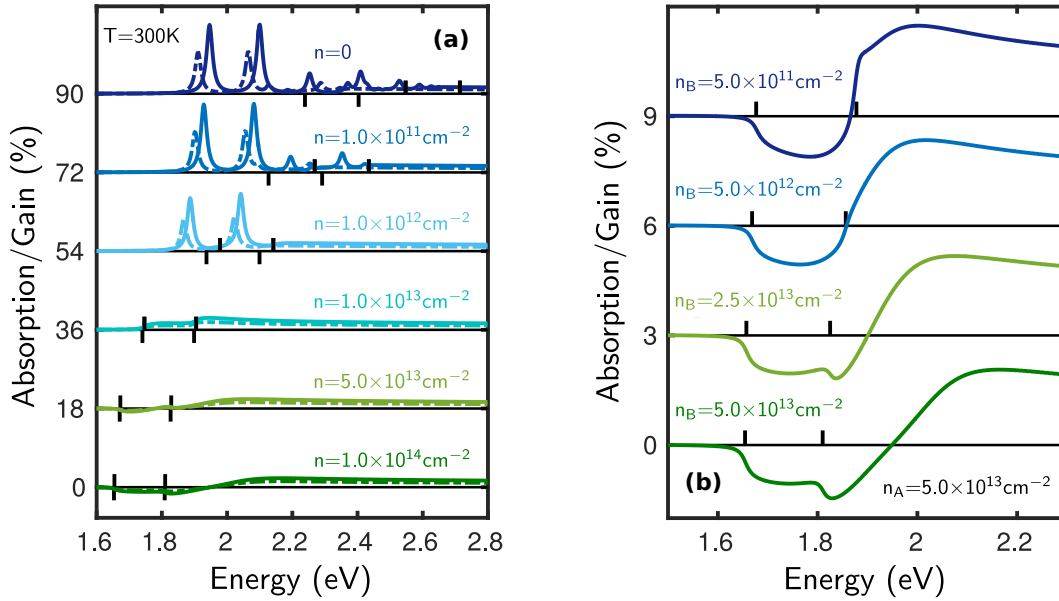


Figure 4.2.: Absorption spectra for MoS<sub>2</sub> at  $T = 300 \text{ K}$  for different carrier densities. Within the numerical simulations a phenomenological dephasing of 10 meV was applied. The range of the absorption axis results from the offsets that were chosen to sufficiently separate the individual spectra. (a) Equal electron and hole densities in the A and B bands. The solid lines show the spectra for a suspended monolayer, the dashed lines for a monolayer on a SiO<sub>2</sub> substrate. The black markers indicate the respective renormalized A and B band gaps  $E_g^{A/B}$ , where upwards (downwards) pointing markers correspond to the suspended (SiO<sub>2</sub>-supported) monolayer. (b) Variation of the B-band density for a fixed A-band density of  $n_A = 5.0 \times 10^{13} \text{ cm}^{-2}$ . (Adapted from ref. [II].)

<sup>2</sup>For comparison, optical gain is typically observed in conventional III-V semiconductors for sheet densities in the range of  $10^{12}$ - $10^{13} \text{ cm}^{-2}$  [92].

## 4.2. Pump-probe simulations of MoTe<sub>2</sub>

Pump-probe experiments are well established to explore the carrier dynamics and gain build-up in semiconductors after optical excitation. In our numerical experiment that led to publication [IV] and is summarized within this section a single SiO<sub>2</sub>-supported MoTe<sub>2</sub> layer was excited nonresonantly with a high-intensity linear-polarized pump pulse at room temperature. Further details on the excitation conditions are explicitly stated in ref. [IV]. Under these conditions, an uncorrelated electron-hole plasma was generated in the  $K$  and  $K'$  valleys of the BZ. Fig. 4.3 shows the single-particle band structure of monolayer MoTe<sub>2</sub> including the labels of the distinct valleys. Approximating the latter with the relativistic dispersion (2.4) in the vicinity of the  $K/K'$  points yielded necessary material parameters of the MDF-model Hamiltonian. For further information regarding the MoTe<sub>2</sub> material parameters, including bulk dielectric constants and *ab-initio* based form factors, see app. A.

It is important to recall that the MDF model is restricted to the carrier dynamics in the vicinity of the  $K/K'$  points of BZ. The inclusion of  $K$ - $\Sigma$  and  $K$ - $K'$  intervalley-scattering processes requires an anisotropic description of the complete BZ which is

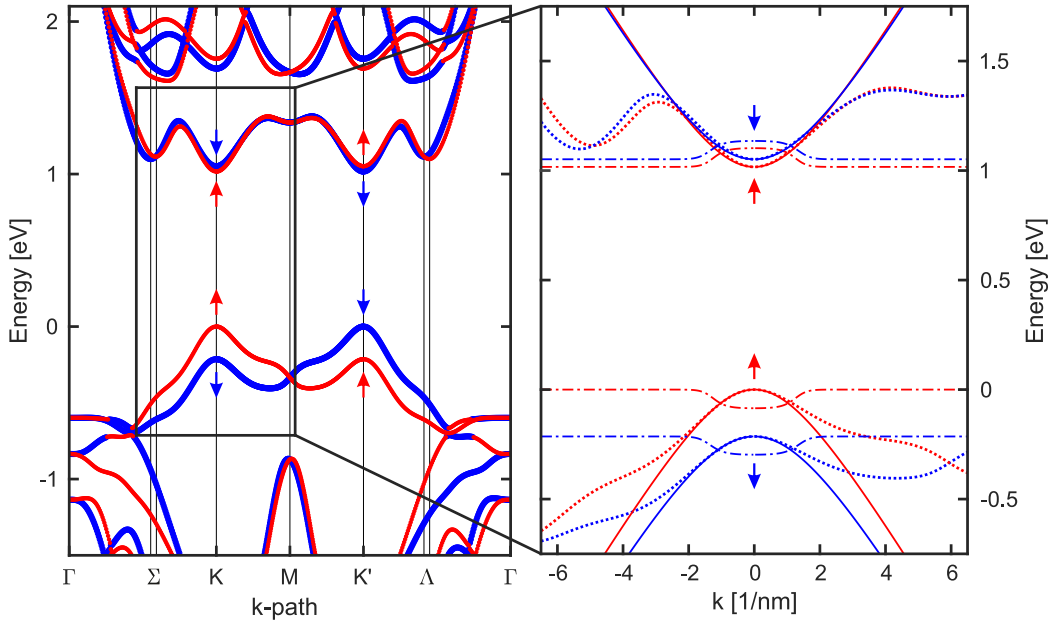


Figure 4.3.: Left: Single-particle band structure of monolayer MoTe<sub>2</sub>. Bands with spin up are depicted in red, bands with spin down in blue. Right: Relevant bands (dotted) with the approximated unrenormalized relativistic band dispersion (solid). The dashed-dotted lines show the equilibrium carrier distributions (2.5 ps after excitation) for the excitation conditions considered in ref. [IV]. For the distributions the baseline is taken to be the edge of the corresponding band and the maximum values are set to be the corresponding chemical potentials. (Adapted from ref. [IV].)

beyond the scope of this work. Note that ultrafast  $K$ - $\Sigma$  intervalley scattering on the timescale of 50-100 fs was observed in indirect-gap bulk MoS<sub>2</sub> [93] and WSe<sub>2</sub> [94] where the conduction-band minimum is in the  $\Sigma$  valley. For direct-gap TMDCs with a non-vanishing side-valley offset and considerably large barriers, such as monolayer MoTe<sub>2</sub>, these timescales should be longer under the considered excitation conditions.

Probing the strongly excited system with an ultrashort, low-intensity pulse at distinct time delays enabled us to access the time evolution of the linear optical response in the frequency range of interest, i.e. where the dephasing of the excitons and the build-up of optical gain occurred. Even though our isotropic model provides no access to the dynamics of intervalley scattering, the influence of a  $K$ - $\Sigma$  electron drain and  $K$ - $K'$  hole drift on the optical gain was finally estimated for an equilibrium situation where all electrons and holes have relaxed to common chemical potentials.

### 4.2.1. Excitation dynamics and ultrafast band-gap renormalization

For the chosen excitation conditions the optically induced interband polarizations predominantly lead to the generation of an uncorrelated electron-hole plasma. Based on the description of sec. 2.3.3, the generated plasma effectively screens the Coulomb interaction between electrons and holes leading to the replacement of unscreened HF renormalizations by their screened counterparts. Details in the dephasing of the interband polarizations play only a minor role for the carrier-relaxation dynamics [IV]. In this context it was sufficient to treat the polarization equation (2.45) on the level of the screened HF approximation within the pump simulations.

Based on the conclusions of secs. 2.3.3 and 2.3.4, the quantum-Boltzmann-like scattering rates to describe the intraband carrier-relaxation dynamics for the electron-distribution functions were implemented as

$$\begin{aligned} \left. \frac{d}{dt} f_{ik}^e \right|_{\text{el.}} &= \frac{2\pi}{\hbar} \sum_{q \neq 0} W_q \sum_{j,p} (V_q - V_{k-p} \delta_{i,j}) \delta(\tilde{\Sigma}_{ik}^e - \tilde{\Sigma}_{ik-q}^e - \tilde{\Sigma}_{jp}^e + \tilde{\Sigma}_{jp-q}^e) \\ &\quad \times \left\{ f_{ik}^e \bar{f}_{ik-q}^e f_{jp-q}^e \bar{f}_{jp}^e - \bar{f}_{ik}^e f_{ik-q}^e \bar{f}_{jp-q}^e f_{jp}^e \right\} \\ &+ \frac{2\pi}{\hbar} \sum_{q \neq 0} W_q \sum_{j,p} V_q \delta(\tilde{\Sigma}_{ik+q}^e - \tilde{\Sigma}_{ik}^e - \tilde{\Sigma}_{jp}^h + \tilde{\Sigma}_{jp-q}^h) \\ &\quad \times \left\{ f_{ik}^e \bar{f}_{ik+q}^e f_{jp}^h \bar{f}_{jp-q}^h - \bar{f}_{ik}^e f_{ik+q}^e \bar{f}_{jp}^h f_{jp-q}^h \right\}, \end{aligned} \quad (4.9)$$

$$\begin{aligned} \left. \frac{d}{dt} f_{ik}^e \right|_{\text{ph.}} &= \frac{2\pi}{\hbar} \sum_{q \neq 0} g_q g_q^0 \delta(\tilde{\Sigma}_{ik+q}^e - \tilde{\Sigma}_{ik}^e - \hbar\omega_q) \left[ (1 + n_q) f_{ik+q}^e \bar{f}_{ik}^e - n_q f_{ik}^e \bar{f}_{ik+q}^e \right] \\ &+ \frac{2\pi}{\hbar} \sum_{q \neq 0} g_q g_q^0 \delta(\tilde{\Sigma}_{ik-q}^e - \tilde{\Sigma}_{ik}^e + \hbar\omega_q) \left[ n_q f_{ik-q}^e \bar{f}_{ik}^e - (1 + n_q) f_{ik}^e \bar{f}_{ik-q}^e \right], \end{aligned} \quad (4.10)$$

where contributions from the microscopic polarizations were considered small within the remaining scattering terms. The equations for the scattering dynamics of the hole-distribution functions are analog. In eqs. (4.9) and (4.10),  $W_q$  and  $g_q$  denote the

#### 4. Nonlinear optical properties of TMDC monolayers

time-dependent screened Coulomb and Fröhlich interactions that were computed from their respective bare counterparts  $V_q$  and  $g_q^0$  with the aid of the Lindhard polarization function (2.59) in the static limit. Furthermore,  $n_{\mathbf{q}} = \frac{1}{e^{\beta\hbar\omega_{\mathbf{q}}}-1}$  denotes the phonon occupation number corresponding to the LO-phonon energy of  $\hbar\omega_{\mathbf{q}} = 27.72$  meV in monolayer MoTe<sub>2</sub> [45]. Energy conservation of the scattering processes was assured using the numerical energy-conservation function  $\pi\delta_{\eta}(x) = \frac{\hbar\eta}{x^2+(\hbar\eta)^2}$ , where a small broadening  $\hbar\eta$  in the range of 1-5 meV was employed.

The scattering dynamics of the electron and hole distribution functions  $f_{i\mathbf{k}}^{\lambda}$  couple among others to distribution functions  $f_{i\mathbf{k}-\mathbf{q}}^{\lambda}$ . However,  $f_{i\mathbf{k}}^{\lambda}$  is only defined on a rigid, equidistant  $|\mathbf{k}|$ -grid. Therefore, distribution functions of type  $f_{i\mathbf{k}-\mathbf{q}}^{\lambda}$  were approximated using a quadratic spline

$$s_k^{\lambda} = f_{k_{l+1}}^{\lambda} + (k - k_{l+1}) \left. \frac{\partial f_k^{\lambda}}{\partial k} \right|_{k=\bar{k}_{12}} + \frac{(k - k_{l+1})(k - k_{l+2})}{2} \left. \frac{\partial^2 f_k^{\lambda}}{\partial k^2} \right|_{k=\bar{k}_{12}} \quad (4.11)$$

for crystal momenta  $k_{l+1} \leq k < k_{l+2}$  between the two grid points, where the shorthand notations

$$\left. \frac{\partial f_k^{\lambda}}{\partial k} \right|_{k=\bar{k}_{12}} = \frac{f_{k_{l+2}}^{\lambda} - f_{k_{l+1}}^{\lambda}}{k_{l+2} - k_{l+1}}, \quad \left. \frac{\partial^2 f_k^{\lambda}}{\partial k^2} \right|_{k=\bar{k}_{12}} = \frac{\left. \frac{\partial f_k^{\lambda}}{\partial k} \right|_{k=k_{l+2}} - \left. \frac{\partial f_k^{\lambda}}{\partial k} \right|_{k=k_{l+1}}}{k_{l+2} - k_{l+1}}, \quad (4.12)$$

with  $\bar{k}_{12} = (k_{l+1} + k_{l+2})/2$  and  $k_{l+1} = k_l + dk$ , are introduced. It is easily verified that  $s_{k_{l+1}}^{\lambda} = f_{k_{l+1}}^{\lambda}$  and  $s_{k_{l+2}}^{\lambda} = f_{k_{l+2}}^{\lambda}$  hold for the boundaries of the spline. Since a quadratic polynomial requires three coefficients, the final coefficient results from the condition that the curvature of the spline is given by the second derivative of the distribution function in the center of the interval. Employing the symmetric difference quotient for the first derivative at grid point  $k_l$ ,  $\left. \frac{\partial f_k^{\lambda}}{\partial k} \right|_{k=k_l} = \frac{f_{k_{l+1}}^{\lambda} - f_{k_{l-1}}^{\lambda}}{k_{l+1} - k_{l-1}}$ , yields the numerically implemented form

$$f_k^{\lambda} \approx f_{k_{l+1}}^{\lambda} + x_k (f_{k_{l+2}}^{\lambda} - f_{k_{l+1}}^{\lambda}) - \frac{x_k(1-x_k)}{4} (f_{k_{l+3}}^{\lambda} - f_{k_{l+2}}^{\lambda} - f_{k_{l+1}}^{\lambda} + f_{k_l}^{\lambda}), \quad (4.13)$$

where  $x_k = (k - k_{l+1})/dk$ . Note that the interpolation is only possible for crystal momenta  $k < k_{N_k-2}$  where  $N_k$  denotes the number of  $|\mathbf{k}|$ -grid points. Therefore, the  $|\mathbf{k}|$ -grid had to be wide enough to ensure that the distribution functions decay sufficiently towards the end of the grid.

For the calculation of the excitation and subsequent carrier-relaxation dynamics in monolayer MoTe<sub>2</sub> the DBEs were solved in the time domain employing the widely used 4th-order Runge-Kutta algorithm [72]. The results are shown representatively for the A-band electron distribution function  $f_{A,\mathbf{k}}^e(t)$  in fig. 4.4. We predicted extremely efficient intraband carrier-carrier scattering driving the distribution functions into hot quasiequilibrium states near the band edges and away from the excitation energy within a few femtoseconds. In particular, carrier temperatures above 2000 K were observed at the time where the pump maximum hits the sample. Consequently, an

accumulation of carriers at the excitation energy was almost completely avoided. This led to a highly efficient generation of about  $5.20 \times 10^{13}$  electron-hole pairs per cm<sup>2</sup> for the given excitation conditions. Carrier-phonon scattering then drove the hot carriers towards a quasiequilibrium at the temperature of the phonon bath within 2.5 ps.

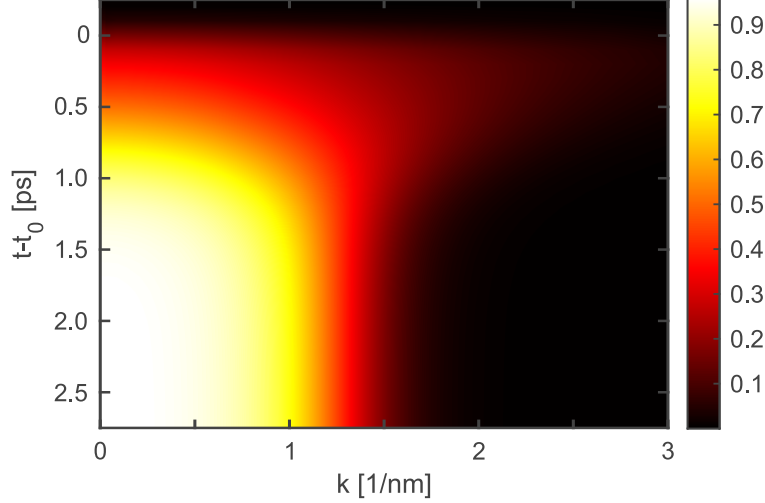


Figure 4.4.: Dynamics of the A-band electron-distribution function in the vicinity of the  $K/K'$  points after excitation with a 300 fs pump pulse with peak amplitude of 1.25 MV/cm at  $t = t_0$ . (Adapted from ref. [IV].)

The calculation of the carrier-carrier scattering rates (4.9) constitute the major numerical challenge because of the fivefold integration, whereas the numerical complexity of carrier-phonon scattering rates (4.10) is comparable to the calculation of screened HF renormalizations. To reduce the numerical effort, scattering rates were not recalculated in every time step of the integration, but only when the electron and hole-distribution functions changed significantly since the previous calculation. The change in the distribution functions was quantified by computing the scattering deviation

$$D_{\text{scatt.}} = \sum_{\lambda, i, k} dk k \left( \frac{f_{ik}^{\lambda, \text{new}} - f_{ik}^{\lambda, \text{old}}}{f_{ik}^{\lambda, \text{new}} + f_{ik}^{\lambda, \text{old}}} \right)^2$$

in every time step prior to the prompt of recalculating the next carrier-carrier scattering rates. The recalculation was triggered whenever  $D_{\text{scatt.}}$  hit the designated threshold value. In this case

- the grids  $\Pi_{\mathbf{q}}(t)$  and  $W_{\mathbf{q}}(t)$  for the Lindhard polarization function and screened Coulomb interaction,
- s-type angular-averaged Coulomb matrix elements  $W_{i, kk'}^{\lambda \mu \mu' \lambda'}(t)$ ,
- carrier-carrier scattering rates  $\left. \frac{d}{dt} f_{i\mathbf{k}}^e \right|_{\text{el.}}$ ,

#### 4. Nonlinear optical properties of TMDC monolayers

- the grid  $g_q(t)$  for the screened Fröhlich interaction,
- and carrier-phonon scattering rates  $\left. \frac{d}{dt} f_{ik}^e \right|_{\text{ph}}$ .

were recalculated in the stated order. The threshold value for  $D_{\text{scatt.}}$  to provide numerically stable simulations is typically found by trial and error.

Numerically verified, the excitation-induced band-gap renormalization of the GEs on the level of screened HF approximation is contained within the renormalized electron and hole energies

$$\tilde{\Sigma}_{ik}^e(t) = \epsilon_{ik}^e - \sum_{k'} dk' k' \left[ W_{i,kk'}^{\text{cccc}}(t) - W_{i,kk'}^{\text{cvcv}}(t) \right] f_{ik'}^e(t), \quad (4.14)$$

$$\tilde{\Sigma}_{ik}^h(t) = \epsilon_{ik}^h + \sum_{k'} dk' k' \left[ W_{i,kk'}^{\text{vvvv}}(t) - W_{i,kk'}^{\text{vcvc}}(t) \right] \left( 1 - f_{ik'}^h(t) \right). \quad (4.15)$$

Eqs. (4.14) and (4.15) are stated in the numerically implemented form using the angular-averaged Coulomb matrix elements  $W_{i,kk'}^{\lambda\mu\mu'\lambda'}(t)$ . Evidently, time-dependent intraband energy differences, e.g.  $\tilde{\Sigma}_{ik}^{e/h}(t) - \tilde{\Sigma}_{ik-q}^{e/h}(t)$ , enter the Lindhard polarization and energy-conserving functions. Knowing that the screened HF renormalizations predominantly introduce a rigid shift to the unrenormalized single-particle energies, intraband energy differences,  $\tilde{\Sigma}_{ik}^{e/h}(t) - \tilde{\Sigma}_{ik-q}^{e/h}(t) \approx \epsilon_{ik}^{e/h} - \epsilon_{ik-q}^{e/h}$ , remain almost unchanged through the course of the excitation. Therefore, Lindhard polarization and energy-conserving functions were computed based on the unrenormalized single-particle energies immensely reducing the numerical effort without noticeable impact on the results. Here, energies of type  $\epsilon_{ik-q}^{e/h}$  were interpolated based on the previous description.

The excitation-induced band gap for given spin and valley indices was estimated from the renormalized electron and hole energies via

$$E_g^i(t) = \tilde{\Sigma}_{ik=0}^h(t) + \tilde{\Sigma}_{ik=0}^e(t). \quad (4.16)$$

In fig. 4.5 the time evolution of the excitation-induced band-gap renormalization  $E_g^i(t) - E_g^i(0)$  (black) and the corresponding total carrier density  $n_i(t) = n_i^h(t) + n_i^e(t)$  (red) are shown. A- and B-band properties are plotted in solid and dashed lines, respectively, and the gray shaded area indicates the envelope of the optical pump pulse. For the given excitation conditions slightly higher carrier densities were induced within the B bands than in the A bands. Due to opposite spin, intravalley relaxation processes between B and A bands were considered negligible.

The generation of excited charge carriers within the respective bands was found to be accompanied by a huge and almost instantaneous reduction of the band gap. As pointed out in sec. 4.1, the band-gap reduction results from combined screening and phase-space-filling effects. Supported by the ultrafast Coulomb scattering the major contribution to screening develops during the build-up of the excited charge carriers and therefore directly correlates to the width and strength of the pump pulse. For the MoTe<sub>2</sub> monolayer we particularly observed a large band-gap shrinkage of about 390 meV already 0.4 ps after the pump-pulse maximum hit the sample. At this point,

the amount of excited charge carriers had just saturated such that further reduction of less than 20 meV on the time scale of the thermalization could be assigned to phase-space filling.

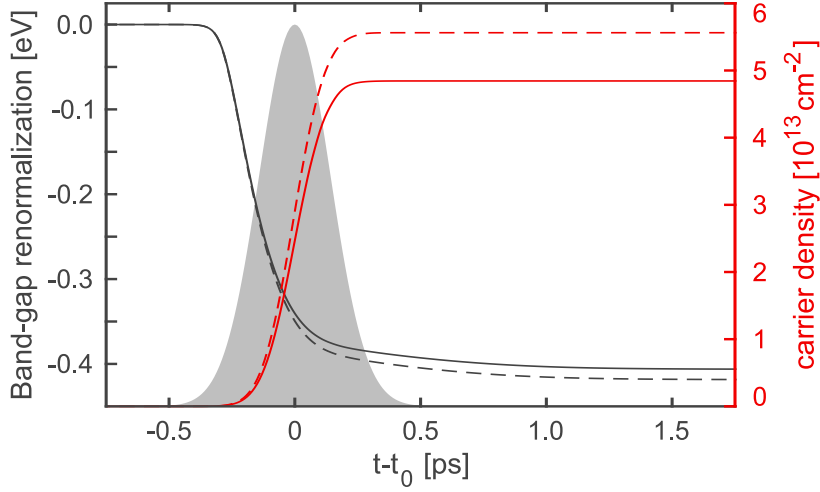


Figure 4.5.: Time evolution of the excitation-induced band-gap renormalization (black) and the density of excited charge carriers (red). The solid lines correspond to the A-band properties, whereas the dashed lines show the B-band properties. The gray shaded area indicates the envelope of the optical pump pulse. (Adapted from ref. [IV].)

### 4.2.2. Build-up of the optical gain

The numerical simulation of pump-probe experiments has the advantage that the time consuming excitation dynamics only have to be computed once assuming a considerable detuning between pump and probe pulses. The time evolution of the linear optical properties, e.g. susceptibility and absorption spectra, then follow from inserting the electron and hole distribution functions of distinct time delays,  $f_{i\mathbf{k}}^{e/h} = f_{i\mathbf{k}}^{e/h}(\tau_d)$  with  $\tau_d = t - t_0$ , into a probe simulation. Here,  $t_0$  is the time where the pump maximum hits the sample. Consequently, pump and probe simulations are numerically decoupled. Note that in this approach the time resolution of the pump-probe scenario is only limited by the step size of the equidistant  $t$ -grid within the pump simulation, whereas it is limited by the temporal width of the probe pulse in experimental setups.

Decoupling pump and probe simulations brought the technical advantage that the probe simulations at distinct time delays could be performed in frequency space. This enabled a dynamic (frequency-dependent) treatment of the carrier and phonon contributions to the EID of the microscopic polarizations,  $\Gamma_{i\mathbf{k}}^{\text{he}}(\omega) = \Gamma_{i\mathbf{k}}^{\text{he}}(\omega)|_{\text{el.}} + \Gamma_{i\mathbf{k}}^{\text{he}}(\omega)|_{\text{ph.}}$ , under the assumption of quasistatic distribution functions. Especially the dynamic treatment of the former turned out to be crucial to avoid unphysical behavior within

#### 4. Nonlinear optical properties of TMDC monolayers

the optical spectra, i.e. exciton resonances dephasing at vanishingly low charge-carrier densities and an uncapped increase of the gain maximum with increasing densities beyond the Mott-transition.

Leading to the time evolution of the absorption spectrum, the frequency-space representation for the polarization equation

$$\begin{aligned} & \left[ \hbar(\omega + i\gamma) - (\Sigma_{ik}^h + \Sigma_{ik}^e) \right] P_{ik}(\omega) + (1 - f_{ik}^h - f_{ik}^e) \sum_{\mathbf{k}' \neq \mathbf{k}} V_{\mathbf{k}-\mathbf{k}', ik', ik}^{\text{cvvc}} P_{ik'}(\omega) - \Gamma_{ik}^{\text{he}}(\omega) \\ & = - (1 - f_{ik}^h - f_{ik}^e) \frac{e}{m_0 c} \mathbf{p}_{i,\text{cv}}(\mathbf{k}) \cdot \mathbf{A}(\omega) \end{aligned} \quad (4.17)$$

was employed in the numerical simulations, where  $f_{ik}^{e/h} = f_{ik}^{e/h}(\tau_d)$  and  $\Sigma_{ik}^{e/h} = \Sigma_{ik}^{e/h}(\tau_d)$ . Since the EID

$$\Gamma_{ik}^{\text{he}}(\omega) = \sum_{\mathbf{k}' \neq \mathbf{k}} \left[ \Delta I_{\mathbf{k}-\mathbf{k}', ik}^{\text{he}}(\omega) + G_{\mathbf{k}-\mathbf{k}', ik}^{\text{he},+}(\omega) + G_{\mathbf{k}-\mathbf{k}', ik}^{\text{he},-}(\omega) - (\mathbf{k} \leftrightarrow \mathbf{k}') \right] \quad (4.18)$$

contains the plasma screening, the first line of eq. (4.17) requires the unscreened HF renormalizations. The linearized dynamic contributions to the EID read

$$\begin{aligned} \Delta I_{\mathbf{k}-\mathbf{k}', ik}^{\text{he}}(\omega) & = W_{\mathbf{k}-\mathbf{k}', ik}^{\text{he}}(\omega) \sum_{\lambda, j, p} \frac{(V_{\mathbf{k}-\mathbf{k}'} - \delta_{i,j} \delta_{\lambda,e} V_{\mathbf{k}-p}) \left\{ \bar{f}_{jp}^{\lambda} f_{jp-\mathbf{k}+\mathbf{k}'}^{\lambda} \bar{f}_{ik'}^e \right\}_{\Sigma} P_{ik}(\omega)}{\Delta \tilde{\Sigma}_{\mathbf{k}-\mathbf{k}', ik}^{\text{he}}(\omega) + \tilde{\Sigma}_{jp-\mathbf{k}+\mathbf{k}'}^{\lambda} - \tilde{\Sigma}_{jp}^{\lambda} + i\hbar\gamma_{\text{T}}} \\ & - W_{\mathbf{k}-\mathbf{k}', ik}^{\text{he}}(\omega) \sum_{\lambda, j, p} \frac{(V_{\mathbf{k}-\mathbf{k}'} - \delta_{i,j} \delta_{\lambda,h} V_{\mathbf{k}'-p}) \left\{ \bar{f}_{jp}^{\lambda} f_{jp-\mathbf{k}+\mathbf{k}'}^{\lambda} \bar{f}_{ik}^h \right\}_{\Sigma} P_{ik'}(\omega)}{\Delta \tilde{\Sigma}_{\mathbf{k}-\mathbf{k}', ik}^{\text{he}}(\omega) + \tilde{\Sigma}_{jp-\mathbf{k}+\mathbf{k}'}^{\lambda} - \tilde{\Sigma}_{jp}^{\lambda} + i\hbar\gamma_{\text{T}}}, \end{aligned} \quad (4.19)$$

$$G_{\mathbf{k}-\mathbf{k}', ik}^{\text{he},+}(\omega) = g_{\mathbf{k}-\mathbf{k}', ik}^{\text{he}}(\omega) g_{\mathbf{k}-\mathbf{k}'}^0 \frac{\left\{ \bar{f}_{ik'}^e n_{\mathbf{k}-\mathbf{k}'} \right\}_{\Sigma} P_{ik}(\omega) - \left\{ \bar{f}_{ik}^h n_{\mathbf{k}-\mathbf{k}'} \right\}_{\Sigma} P_{ik'}(\omega)}{\Delta \tilde{\Sigma}_{\mathbf{k}-\mathbf{k}', ik}^{\text{he}}(\omega) + \hbar\omega_{\mathbf{k}-\mathbf{k}'} + i\hbar\eta}, \quad (4.20)$$

$$G_{\mathbf{k}-\mathbf{k}', ik}^{\text{he},-}(\omega) = g_{\mathbf{k}-\mathbf{k}', ik}^{\text{he}}(\omega) g_{\mathbf{k}-\mathbf{k}'}^0 \frac{\left\{ \bar{f}_{ik'}^e n_{\mathbf{k}-\mathbf{k}'} \right\}_{\Sigma} P_{ik}(\omega) - \left\{ \bar{f}_{ik}^h n_{\mathbf{k}-\mathbf{k}'} \right\}_{\Sigma} P_{ik'}(\omega)}{\Delta \tilde{\Sigma}_{\mathbf{k}-\mathbf{k}', ik}^{\text{he}}(\omega) - \hbar\omega_{\mathbf{k}-\mathbf{k}'} + i\hbar\eta}, \quad (4.21)$$

where we already applied the random-phase approximation (RPA) by neglecting contributions  $\propto P_{jp}(\omega)$  and  $P_{jp-q}(\omega)$ . Furthermore,  $\left\{ \bar{f}_{k_1}^{\lambda} f_{k_2}^{\alpha} \bar{f}_{k_3}^{\beta} \right\}_{\Sigma} \equiv \bar{f}_{k_1}^{\lambda} f_{k_2}^{\alpha} \bar{f}_{k_3}^{\beta} + f_{k_1}^{\lambda} \bar{f}_{k_2}^{\alpha} f_{k_3}^{\beta}$  and  $\left\{ f_{k}^{\lambda} n_q \right\}_{\Sigma} \equiv f_{k}^{\lambda} n_q + \bar{f}_{k}^{\lambda} (1 + n_q)$  are introduced to shorten the notation.

Properties of type  $O_{\mathbf{k}-\mathbf{k}', ik}^{\text{he}}(\omega)$ , i.e. the dynamic polarization function  $\Pi_{\mathbf{k}-\mathbf{k}', ik}^{\text{he}}(\omega)$  and corresponding screened Coulomb and Fröhlich interactions,  $W_{\mathbf{k}-\mathbf{k}', ik}^{\text{he}}(\omega)$  and  $g_{\mathbf{k}-\mathbf{k}', ik}^{\text{he}}(\omega)$ , respectively, follow the shorthand notation

$$O_{\mathbf{k}-\mathbf{k}', ik}^{\text{he}}(\omega) \equiv O_{\mathbf{k}-\mathbf{k}'}(\Delta \tilde{\Sigma}_{\mathbf{k}-\mathbf{k}', ik}^{\text{he}}(\omega)/\hbar + i\gamma_{\text{T}}), \quad (4.22)$$

$$\Delta \tilde{\Sigma}_{\mathbf{k}-\mathbf{k}', ik}^{\text{he}}(\omega) \equiv \hbar\omega - \tilde{\Sigma}_{ik}^h - \tilde{\Sigma}_{ik'}^e. \quad (4.23)$$

Below, details on the numerical implementation of the dynamic polarization-carrier scattering are highlighted by taking the example of the contribution  $\Delta I_{\mathbf{k}-\mathbf{k}', ik}^{\text{he}}(\omega)$ .

Pursuing the solution of eq. (4.17) via matrix inversion, the first (second) line of eq. (4.19) contributes to the diagonal (nondiagonal) polarization-carrier scattering matrix, suggesting a decomposition

$$\Gamma_{i\mathbf{k}}^{\text{he}}(\omega)\Big|_{\text{el.}} = \Gamma_{i\mathbf{k}}^{\text{D}}(\omega)\Big|_{\text{el.}} P_{i\mathbf{k}}(\omega) - \sum_{\mathbf{k}' \neq \mathbf{k}} \Gamma_{i\mathbf{k},i\mathbf{k}'}^{\text{ND}}(\omega)\Big|_{\text{el.}} P_{i\mathbf{k}'}(\omega). \quad (4.24)$$

Even in an isotropic picture, the elements of  $\Gamma_{i\mathbf{k}}^{\text{D}}(\omega)\Big|_{\text{el.}}$  and  $\Gamma_{i\mathbf{k},i\mathbf{k}'}^{\text{ND}}(\omega)\Big|_{\text{el.}}$  are described by multidimensional integrals and have to be solved for each component of the  $\omega$ -grid. Without further approximations, this is extremely challenging from a numerical standpoint. However, the numerical effort could be immensely reduced by additionally introducing the function

$$\Lambda_{\mathbf{q}}(\omega) = \sum_{\lambda,j,p} \frac{f_{j\mathbf{p}-\mathbf{q}}^{\lambda} \bar{f}_{j\mathbf{p}}^{\lambda}}{\hbar\omega + \tilde{\Sigma}_{j\mathbf{p}-\mathbf{q}}^{\lambda} - \tilde{\Sigma}_{j\mathbf{p}}^{\lambda}}, \quad (4.25)$$

similar to the Lindhard polarization function (2.58), and by defining  $\Lambda_{\mathbf{k}-\mathbf{k}',i\mathbf{k}}^{\text{he}}(\omega)$  following the notation of eqs. (4.22) and (4.23). Excluding exchange contributions, i.e. contributions  $\propto V_{\mathbf{k}-\mathbf{p}}$  and  $V_{\mathbf{k}'-\mathbf{p}}$  that were found to be negligible, eq. (4.19) reads

$$\begin{aligned} \Delta I_{\mathbf{k}-\mathbf{k}',i\mathbf{k}}^{\text{he}}(\omega) &= W_{\mathbf{k}-\mathbf{k}',i\mathbf{k}}^{\text{he}}(\omega) V_{\mathbf{k}-\mathbf{k}'} \left[ \Lambda_{\mathbf{k}-\mathbf{k}',i\mathbf{k}}^{\text{he}}(\omega) - \Pi_{\mathbf{k}-\mathbf{k}',i\mathbf{k}}^{\text{he}}(\omega) f_{i\mathbf{k}}^{\text{e}} \right] P_{i\mathbf{k}}(\omega) \\ &\quad - W_{\mathbf{k}-\mathbf{k}',i\mathbf{k}}^{\text{he}}(\omega) V_{\mathbf{k}-\mathbf{k}'} \left[ \Lambda_{\mathbf{k}-\mathbf{k}',i\mathbf{k}}^{\text{he}}(\omega) - \Pi_{\mathbf{k}-\mathbf{k}',i\mathbf{k}}^{\text{he}}(\omega) f_{i\mathbf{k}}^{\text{h}} \right] P_{i\mathbf{k}'}(\omega). \end{aligned} \quad (4.26)$$

Evidently, the entire numerical complexity is now transferred to the quantities  $\Lambda_{\mathbf{k}-\mathbf{k}',i\mathbf{k}}^{\text{he}}(\omega)$  and  $\Pi_{\mathbf{k}-\mathbf{k}',i\mathbf{k}}^{\text{he}}(\omega)$ . Rather than computing both quantities for all combinations of  $|\mathbf{k} - \mathbf{k}'|$  and  $\omega$ , resulting in a four-dimensional array,  $\Lambda_{\mathbf{q}}(\omega' + i\gamma_{\text{T}})$  and  $\Pi_{\mathbf{q}}(\omega' + i\gamma_{\text{T}})$  were computed for the extended frequency range

$$\min[\Delta \Sigma_{\mathbf{k}-\mathbf{k}',i\mathbf{k}}^{\text{he}}(\omega)/\hbar] \leq \omega' \leq \max[\Delta \Sigma_{\mathbf{k}-\mathbf{k}',i\mathbf{k}}^{\text{he}}(\omega)/\hbar]. \quad (4.27)$$

Within the calculation of the diagonal and nondiagonal polarization-carrier scattering matrices,  $\Lambda_{\mathbf{k}-\mathbf{k}',i\mathbf{k}}^{\text{he}}(\omega)$  was determined from  $\Lambda_{\mathbf{q}}(\omega' + i\gamma_{\text{T}})$  by projecting  $\Delta \Sigma_{\mathbf{k}-\mathbf{k}',i\mathbf{k}}^{\text{he}}(\omega)/\hbar$  onto the closest  $\omega'$ -grid point, followed by interpolating  $\Lambda_{\mathbf{k}-\mathbf{k}'}(\omega' + i\gamma_{\text{T}})$  based on the computed  $\Lambda_{\mathbf{q}}(\omega' + i\gamma_{\text{T}})$  array employing the interpolation scheme described previously. Here, a resolution of 1-5 meV for the  $\omega'$ -grid was sufficient and the results varied very little over a wide range of triplet dephasings  $\gamma_{\text{T}} = 50\text{-}350$  meV. Thus, the numerical effort to compute the polarization-carrier scattering matrices was effectively reduced by two dimensions at the cost of an extended frequency grid.

The procedure to determine  $\Pi_{\mathbf{k}-\mathbf{k}',i\mathbf{k}}^{\text{he}}(\omega)$  is correspondingly. Note that the latter then automatically yields the dynamically screened Coulomb and Fröhlich interactions,  $W_{\mathbf{k}-\mathbf{k}',i\mathbf{k}}^{\text{he}}(\omega)$  and  $g_{\mathbf{k}-\mathbf{k}',i\mathbf{k}}^{\text{he}}(\omega)$ , respectively. Therefore, the numerical implementation of the polarization-phonon scattering contributions is accordingly.

For the time evolution of the optical absorption spectrum, depicted in fig. 4.6, we considered probing with a low-intensity, linear-polarized pulse at different delay times

#### 4. Nonlinear optical properties of TMDC monolayers

in the excitation (a) and thermalization (b) regimes. To cover the wide range of several hundred meV in energies, a probe pulse with a temporal width of about 10 fs was required. From an experimental standpoint such an ultrashort probe pulse is crucial to provide the necessary time resolution to study the evolution of the optical response, especially during the excitation process.

In the excitation regime pump-probe delays were increased from  $\tau_d = -0.30$  to  $\tau_d = -0.05$  ps with increments of 0.05 ps. For comparison, the optical absorption spectrum of the monolayer prior to excitation is depicted in black. The initial increase of excited charge carriers simultaneously led to dephasing, excitation-induced band-gap shrinkage, and reduction of the exciton binding energy. As a result of compensating effects, practically no shift of the respective 1s-exciton resonance positions was ob-

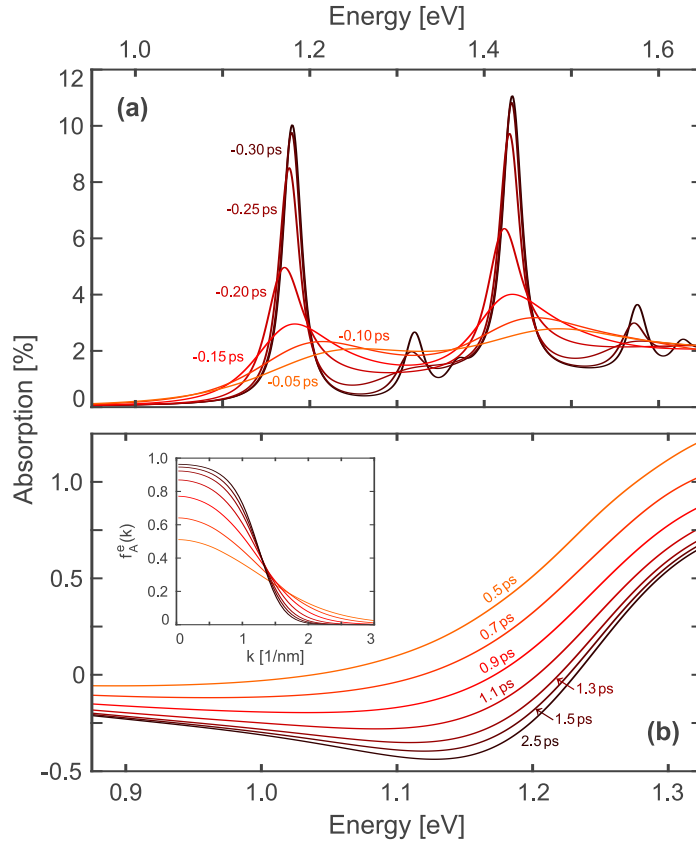


Figure 4.6.: Optical absorption spectra at distinct pump-probe delays. (a) Excitation regime. Pump-probe delays increase from  $\tau_d = -0.30$  ps to  $\tau_d = -0.05$  ps in 0.05 ps steps. The black solid line represents the low-density limit before the excitation. (b) Thermalization regime. Pump-probe delays increase from  $\tau_d = 0.5$  ps to  $\tau_d = 1.5$  ps in 0.2 ps steps. The absorption spectrum in the quasiequilibrium limit ( $\tau_d \approx 2.5$  ps) is shown in black. The corresponding A-band distribution functions are depicted in the inset. (According to ref. [IV].)

served under the given excitation conditions. At a density of about  $3.36 \times 10^{13} \text{ cm}^{-2}$ , corresponding to  $\tau_d = -0.05 \text{ ps}$ , the exciton resonances were found to completely bleach out, defining the Mott-density [IV].

In the thermalization regime pump-probe delays increased from  $\tau_d = 0.5 \text{ ps}$  to  $\tau_d = 1.5 \text{ ps}$  with increments of  $0.2 \text{ ps}$ . The inset displays snapshots of the corresponding A-band electron distribution function. Motivated by the high barriers between the  $K/K'$  and  $\Sigma/\Lambda$  valleys, side-valley drain of the excited carriers was neglected on the fast carrier-relaxation timescale. At around  $\tau_d = 0.5 \text{ ps}$  occupation inversion occurred leading to optical gain in the spectrum. Thermal equilibrium was reached after about  $2.5 \text{ ps}$  (black curve) where broad A-band optical gain peaked at an energy of  $1.13 \text{ eV}$ , slightly below the low-density A-exciton resonance. The gain maximum, approaching  $0.5 \%$  amplification of the incident light, was found to be clearly below A-band continuum absorption. Consequently, the latter overcompensated B-band gain, yielding a net absorption in the energy range of the B-exciton series [IV].

### 4.2.3. Influence of side-valley effects on the optical gain

The single-particle band structure of MoTe<sub>2</sub> displays six local conduction-band minima, three for each spin orientation, at the  $\Sigma/\Lambda$  points of the hexagonal BZ. For the intermediate state considered previously, an electron drain from the  $K/K'$  to the  $\Sigma/\Lambda$  valleys as well as a hole drift between the  $K$  and  $K'$  valleys results from equilibration within the entire BZ. In a true equilibrium situation, all electrons and holes have relaxed to common chemical potentials,  $\mu^e$  and  $\mu^h$ , respectively.

In order to estimate the influence of the electronic side-valley drain and hole drift on the optical spectra, we decomposed the electron and hole energies of the bands under consideration

$$\epsilon_{s,\mathbf{k}}^{e,\text{“full”}} \approx \sum_{\tau_s} \text{dgn}(\tau_s) \epsilon_{\tau_s\mathbf{k}}^e \quad , \quad \epsilon_{s,\mathbf{k}}^{h,\text{“full”}} \approx \epsilon_{K_s\mathbf{k}}^h + \epsilon_{K'_s\mathbf{k}}^h \quad (4.28)$$

into contributions  $\epsilon_{\tau_s\mathbf{k}}^{e/h} = \epsilon_{s\mathbf{k}-\mathbf{k}_{\tau_s}}^{e/h}$  in the vicinity of the respective valleys. Therein,  $\mathbf{k}_{\tau_s}$  denotes the reciprocal lattice vector of valley  $\tau_s$  within the BZ. Furthermore, the inclusion of  $\text{dgn}(\tau_s) = 1$  for  $\tau_s \in \{K_s, K'_s\}$  and  $\text{dgn}(\tau_s) = 3$  for  $\tau_s \in \{\Sigma_s, \Lambda_s\}$  assured the threefold degeneracy of the side valleys for each spin orientation. In the vicinity of the respective valleys, electron and hole energies were considered to be isotropic. Since the approximation of the relevant bands by the MDF model is restricted to the vicinity of the  $K/K'$  points, we applied an effective-mass approximation  $\epsilon_{\tau_s\mathbf{k}}^e = \frac{\hbar^2(\mathbf{k}-\mathbf{k}_{\tau_s})^2}{2m_{\tau_s}^*}$  for the electronic states in the vicinity of the  $\Sigma/\Lambda$  points.

The large detuning of the  $\Sigma/\Lambda$  valleys makes their contribution to the interband polarizations negligible in the energy range of interest. As a result, all side-valley properties appear under  $\mathbf{k}$ -space integrals always allowing a shift in crystal momenta such that the entire simulations could be performed on single dens  $|\mathbf{k}|$ -grid. The corresponding renormalized electron and hole energies  $\tilde{\Sigma}_{\tau_s\mathbf{k}}^{e/h}$  were computed employing

#### 4. Nonlinear optical properties of TMDC monolayers

the static limit of the Lindhard polarization function

$$\Pi_{\mathbf{q}}(\omega) = \Pi_{\mathbf{q}}^{K/K'}(\omega) + \Pi_{\mathbf{q}}^{\Sigma/\Lambda}(\omega) \quad (4.29)$$

within the screened Coulomb interaction. Therein, side-valley contributions were included, in addition to the  $K/K'$ -valley contributions described previously, via

$$\Pi_{\mathbf{q}}^{\Sigma/\Lambda}(\omega) = 3 \times \sum_{s,\mathbf{p}} \sum_{\tau_s \in \{\Sigma_s, \Lambda_s\}} \frac{f_{\tau_s \mathbf{p}-\mathbf{q}}^e - f_{\tau_s \mathbf{p}}^e}{\hbar\omega + \tilde{\Sigma}_{\tau_s \mathbf{p}-\mathbf{q}}^e - \tilde{\Sigma}_{\tau_s \mathbf{p}}^e}. \quad (4.30)$$

Regarding the dynamic EID, side-valley contributions  $\Lambda_{\mathbf{q}}^{\Sigma/\Lambda}(\omega)$  contributed accordingly to  $\Lambda_{\mathbf{q}}(\omega)$ . The common chemical potentials  $\mu^{e/h}$  to setup the Fermi-Dirac distributions  $f_{\tau_s \mathbf{k}}^{e/h}$  of the distinct valleys were determined by the numerical solution of

$$0 = n^e - \frac{1}{\mathcal{A}} \sum_{s,\mathbf{k}} \sum_{\tau_s} \text{dgn}(\tau_s) f_{\tau_s \mathbf{k}}^e(\mu^e, T), \quad (4.31)$$

$$0 = n^h - \frac{1}{\mathcal{A}} \sum_{s,\mathbf{k}} \sum_{\tau_s \in \{K_s, K'_s\}} f_{\tau_s \mathbf{k}}^h(\mu^h, T), \quad (4.32)$$

for given electron and hole densities  $n^{e/h}$  and temperature  $T$ . Overall charge-carrier neutrality was assured by the condition  $n^e = n^h$ .

In order to rule out an excitation-dependent roll-over from a direct to an indirect band gap that has been reported in recent theoretical works [95, 96] for closely related material systems, eqs. (4.29) - (4.32) in combination with  $\tilde{\Sigma}_{\tau_s \mathbf{k}}^{e/h}$  needed to be determined self-consistently. After initializing the required quantities based on the approximated bands  $\epsilon_{\tau_s \mathbf{k}}^{e/h}$ , the entirety of

- renormalized electron and hole energies  $\tilde{\Sigma}_{\tau_s \mathbf{k}}^{e/h}$ ,
- Fermi-Dirac distributions  $f_{\tau_s \mathbf{k}}^{e/h}$ ,
- Lindhard polarization function  $\Pi_{\mathbf{q}}$  and screened Coulomb interaction  $W_{\mathbf{q}}$ ,
- s-type angular-averaged Coulomb matrix elements  $W_{\tau_s, \mathbf{k} \mathbf{k}'}^{\lambda \mu \mu' \lambda'}$ ,

were calculated iteratively in the stated order for given input carrier densities  $n^{e/h}$ . Since all properties are either directly or indirectly connected, this leads to an iteration circuit. In practice, convergence was achieved within a few ten iterations of the circuit.

As reported in ref. [IV], we found no evidence of an excitation-induced direct-to-indirect transition for monolayer MoTe<sub>2</sub>. The property with dominating influence on the electron drain to the side valleys is offset between the  $\Sigma/\Lambda$ - and  $K/K'$ -valley minima in the conduction bands. Due to the energetically favorable conduction-band occupation in the  $K/K'$  valleys, renormalization effects even led to an increase of the side-valley offsets with an increasing density of excited carriers. In the high-excitation regime up to 25 % of the excitation-induced electrons were predicted to drain towards

the  $\Sigma/\Lambda$  valleys. Besides the electron drain, equilibration introduces a pronounced drift of the hole density between the  $K$  and  $K'$  valleys. As a consequence of the large valence-band splitting of about 230 meV, practically the entirety of holes was found to occupy the energetically favorable split-up valence bands in equilibrium.

After initializing the excited equilibrium state, the optical spectra were computed based on eqs. (4.17)-(4.21). The results are plotted in solid lines in fig. 4.7. Within the simulations, we increased the carrier densities in the high-excitation regime from  $2.0 \times 10^{13} \text{ cm}^{-2}$  (orange) to  $1.2 \times 10^{14} \text{ cm}^{-2}$  (black). For comparison, the dotted lines show the optical spectra before equilibration within the entire BZ, where all carriers were assumed to be located in the  $K$  and  $K'$  valleys. Clearly noticeable, equilibration led to a net increase of the optical gain. Whereas the electron drain to the side valleys alone would cause a slight efficiency drop, the pronounced hole drift between the  $K$  and  $K'$  valleys was found to drastically increase the amount of optically recombining holes leading to an increased peak gain of 0.83 % for the highest density considered.

Normalizing the latter with respect to the thickness of the monolayer yields a peak gain above  $10^5 \text{ cm}^{-1}$ . It is interesting to compare this value to a gain maximum of about  $5000 \text{ cm}^{-1}$  that can be realized in conventional III-V semiconductors [92]. While this comparison is hypothetical, not least because increasing the number of layers would introduce a direct-to-indirect transition, it shows the potential for achieving pronounced plasma-induced optical gain in a single MoTe<sub>2</sub> layer.

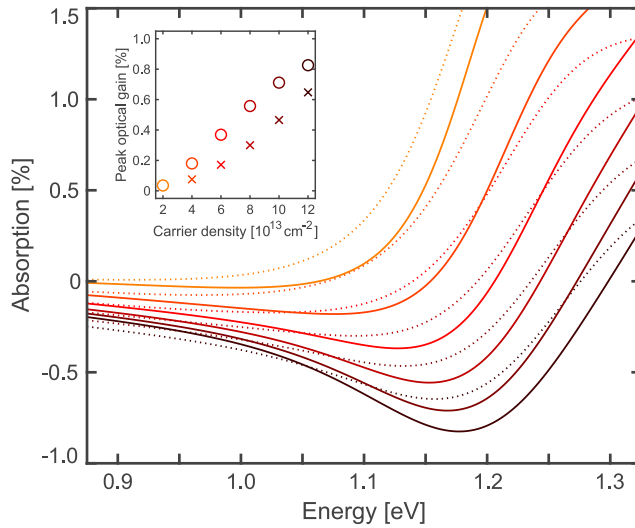


Figure 4.7.: Optical absorption spectra before (dotted) and after (solid lines) equilibration of the carriers between the different valleys. Before equilibration, all carriers are located in the  $K$  and  $K'$  valleys. The inset shows the peak optical gain for the corresponding charge-carrier densities after (before) equilibration in circles (crosses). (According to ref. [IV].)



## Conclusion and outlook

In this thesis, theoretical investigations on the  $K/K'$ -point linear and nonlinear optical properties of various semiconducting TMDC systems are summarized. To obtain the results of these investigations, the combined gap and Dirac-Bloch equation scheme was employed that is based on the MDF-model Hamiltonian [14]. Therein, the GEs emerged as a self-consistent method to compute the ground-state renormalization prior to excitation and the renormalization of the single-particle energies in the presence of excited charge carriers. The knowledge of both is of fundamental importance for the calculation of the optical properties that followed from the solution of the DWE and DBEs. The studied material systems were a stack of single van der Waals bonded MoS<sub>2</sub> layers, suspended and substrate-supported monolayers of MoS<sub>2</sub>, WS<sub>2</sub>, MoSe<sub>2</sub>, WSe<sub>2</sub> and MoTe<sub>2</sub>, as well as WSe<sub>2</sub>/MoS<sub>2</sub> and WSe<sub>2</sub>/MoSe<sub>2</sub> hetero-bilayers.

Chapter 3 contains the results of refs. [I, III] that focus on the ground-state and excitonic properties of layered TMDC systems. In the first section, general aspects of solving the GEs and DWE were discussed. The ground-state renormalization predominantly introduced a rigid shift to the single-particle bands towards larger band gaps. The subsequent solution of the DWE revealed a blue shift of the s-type excitonic resonances with increasing Coulomb couplings as well as a fine structure that contains a pronounced splitting of the  $2p$  states. The former has been experimentally observed for the  $1s$  and  $2s$  resonances in WS<sub>2</sub> monolayers [24]. To perform quantitative calculations of the ground-state and excitonic properties of layered TMDCs, the theoretical framework was complemented by a highly efficient anisotropic dielectric model for the Coulomb potential in layered materials. Therein, an effective thickness was introduced as a single variational parameter to account for the finite out-of-plane extension of the individual layers. Adjusting this parameter to match the experimentally determined  $A_{1s}$ -exciton resonance for a given material and dielectric environment, the results of secs. 3.2 and 3.3 showed that our model is capable of predicting the  $K/K'$ -point band-gap energies and excitonic spectra of the stated TMDC systems for arbitrary layer numbers and environments. In particular, our results led to a reinterpretation of the bulk exciton series of MoS<sub>2</sub> as a combined 2D intra- and interlayer exciton series. This chapter closes with a summary of our theoretical study

## 5. Conclusion and outlook

of intra- and interlayer excitons in AA'-stacked WSe<sub>2</sub>/MoS<sub>2</sub> and WSe<sub>2</sub>/MoSe<sub>2</sub> heterobilayers. There, DFT calculations complemented the recently established GE and DBE scheme. Analyzing the ion contributions of the metal atoms to the bands of interest yielded a clear assignment between bands and layers in the vicinity of the  $K/K'$  points. Thus, our theoretical framework could also be applied to the investigation of TMDC heterostructures. While theory-experiment comparisons were avoided for artificially strained bilayer WSe<sub>2</sub>/MoS<sub>2</sub>, the spectra of rather unstrained bilayer WSe<sub>2</sub>/MoSe<sub>2</sub> revealed resonances for the tightly bound intra- and interlayer excitons that are in good agreement with experimental findings [87–89]. The small oscillator strength yielded long-lived interlayer excitons with radiative lifetimes two orders of magnitude larger than those of the intralayer excitons.

Chapter 4 summarizes the results of refs. [II, IV] where monolayer TMDCs were studied in the nonlinear excitation regime. The first part focuses on the observation of optical gain in the spectra of MoS<sub>2</sub> monolayers for thermal charge carriers, accompanied by a huge excitation-induced band-gap renormalization. Employing screened HF approximation, a band-gap reduction in the range of 600-800 meV was found for SiO<sub>2</sub>-supported and suspended MoS<sub>2</sub>. For carrier densities in the range of 10<sup>11</sup>-10<sup>13</sup> cm<sup>-2</sup>, the computed optical spectra, excitation-induced band-gap renormalization and exciton binding energies are in good agreement with earlier theoretical investigations on MoS<sub>2</sub> [97]. Above a Mott-density of about 10<sup>13</sup> cm<sup>-2</sup>, broadband plasma gain below the low-density A-exciton resonance was predicted which had been observed in few-layer WS<sub>2</sub> [30], but not yet in monolayer MoS<sub>2</sub>. The second part summarizes the results on the dynamics of the band-gap renormalization and gain build-up in SiO<sub>2</sub>-supported monolayer MoTe<sub>2</sub> after strong nonresonant optical excitation. To obtain these results, the DBEs were extended by including quantum-Boltzmann-like scattering rates to describe incoherent carrier- and phonon-scattering processes of the microscopic polarizations and charge-carrier occupations. Our numerical experiment revealed an enormous excitation-induced band-gap reduction on the timescale of the optical pulse which has recently been observed in monolayer MoS<sub>2</sub> [31, 32]. As a result of efficient phonon-coupling, thermalization led to gain build-up on a few-picosecond timescale. Based on the dynamical treatment of the EID the gain maximum occurred slightly below the low-density A-exciton resonance, yielding an amplification of close to 0.5 % of the incident light. Considering true equilibrium situations this output was predicted to be even larger, marking monolayer MoTe<sub>2</sub> as a prime candidate among semiconducting TMDCs to achieve plasma-induced optical gain.

In conclusion, the presented GE and DBE approach enables quantitative and predictive microscopic modeling of the  $K/K'$ -point optical properties of a variety of semiconducting TMDC systems in the linear and nonlinear excitation regimes. By employing *ab-initio* based form factors, the only free parameter in this theory – namely the effective-thickness parameter – finally gets eliminated. However, in order to quantitatively describe phenomena like the intervalley scattering of a generated electron-hole plasma, anisotropic modeling of the full-BZ dynamics beyond the restriction of the MDF model is required.

## List of material parameters

For the results presented within the scope of this thesis, the following *ab-initio* based material parameters served as input for the employed MDF model. They are listed for each publication contributing to the results of this thesis.

### Material parameters contributing to publications [I, II]

At the time we started our investigations on the linear and nonlinear optical properties of the diverse TMDC mono- and multilayer structures, no DFT computations on TMDCs were performed in our research group. Thus, the entirety of required material parameters for the TMDC materials of interest were obtained from external DFT investigations.

Material	Spin	$\Delta/\text{eV}$	$E_F/\text{eV}$	$\hbar v_F/(\text{eV}\text{\AA})$	$D/\text{\AA}$	$\epsilon_{\parallel}^B$	$\epsilon_{\perp}^B$	$\epsilon_{\parallel}$	$d/\text{\AA}$
MoS <sub>2</sub>	↑	1.585	0.793	3.512	6.2	8.29	3.92	4.54	4.47
	↓	1.735	0.718						
WS <sub>2</sub>	↑	1.575	0.788	4.380	6.2	7.95	5.14	4.83	2.78
	↓	2.005	0.573						
MoSe <sub>2</sub>	↑	1.380	0.690	3.114	6.5	9.05	6.07	5.01	4.96
	↓	1.560	0.600						
WSe <sub>2</sub>	↑	1.370	0.685	3.939	6.5	7.25	5.16	3.36	5.17
	↓	1.830	0.455						

Table A.1.: Material parameters for MoS<sub>2</sub>, WS<sub>2</sub>, MoSe<sub>2</sub> and WSe<sub>2</sub> based on the DFT calculations of refs. [14, 98]. (Adapted from ref. [I].)

The material parameters summarized in tab. A.1 are based on the investigations of refs. [14, 98]. In repetition of the main text,  $\Delta$  and  $E_F$  denote the spin-dependent  $K/K'$ -point transition energies and Fermi levels. Furthermore,  $v_F$ ,  $D$ ,  $\epsilon_{\parallel}^B$  and  $\epsilon_{\perp}^B$  are the Fermi-velocity, out-of-plane lattice constant, in- and out-of-plane bulk dielectric constants, and  $\epsilon_{\parallel}$  only contains the nonresonant 2D background screening contribu-

### A. List of material parameters

tions. The only free parameter in our theory was the effective-thickness parameter  $d$  entering the Ohno-potential form factor.

The listed material parameters entered the numerical simulations contributing to the results of refs. [I, II]. They stated for both bands, spin-up and spin-down, at a given valley, i.e. the  $K$  valley. The  $K'$ -valley properties are then obtained by interchanging the spin components. The nonresonant in-plane dielectric constants were obtained from the bulk values with the aid of relation (2.20).

### Material parameters contributing to publication [III]

The DFT simulations, providing the band-structure information for our investigations published in refs. [III, IV], were performed in our research group by U. Huttner. For details on the DFT simulations, we refer to the respective publications.

The resulting material parameters that have been employed for the calculation of the excitonic properties of the  $\text{WSe}_2/\text{MoS}_2$  and  $\text{WSe}_2/\text{MoSe}_2$  hetero-bilayers are summarized in tab. A.2. In addition to the properties introduced previously,  $\epsilon_K^c$  ( $\epsilon_K^v$ ) denotes the  $K$ -valley energies of the spin-split conduction (valence) bands. Based on  $\epsilon_K^c$  and  $\epsilon_K^v$ , the  $K$ -valley transition energies and Fermi levels were computed by  $\Delta = \epsilon_K^c - \epsilon_K^v$  and  $E_F = (\epsilon_K^c + \epsilon_K^v)/2$ , respectively.

$n$	$m$	Spin	$\epsilon_K^c/\text{eV}$	$\epsilon_K^v/\text{eV}$	$d_{cv,K}^{nm}/(\text{e}\text{\AA})$	$\Delta/\text{eV}$	$E_F/\text{eV}$	$\hbar v_F/(\text{eV}\text{\AA})$
MoS <sub>2</sub>	MoS <sub>2</sub>	↑	0.406	-1.050	3.54	1.456	-0.322	3.645
		↓	0.409	-1.200	3.17	1.609	-0.396	3.607
WSe <sub>2</sub>	WSe <sub>2</sub>	↑	1.584	-0.429	2.57	2.013	0.578	3.658
		↓	1.688	0.0	3.47	1.688	0.844	4.142
MoS <sub>2</sub>	WSe <sub>2</sub>	↑	0.406	-0.429	0.42	0.835		
		↓	0.409	0.0	0.46	0.409		
WSe <sub>2</sub>	MoS <sub>2</sub>	↑	1.584	-1.050	0.14	2.634		
		↓	1.688	-1.200	0.08	2.888		
MoSe <sub>2</sub>	MoSe <sub>2</sub>	↑	1.097	-0.310	3.10	1.407	0.394	3.084
		↓	1.117	-0.516	2.80	1.633	0.301	3.233
WSe <sub>2</sub>	WSe <sub>2</sub>	↑	1.344	-0.480	2.85	1.824	0.432	3.676
		↓	1.393	0.0	4.11	1.393	0.697	4.048
MoSe <sub>2</sub>	WSe <sub>2</sub>	↑	1.097	-0.480	0.94	1.577		
		↓	1.117	0.0	0.48	1.117		
WSe <sub>2</sub>	MoSe <sub>2</sub>	↑	1.344	-0.310	1.06	1.654		
		↓	1.393	-0.516	0.33	1.909		

Table A.2.: DFT-based material parameters for the  $\text{WSe}_2/\text{MoS}_2$  (upper half) and  $\text{WSe}_2/\text{MoSe}_2$  (lower half) hetero-bilayer structures.

From the  $K$ -point intraband dipoles,  $d_{cv,K}^{mn}$ , the Fermi-velocities were obtained via  $\hbar v_{F,n} = \Delta_{nn} d_{cv,K}^{nn}/(e\sqrt{2})$ . Note that at this point we still employed the dielectric constants and effective-thickness parameters summarized in tab. A.1.

For the calculation of the excitonic properties and corresponding optical spectra the solution of Poisson's equation for the hetero-bilayer environment was required. It can be written in the compact form

$$\begin{aligned}\phi_0^{2D}(\mathbf{q}, z_1, z_1) &= \frac{4\pi}{q} \frac{[\alpha_1^+(q) + \alpha_1^-(q)] \times [\alpha_2^+(q)\beta_{21}^+(q) + \alpha_2^-(q)\beta_{21}^-(q)]}{\mathcal{N}(2q)}, \\ \phi_0^{2D}(\mathbf{q}, z_1, z_2) &= \frac{4\pi}{q} \frac{[\alpha_1^+(q) + \alpha_1^-(q)] \times [\alpha_2^+(q) + \alpha_2^-(q)]}{\mathcal{N}(2q)} = \phi_0^{2D}(\mathbf{q}, z_2, z_1), \\ \phi_0^{2D}(\mathbf{q}, z_2, z_2) &= \frac{4\pi}{q} \frac{[\alpha_1^+(q)\beta_{12}^+(q) + \alpha_1^-(q)\beta_{12}^-(q)] \times [\alpha_2^+(q) + \alpha_2^-(q)]}{\mathcal{N}(2q)},\end{aligned}$$

for the numerically relevant cases,  $z_1 = D_1/2$  and  $z_2 = D_1 + D_2/2$ , where

$$\begin{aligned}\alpha_i^\pm(q) &= (\kappa_i \pm \epsilon_i) e^{\pm \frac{q}{2} \bar{\kappa}_i D_i}, \\ \beta_{ij}^\pm(q) &= \frac{\kappa_i + \kappa_j}{2\kappa_j} e^{\pm \frac{q}{2} (\bar{\kappa}_i D_i + \bar{\kappa}_j D_j)} - \frac{\kappa_i - \kappa_j}{2\kappa_j} e^{\pm \frac{q}{2} (\bar{\kappa}_i D_i - \bar{\kappa}_j D_j)}, \\ \mathcal{N}(q) &= (\kappa_2 + \kappa_1) [\alpha_1^+(q)\alpha_2^+(q) - \alpha_1^-(q)\alpha_2^-(q)] \\ &\quad - (\kappa_2 - \kappa_1) [\alpha_1^+(q)\alpha_2^-(q) - \alpha_1^-(q)\alpha_2^+(q)],\end{aligned}$$

and  $\kappa_i = \sqrt{\epsilon_{\parallel,i}^c \epsilon_{\perp,i}^c}$ ,  $\bar{\kappa}_i = \sqrt{\frac{\epsilon_{\parallel,i}^c}{\epsilon_{\perp,i}^c}}$  are introduced to shorten the notation. Although we investigated freely suspended hetero-bilayers in ref. [III], the stated solution applies for any surrounding dielectrics parameterized by  $\epsilon_1$  and  $\epsilon_2$ .

### Material parameters contributing to publication [IV]

The MoTe<sub>2</sub> material parameters, entering the modeling of the band-structure and optical properties in the vicinity of the  $K/K'$  and  $\Sigma/\Lambda$  valleys, are presented in tab. A.3. Here, not only the band structure and dipole matrix elements resulted from internal DFT calculations but also the bulk dielectric constants.

Spin	$\epsilon_K^c/\text{eV}$	$\epsilon_K^v/\text{eV}$	$\epsilon_\Sigma^c/\text{eV}$	$m_K^*/m_0$	$m_\Sigma^*/m_0$	$d_K^\pm/(\text{e}\text{\AA})$	$\epsilon_\parallel^B$	$\epsilon_\perp^B$	$D/\text{\AA}$
$\uparrow$	1.017	0.0	1.114	0.607	0.407	3.51	20.30	10.90	6.99
$\downarrow$	1.052	-0.214	1.099	0.728	0.428	2.88			

Table A.3.: MoTe<sub>2</sub> material parameters, i.e. the conduction-band (valence-band) valley minima (maxima)  $\epsilon_K^c$  and  $\epsilon_\Sigma^c$  ( $\epsilon_K^v$ ), effective masses  $m_K^*$  and  $m_\Sigma^*$ , dipole matrix elements  $d_K^\pm$ , as well as the bulk dielectric constants  $\epsilon_\parallel^B$ ,  $\epsilon_\perp^B$  and out-of-plane lattice constant  $D$ . For the  $K'$  and  $\Lambda$  valleys, the spin components are interchanged. (According to ref. [IV].)

Please note, the Fermi-velocities (see tab. A.4) resulted from approximating the band structure in the vicinity of the  $K$  point by the relativistic dispersion (2.4) and

### A. List of material parameters

the  $K$ -point dipole matrix elements  $d_K^\pm$  were computed accordingly. The computed dipole matrix elements, stated in tab. A.3, were found to be in very good agreement with the DFT values of 3.71 eÅ and 3.03 eÅ, respectively.

Spin	$\Delta/\text{eV}$	$E_F/\text{eV}$	$\hbar v_F/(\text{eV}\text{\AA})$	$\epsilon_{\parallel}$
$\uparrow$	1.017	0.509	2.526	15.32
$\downarrow$	1.266	0.419	2.574	

Table A.4.: Resulting MDF-model parameters and nonresonant 2D contribution to the in-plane dielectric tensor for MoTe<sub>2</sub>. (According to ref. [IV].)

All form-factor calculations were performed in our research group by J. Neuhaus. It was shown in ref. [55] that the different  $K$ -valley form factors are almost identical for wave vectors  $|\mathbf{k} - \mathbf{k}'| \lesssim 0.3 \text{ \AA}^{-1}$ . Note that exciton wave functions,  $\psi_\nu(\bar{\mathbf{k}})$ , microscopic polarizations,  $P_{\mathbf{k}}$ , and electron (hole) distributions,  $f_{\mathbf{k}}^{e/h}$ , have almost completely decayed beyond this point in  $\mathbf{k}$ -space. On the contrary, the Coulomb-hole contribution, which is majorly responsible for the ground-state renormalization, is a Coulomb-interaction integral that is not restricted by any distribution function. Therefore, form-factor details for larger wave vectors matter. There, the form factor  $F_K^{\text{vvvv}}(\mathbf{k} - \mathbf{k}')$  enters the dominating intraband contributions. From this standpoint, it was reasonable to include finite-thickness effects by employing the single form factor  $F_K(\mathbf{k} - \mathbf{k}') = F_K^{\text{vvvv}}(\mathbf{k} - \mathbf{k}')$  for all  $K$ -point Coulomb matrix elements as long as MDF-model prefactors were still included.

For the the inclusion of side-valley effects as described in sec. 4.2.3, the  $\Sigma$ -point Coulomb matrix elements where the form factor  $F_\Sigma(\mathbf{k} - \mathbf{k}') = F_\Sigma^{\text{cccc}}(\mathbf{k} - \mathbf{k}')$  enters were required. Ultimately, the parameters for the exponential fit of the form factors are provided in tab. A.5.

Form factor	$b_1/\text{\AA}$	$b_2/\text{\AA}^2$
$F_K(\mathbf{k} - \mathbf{k}')$	2.05	3.31
$F_\Sigma(\mathbf{k} - \mathbf{k}')$	2.28	8.24

Table A.5.: Fit parameters for the MoTe<sub>2</sub> form factors.

## Bibliography

- [1] K. S. Novoselov, A. K. Geim, S. V. Morozov, D. Jiang, Y. Zhang, S. V. Dubonos, I. V. Grigorieva, and A. A. Firsov, “Electric Field Effect in Atomically Thin Carbon Films”, *Science* **306**, 666–669 (2004).
- [2] K. I. Bolotin, K. J. Sikes, Z. Jiang, M. Klima, G. Fudenberg, J. Hone, P. Kim, and H. L. Stormer, “Ultrahigh electron mobility in suspended graphene”, *Solid State Commun.* **146**, 351–355 (2008).
- [3] C. Lee, X. Wei, J. W. Kysar, and J. Hone, “Measurement of the Elastic Properties and Intrinsic Strength of Monolayer Graphene”, *Science* **321**, 385–388 (2008).
- [4] A. K. Geim and I. V. Grigorieva, “Van der Waals heterostructures”, *Nature* **499**, 419–425 (2013).
- [5] K. S. Novoselov, A. Mishchenko, A. Carvalho, and A. H. Castro Neto, “2D materials and van der Waals heterostructures”, *Science* **353**, aac9439 (2016).
- [6] A. R. Beal, J. C. Knights, and W. Y. Liang, “Transmission spectra of some transition metal dichalcogenides. II. Group VIA: trigonal prismatic coordination”, *J. Phys. C: Solid State Phys.* **5**, 3540–3551 (1972).
- [7] J. Bordas and E. A. Davis, “Electromodulation Spectroscopy of Excitons: Molybdenum Disulphide”, *Phys. Status Solidi B* **60**, 505–510 (1973).
- [8] E. Fortin and F. Raga, “Excitons in molybdenum disulphide”, *Phys. Rev. B* **11**, 905–912 (1975).
- [9] R. A. Neville and B. L. Evans, “The Band Edge Excitons in 2H-MoS<sub>2</sub>”, *Phys. Status Solidi B* **73**, 597–606 (1976).
- [10] A. Anedda, E. Fortin, and F. Raga, “Optical Spectra in WSe<sub>2</sub>”, *Can. J. Phys.* **57**, 368–374 (1979).
- [11] A. Anedda and E. Fortin, “Exciton Spectra in MoSe<sub>2</sub>”, *J. Phys. Chem. Solids* **41**, 865–869 (1980).

## Bibliography

- [12] K. F. Mak, C. Lee, J. Hone, J. Shan, and T. F. Heinz, “Atomically Thin MoS<sub>2</sub>: A New Direct-Gap Semiconductor”, *Phys. Rev. Lett.* **105**, 136805 (2010).
- [13] A. Splendiani, L. Sun, Y. Zhang, T. Li, J. Kim, C.-Y. Chim, G. Galli, and F. Wang, “Emerging Photoluminescence in Monolayer MoS<sub>2</sub>”, *Nano Lett.* **10**, 1271–1275 (2010).
- [14] D. Xiao, G.-B. Liu, W. Feng, X. Xu, and W. Yao, “Coupled Spin and Valley Physics in Monolayers of MoS<sub>2</sub> and Other Group-VI Dichalcogenides”, *Phys. Rev. Lett.* **108**, 196802 (2012).
- [15] B. Radisavljevic, M. B. Whitwick, and A. Kis, “Integrated Circuits and Logic Operations Based on Single-Layer MoS<sub>2</sub>”, *ACS Nano* **5**, 9934–9938 (2011).
- [16] O. Lopez-Sanchez, E. Alarcon Llado, V. Koman, A. Fontcuberta i Morral, A. Radenovic, and A. Kis, “Light Generation and Harvesting in a van der Waals Heterostructure”, *ACS Nano* **8**, 3042–3048 (2014).
- [17] M.-L. Tsai, S.-H. Su, J.-K. Chang, D.-S. Tsai, C.-H. Chen, C.-I. Wu, L.-J. Li, L.-J. Chen, and J.-H. He, “Monolayer MoS<sub>2</sub> Heterojunction Solar Cells”, *ACS Nano* **8**, 8317–8322 (2014).
- [18] Y. Ye, Z. J. Wong, X. Lu, X. Ni, H. Zhu, X. Chen, Y. Wang, and X. Zhang, “Monolayer excitonic laser”, *Nat. Photon.* **9**, 733–737 (2015).
- [19] S. Wu, S. Buckley, J. R. Schaibley, L. Feng, J. Yan, D. G. Mandrus, F. Hatami, W. Yao, J. Vučković, A. Majumdar, and X. Xu, “Monolayer semiconductor nanocavity lasers with ultralow thresholds”, *Nature* **520**, 69–72 (2015).
- [20] Y. Li, J. Zhang, D. Huang, H. Sun, F. Fan, J. Feng, Z. Wang, and C. Z. Ning, “Room-temperature continuous-wave lasing from monolayer molybdenum ditelluride integrated with a silicon nanobeam cavity”, *Nat. Nanotech.* **12**, 987–992 (2017).
- [21] Z. Ye, T. Cao, K. O’Brien, H. Zhu, X. Yin, Y. Wang, S. G. Louie, and X. Zhang, “Probing excitonic dark states in single-layer tungsten disulphide”, *Nature* **513**, 214–218 (2014).
- [22] A. Chernikov, T. C. Berkelbach, H. M. Hill, A. Rigosi, Y. Li, O. B. Aslan, D. R. Reichman, M. S. Hybertsen, and T. F. Heinz, “Exciton Binding Energy and Nonhydrogenic Rydberg Series in Monolayer WS<sub>2</sub>”, *Phys. Rev. Lett.* **113**, 076802 (2014).
- [23] K. He, N. Kumar, L. Zhao, Z. Wang, K. F. Mak, H. Zhao, and J. Shan, “Tightly Bound Excitons in Monolayer WSe<sub>2</sub>”, *Phys. Rev. Lett.* **113**, 026803 (2014).
- [24] A. Raja, A. Chaves, J. Yu, G. Arefe, H. M. Hill, A. F. Rigosi, T. C. Berkelbach, P. Nagler, C. Schüller, T. Korn, C. Nuckolls, J. Hone, L. E. Brus, T. F. Heinz, D. R. Reichman, and A. Chernikov, “Coulomb engineering of the bandgap and excitons in two-dimensional materials”, *Nat. Commun.* **8**, 15251 (2017).

- [25] A. Arora, M. Drüppel, R. Schmidt, T. Deilmann, R. Schneider, M. R. Molas, P. Marauhn, S. M. de Vasconcellos, M. Potemski, M. Rohlfing, and R. Bratschitsch, “Interlayer excitons in a bulk van der Waals semiconductor”, *Nat. Commun.* **8**, 639 (2017).
- [26] F. Ceballos, M. Z. Bellus, H.-Y. Chiu, and H. Zhao, “Ultrafast Charge Separation and Indirect Exciton Formation in a MoS<sub>2</sub> MoSe<sub>2</sub> van der Waals Heterostructure”, *ACS Nano* **8**, 12717–12724 (2014).
- [27] X. Hong, J. Kim, S.-F. Shi, Y. Zhang, C. Jin, Y. Sun, S. Tongay, J. Wu, Y. Zhang, and F. Wang, “Ultrafast charge transfer in atomically thin MoS<sub>2</sub>/WS<sub>2</sub> heterostructures”, *Nat. Nanotechnol.* **9**, 682–686 (2014).
- [28] R. Cheng, D. Li, H. Zhou, C. Wang, A. Yin, S. Jiang, Y. Liu, Y. Chen, Y. Huang, and X. Duan, “Electroluminescence and Photocurrent Generation from Atomically Sharp WSe<sub>2</sub>/MoS<sub>2</sub> Heterojunction p–n Diodes”, *Nano Lett.* **14**, 5590–5597 (2014).
- [29] M. M. Furchi, A. Pospischil, F. Libisch, J. Burgdörfer, and T. Mueller, “Photovoltaic Effect in an Electrically Tunable van der Waals Heterojunction”, *Nano Lett.* **14**, 4785–4791 (2014).
- [30] A. Chernikov, C. Ruppert, H. M. Hill, A. F. Rigosi, and T. F. Heinz, “Population inversion and giant bandgap renormalization in atomically thin WS<sub>2</sub> layers”, *Nat. Photon.* **9**, 466–470 (2015).
- [31] S. Ulstrup, A. G. Čabo, J. A. Miwa, J. M. Riley, S. S. Grønberg, J. C. Johannsen, C. Cacho, O. Alexander, R. T. Chapman, E. Springate, M. Bianchi, M. Dendzik, J. V. Lauritsen, P. D. C. King, and P. Hofmann, “Ultrafast Band Structure Control of a Two-Dimensional Heterostructure”, *ACS Nano* **10**, 6315–6322 (2016).
- [32] F. Liu, M. E. Ziffer, K. R. Hansen, J. Wang, and X. Zhu, “Direct Determination of Band-Gap Renormalization in the Photoexcited Monolayer MoS<sub>2</sub>”, *Phys. Rev. Lett.* **122**, 246803 (2019).
- [33] T. Stroucken, J. H. Grönqvist, and S. W. Koch, “Optical response and ground state of graphene”, *Phys. Rev. B* **84**, 205445 (2011).
- [34] T. Stroucken, J. H. Grönqvist, and S. W. Koch, “Screening and gap generation in bilayer graphene”, *Phys. Rev. B* **87**, 245428 (2013).
- [35] T. Stroucken and S. W. Koch, “Optically bright *p*-excitons indicating strong Coulomb coupling in transition-metal dichalcogenides”, *J. Phys.: Condens. Matter* **27**, 345003 (2015).
- [36] T. Stroucken and S. W. Koch, “Microscopic Theory for the Groundstate and Linear Optical Response of Novel Two-Dimensional Materials with Hexagonal Symmetry”, in *Optical Properties of Graphene*, edited by R. Binder (World Scientific Publishing, Singapore, 2017), pp. 43–84.
- [37] P. R. Wallace, “The Band Theory of Graphite”, *Phys. Rev.* **71**, 622–634 (1947).

- [38] A. K. Geim and K. S. Novoselov, “The rise of graphene”, *Nat. Mater.* **6**, 183–191 (2007).
- [39] A. Kuc, N. Zibouche, and T. Heine, “Influence of quantum confinement on the electronic structure of the transition metal sulfide  $TS_2$ ”, *Phys. Rev. B* **83**, 245213 (2011).
- [40] Y. Ding, Y. Wang, J. Ni, L. Shi, S. Shi, and W. Tang, “First principles study of structural, vibrational and electronic properties of graphene-like  $MX_2$  (M=Mo, Nb, W, Ta; X=S, Se, Te) monolayers”, *Physica B: Phys. Condens. Matter* **406**, 2254–2260 (2011).
- [41] S. W. Han, H. Kwon, S. K. Kim, S. Ryu, W. S. Yun, D. H. Kim, J. H. Hwang, J.-S. Kang, J. Baik, H. J. Shin, and S. C. Hong, “Band-gap transition induced by interlayer van der Waals interaction in  $MoS_2$ ”, *Phys. Rev. B* **84**, 045409 (2011).
- [42] H. Shi, H. Pan, Y.-W. Zhang, and B. I. Yakobson, “Quasiparticle band structures and optical properties of strained monolayer  $MoS_2$  and  $WS_2$ ”, *Phys. Rev. B* **87**, 155304 (2013).
- [43] G.-B. Liu, W.-Y. Shan, Y. Yao, W. Yao, and D. Xiao, “Three-band tight-binding model for monolayers of group-VIB transition metal dichalcogenides”, *Phys. Rev. B* **88**, 085433 (2013).
- [44] G.-B. Liu, D. Xiao, Y. Yao, X. Xu, and W. Yao, “Electronic structures and theoretical modelling of two-dimensional group-VIB transition metal dichalcogenides”, *Chem. Soc. Rev.* **44**, 2643–2663 (2015).
- [45] T. Sohler, M. Calandra, and F. Mauri, “Two-dimensional Fröhlich interaction in transition-metal dichalcogenide monolayers: Theoretical modeling and first-principles calculations”, *Phys. Rev. B* **94**, 085415 (2016).
- [46] C. E. Stevens, T. Stroucken, A. V. Stier, J. Paul, H. Zhang, P. Dey, S. A. Crooker, S. W. Koch, and D. Karaickaj, “Superradiant coupling effects in transition-metal dichalcogenides”, *Optica* **5**, 749–755 (2018).
- [47] E. Anderson, Z. Bai, C. Bischof, S. Blackford, J. Demmel, J. Dongarra, J. Du Croz, A. Greenbaum, S. Hammarling, A. McKenney, and D. Sorensen, *LAPACK users’ guide*, 3rd ed. (Society for Industrial and Applied Mathematics, Philadelphia, PA, 1999).
- [48] P. Cudazzo, I. V. Tokatly, and A. Rubio, “Dielectric screening in two-dimensional insulators: Implications for excitonic and impurity states in graphene”, *Phys. Rev. B* **84**, 085406 (2011).
- [49] S. Latini, T. Olsen, and K. S. Thygesen, “Excitons in van der Waals heterostructures: The important role of dielectric screening”, *Phys. Rev. B* **92**, 245123 (2015).
- [50] K. Andersen, S. Latini, and K. S. Thygesen, “Dielectric Genome of van der Waals Heterostructures”, *Nano Lett.* **15**, 4616–4621 (2015).

- [51] D. Y. Qiu, F. H. da Jornada, and S. G. Louie, “Screening and many-body effects in two-dimensional crystals: Monolayer MoS<sub>2</sub>”, *Phys. Rev. B* **93**, 235435 (2016).
- [52] L. S. R. Cavalcante, A. Chaves, B. Van Duppen, F. M. Peeters, and D. R. Reichman, “Electrostatics of electron-hole interactions in van der Waals heterostructures”, *Phys. Rev. B* **97**, 125427 (2018).
- [53] A. S. Rodin and A. H. Castro Neto, “Excitonic collapse in semiconducting transition-metal dichalcogenides”, *Phys. Rev. B* **88**, 195437 (2013).
- [54] S. C. Liebscher, “Quantenmechanische Beschreibung quasi-zweidimensionaler Halbleitersysteme”, Written part of first state exam (Fachbereich Physik, Philipps-Universität Marburg, 2018).
- [55] J. Neuhaus, “Mikroskopische Modellierung der Coulomb Wechselwirkung in TMDCs”, Master thesis (Fachbereich Physik, Philipps-Universität Marburg, 2019).
- [56] L. D. Landau and E. M. Lifshitz, *Electrodynamics of Continuous Media*, 1st ed., Vol. 8, Course of Theoretical Physics (Pergamon Press, 1960).
- [57] M. Lindberg and S. W. Koch, “Effective Bloch equations for semiconductors”, *Phys. Rev. B* **38**, 3342–3350 (1988).
- [58] H. Haug and S. W. Koch, *Quantum Theory of the Optical and Electronic Properties of Semiconductors*, 5th ed. (World Scientific Publishing, Singapore, 2009).
- [59] M. Kira and S. W. Koch, *Semiconductor Quantum Optics* (Cambridge University Press, 2011).
- [60] R. J. Elliott, “Intensity of Optical Absorption by Excitons”, *Phys. Rev.* **108**, 1384–1389 (1957).
- [61] T. Stroucken, A. Knorr, P. Thomas, and S. W. Koch, “Coherent dynamics of radiatively coupled quantum-well excitons”, *Phys. Rev. B* **53**, 2026–2033 (1996).
- [62] L. Meckbach, “Exzitronische Eigenschaften von TMDCs”, Master thesis (Fachbereich Physik, Philipps-Universität Marburg, 2017).
- [63] M. Kira and S. W. Koch, “Many-body correlations and excitonic effects in semiconductor spectroscopy”, *Prog. Quantum Electron.* **30**, 155–296 (2006).
- [64] M. Kira and S. W. Koch, “Quantum-optical spectroscopy of semiconductors”, *Phys. Rev. A* **73**, 013813 (2006).
- [65] M. Kira and S. W. Koch, “Cluster-expansion representation in quantum optics”, *Phys. Rev. A* **78**, 022102 (2008).
- [66] N. S. Rytova, “The screened potential of a point charge in a thin film”, *Moscow University Physics Bulletin* **22**, 18–21 (1967).
- [67] L. V. Keldysh, “Coulomb interaction in thin semiconductor and semimetal films”, *JETP Lett.* **29**, 658–661 (1979).
- [68] O. Pulci, P. Gori, M. Marsili, V. Garbuio, R. D. Sole, and F. Bechstedt, “Strong excitons in novel two-dimensional crystals: Silicane and germanane”, *Europhys. Lett.* **98**, 37004 (2012).

- [69] T. C. Berkelbach, M. S. Hybertsen, and D. R. Reichman, “Theory of neutral and charged excitons in monolayer transition metal dichalcogenides”, *Phys. Rev. B* **88**, 045318 (2013).
- [70] F. Wu, F. Qu, and A. H. MacDonald, “Exciton band structure of monolayer MoS<sub>2</sub>”, *Phys. Rev. B* **91**, 075310 (2015).
- [71] M. Van der Donck, M. Zarenia, and F. M. Peeters, “Excitons and trions in monolayer transition metal dichalcogenides: A comparative study between the multiband model and the quadratic single-band model”, *Phys. Rev. B* **96**, 035131 (2017).
- [72] W. H. Press, S. Teukolsky, W. T. Vetterling, and B. P. Flannery, *Numerical recipes in fortran (2nd ed.): the art of scientific computing*, 2nd ed. (Cambridge University Press, USA, 1992).
- [73] W. Nolting, *Quantenmechanik - Methoden und Anwendungen*, 8th ed., Vol. 5/2, *Grundkurs Theoretische Physik* (Springer Spektrum, 2015).
- [74] G. Kioseoglou, A. T. Hanbicki, M. Currie, A. L. Friedman, D. Gunlycke, and B. T. Jonker, “Valley polarization and intervalley scattering in monolayer MoS<sub>2</sub>”, *Appl. Phys. Lett.* **101**, 221907 (2012).
- [75] K. F. Mak, K. He, C. Lee, G. H. Lee, J. Hone, T. F. Heinz, and J. Shan, “Tightly bound trions in monolayer MoS<sub>2</sub>”, *Nat. Mater.* **12**, 207–211 (2013).
- [76] A. A. Mitioglu, K. Galkowski, A. Surrente, L. Klopotoski, D. Dumcenco, A. Kis, D. K. Maude, and P. Plochocka, “Magnetoexcitons in large area CVD-grown monolayer MoS<sub>2</sub> and MoSe<sub>2</sub> on sapphire”, *Phys. Rev. B* **93**, 165412 (2016).
- [77] F. Cadiz, C. Robert, G. Wang, W. Kong, X. Fan, M. Blei, D. Lagarde, M. Gay, M. Manca, T. Taniguchi, K. Watanabe, T. Amand, X. Marie, P. Renucci, S. Tongay, and B. Urbaszek, “Ultra-low power threshold for laser induced changes in optical properties of 2D molybdenum dichalcogenides”, *2D Mater.* **3**, 045008 (2016).
- [78] A. R. Klots, A. K. M. Newaz, B. Wang, D. Prasai, H. Krzyzanowska, J. Lin, D. Caudel, N. J. Ghimire, J. Yan, B. L. Ivanov, K. A. Velizhanin, A. Burger, D. G. Mandrus, N. H. Tolik, S. T. Pantelides, and K. I. Bolotin, “Probing excitonic states in suspended two-dimensional semiconductors by photocurrent spectroscopy”, *Sci. Rep.* **4**, 6608 (2014).
- [79] C. Robert, M. A. Semina, F. Cadiz, M. Manca, E. Courtade, T. Taniguchi, K. Watanabe, H. Cai, S. Tongay, B. Lassagne, P. Renucci, T. Amand, X. Marie, M. M. Glazov, and B. Urbaszek, “Optical spectroscopy of excited exciton states in MoS<sub>2</sub> monolayers in van der Waals heterostructures”, *Phys. Rev. Mat.* **2**, 011001 (2018).
- [80] J. S. Ross, S. Wu, H. Yu, N. J. Ghimire, A. M. Jones, G. Aivazian, J. Yan, D. G. Mandrus, D. Xiao, W. Yao, and X. Xu, “Electrical control of neutral and charged excitons in a monolayer semiconductor”, *Nat. Commun.* **4**, 1474 (2013).

- [81] G. Wang, X. Marie, I. Gerber, T. Amand, D. Lagarde, L. Bouet, M. Vidal, A. Balocchi, and B. Urbaszek, “Giant Enhancement of the Optical Second-Harmonic Emission of  $\text{We}_2$  Monolayers by Laser Excitation at Exciton Resonances”, *Phys. Rev. Lett.* **114**, 097403 (2015).
- [82] L. Dagum and R. Menon, “OpenMP: an industry standard API for shared-memory programming”, *Computational Science & Engineering, IEEE* **5**, 46–55 (1998).
- [83] W. S. Yun, S. W. Han, S. C. Hong, I. G. Kim, and J. D. Lee, “Thickness and strain effects on electronic structures of transition metal dichalcogenides:  $2\text{H-MX}_2$  semiconductors ( $M=\text{Mo, W}$ ;  $X=\text{S, Se, Te}$ )”, *Phys. Rev. B* **85**, 033305 (2012).
- [84] H.-P. Komsa and A. V. Krasheninnikov, “Effects of confinement and environment on the electronic structure and exciton binding energy of  $\text{MoS}_2$  from first principles”, *Phys. Rev. B* **86**, 241201 (2012).
- [85] A. Kormányos, G. Burkard, M. Gmitra, J. Fabian, V. Zólyomi, N. D. Drummond, and V. Fal’ko, “ $k \cdot p$  theory for two-dimensional transition metal dichalcogenide semiconductors”, *2D Mater.* **2**, 022001 (2015).
- [86] H. Fang, C. Battaglia, C. Carraro, S. Nemsak, B. Ozdol, J. S. Kang, H. A. Bechtel, S. B. Desai, F. Kronast, A. A. Unal, G. Conti, C. Conlon, G. K. Palsson, M. C. Martin, A. M. Minor, C. S. Fadley, E. Yablonovitch, R. Maboudian, and A. Javey, “Strong interlayer coupling in van der Waals heterostructures built from single-layer chalcogenides”, *Proc. Natl Acad. Sci.* **111**, 6198–6202 (2014).
- [87] P. Rivera, J. R. Schaibley, A. M. Jones, J. S. Ross, S. Wu, G. Aivazian, P. Klement, K. Seyler, G. Clark, N. J. Ghimire, J. Yan, D. G. Mandrus, W. Yao, and X. Xu, “Observation of long-lived interlayer excitons in monolayer  $\text{MoSe}_2$ - $\text{WSe}_2$  heterostructures”, *Nat. Commun.* **6**, 6242 (2015).
- [88] P. Nagler, M. V. Ballottin, A. A. Mitioglu, F. Mooshammer, N. Paradiso, C. Strunk, R. Huber, A. Chernikov, P. C. M. Christianen, C. Schüller, and T. Korn, “Giant magnetic splitting inducing near-unity valley polarization in van der Waals heterostructures”, *Nat. Commun.* **8**, 1551 (2017).
- [89] N. R. Wilson, P. V. Nguyen, K. Seyler, P. Rivera, A. J. Marsden, Z. P. L. Laker, G. C. Constantinescu, V. Kandyba, A. Barinov, N. D. M. Hine, X. Xu, and D. H. Cobden, “Determination of band offsets, hybridization, and exciton binding in 2D semiconductor heterostructures”, *Sci. Adv.* **3**, e1601832 (2017).
- [90] J. S. Ross, P. Rivera, J. Schaibley, E. Lee-Wong, H. Yu, T. Taniguchi, K. Watanabe, J. Yan, D. Mandrus, D. Cobden, W. Yao, and X. Xu, “Interlayer Exciton Optoelectronics in a 2D Heterostructure p-n Junction”, *Nano Lett.* **17**, 638–643 (2017).
- [91] M. Schäfer, M. Werchner, W. Hoyer, M. Kira, and S. W. Koch, “Quantum theory of luminescence in multiple-quantum-well Bragg structures”, *Phys. Rev. B* **74**, 155315 (2006).

- [92] See <http://www.nlcstr.com/publications.htm> and <http://www.nlcstr.com/examples0.htm> for examples. Accessed on March 8, 2020.
- [93] R. Wallauer, J. Reimann, N. Armbrust, J. Gdde, and U. Hfer, “Intervalley scattering in MoS<sub>2</sub> imaged by two-photon photoemission with a high-harmonic probe”, *Appl. Phys. Lett.* **109**, 162102 (2016).
- [94] R. Bertoni, C. W. Nicholson, L. Waldecker, H. Hbener, C. Monney, U. De Giovannini, M. Puppin, M. Hoesch, E. Springate, R. T. Chapman, C. Cacho, M. Wolf, A. Rubio, and R. Ernstorfer, “Generation and Evolution of Spin-, Valley-, and Layer-Polarized Excited Carriers in Inversion-Symmetric WSe<sub>2</sub>”, *Phys. Rev. Lett.* **117**, 277201 (2016).
- [95] D. Erben, A. Steinhoff, C. Gies, G. Schnhoff, T. O. Wehling, and F. Jahnke, “Excitation-induced transition to indirect band gaps in atomically thin transition-metal dichalcogenide semiconductors”, *Phys. Rev. B* **98**, 035434 (2018).
- [96] F. Lohof, A. Steinhoff, M. Florian, M. Lorke, D. Erben, F. Jahnke, and C. Gies, “Excitation-induced transition to indirect band gaps in atomically thin transition-metal dichalcogenide semiconductors”, *Nano Lett.* **19**, 210–217 (2019).
- [97] A. Steinhoff, M. Rsner, F. Jahnke, T. O. Wehling, and C. Gies, “Influence of Excited Carriers on the Optical and Electronic Properties of MoS<sub>2</sub>”, *Nano Lett.* **14**, 3743–3748 (2014).
- [98] R. K. Ghosh and S. Mahapatra, “Monolayer Transition Metal Dichalcogenide Channel-Based Tunnel Transistor”, *IEEE J. Electron Devices Soc.* **1**, 175–180 (2013).

## Publications

This chapter contains the publications whose material was subject of this thesis. First, the abstracts of each publication are listed and afterwards the publications themselves have been included.

**Paper I:** *Influence of the effective layer thickness on the ground-state and excitonic properties of transition-metal dichalcogenide systems*

A self-consistent scheme for the calculations of the interacting ground state and the near band-gap optical spectra of mono- and multilayer transition-metal-dichalcogenide systems is presented. The approach combines a dielectric model for the Coulomb interaction potential in a multilayer environment, gap equations for the renormalized ground state, and the Dirac-Wannier equation to determine the excitonic properties. To account for the extension of the individual monolayers perpendicular to their basic plane, an effective thickness parameter in the Coulomb interaction potential is introduced. Numerical evaluations show that the resulting finite thickness effects lead to significant modifications in the optical spectra, reproducing the experimentally observed nonhydrogenic features of the excitonic resonance series. Applying the theory for a variety of experimentally relevant configurations, a consistent description of the near band-gap optical properties is obtained all the way from monolayer to bulk. In addition to the well-known in-plane excitons, also interlayer excitons occur in multilayer systems suggesting a reinterpretation of experimental results obtained for bulk material.

**Paper II:** *Giant excitation induced bandgap renormalization in TMDC monolayers*

Optical absorption and gain spectra in MoS<sub>2</sub> monolayers with thermal carrier distributions are calculated from the combined gap and Dirac-Bloch equations. It is shown that the excited carriers lead to a bandgap renormalization as large as 800 meV for a suspended monolayer MoS<sub>2</sub>. Above the critical density, optical gain is obtained over an approx. 400 meV broad spectral range above the gap. Whereas the absorption spectra in the low density regime are very sensitive to

the dielectric environment, the spectra become purely intrinsic at elevated carrier densities.

**Paper III:** *Interlayer excitons in transition-metal dichalcogenide heterostructures with type-II band alignment*

Combining *ab initio* density functional theory with the Dirac-Bloch and gap equations, excitonic properties of transition-metal dichalcogenide hetero-bilayers with type-II band alignment are computed. The existence of interlayer excitons is predicted, whose binding energies are as large as 350 meV, only roughly 100 meV less than those of the coexisting intralayer excitons. The oscillator strength of the interlayer excitons reaches a few percent of the intralayer exciton resonances and their radiative lifetime is two orders of magnitude larger than that of the intralayer excitons.

**Paper IV:** *Ultrafast band-gap renormalization and build-up of optical gain in monolayer  $\text{MoTe}_2$*

The dynamics of band-gap renormalization and gain build-up in monolayer  $\text{MoTe}_2$  is investigated by evaluating the nonequilibrium Dirac-Bloch equations with the incoherent carrier-carrier and carrier-phonon scattering treated via quantum-Boltzmann type scattering equations. For the case where an approximately 300-fs-long high-intensity optical pulse generates charge-carrier densities in the gain regime, the strong Coulomb coupling leads to a relaxation of excited carriers on a few-femtosecond timescale. The pump-pulse generation of excited carriers induces a large band-gap renormalization during the timescale of the pulse. Efficient phonon coupling leads to a subsequent carrier thermalization within a few picoseconds, which defines the timescale for the optical gain build-up energetically close to the low-density exciton resonance.

# Paper I

**L. Meckbach**, T. Stroucken, and S. W. Koch

“Influence of the effective layer thickness on the ground-state and excitonic properties of transition-metal dichalcogenide systems”

Phys. Rev. B **97**, 035425 (2018) DOI: 10.1103/PhysRevB.97.035425



## Influence of the effective layer thickness on the ground-state and excitonic properties of transition-metal dichalcogenide systems

L. Meckbach, T. Stroucken,<sup>\*</sup> and S. W. Koch

*Department of Physics and Material Sciences Center, Philipps University Marburg, Renthof 5, D-35032 Marburg, Germany*



(Received 26 September 2017; revised manuscript received 22 December 2017; published 18 January 2018)

A self-consistent scheme for the calculations of the interacting ground state and the near band-gap optical spectra of mono- and multilayer transition-metal-dichalcogenide systems is presented. The approach combines a dielectric model for the Coulomb interaction potential in a multilayer environment, gap equations for the renormalized ground state, and the Dirac-Wannier equation to determine the excitonic properties. To account for the extension of the individual monolayers perpendicular to their basic plane, an effective thickness parameter in the Coulomb interaction potential is introduced. Numerical evaluations show that the resulting finite thickness effects lead to significant modifications in the optical spectra, reproducing the experimentally observed nonhydrogenic features of the excitonic resonance series. Applying the theory for a variety of experimentally relevant configurations, a consistent description of the near band-gap optical properties is obtained all the way from monolayer to bulk. In addition to the well-known in-plane excitons, also interlayer excitons occur in multilayer systems suggesting a reinterpretation of experimental results obtained for bulk material.

DOI: [10.1103/PhysRevB.97.035425](https://doi.org/10.1103/PhysRevB.97.035425)

### I. INTRODUCTION

The optical and electronic properties of bulk transition-metal dichalcogenide systems (TMDCs) have been investigated intensively already in the 1970s [1–6]. The excitonic series observed in the optical absorption spectra could be attributed to transitions at the  $K$  points of the Brillouin zone, which nowadays are often referred to as Dirac points [1–6]. However, as bulk TMDCs are indirect band gap semiconductors, these materials have only played a minor role in the field of semiconductor optics in the following decades.

More recently, the interest in TMDCs and their optical properties has been revived with the ability to fabricate them as monolayers. Unlike their bulk counterparts, monolayers of several semiconducting TMDCs display a direct gap at the  $K$  points of their respective Brillouin zone with a transition energy in the visible range [7–12]. These systems exhibit a pronounced light-matter coupling and strong excitonic effects [13–16]. The availability of different materials with a similar lattice structure but different band gaps renders this material class extremely interesting as building blocks for heterostructures [17,18], and allows for the engineering of the overall electronic and optical properties to a wide extend.

For the systematic design and engineering of the electronic and optical properties of TMDC systems, it is highly desirable to have a predictive microscopic theory that includes the fundamental structural properties as well as the strong Coulomb interaction effects among the electronic excitations. In this article, we present a theoretical framework that allows us to determine both, the Coulombic renormalization of the  $K$  point band gap and the excitonic states. Our approach combines a dielectric model to determine the Coulomb interaction potential in a multilayer environment, the gap equations

for the renormalized ground state, and the Dirac-Wannier equation—a generalization of the Mott-Wannier equation—for the calculation of the excitonic states.

Starting point of our theory is an effective two-band Hamiltonian, for which we use the massive Dirac-Fermion model (MDF) [19]. Within the MDF, the gap equations and the Dirac-Wannier equation can be derived as static and linear part of the Dirac-Bloch equations, i.e., the coupled equations of motion for the interband polarization and the electron-hole populations [20]. As our approach is based on the equations of motion approach, it can easily be extended to describe the nonlinear and dynamical optical properties.

In order to account for the finite out-of-plane monolayer extension, we introduce a thickness parameter  $d$  in the effective Coulomb potential governing the interaction between the electronic excitations. The precise value of  $d$  is determined by fitting a single spectral feature, e.g., the exact value of the energetically lowest excitonic resonance, to available experimental data. As all other parameters are extracted from first-principles density functional theory (DFT) calculations,  $d$  is the only adjustable parameter in our theory. Once  $d$  is fixed for a given material system, we are able to predict the band gap and all the excitonic resonances for arbitrary dielectric environment and number of layers. Furthermore, we are able to study the optical properties for multilayered structures and, in particular, the transition from a monolayer to bulk.

The paper is organized as follows. In Sec. II, we present the model system used for the calculations of the  $K$  point ground state and the optical properties of a multilayer structure. In Sec. III, we derive the Wannier equation for the Dirac excitons and the gap equations that determine the renormalization ground-state properties. In Sec. IV, we investigate finite thickness effects and the scaling properties of the coupled gap and Wannier equations for the simplified case of a constant background screening. The results show that finite thickness

<sup>\*</sup>Corresponding author: [tineke.stroucken@physik.uni-marburg.de](mailto:tineke.stroucken@physik.uni-marburg.de)

effects lead to drastic modifications of the excitonic spectra. In Sec. V, we analyze the band-gap renormalization and near band-gap optical properties for a variety of monolayer systems. The results for multilayer configurations are discussed in Sec. VI before we present a brief summary and discussion of our approach. In the appendix, we summarize important aspects of the electrostatic ingredients of our model, including the determination of the effective Coulomb interaction and screening properties. Furthermore, we list the material parameters used in our numerical evaluations.

## II. MODEL SYSTEM

Our model system is a stack of  $N$  identical van-der-Waals bonded TMDC monolayers. Systematic studies of the band structure as a function of the number of layers [7–10] show that the transition from direct to indirect occurs already when going from a monolayer to a bilayer configuration. This feature has been confirmed experimentally by layer number dependent PL measurements [11,12].

At the same time, the DFT band-structure investigations show that the band structure details around the  $K$  points, which govern the optical absorption properties, are pretty much preserved while increasing the number of layers from monolayer to bulk [7–12]. At the  $K$  points, the out-of-plane effective masses of the valence and conduction bands are typically much larger than those of the in-plane directions [21]. Consequently, the out-of-plane component of the kinetic energy can be neglected and the quasiparticles at the  $K$  points can be considered as quasi-two-dimensional particles well confined within the layers. Based on this observation, we treat the  $K$  point dynamics in a multilayer stack as  $N$  electronically independent layers that are coupled via the Coulomb potential within the respective dielectric environment:

$$H = \sum_n (H_0^n + H_I^n) + \frac{1}{2} \sum_{nm, \mathbf{q}} V_{\mathbf{q}}^{nm} \hat{\rho}_{\mathbf{q}}^n \hat{\rho}_{-\mathbf{q}}^m.$$

Here,  $H_0^n$  describes the free-particle Hamiltonian of the  $n$ th layer,  $H_I^n$  contains the light-matter interaction, and the last term is the Coulomb interaction, respectively. We assume that  $\hat{\rho}_{\mathbf{q}}^n$ , the charge density of the  $n$ th layer, is strongly localized within that layer. Treating the Hamiltonian of the isolated monolayer within an effective two-band model, screening of the bands under consideration is included dynamically, whereas the Coulomb matrix element  $V_{\mathbf{q}}^{nm}$  contains the screening of all the other bands and the dielectric environment.

### A. The massive Dirac fermion Hamiltonian

According to *ab initio* methods based on DFT, the highest conduction and the lowest valence band are predominantly composed of  $d$ -type atomic orbitals of the metal atom [22]. Combining the relevant atomic orbitals that contribute to the valence and conduction bands into a two-component pseudo spinor, the minimal two-band Hamiltonian describing the near  $K$  point properties in lowest order  $\mathbf{k} \cdot \mathbf{p}$  theory can be written as [19]

$$\hat{H}_0^n = \sum_{s\tau, \mathbf{k}} \hat{\Psi}_{n s \tau \mathbf{k}}^\dagger \left( a t \mathbf{k} \cdot \hat{\sigma}_\tau + \frac{\Delta}{2} \hat{\sigma}_z - s \tau \lambda \frac{\hat{\sigma}_z - 1}{2} \right) \hat{\Psi}_{n s \tau \mathbf{k}}. \quad (1)$$

Here,  $\tau = \pm 1$  is the so-called valley index, whereas  $\Delta$ ,  $2\lambda$ ,  $t$ , and  $a$  denote the energy gap, the effective spin splitting of the valence bands, the effective hopping matrix element, and the lattice constant, respectively. The operator  $\hat{\Psi}_{n s \tau \mathbf{k}}$  is the tensor product of the electron spin state and the two component quasi-spinor in the  $n$ th layer. The Pauli matrices  $\hat{\sigma}_\tau = (\tau \hat{\sigma}_x, -\hat{\sigma}_y)$  and  $\hat{\sigma}_z$  act in the pseudo-spin space and  $s$  is the  $z$  component of the real spin, respectively. The eigenstates of  $\hat{H}_0$  have the relativistic dispersion

$$\epsilon_{s\tau k} = \pm \frac{1}{2} \sqrt{\Delta_{s\tau}^2 + (2\hbar v_F k)^2},$$

where  $\Delta_{s\tau} = \Delta - s\tau\lambda$  denotes the spin and valley dependent energy gap at the  $K$  points and  $v_F = at/\hbar$  is the Fermi velocity.

Employing the minimal substitution principle, the light-matter (LM) Hamiltonian is obtained as

$$H_I^n = -e \frac{v_F}{c} \sum_{s\tau \mathbf{k}} \hat{\Psi}_{n s \tau \mathbf{k}}^\dagger \mathbf{A}^n \cdot \hat{\sigma}_\tau \hat{\Psi}_{n s \tau \mathbf{k}}, \quad (2)$$

where  $\mathbf{A}^n = \mathbf{A}(z_n)$  is the optical field at the position of the  $n$ th layer. Expanding the charge density in terms of the pseudospinors, we find for the Coulomb interaction

$$H_C^n = \frac{1}{2} \sum_{m \mathbf{k} \mathbf{k}' \mathbf{q}} : \hat{\Psi}_{n s \tau \mathbf{k}-\mathbf{q}}^\dagger \hat{\Psi}_{n s \tau \mathbf{k}} V_{\mathbf{q}}^{nm} \hat{\Psi}_{m s \tau \mathbf{k}'+\mathbf{q}}^\dagger \hat{\Psi}_{m s \tau \mathbf{k}'} : ,$$

where  $: \cdot :$  denotes normal ordering.

### B. Coulomb potential in a multilayer environment

The Coulomb interaction potential in our two-band Hamiltonian contains screening contributions from the system's environment, such as substrate screening, etc., and possible nonresonant intrinsic contributions arising from all other bands. To avoid double counting, it is important to separate the contributions of the explicitly treated bands from the rest. Since the DFT dielectric tensor contains all the ingredients, the separation of resonant and nonresonant contributions is a nontrivial task.

Here, we develop a scheme that combines bulk DFT calculations of the dielectric tensor with analytical results obtained within the MDF model that allows us to determine the fully screened and nonresonantly screened (“bare”) Coulomb potential for various dielectric environments. To derive the Coulomb interaction potential in the multilayer environment, we start from Maxwell's equations

$$\nabla \cdot \mathbf{D} = 4\pi \rho_{\text{ext}}, \quad (3)$$

$$\nabla \cdot \mathbf{B} = 0, \quad (4)$$

$$\nabla \times \mathbf{H} - \frac{1}{c} \dot{\mathbf{D}} = \frac{4\pi}{c} \mathbf{j}_{\text{ext}}, \quad (5)$$

$$\nabla \times \mathbf{E} + \frac{1}{c} \dot{\mathbf{B}} = 0. \quad (6)$$

For the layered material, we make the ansatz

$$\mathbf{B} = \mathbf{H}, \quad \mathbf{D} = \epsilon_{\parallel} \mathbf{E}_{\parallel} + \epsilon_{\perp} E_z \mathbf{e}_z + 4\pi \mathbf{P}, \quad (7)$$

where  $\epsilon_{\parallel} \equiv \epsilon_{\parallel}(z)$  and  $\epsilon_{\perp} \equiv \epsilon_{\perp}(z)$  represent the nonresonant contributions to the anisotropic dielectric tensor and  $\mathbf{P}$  contains

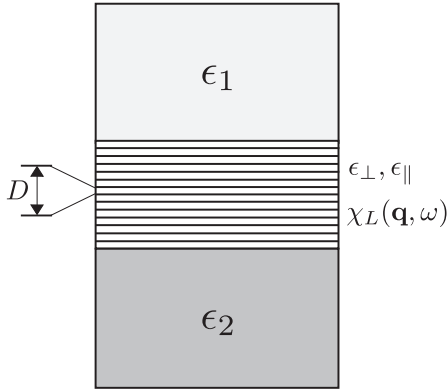


FIG. 1. Schematic of the model system. The distance between the van der Waals bonded layers is denoted by  $D$ .

all nonlocal, time and frequency dependent resonant contributions. The nonresonant contributions are assumed to be local in space and time and constant within a slab of thickness  $L = ND$ , where  $N$  is the number of layers and  $D$  the natural layer-to-layer distance in the bulk parent material (see Fig. 1).

As the considered structure is homogeneous with respect to the in-plane coordinates but inhomogeneous with respect to the out-of-plane coordinates, we use a mixed  $(\mathbf{q}, z)$  representation in the following, where  $\mathbf{q}$  is the in-plane wave vector. With  $\mathbf{B} = \nabla \times \mathbf{A}$ ,  $\mathbf{E} = -\dot{\mathbf{A}}/c - \nabla\phi$  and the generalized Coulomb gauge  $\epsilon_{\parallel}\nabla_{\parallel} \cdot \mathbf{A}_{\parallel} + \epsilon_{\perp}\partial_z A_z = 0$ , a division into in-plane transverse and longitudinal contributions yields Poisson's equation for the scalar potential

$$(-\epsilon_{\perp}\partial_z^2 + \epsilon_{\parallel}\mathbf{q}^2)\phi = 4\pi(\rho_{\text{ext}} - i\mathbf{q} \cdot \mathbf{P}_{\parallel}^L - \partial_z P_z). \quad (8)$$

The solution of this equation for a  $\delta$  inhomogeneity  $\rho_{\text{ext}} = \delta(z - z')$  and  $\mathbf{P}_{\parallel}^L = 0$  determines the bare Coulomb potential  $V_{\mathbf{q}}(z, z')$ . Correspondingly, the screened Coulomb potential is obtained as solution of Poisson's equation with resonant contributions. Provided the nonresonant contributions to the dielectric tensor are known, the bare Coulomb interaction can be obtained analytically from Eq. (8).

For the resonant contributions to the longitudinal polarization, we assume that these are composed of a sum of localized (2D) parts, that are treated within linear response. In the strict 2D limit, these can be expressed as

$$\mathbf{P} = -ie^2\mathbf{q} \sum_{n=1}^N \chi_L(\mathbf{q}, \omega)\phi(\mathbf{q}, z_n, \omega)\delta(z - z_n), \quad (9)$$

where  $z_n = (n - 1/2)D$  is the central position of the  $n$ th layer and  $\chi_L(\mathbf{q}, \omega)$  is the longitudinal susceptibility, respectively. The longitudinal susceptibility is related to the polarization function of the 2D layer via  $\chi_L(\mathbf{q}, \omega) = -\Pi(\mathbf{q}, \omega)/q^2$ . Within the MDF model, for each spin and valley combination, the long-wavelength limit of the static RPA polarization function gives [23]

$$\Pi(\mathbf{q}, 0) = -\frac{1}{6\pi} \frac{q^2}{\Delta_{s\tau}},$$

where  $\Delta_{s\tau}$  is the spin and valley dependent gap at the Dirac points. Summing over the spin and valley indices, one finds

$$r_0 = \lim_{\mathbf{q} \rightarrow 0} 2\pi e^2 \chi_L(\mathbf{q}, 0) = \frac{2e^2(\Delta_A + \Delta_B)}{3\Delta_A\Delta_B},$$

which is of the order of  $10\text{\AA}$  for a typical  $\text{MX}_2$  monolayer, independent of the dielectric environment.

Inserting Eq. (9) into Eq. (8), we obtain for the screened Coulomb interaction

$$V_{S,\mathbf{q}}^{nm}(\omega) = \sum_{l=1}^N (\delta_{nl} + e^2 q^2 \chi_L(\mathbf{q}, \omega) V_{\mathbf{q}}^{nl})^{-1} V_{\mathbf{q}}^{lm}. \quad (10)$$

Equation (10) expresses the screened Coulomb interaction in terms of the bare potential and an inverse nonlocal dielectric function. With the aid of the screened and unscreened interaction, we can define the local dielectric functions  $\epsilon^n(\mathbf{q}, \omega) = V_{\text{vac},\mathbf{q}}^{nn}/V_{S,\mathbf{q}}^{nn}(\omega)$ , where  $V_{\text{vac},\mathbf{q}}^{nn} = 2\pi/|\mathbf{q}|$  is the 2D Coulomb potential in vacuum. Similarly, we introduce the resonant and nonresonant contributions of the local dielectric functions as  $\epsilon_{\text{res}}^n(\mathbf{q}, \omega) = V_{\mathbf{q}}^{nn}/V_{S,\mathbf{q}}^{nn}(\omega)$  and  $\epsilon_{\text{nr}}^n(\mathbf{q}, \omega) = V_{\text{vac},\mathbf{q}}^{nn}/V_{\mathbf{q}}^{nn}$ , respectively. In general, each layer within the multilayer environment has a different local dielectric function reflecting its respective dielectric environment.

For a bulk material consisting of  $N \gg 1$  regularly spaced layers, Eq. (8) can be solved by a Fourier transformation, giving

$$V_S(\mathbf{q}, q_z) = \frac{4\pi}{\epsilon_{\perp}q_z^2 + \mathbf{q}^2(\epsilon_{\parallel} + 4\pi e^2 \chi_L(\mathbf{q}, \omega)/D)},$$

where  $D$  is the layer-to-layer distance. Comparison with the 3D anisotropic Coulomb interaction suggests that the bulk in-plane dielectric constant is given by

$$\epsilon_{\parallel}^B = \epsilon_{\parallel} + \lim_{\mathbf{q} \rightarrow 0} 4\pi e^2 \chi_L(\mathbf{q}, \omega)/D.$$

We use this relation and the bulk values for the macroscopic background dielectric constants obtained by DFT [24] to determine the required values of  $\epsilon_{\parallel}$  and  $\epsilon_{\perp}$ .

### C. Quasi-2D Coulomb potential

Computing the Coulomb potential for a strictly 2D layer ignores the fact that the spatial carrier distribution in the out-of-plane direction has a finite extension and is not a sharp  $\delta$  function at the central layer position. Hence, instead of solving Poisson's equation with a  $\delta$  singularity, we have to compute the scalar potential for a charge distribution  $\rho_{\mathbf{q}}(z - z_n)$  induced by the charge density in the  $n$ th layer and replace Eq. (9) by (see Appendix A)

$$\mathbf{P} = -ie^2\mathbf{q} \sum_{n=1}^N \chi_L(\mathbf{q}, \omega)\rho_{\mathbf{q}}(z - z_n) \times \int_{-D/2}^{D/2} dz' \phi(\mathbf{q}, z', \omega)\rho_{-\mathbf{q}}(z' - z_n). \quad (11)$$

Defining the quasi-2D Coulomb potential between different layers as

$$\bar{V}_{\mathbf{q}}^{nm} = \int_{-D/2}^{D/2} dz \int_{-D/2}^{D/2} dz' \rho_{-\mathbf{q}}(z' - z_n) V_{\mathbf{q}}(z, z') \rho_{\mathbf{q}}(z - z_m)$$

and similar for the screened interaction potential, Eq. (10) remains valid with all matrix elements replaced by the quasi-2D ones.

In order to have a simple expression, we use in the following the 2D Ohno potential:

$$\tilde{V}_{\mathbf{q}}^{nm} \approx V_{\mathbf{q}}^{nm} e^{-qd},$$

as approximation for the bare quasi-2D potential. Here,  $d$  denotes the effective thickness parameter accounting for finite out-of-plane extension of the carrier densities. Additional to the effective thickness parameter  $d$ , both the nonresonantly screened and fully screened Coulomb matrix elements depend on the natural layer-to-layer distance  $D$ , via the solution of Poisson's equation including the nonresonant background contributions to the dielectric screening.

### III. METHODS

The Coulomb interaction leads to renormalizations of the single-particle band structure and to excitonic effects in the optical properties of a semiconductor. In this section, we follow the derivation in Ref. [20] to show how both of these features are obtained within the equations of motion (EOM) approach. Here, one derives the equations of motion for the interband polarization and the valence and conduction band occupation probabilities to obtain the semiconductor Bloch equations (SBE) [25], which describe excitonic effects as well as the excitation dependent energy renormalizations.

As input for the SBE, one needs the single-particle band structure and the system's ground-state properties. Since DFT-based band-structure calculations usually underestimate the unexcited band gap, one often uses the experimental values instead of the DFT results. Whereas this approach works well for the typical GaAs-type bulk or mesoscopic semiconductor structures, the fundamental gap of mono- or few-layer TMDCs is experimentally difficult to access and depends strongly on the dielectric environment. Therefore, it is desirable to compute the gap renormalization self-consistently from first principles.

#### A. Gap equations

As shown in Refs. [20,26], the combination of the EOM with a variational approach yields a set of coupled integral equations—the gap equations—for the renormalized band gap and the Fermi velocity. The gap equations are nonperturbative and can be derived on the same level of approximation as the EOM for the excitation dynamics. We define the dynamical variables

$$\Gamma_{s\tau\mathbf{k}} = f_{s\tau\mathbf{k}}^b - f_{s\tau\mathbf{k}}^a = \langle \hat{b}_{s\tau\mathbf{k}}^\dagger \hat{b}_{s\tau\mathbf{k}} \rangle - \langle \hat{a}_{s\tau\mathbf{k}}^\dagger \hat{a}_{s\tau\mathbf{k}} \rangle, \quad (12)$$

$$\Pi_{s\tau\mathbf{k}} = \langle \hat{b}_{s\tau\mathbf{k}}^\dagger \hat{a}_{s\tau\mathbf{k}} \rangle, \quad (13)$$

where  $\hat{a}_{s\tau\mathbf{k}}^\dagger$  and  $\hat{b}_{s\tau\mathbf{k}}^\dagger$  create a particle in the basis states spanning the pseudospinor  $\hat{\Psi}_{s\tau\mathbf{k}}^\dagger$ . Since the ground state should be static, we search for the stationary solutions of Heisenberg's equations of motion,

$$i\hbar \frac{d}{dt} \Pi_{s\tau\mathbf{k}} = (\Delta_{s\tau} + \hat{V}[\Gamma_{s\tau}]) \Pi_{s\tau\mathbf{k}} + (\tau \hbar v_F k e^{i\tau\theta_{\mathbf{k}}} - \hat{V}[\Pi_{s\tau}]) \Gamma_{s\tau\mathbf{k}}, \quad (14)$$

$$i\hbar \frac{d}{dt} \Gamma_{s\tau\mathbf{k}} = 2\Pi_{s\tau\mathbf{k}} (\tau \hbar v_F k e^{-i\tau\theta_{\mathbf{k}}} - \hat{V}[\Pi_{s\tau}^*]) - 2\Pi_{s\tau\mathbf{k}}^* (\tau \hbar v_F k e^{i\tau\theta_{\mathbf{k}}} - \hat{V}[\Pi_{s\tau}]) \quad (15)$$

in the absence of an externally applied optical field. To simplify the notation, we introduced the functional relation  $\hat{V}[f] \equiv \sum_{\mathbf{k}'} V_{|\mathbf{k}-\mathbf{k}'|} f_{\mathbf{k}'}$ . Demanding a stationary solution, we find

$$0 = \tilde{\Delta}_{s\tau\mathbf{k}} \Pi_{s\tau\mathbf{k}} + \tau \hbar \tilde{v}_{s\tau\mathbf{k}} k e^{i\tau\theta_{\mathbf{k}}} \Gamma_{s\tau\mathbf{k}}, \quad (16)$$

$$0 = \text{Im}[\Pi_{s\tau\mathbf{k}} \tau \hbar \tilde{v}_{s\tau\mathbf{k}} k e^{-i\tau\theta_{\mathbf{k}}}], \quad (17)$$

where

$$\tilde{\Delta}_{s\tau\mathbf{k}} = \Delta_{s\tau} + \hat{V}[\Gamma_{s\tau}], \quad (18)$$

$$\tau \hbar \tilde{v}_{s\tau\mathbf{k}} k e^{i\tau\theta_{\mathbf{k}}} = \tau \hbar v_F k e^{i\tau\theta_{\mathbf{k}}} - \hat{V}[\Pi_{s\tau}] \quad (19)$$

are the renormalized band-gap energy and Fermi velocity, respectively. Together with the relation  $1 = \Gamma_{s\tau\mathbf{k}}^2 + 4|\Pi_{s\tau\mathbf{k}}|^2$ , which holds for any coherent state, we obtain the algebraic equations

$$\Pi_{s\tau\mathbf{k}} = -\frac{\tau \hbar \tilde{v}_{s\tau\mathbf{k}} k}{2\tilde{\epsilon}_{s\tau\mathbf{k}}} e^{i\tau\theta_{\mathbf{k}}}, \quad (20)$$

$$\Gamma_{s\tau\mathbf{k}} = \frac{\tilde{\Delta}_{s\tau\mathbf{k}}}{2\tilde{\epsilon}_{s\tau\mathbf{k}}} \quad (21)$$

with

$$\tilde{\epsilon}_{s\tau\mathbf{k}} = \frac{1}{2} \sqrt{\tilde{\Delta}_{s\tau\mathbf{k}}^2 + (2\hbar \tilde{v}_{s\tau\mathbf{k}} k)^2}. \quad (22)$$

Inserting Eqs. (20) and (21) into Eqs. (16) and (17) yields the closed set of integral equations, the gap equations, as

$$\begin{aligned} \tilde{\Delta}_{s\tau\mathbf{k}} &= \Delta_{s\tau} + \frac{1}{2} \sum_{\mathbf{k}'} V_{|\mathbf{k}-\mathbf{k}'|} \frac{\tilde{\Delta}_{s\tau\mathbf{k}'}}{\tilde{\epsilon}_{s\tau\mathbf{k}'}} \\ \tilde{v}_{s\tau\mathbf{k}} &= v_F + \frac{1}{2} \sum_{\mathbf{k}'} V_{|\mathbf{k}-\mathbf{k}'|} \frac{k'}{k} \frac{\tilde{v}_{s\tau\mathbf{k}'}}{\tilde{\epsilon}_{s\tau\mathbf{k}'}} e^{-i\tau(\theta_{\mathbf{k}} - \theta_{\mathbf{k}'})}. \end{aligned} \quad (23)$$

It is easily verified that  $\tilde{\Delta}_{s\tau\mathbf{k}}$  and  $\tilde{v}_{s\tau\mathbf{k}}$  define the mean-field Hamiltonian

$$\hat{H}^{MF} = \sum_{s,\tau,\mathbf{k}} \hat{\Psi}_{s\tau\mathbf{k}}^\dagger \left( \hbar \tilde{v}_{s\tau\mathbf{k}} \mathbf{k} \cdot \hat{\sigma}_\tau + \frac{\tilde{\Delta}_{s\tau\mathbf{k}}}{2} \hat{\sigma}_z \right) \hat{\Psi}_{s\tau\mathbf{k}} \quad (24)$$

with the eigenvalues  $\pm \tilde{\epsilon}_{s\tau\mathbf{k}}$ . The corresponding eigenstates are given by

$$\Psi_{\mathbf{k}}^c = \begin{pmatrix} u_{s\tau k} \\ v_{s\tau k} e^{-i\tau\theta_{\mathbf{k}}} \end{pmatrix}, \quad \Psi_{\mathbf{k}}^v = \begin{pmatrix} v_{s\tau k} e^{i\tau\theta_{\mathbf{k}}} \\ -u_{s\tau k} \end{pmatrix}, \quad (25)$$

where  $u_{s\tau k} = \sqrt{(\tilde{\epsilon}_{s\tau k} + \tilde{\Delta}_{s\tau k}/2)/2\tilde{\epsilon}_{s\tau k}}$  and  $v_{s\tau k} = \sqrt{(\tilde{\epsilon}_{s\tau k} - \tilde{\Delta}_{s\tau k}/2)/2\tilde{\epsilon}_{s\tau k}}$ . As usual in intrinsic semiconductors, the ground state is characterized by a completely filled valence and empty conduction band, respectively. Since  $\tilde{\epsilon}_{s\tau\mathbf{k}} > \epsilon_{s\tau\mathbf{k}}$ , the total energy lies below the energy of the noninteracting ground state.

### B. Dirac-Bloch and Dirac-Wannier equations

To determine the excitation dynamics of our model system, we transform the Hamiltonian into the electron-hole picture using the *renormalized* band structure and eigenstates. Furthermore, we use the interband transition amplitudes and occupation numbers of the renormalized bands as dynamical variables,

$$P_{s\tau\mathbf{k}} = \langle v_{s\tau\mathbf{k}}^\dagger c_{s\tau\mathbf{k}} \rangle, \quad (26)$$

$$f_{s\tau\mathbf{k}} = 1 - \langle v_{s\tau\mathbf{k}}^\dagger v_{s\tau\mathbf{k}} \rangle = \langle c_{s\tau\mathbf{k}}^\dagger c_{s\tau\mathbf{k}} \rangle, \quad (27)$$

where  $v_{s\tau\mathbf{k}}^\dagger$  and  $c_{s\tau\mathbf{k}}^\dagger$  create a particle in the renormalized valence and conduction bands, respectively. It is easily verified that, using the renormalized bands, the ground-state expectation values are given by  $P_{s\tau\mathbf{k}} = f_{s\tau\mathbf{k}} = 0$  (note: this is not true for the transition amplitudes and occupation numbers within the unrenormalized bands!).

At the Hartree-Fock level, the resulting Heisenberg EOM for the dynamical variables are given by [20]

$$i\hbar \frac{d}{dt} P_{s\tau\mathbf{k}} = 2 \left( \Sigma_{s\tau\mathbf{k}} - \frac{1}{c} \mathbf{A} \cdot \mathbf{j}_{s\tau\mathbf{k}} \right) P_{s\tau\mathbf{k}} - (1 - 2f_{s\tau\mathbf{k}}) \Omega_{s\tau\mathbf{k}} - i\hbar \frac{d}{dt} P_{s\tau\mathbf{k}} \Big|_{\text{coll}}, \quad (28)$$

$$\hbar \frac{d}{dt} f_{s\tau\mathbf{k}} = -2\text{Im}[P_{s\tau\mathbf{k}}^* \Omega_{s\tau\mathbf{k}}] - \hbar \frac{d}{dt} f_{s\tau\mathbf{k}} \Big|_{\text{coll}}. \quad (29)$$

In these *Dirac-Bloch equations* (DBE), the Coulomb interaction leads to excitation dependent renormalizations of the single-particle energy and the Rabi frequency,

$$\begin{aligned} \Sigma_{s\tau\mathbf{k}} &= \tilde{\epsilon}_{s\tau\mathbf{k}} - \sum_{\mathbf{k}'} V_{|\mathbf{k}-\mathbf{k}'|} [W_{cccc}(\mathbf{k}, \mathbf{k}') - W_{cvcv}(\mathbf{k}, \mathbf{k}')] f_{s\tau\mathbf{k}'} \\ &+ \sum_{\mathbf{k}'} V_{|\mathbf{k}-\mathbf{k}'|} [W_{ccvc}(\mathbf{k}, \mathbf{k}') P_{s\tau\mathbf{k}'} + \text{c.c.}], \quad (30) \\ \Omega_{s\tau\mathbf{k}} &= \sum_{\mathbf{k}'} V_{|\mathbf{k}-\mathbf{k}'|} [W_{ccvv}(\mathbf{k}, \mathbf{k}') P_{s\tau\mathbf{k}'} + W_{cvcv}(\mathbf{k}, \mathbf{k}') P_{s\tau\mathbf{k}'}^* \\ &- 2W_{cvcv}(\mathbf{k}, \mathbf{k}') f_{s\tau\mathbf{k}'}] + \tau \sqrt{2} \frac{eV_F}{c} \\ &\times (v_k^2 e^{2i\tau\theta_k} A^{-\tau} - u_k^2 A^\tau), \quad (31) \end{aligned}$$

whereas ground-state renormalizations are contained in the renormalized dispersion  $\tilde{\epsilon}_{s\tau\mathbf{k}}$ . Here,

$$W_{\alpha\alpha'\beta\beta'}(\mathbf{k}, \mathbf{k}') = \langle \alpha\mathbf{k} | \alpha'\mathbf{k}' \rangle \langle \beta\mathbf{k}' | \beta'\mathbf{k} \rangle$$

contains the overlap matrix elements between the renormalized conduction and valence bands. Despite the formal equivalence of Eqs. (28) and (29) to the standard SBE, the renormalized single-particle energy and Rabi frequency differ from the standard expressions by the Coulomb matrix elements for scattering processes across the bands, i.e., Auger-type processes and electron-hole pair creation and annihilation. In Eqs. (28) and (29), the terms  $d/dt|_{\text{coll}}$  refer to incoherent scattering contributions beyond the Hartree-Fock approximation and  $\mathbf{j}_{s\tau\mathbf{k}} = -\tau \frac{e}{\hbar} \nabla_{\mathbf{k}} \tilde{\epsilon}_{s\tau\mathbf{k}}$  is the intraband current matrix element, respectively.

The Dirac-Wannier equation (DWE) is obtained from the DBE as homogeneous part of the linearized polarization equation,

$$2\tilde{\epsilon}_{s\tau\mathbf{k}} \varphi_{s\tau\lambda}(\mathbf{k}) - \sum_{\mathbf{k}'} V_{|\mathbf{k}-\mathbf{k}'|} [W_{ccvv}(\mathbf{k}, \mathbf{k}') \varphi_{s\tau\lambda}(\mathbf{k}') + W_{cvcv}(\mathbf{k}, \mathbf{q}) \varphi_{s\tau\lambda}^*(\mathbf{k}')] = E_{s\tau\lambda} \varphi_{s\tau\lambda}(\mathbf{k}). \quad (32)$$

Apart from the dispersion, the DWE differs from the standard Mott-Wannier equation by the last term on the left-hand side (l.h.s.) of Eq. (32), that describes a coupling of the  $\varphi$  and  $\varphi^*$  by spontaneous pair creation and annihilation. In view of the large gap in semiconducting TMDCs, these contributions are frequently neglected. However, the validity of this approximation is not *a priori* clear since it actually depends on the strength of the Coulomb interaction. In our evaluations in this paper, we therefore avoid the wide-gap approximation (WGA).

### IV. FINITE THICKNESS EFFECTS

In the strict 2D limit, the exciton binding and wave functions at the origin become singular in the regime of strong Coulomb interactions [23,27] leading to an excitonic collapse of the interacting ground state. In this case, the system undergoes a transition into an excitonic insulator state, where the bright optical resonances correspond to intraexcitonic transitions of a BCS-like excitonic condensate [20,27]. A similar divergence of the binding energy and wave functions is known in QED for hydrogenlike atoms with  $Z > 137$ . In QED, this ‘‘catastrophe’’ is treated via a regularization of the Coulomb-potential accounting for a small but finite extension of the nucleus, i.e., by replacing the  $1/r$  potential by the Ohno potential  $1/\sqrt{r^2 + d^2}$ .

In this section, we apply a similar procedure and investigate the influence of finite thickness effects on the gap and exciton equations for a monolayer with a constant background screening  $\kappa$ , i.e., we use the  $k$ -space representation of the Ohno potential  $\bar{V}_{\mathbf{q}} = 2\pi e^2 e^{-q^d} / \kappa q$ . This potential is appropriate for both, a monolayer embedded in bulk with  $\kappa = \sqrt{\epsilon_{\parallel} \epsilon_{\perp}}$  and for the long wavelength limit  $qD \rightarrow 0$  of a monolayer on a substrate with  $\kappa = (\epsilon_S + 1)/2$  (see Appendix).

In order to unify the description of different material systems and to identify the general aspects of the obtained results, it is often advantageous to introduce scaled units. For the problem under investigation here, one can either choose relativistic or excitonic units. As the only absolute energy value entering into the DWE, one can use the single-particle gap  $\Delta$  as energy unit. The single-particle dispersion is then found as  $\epsilon_k / \Delta = \pm \frac{1}{2} \sqrt{1 + (k\lambda_C)^2}$ , where  $\lambda_C = 2\hbar v_F / \Delta$  is the Compton wavelength of the electrons and holes. For typical TMDC parameters, the Compton wavelength is on the order 4–6 Å, i.e., on the order of the lattice constant and the natural layer-to-layer distance in bulk. Using the Compton wavelength as length scale, the scaled quasi-2D Coulomb potential is given by

$$\bar{\bar{V}}_{\mathbf{q}} = \frac{\bar{V}_{\mathbf{q}}}{\Delta} = \frac{\pi\alpha}{\bar{q}} e^{-\bar{q}\bar{d}}, \quad (33)$$

which is characterized by the parameter combination  $\alpha = e^2 / \kappa \hbar v_F$ , which is typically in the range  $3/\kappa$  to  $5/\kappa$ . The Compton wavelength allows one to distinguish between the

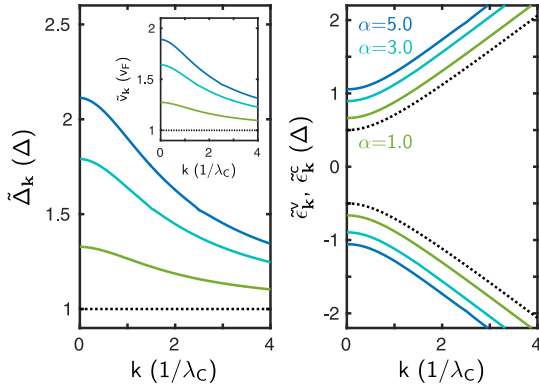


FIG. 2. Renormalized band gap energy (left) and Fermi-velocity (inset) distributions for  $d = 1.0 \lambda_C$  and  $\alpha = 1.0$  (green), 3.0 (cyan), and 5.0 (blue). The resulting renormalized single-particle dispersion is shown on the right. The black dotted lines represent the noninteracting ground state properties.

relativistic and the nonrelativistic regimes, where the latter one is found on a length scale large compared to the Compton wavelength.

Using scaled units, it is easily shown that the total Hamiltonian is characterized by two parameters, namely the effective fine structure constant  $\alpha$  and the effective thickness parameter  $\bar{d}$ . Consequently, both the gap equations and the exciton equation are characterized by the same parameters. The long-wavelength limit of the resonant part of the RPA dielectric function in scaled units is obtained as

$$\epsilon_{\text{res}}(\mathbf{q}) = 1 + \frac{2}{3} \alpha q \bar{\lambda}_C e^{-q \bar{d}},$$

where  $\bar{\lambda}_C = (\lambda_C^A + \lambda_C^B)/2$  is the average of the respective Compton wavelengths associated with the gap of the  $A$  and  $B$  excitons. This dielectric function is of a similar form as the potential first introduced by Keldysh [28] for a thin sheet with constant sheet polarizability and has been used by several authors [13, 29–33] to model the excitonic properties of TMDCs. As a consequence of the Ohno potential, the dielectric function does not increase to infinity with increasing  $q$  but approaches its maximum value at  $q = 1/d$ . A similar behavior has been found by first principle calculations including finite thickness effects [33, 52] or using a truncated Coulomb potential [34]. Furthermore, the screening length  $\frac{2}{3} \alpha \bar{\lambda}_C$  contains resonant contributions only.

When discussing excitonic properties, it is sometimes useful to resort to excitonic units. The Compton wavelength and the (3D) exciton Bohr radius  $a_0 = \hbar^2 \kappa / m_r e^2$  are related via  $a_B = 2 \lambda_C / \alpha$ , and the exciton Rydberg  $Ry = m_r e^4 / 2 \hbar^2 \kappa^2$  is related to the gap via  $Ry = \alpha^2 \Delta / 8$ , respectively. In the following, we will use both unit systems in order to emphasize systematic dependencies and the essential underlying physics.

### A. Numerical solution of the gap equations

Examples of our numerical solutions of the gap equations (23) are shown in Fig. 2. Here, we plot  $\tilde{\Delta}_k$  and  $\tilde{v}_k$  as well as the resulting renormalized single-particle dispersion  $\tilde{\xi}_k$  for various values of  $\alpha$  and a fixed thickness parameter  $d = 1.0 \lambda_C$ .

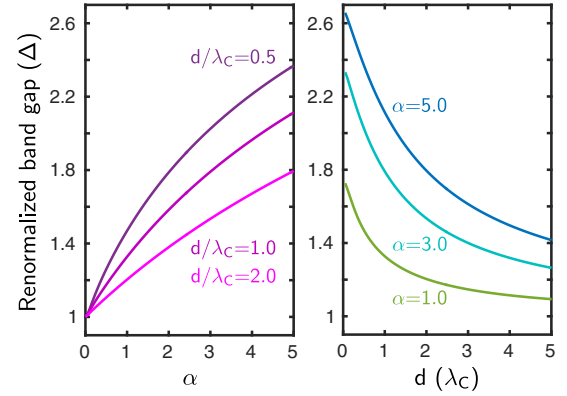


FIG. 3. Left: Renormalized gap as function of coupling constant  $\alpha$  for three different thickness parameters  $d = 0.5 \lambda_C$ ,  $1.0 \lambda_C$ , and  $2.0 \lambda_C$ . Right: Dependence of the renormalized gap on the effective thickness parameter  $d$  for three values of the coupling constant  $\alpha = 1.0$ , 3.0, and 5.0.

Both  $\tilde{\Delta}_k$  (left) and  $\tilde{v}_k$  (inset) have their maxima at  $k = 0$  and converge to their respective noninteracting ground-state values  $\Delta$  and  $v_F$  (respective black dotted lines) for large  $k$ . Within a good approximation, the renormalization of the band gap energy and the Fermi velocity leads to a rigid shift of the noninteracting single-particle dispersion (right panel in Fig. 2), in agreement with reported predictions based on the GW approximation [34–37].

Since the renormalization does not lead to a deformation of the single-particle band structure, it only shifts the energetic position of the excitonic resonances in the respective optical spectra but does not influence their binding energies. Hence it suffices to study the overall gap shift as function of the system parameters  $\alpha$  and  $d$ . For this purpose, we plot in the left panel of Fig. 3 the computed dependence of the renormalized gap on  $\alpha$  for three different values of the effective thickness parameter. As we can see, the gap increases linearly with  $\alpha$  for small values of the coupling strength switching over to a logarithmic increase for large coupling strengths.

In the right panel of Fig. 3, we show the computed values of the renormalized gap as function of the effective thickness parameter  $d$  for three different values of  $\alpha$ . We notice a sensitive  $d$  dependence of the gap in the region where  $d \lesssim \alpha \lambda_C$ , which is typically realized in TMDC structures.

### B. Numerical solution of the Dirac-Wannier equation

Often [13, 31, 33], the excitonic properties of TMDCs are treated in the wide gap approximation (WGA) where the relativistic quasi-particle dispersion can be approximated by parabolic bands and all contributions  $\propto v_k v_{k'}$  in the Coulomb matrix elements can be neglected. As a result, the excitonic states become independent of the Compton wavelength and the only remaining length scales are the effective sheet thickness  $d$  and the exciton Bohr radius  $a_B$ . Moreover, states with  $m = \pm|m|$  are degenerate.

Since the only energy scale other than the gap is the exciton Rydberg energy, the WGA is actually equivalent to the nonrelativistic approximation  $\alpha \ll 1$ . For typical TMDC parameters, the effective coupling constant is in the range

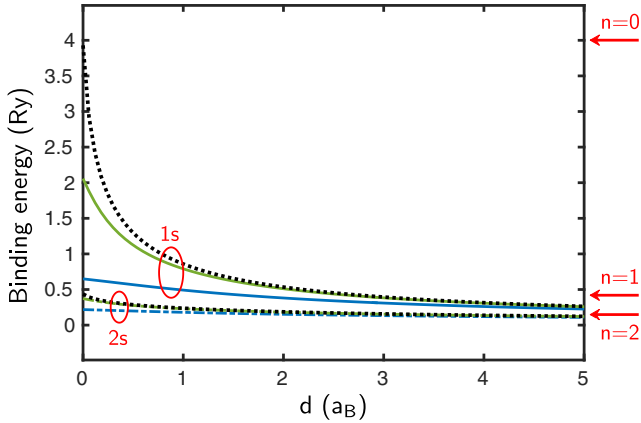


FIG. 4. Binding energy of the  $1s$  and  $2s$  exciton in dependence of the effective thickness parameter  $d$  for  $\alpha = 1.0$  (green) and  $3.0$  (blue). The black dotted lines show the nonrelativistic case for parabolic bands. The strict 2D nonrelativistic limit ( $d = 0$ ) is marked by the arrows.

of  $\alpha \propto 3/\kappa$  to  $5/\kappa$ , clearly questioning the WGA. Corrections to the WGA result both from the full relativistic dispersion and from the lifting of the degeneracy between states with opposite orbital angular momentum [32,38]

Numerically solving the full DWE (32), we obtain the results shown in Fig. 4. Here, we plot the binding energies of the  $1s$  (solid lines) and  $2s$  exciton (dashed lines) as functions of the effective thickness parameter in excitonic units for  $\alpha = 1.0$  and  $\alpha = 3.0$ . For reference, the arrows mark the binding of the exciton states with main quantum number  $n = 0, 1$ , and  $2$  within the 2D hydrogen model.

For finite values for the effective sheet thickness  $d$ , the Coulomb interaction close to the origin is weakened relative to the strict 2D case, affecting particularly the strongest bound  $s$ -type excitons with large probability density at the origin. Figure 4 clearly shows that the binding energies of the  $1s$  and  $2s$  excitons vary strongly with the sheet thickness in the regime where  $d \approx a_B$  and become pretty much  $d$  independent for  $d \gg a_B$ . In that limit, the binding energy of the  $1s$  exciton drops below the value of the  $n = 1$  2D exciton state. At the same time, the  $2s$  binding energy seems to converge toward the  $n = 2$  value of the 2D limit leading to an overall strongly nonhydrogenic behavior of the exciton series similar to the experimental observations [13,14,39,40]. This behavior is quite different from what is known for semiconductor quantum wells, where the exciton series changes from a 2D to 3D Rydberg series if the sample dimensions exceed the exciton Bohr radius.

The combined solution of the gap equations (23) together with the DWE (32) allows us to determine the energetic positions of the excitonic resonances in an optical spectrum. In Fig. 5, we show the results for the five lowest  $s$ -type excitonic states for a fixed thickness  $d = 1.0 \lambda_C$  as function of coupling strength  $\alpha$ . For reference, we also plot the variation of the renormalized band gap at one of the Dirac points (black dotted line). As expected, the binding energies increase with increasing Coulomb coupling strength. However, the increased binding is overcompensated by the band-gap renormalization,

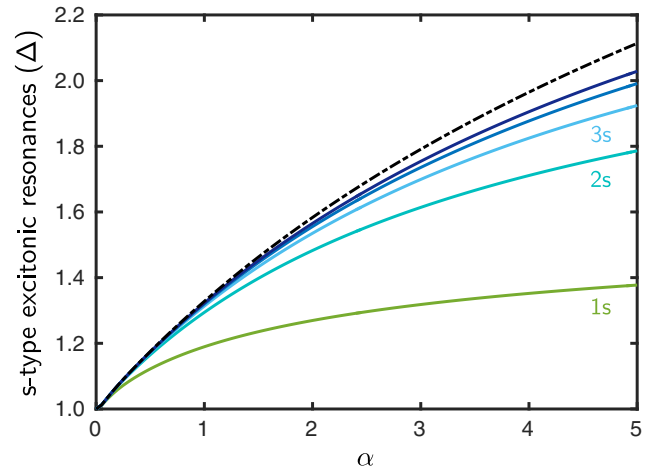


FIG. 5. Lowest  $s$ -type energy eigenvalues of the Dirac-Wannier equation as a function of  $\alpha$  with respect to the renormalized single-particle dispersion. The black dashed-dotted line indicates the renormalized band gap. The effective thickness parameter has been set to  $d = 1.0 \lambda_C$ .

leading to an overall blue shift of the excitonic resonance spectrum. In the limit of strong Coulomb coupling, the increase of the  $1s$ -exciton binding energy is almost canceled by the renormalization of the band gap, such that the lowest exciton resonance depends only weakly on the coupling strength.

As the contributions to the Coulomb matrix elements  $\propto v_k$  display a different angle dependence as the dominant contributions  $\propto u_k$ , corrections beyond the WGA or parabolic approximation not only affect the binding of the bright  $s$ -type states, but also lead to a fine structure in the exciton spectrum lifting the degeneracy between states with opposite orbital angular momentum. In Fig. 6, we show the splitting of the lowest  $p$  states for a fixed effective thickness  $d = 1.0 \lambda_C$ . In the limit of small values for the Coulomb coupling, the splitting increases quadratically switching over to a linear increase for large values of  $\alpha$ , respectively. For a suspended

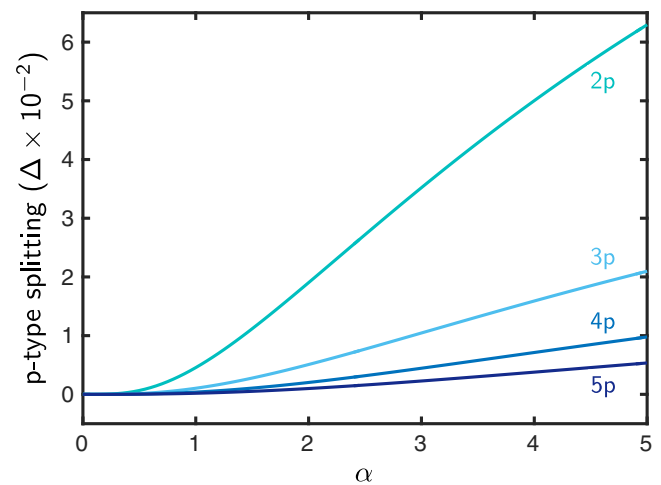


FIG. 6. Fine structure of the excitonic spectra, illustrated by the splitting of the lowest  $p$ -type excitonic states.

monolayer ( $\alpha \approx 3.0$  to  $5.0$ ), the splitting of the  $2p$  states can be as high as 5% to 6% of the noninteracting energy gap. For supported monolayers, e.g., on a  $\text{SiO}_2$  substrate ( $\alpha \approx 1.2$  to  $2.0$ ), our calculations predict a splitting on the order of 10 to 15 meV, depending on the noninteracting gap of the specific material and on the screening. This value should be in the experimentally accessible range.

### V. MONOLAYER STRUCTURES: COMPARISON WITH EXPERIMENT

So far, we investigated the excitonic scaling properties and the influence of finite layer thickness within a simplified model for the dielectric environment. In this section, we extend this approach and numerically study the properties of realistic monolayer TMDC systems using the full solution of Poisson's equation within the anisotropic dielectric environment for different TMDCs.

For the MDF material parameters, we use the values given in Ref. [19]. To determine the Coulomb potential, we take the bulk in-plane and out-of-plane dielectric constants from Ref. [24], and determine the background contributions by subtracting the resonant contributions calculated within the MDF model, as described in Sec. II B. A full list of the parameters for the different material systems can be found in the appendix.

In a first step, we fix the only undetermined parameter in our theory, namely the effective thickness parameter  $d$ . To this end, we plot the renormalized gap and exciton resonances as function of  $d$  and compare the resulting predictions with experimentally available data. In Fig. 7, we show the result of this procedure for the example of  $\text{MoS}_2$  on  $\text{SiO}_2$ , where we use a constant dielectric constant  $\epsilon_S = 2.1025$  for the  $\text{SiO}_2$  substrate. Here, we fit the effective thickness parameter such that we obtain  $E_{1s} = 1.94$  eV as the energy of the lowest exciton resonance, which is in the range of measured values [41–44]. As can be recognized, best agreement is obtained for an effective thickness parameter  $d = 4.47$  Å,

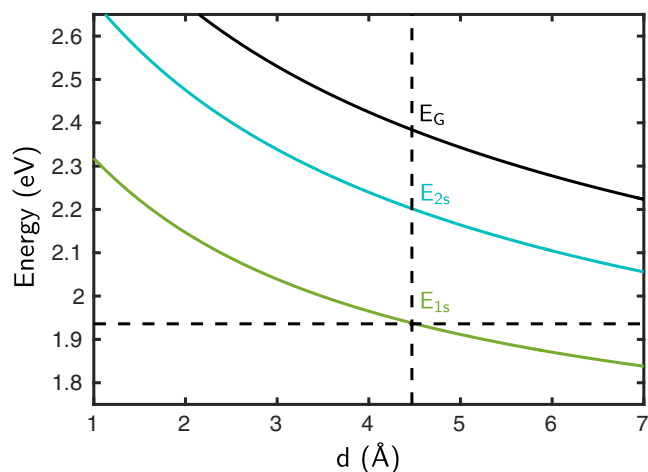


FIG. 7. Predicted resonance positions for  $\text{MoS}_2$  on  $\text{SiO}_2$  as function of effective thickness. The solid lines show the theoretical position of the  $1s$  (green),  $2s$  (cyan) resonance and the gap (black), the dashed lines mark the target energy value for the A-exciton resonance  $E_{1s}$  and the best fit for the thickness parameter.

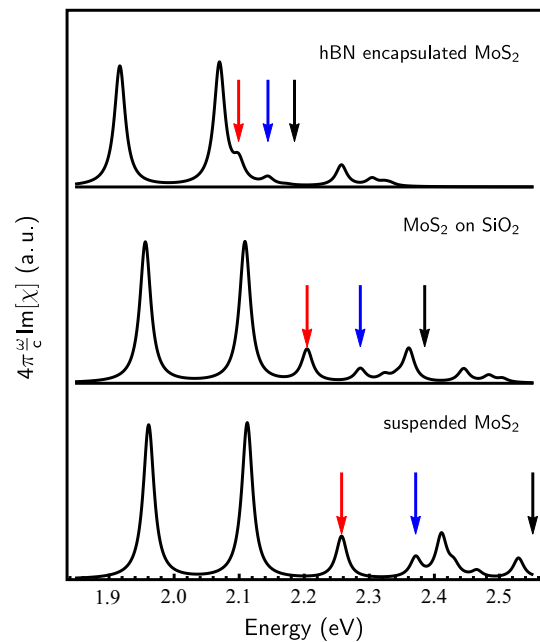


FIG. 8. Calculated spectra for  $\text{MoS}_2$  within different dielectric environments using the same thickness parameter  $d = 4.47$  Å. (Top) encapsulated with hBN, using  $\epsilon_{\text{hBN}} = 2.89$ , (middle) on  $\text{SiO}_2$  ( $\epsilon_{\text{SiO}_2} = 2.1$ ), (bottom) freely suspended. The red and blue arrows indicate the spectral position of the  $A_{2s}$  and  $A_{3s}$  exciton resonances, and the black arrows the renormalized gap of the A-exciton series. All spectra have been calculated using a phenomenological dephasing rate  $\hbar\gamma = 10$  meV.

which is smaller than the layer separation  $D = 6.2$  Å for  $\text{MoS}_2$ . The corresponding values for the band gap and the first excited exciton resonance are then  $E_G = 2.39$  eV and  $E_{2s} = 2.204$  eV, giving binding energies of  $E_{1s}^B = 434$  meV and  $E_{2s}^B = 186$  meV for  $\text{MoS}_2$  on  $\text{SiO}_2$  respectively.

Since the value for the gap is difficult to determine experimentally, we cannot directly compare the findings for the band gap and exciton binding energy with experiment. However, we can use the optimized effective thickness value to predict the band-gap and exciton resonances for different dielectric environments. In Fig. 8, we show the computed spectra for an hBN encapsulated  $\text{MoS}_2$  monolayer (upper part), a  $\text{MoS}_2$  monolayer on a  $\text{SiO}_2$  substrate (middle part), and a suspended monolayer (lower part), respectively. With increasing environmental screening, we observe a large shift of the fundamental gap from  $E_G = 2.55$  eV for the A exciton in a suspended layer to  $E_G = 2.18$  eV for the A gap of a hBN encapsulated layer. Together with the large band-gap shift, we obtain a reduction of the  $1s$  exciton binding energy such that the combination of both effects results in a small net red shift of the lowest  $A_{1s}$  exciton resonance in the range of 10 to 50 meV when going from a suspended monolayer to a  $\text{SiO}_2$  supported and hBN encapsulated monolayer.

The obtained values for a suspended monolayer ( $E_{1s} = 1.96$  eV and a binding energy of  $E_{1s}^B = 0.599$  eV) are in pretty good agreement with experimental photocurrent spectroscopy observations reported in Ref. [45], where the lowest exciton resonance was found slightly above 1.9 eV with a binding

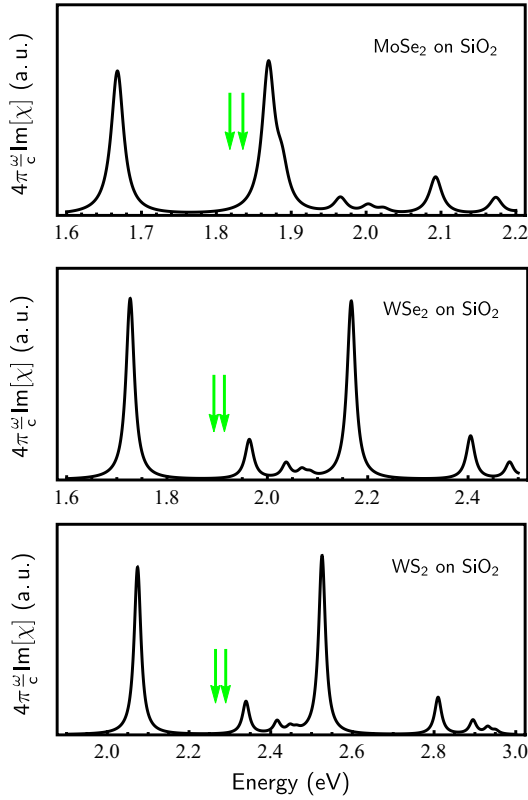


FIG. 9. Calculated spectra different TMDC monolayers supported by a SiO<sub>2</sub> substrate. (Top) MoSe<sub>2</sub>, (middle) WSe<sub>2</sub>, and (bottom) WS<sub>2</sub>. The green arrows indicate the spectral position of the  $A_{2p}$  exciton resonances, which are several tens of meV below the  $A_{2s}$  resonances and are splitted by approximately 10 meV. The spectra have been calculated using an effective thickness parameter of  $d = 4.96$  Å for MoSe<sub>2</sub>,  $d = 5.17$  Å for WSe<sub>2</sub>, and  $d = 2.78$  Å for WS<sub>2</sub> and a phenomenological dephasing rate  $\hbar\gamma = 10$  meV.

energy of  $E_b \geq 570$  meV. On the purely theoretical side, our results are close to the values  $E_G = 2.54$  eV and  $E_{1s}^B = 0.63$  eV computed in Ref. [34] from *ab initio* methods based on many-body perturbation theory and the Bethe-Salpeter equation (BSE).

For the hBN encapsulated MoS<sub>2</sub> monolayer, we find the lowest three  $s$ -type resonances of the A-exciton series at  $E_{1s} = 1.917$  eV,  $E_{2s} = 2.10$  eV, and  $E_{3s} = 2.14$  eV, and the lowest B resonance at 2.070 eV. These predictions are in excellent agreement with recent experimental findings [46] of  $E_{1s} = 1.926$  eV,  $E_{2s} = 2.10$  eV, and  $E_{3s} = 2.12$  eV, and the 1s B-exciton resonance at  $E = 2.08$  eV, respectively.

In Fig. 9, we show the calculated spectra for SiO<sub>2</sub> supported MoSe<sub>2</sub>, WSe<sub>2</sub>, and WS<sub>2</sub> monolayers. For each material, we adjusted the effective thickness parameters to reproduce the respective lowest experimentally observed  $A_{1s}$  resonances, i.e.,  $E_{1s} = 1.66$  eV for MoSe<sub>2</sub> [44,47],  $E_{1s} = 1.74$  eV for WSe<sub>2</sub> [40], and  $E_{1s} = 2.09$  eV for WS<sub>2</sub> [13], yielding  $d = 4.96, 5.17,$  and  $2.78$  Å, respectively. For all material systems, the effective thickness is within the physical range  $d \lesssim D$ .

For MoSe<sub>2</sub>, the resulting  $A_{2s}$  resonance is slightly above the lowest  $B_{1s}$  resonance, and can be observed as shoulder on the high energy side of the lowest B exciton. This interference

of different exciton species makes it hard to resolve them experimentally, which probably explains the lack of reliable experimental data on the  $A_{2s}$  resonance of MoSe<sub>2</sub> on SiO<sub>2</sub>. However, we could recently show excellent agreement for the higher exciton resonances in hBN-encapsulated MoSe<sub>2</sub> monolayers, strongly supporting the validity of our model system [48].

For SiO<sub>2</sub> supported WSe<sub>2</sub> and WS<sub>2</sub>, where the spin splitting of the valence bands is large enough to avoid interference of the A- and B-exciton series, higher excited states could be resolved experimentally. The observed resonances are around 1.9 and 2 eV in WSe<sub>2</sub> [40], and around 2.25 and 2.3 eV in WS<sub>2</sub> [13], respectively. Comparison with our theoretical predictions of  $E_{2s} = 1.964$  eV and  $E_{3s} = 2.037$  eV in WSe<sub>2</sub> and  $E_{2s} = 2.339$  eV and  $E_{3s} = 2.41$  eV in WS<sub>2</sub> shows that the spacing between the exciton ground state and the excited states seems to be overestimated by our theory. However, it has been pointed out in the literature [49], that due to the specific  $D_{3h}$  point symmetry of the TMDC monolayers, also  $p$ -type states can be accessed by one-photon spectroscopy. Though the detailed analysis of the  $p$ -type states excitation scenario is beyond the scope of this paper, we can compute the spectral position of the  $p$ -type resonances. We obtain  $E_{2p_1} = 1.893$  eV and  $E_{2p_{-1}} = 1.914$  eV for WSe<sub>2</sub>, and  $E_{2p_1} = 2.265$  eV and  $E_{2p_{-1}} = 2.290$  eV for WS<sub>2</sub>, precisely where the observed resonances in the computed spectra of Fig. 9 are missing. Therefore purely based on the energetic position comparison with our theoretical model, we would assign these resonances to  $p$ -type states.

## VI. MULTILAYER STRUCTURES

Once the effective thickness parameter is fixed, we are not only able to compute the renormalized bands and resonance positions for samples on arbitrary substrates, but also for samples with an arbitrary number of layers. If we increase the number of layers, the number of bands within the first 2D Brillouin zone is increased accordingly. For the effective 2D quasiparticles that are localized well within a given layer, we can use the layer number  $n$  within the stack as a good quantum number. In the following, we introduce the notation  $E_G(n, m) = E_{nq=0}^c - E_{mq=0}^v$  for the transition energy between the maximum of the  $n$ th valence band and the minimum of the  $m$ th conduction band at the  $K$  points, and a similar notation for the exciton resonances.

In Fig. 10, we show the variation of the renormalized valence-to-conduction band transition energies  $E_G(n, n)$  and of the corresponding lowest exciton resonances  $E_{1s}(n, n)$  with increasing number of layers. Since the effective local dielectric functions differ for different layers in the sample, the degeneracy of the noninteracting bands associated with different layers is lifted by the Coulomb renormalizations, leading to additional resonances in the optical spectra of the multilayer structure.

For each value of  $N$ , the dots in Fig. 10 denote the transition energies  $E_G(n, n)$  and  $E_{1s}(n, n)$  for  $n = 1, N$ . For the example of a suspended sample, bands associated with mirror identical layers (e.g., top and bottom layers) are still degenerate, leading to  $N/2$  ( $N$  even) or  $(N + 1)/2$  ( $N$  odd) distinct transition energies, and the lines represent their average, weighted by the respective degeneracy factors. In the bulk limit  $N \rightarrow \infty$ ,

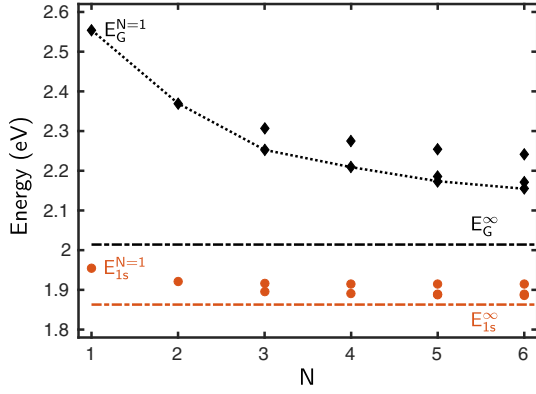


FIG. 10. (Left) Renormalized free-particle transition energies and exciton positions as function of total layer number  $N$  for suspended  $\text{MoS}_2$  using  $d = 4.47 \text{ \AA}$ . With increasing layer number the number of bands increases accordingly and are classified by the layer index  $n = 1, \dots, N$  (see text for explanation). The black diamonds show the free particle transition energies  $E_G(n, n)$  and the orange dots the lowest exciton resonance positions  $E_{1s}(n, n)$  in the individual layers. The dashed line indicates the weighted average for the free particle transition, see text for explanation. The dashed-dotted lines indicate the bulk limit  $N \rightarrow \infty$ .

we find  $E_G^\infty = 2.03$  and  $E_{1s}^\infty = 1.88$ , giving a binding energy of 150 meV for the lowest lying bulk exciton. These values are in good agreement with *GW-BSE* based *ab initio* results reported in Ref. [35], where a binding energy of 130 meV was found for the bulk *A* exciton. For reference, the respective bulk limits for the band gap and lowest exciton are indicated in Fig. 10 by the dashed lines.

Besides their intralayer interaction, the electrons and holes in a multilayer structure interact also with carriers in neighboring layers with the possibility to form bound interlayer excitons. To illustrate these features, we plot in Fig. 11 the free-particle transition energies  $E_G(n, n)$  and resonance energies  $E_{1s}(n, n)$  for intralayer excitons where the electron-hole pair resides within the same layer, as well as the interlayer transition energies  $E_G(1, n)$  and  $E_G(25, n)$ , and energies of interlayer excitons  $E_{1s}(1, n)$  and  $E_{1s}(25, n)$  where an electron is confined in the  $n$ th layer and the hole in top or middle layer, respectively. We see that the interlayer excitons form a whole spectral series with decreasing binding energy for increasing spatial electron-hole separation.

Due to our model assumption of electronically independent layers, the interlayer excitons are optically dark and cannot be observed in optical spectra. However, if we relax the assumption of electronically fully independent layers but allow for a finite overlap of the electron and hole wave functions in different layers, these interlayer excitons gain a finite oscillator strength, that decreases rapidly with increasing layer separation. Assuming Gaussian distributions of width  $d$  for the electron and hole densities, we can estimate the electron-hole overlap between different layers from the integral  $|\int dz \phi_e(z) \phi_h(z - nD)|^2$  determining the oscillator strength for the respective interlayer excitons.

Using these model assumptions, we can compute optical absorption spectra for different multilayer systems. In Fig. 12, we show the results for a suspended mono- and bilayer  $\text{MoS}_2$ , using the screened Coulomb potential and thickness  $d = 4.47 \text{ \AA}$ . The signature in the spectral range between the lowest *A* and *B* excitons, that are red shifted by roughly 30 meV, is the lowest interlayer exciton. Furthermore, we see

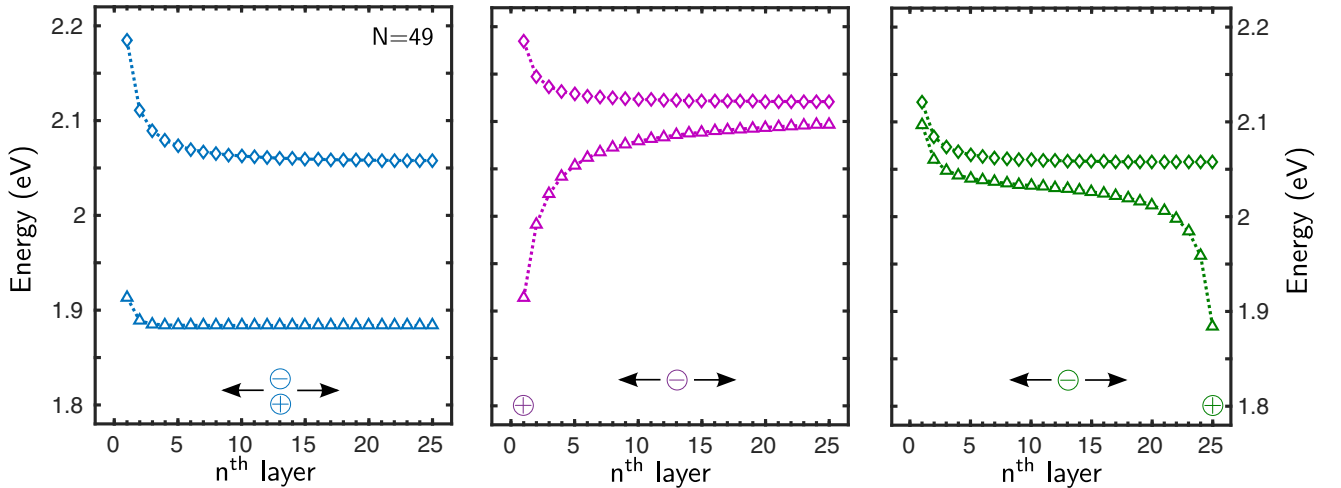


FIG. 11. Transition energies for intra- and interlayer excitons in a suspended  $\text{MoS}_2$  sample consisting of  $N = 49$  layers. Results are shown for layers with  $1 \leq n \leq 25$ . Transitions energies for electron-hole pairs where one particle is confined in layers with  $n > 25$  are identical to those with  $n' = 50 - n$  by inversion symmetry. (Left) Free particle transition energy  $E_G(n, n)$  (diamonds) and lowest exciton resonance  $E_{1s}(n, n)$  (triangles) for electron-hole pairs where both particles are localized within the  $n$ th layer. (Middle) Free particle transition energy  $E_G(1, n)$  (diamonds) and lowest exciton resonance  $E_{1s}(1, n)$  (triangles) for electron-hole pairs where one particle (here the hole) is localized in the top layer ( $n = 1$ ), and the other particle in the  $n$ th layer. (Right) Free-particle transition energy  $E_G(25, n)$  (diamonds) and lowest exciton resonance  $E_{1s}(25, n)$  (triangles) for electron-hole pairs where one particle (here the hole) is localized in the middle layer ( $n = 25$ ), and the other particle in the  $n$ th layer. The  $\ominus$  and  $\oplus$  symbols in the bottom range of the figures indicate the respective position the electron and hole within the sample and the arrows identify that particle whose position is varied along the figure axis.

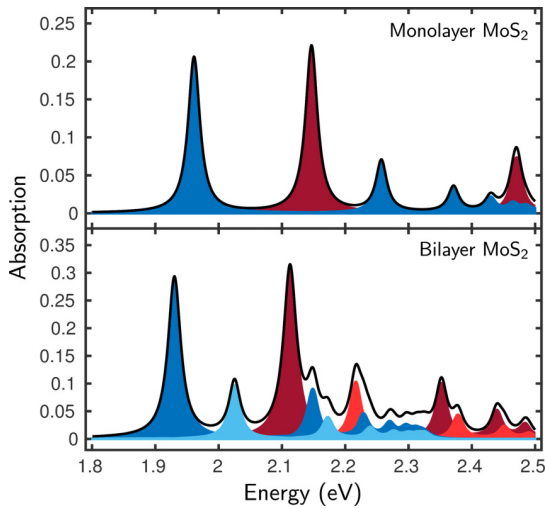


FIG. 12. Calculated absorption spectra of a suspended mono- and bilayer MoS<sub>2</sub>. The black lines show the total absorption spectra, whereas the dark blue and dark red fillings correspond to the *A* and *B* intralayer contributions, and the light blue and light red fillings to the *A* and *B* interlayer contributions, respectively. Spectra have been calculated using a nonradiative homogeneous linewidth  $\hbar\gamma = 10$  meV.

a clear red shift of the excited intralayer excitons in the bilayer relative to the monolayer.

In Fig. 13, we show the spectrum for a multilayer sample in the limit  $N \rightarrow \infty$  in the spectral region of the *A*-exciton resonance series. The dominant peak at  $E = 1.875$  eV and the absorption features slightly below the gap (at 2.03 eV) correspond to the *A*-intralayer exciton series. The pronounced feature around  $E = 1.93$  eV results from the next-neighbor interlayer exciton, where electrons and holes are confined in neighboring layers.

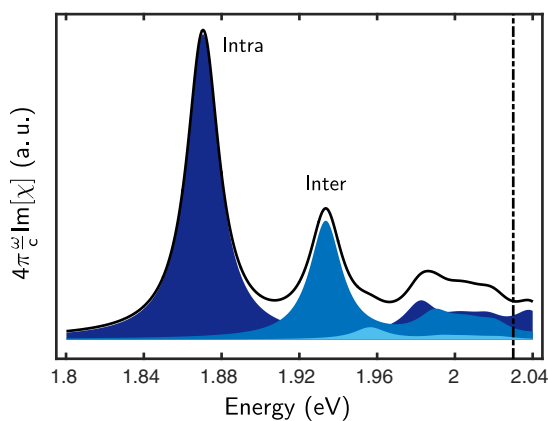


FIG. 13. Imaginary part of the linear susceptibility of MoS<sub>2</sub> in the bulk limit using a homogeneous linewidth  $\hbar\gamma = 10$  meV. The black line shows the imaginary part of the total linear susceptibility, whereas the dark blue filling shows the intralayer contributions, the blue filling the next-neighbor interlayer, and the light blue filling the next-next-nearest-neighbor interlayer excitons contributions respectively. The dashed line around 2.03 eV indicates the position of the renormalized *A*-exciton gap.

It is interesting to compare these predictions with experimental findings on *bulk* MoS<sub>2</sub> for which the absorption spectrum has been measured already in the 1970s [1,2,4]. Transitions that were associated with the *A* exciton at the *K* points of the Brillouin zone have been observed around 1.92, 1.96 and 1.99 eV, and the *A*-exciton gap has been estimated to be at 2.04 eV. In the original publication, the resonance features were interpreted as a ground state and excited states of a single 3D exciton series. However, neither the resonance positions nor the oscillator strength agree with the expectations based on an anisotropic 3D Rydberg series. Using an effective dielectric constant of  $\kappa = \sqrt{\epsilon_{\parallel}\epsilon_{\perp}} = 4.3$  to account for the anisotropy of the layered structure, an exciton Rydberg of 181 meV was found from the Wannier-Mott exciton model, whereas the assumption that the *A*<sub>2s</sub> and *A*<sub>3s</sub> resonances were accurately described by the 3D hydrogen model yielded an exciton Rydberg of 169 meV. Both values give an energy difference for  $\Delta E_{1s-2s} \propto 130$  meV, much larger than the observed energy difference of approximately 40 meV. These deviations have been discussed in the literature and have been explained by so called “central-cell corrections.”

The remarkable agreement of the spectral signatures in Fig. 13 with the measured resonances suggests the reinterpretation of the bulk exciton series as 2D intra- and interlayer excitons, despite some small deviations in the absolute positions of the dominant absorption peaks. It is interesting to note that with this association, the resonances of the intralayer series approximately exhibit a  $1/n^2$  behavior, i.e., just like the usual Rydberg bulk exciton series.

Our interpretation is further supported by recent measurements on bulk MoS<sub>2</sub> [50]. Here, a bias-dependent relative oscillator strength between the two dominant features has been observed, indicating a distinct *z* dependence of both signatures. Furthermore, interlayer excitons in bulk MoTe<sub>2</sub> have been identified recently via magnetic field measurements [51].

## VII. DISCUSSION

In conclusion, we present a theoretical framework that allows us to compute the band-gap renormalization and *K* point excitonic resonances of TMDC mono- and multilayer structures. Our method contains the effective monolayer thickness as undetermined parameter. For a variety of material systems, we show that by fitting this single parameter to obtain agreement for the lowest exciton resonance of a supported monolayer, we are able to compute the band-gap and excitonic spectra of the respective samples with arbitrary layer numbers and substrates. In particular, we are able to predict the evolution of the band-gap and near-band-gap excitonic spectra over the whole range from monolayer to bulk. Our predictions for the bulk limit are in excellent agreement with experimental observations, suggesting a reinterpretation of the bulk *A* and *B* excitonic series in terms of effectively 2D intra- and interlayer excitons.

Our method combines an electrostatic model for the dielectric properties of a layered van der Waals material, the gap equations to determine the renormalized gap, and the Dirac-Bloch or Dirac-Wannier equation to determine the excitation properties. Recently, several electrostatic models to treat the

dielectric screening in a layered van der Waals structures have been proposed in the literature [33,34,52,53]. Similar to our approach, the dielectric function of the multilayer structure has been calculated by treating the response function of an individual layer as building block for the multilayer dielectric function, assuming a purely electrostatic interaction between the layers. The major difference between our ansatz and existing models in the literature is that in most other models, the monolayer response function is obtained from DFT calculations for a monolayer, whereas we combine DFT calculations for *bulk* with analytical calculations for the dielectric screening of the band under consideration. This avoids a double counting of contributions of the considered bands and ensures the correct bulk limit for large multilayer structures.

It is interesting, to compare our method with the well established *GW*-BSE approach where the quasiparticle band gap is computed from many-body perturbation theory on top of the DFT band structure. Subsequently, the excitonic states are obtained as solution of the BSE. The major strength of this *GW*-BSE approach is that it is fully *ab initio* and as such free of any undetermined parameters. However, this comes at the price of being numerically very demanding. The treatment of quasi-2D structures within *GW*-BSE is computationally even more challenging as it requires large supercells to avoid spurious interactions between adjacent layers. The numerical complexity of the *GW*-BSE approach has not only lead to a wide range of reported predictions for the band-gap and exciton bindings, but it also limits its practical application to the description of ground-state and linear optical properties.

Methodically, our approach displays several similarities to the *GW*-BSE approach. Similarly as *GW*, the gap equations provide a correction to the DFT band structure and a subsequent solution of the Dirac-Wannier equation within the renormalized bands gives access to the excitonic states. However, whereas the *GW*-BSE equations involve many bands, our approach is explicitly based on a two-band Hamiltonian, thus reducing the numerical effort enormously. Though an effective two-band Hamiltonian restricts the applicability of our method to the simulation of the near band-gap optical properties, our method is extremely flexible to model different dielectric environments and can be easily extended to describe nonlinear optical experiments.

Both qualitatively and quantitatively, our predictions are in very good agreement with well-converged *GW*-BSE based results [34]. This, in addition to the excellent agreement with experimental observations can be taken as strong indications that our model system captures the essential physics around the *K* points of the Brillouin zone. In particular, we identify finite thickness effects as essentially responsible for the observed nonhydrogenicity not only of monolayer spectra, but also of multilayer spectra in the bulk limit.

## ACKNOWLEDGMENTS

This work is a project of the Collaborative Research Center SFB 1083 funded by the Deutsche Forschungsgemeinschaft. We thank M. Rohlfing for stimulating discussions and for sharing his results on interlayer excitons in TMDCs prior to publication.

## APPENDIX A: SOLUTION OF POISSON'S EQUATION

### 1. Bare Coulomb interaction

The “bare” Coulomb interaction corresponds to the Green function of Poisson’s equation, i.e., is obtained as the solution of Eq. (8) for the scalar potential with  $\delta$  inhomogeneity  $\rho(\mathbf{q}_{\parallel}, z) = \delta(z - z')$  in the absence of a resonant polarization, but in the presence of the inhomogeneous, anisotropic background. For a slab geometry consisting of thickness  $L = ND$  on a substrate with dielectric constant  $\epsilon_S$ , we have a spatial profile of the background dielectric tensor:

$$\epsilon_{\parallel}(z) = \begin{cases} 1 & z < 0, \\ \epsilon_{\parallel} & 0 < z < L, \\ \epsilon_S & L < z \end{cases}, \quad \epsilon_{\perp}(z) = \begin{cases} 1 & z < 0, \\ \epsilon_{\perp} & 0 < z < L, \\ \epsilon_S & L < z. \end{cases}$$

Within the slab, the resulting Coulomb potential of a point charge located at  $0 < z' < L$  is given by

$$V_{\mathbf{q}}(z, z') = \frac{2\pi}{\kappa q} \left( e^{-\sqrt{\frac{\epsilon_{\parallel}}{\epsilon_{\perp}}} q_{\parallel} |z-z'|} + c_1 e^{-\sqrt{\frac{\epsilon_{\parallel}}{\epsilon_{\perp}}} q_{\parallel} (z+z')} + c_2 e^{-\sqrt{\frac{\epsilon_{\parallel}}{\epsilon_{\perp}}} q_{\parallel} (2L-z-z')} + c_3 e^{-\sqrt{\frac{\epsilon_{\parallel}}{\epsilon_{\perp}}} q_{\parallel} (2L-z+z')} + c_3 e^{-\sqrt{\frac{\epsilon_{\parallel}}{\epsilon_{\perp}}} q_{\parallel} (2L+z-z')} \right) \quad (\text{A1})$$

with

$$\begin{aligned} \kappa &= \sqrt{\epsilon_{\parallel} \epsilon_{\perp}}, \\ c_1 &= \frac{(\kappa + \epsilon_S)(\kappa - 1)}{\mathcal{N}}, \\ c_2 &= \frac{(\kappa - \epsilon_S)(\kappa + 1)}{\mathcal{N}}, \\ c_3 &= \frac{(\kappa - \epsilon_S)(\kappa - 1)}{\mathcal{N}}, \\ \mathcal{N} &= (\kappa + \epsilon_S)(\kappa + 1) - (\kappa - \epsilon_S)(\kappa - 1) e^{-2\sqrt{\frac{\epsilon_{\parallel}}{\epsilon_{\perp}}} q_{\parallel} L}. \end{aligned}$$

In Eq. (A1), the first term describes the direct interaction between the two point charges, the second term interaction of the point charge at  $z$  with the image charge of  $z'$  from the vacuum/multilayer interface, the third term correspondingly from the multilayer/substrate interface and the last term the interaction between image charges from both interfaces. Interaction with higher order image charges are contained in the denominator  $\mathcal{N}$ .

Relevant for the intralayer exciton and band gap renormalization is the intralayer Coulomb potential  $V_{\mathbf{q}}(z_n, z_n)$  with  $z_n = (n - 1/2)D$ :

$$V_{\mathbf{q}}(z_n, z_n) = \frac{2\pi}{\kappa q} \left( 1 + c_1 e^{-\sqrt{\frac{\epsilon_{\parallel}}{\epsilon_{\perp}}} q_{\parallel} (2n-1)D} + c_2 e^{-\sqrt{\frac{\epsilon_{\parallel}}{\epsilon_{\perp}}} q_{\parallel} 2(N-n-1/2)D} + 2c_3 e^{-\sqrt{\frac{\epsilon_{\parallel}}{\epsilon_{\perp}}} q_{\parallel} 2L} \right).$$

For  $\sqrt{\frac{\epsilon_{\parallel}}{\epsilon_{\perp}}} q_{\parallel} L \ll 1$ , the intralayer Coulomb potential reduces to  $V = 4\pi/(\epsilon_S + 1)q_{\parallel}$ , i.e., to the vacuum 2D Coulomb interaction screened by substrate screening only, while if  $\sqrt{\frac{\epsilon_{\parallel}}{\epsilon_{\perp}}} q_{\parallel} L \gg$

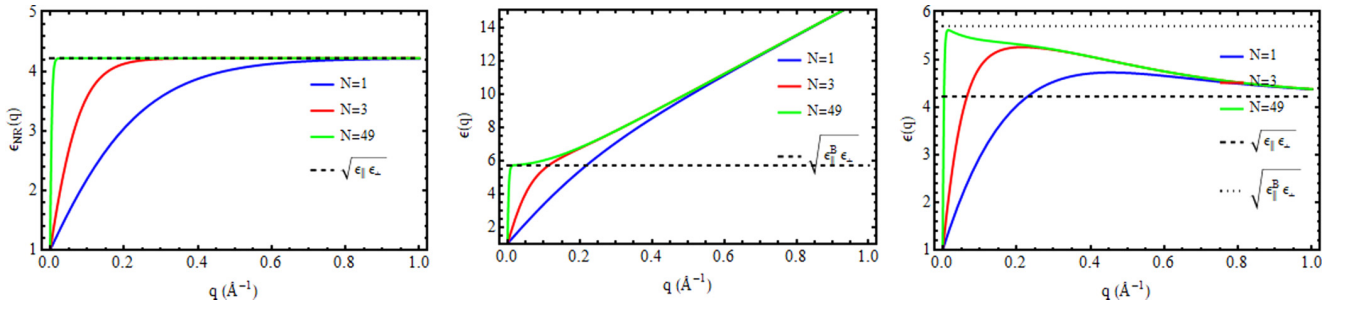


FIG. 14. (Left) Nonresonant contributions to the dielectric function for the middle layer of a suspended MoS<sub>2</sub> sample consisting of  $N$  layers. (Middle) Total effective dielectric function for middle layer of a suspended MoS<sub>2</sub> sample with  $N$  layers within the strict 2D limit. (Right) Total effective dielectric function for middle layer of a suspended MoS<sub>2</sub> sample with  $N$  layers including finite size effects with an effective layer thickness  $d = 4.3$  Å.

1, it reduces to

$$\frac{2\pi}{\kappa q_{\parallel}} \left( 1 + \frac{\kappa - 1}{\kappa + 1} e^{-\sqrt{\frac{\epsilon_{\parallel}}{\epsilon_{\perp}}} q_{\parallel} 2(n-1/2)D} + \frac{\kappa - \epsilon_S}{\kappa + \epsilon_S} e^{-\sqrt{\frac{\epsilon_{\parallel}}{\epsilon_{\perp}}} q_{\parallel} 2(N-n-1/2)D} \right).$$

In the left part of Fig. 14, we show the nonresonant contribution to local dielectric functions for the middle layer of a suspended MoS<sub>2</sub> sample consisting of 1, 3, and 49 layers. At small wave numbers, the dielectric function of the middle layer can be approximated by a first order Taylor expansion, giving

$$\epsilon(q) \approx \frac{\epsilon_S + 1}{2} + N \frac{2\epsilon_{\parallel}\epsilon_{\perp} - \epsilon_S^2 - 1}{4\epsilon_{\perp}} qD.$$

The linear approximations corresponds to a Keldysh potential [28,29,31] with background screening  $(\epsilon_S + 1)/2$  and screening length  $r = N \frac{2\epsilon_{\parallel}\epsilon_{\perp} - \epsilon_S^2 - 1}{2\epsilon_{\perp}(\epsilon_S + 1)} D$ . However, the linear approximation breaks down if  $qND > 1$ , where the dielectric function approaches its bulk value. Estimating the relevant  $q$  values by the inverse exciton radius  $r_X$  (note: the exciton radius should not be interchanged with the exciton Bohr radius; only for hydrogenlike excitons these values coincide), this means that the total sample dimensions should not exceed the in-plane exciton radius. While this condition may hold for a monolayer, it is clearly invalid for a multilayer structure with large layer numbers. As can be recognized in Fig. 14, in a sample with 49 layers the nonresonant dielectric function jumps to its bulk background value at infinitesimal  $q$  values.

## 2. Screening

Within linear response theory, the polarization in an inhomogeneous medium induced by an external perturbation field  $\phi$  can be expressed in terms of a nonlocal susceptibility

$$\mathbf{P}_L(\mathbf{q}, z, \omega) = -ie^2 \mathbf{q} \int dz' \chi_L(\mathbf{q}, z, z', \omega) \phi(\mathbf{q}, z', \omega),$$

where the  $z$  dependence of the susceptibility reflects the spatial profile of the induced carrier density. For the multilayer system, we assume charge distributions well localized within the layers, such that the integration region can be restricted to

a region of thickness  $D$  around the layer centers:

$$\mathbf{P}_L(\mathbf{q}, z, \omega) = -ie^2 \mathbf{q} \sum_{n=1}^N \rho_{\mathbf{q}}(z - z_n) \chi_L(\mathbf{q}, \omega) \bar{\phi}^n(\mathbf{q}, \omega),$$

where

$$\bar{\phi}^n(\mathbf{q}, \omega) = \int_{-D/2}^{D/2} dz' \rho_{-\mathbf{q}}(z' - z_n) \phi(\mathbf{q}, z', \omega).$$

In the strict 2D limit, this corresponds to ansatz (9) of the main text. The formal solution of Eq. (8) with charge distribution  $\rho_{\text{ext}}(\mathbf{q}, z)$  is then given by

$$\begin{aligned} \phi(\mathbf{q}, z, \omega) &= \phi_{\text{ext}}(\mathbf{q}, z, \omega) - e^2 q^2 \sum_n \chi_L(\mathbf{q}, \omega) \\ &\times \int dz' V_{\mathbf{q}}(z, z') \rho_{\mathbf{q}}(z' - z_n) \bar{\phi}^n(\mathbf{q}, \omega) \\ &\approx \phi_{\text{ext}}(\mathbf{q}, z, \omega) - e^2 q^2 \sum_n \chi_L(\mathbf{q}, \omega) \\ &\times \int_{-D/2}^{D/2} dz' V_{\mathbf{q}}(z, z') \rho_{\mathbf{q}}(z' - z_n) \bar{\phi}^n(\mathbf{q}, \omega), \quad (\text{A2}) \end{aligned}$$

where  $V_{\mathbf{q}}(z, z')$  is the Coulomb interaction screened by the anisotropic background given in Eq. (A1) and

$$\phi_{\text{ext}}(\mathbf{q}, z, \omega) = \int dz' V_{\mathbf{q}}(z, z') \rho_{\text{ext}}(\mathbf{q}, z')$$

is the potential of the external charge distribution. Multiplication of Eq. (A2) with  $\rho_{-\mathbf{q}}(z - z_m)$  and integration over  $z$  gives

$$\bar{\phi}^m(\mathbf{q}, \omega) = \bar{\phi}_{\text{ext}}^m(\mathbf{q}, \omega) - e^2 q^2 \sum_n \chi_L(\mathbf{q}, \omega) \bar{V}_{\mathbf{q}}^{mn} \bar{\phi}^n(\mathbf{q}, \omega) \quad (\text{A3})$$

with the quasi-2D bare Coulomb potential

$$\bar{V}_{\mathbf{q}}^{mn} = \int_{-D/2}^{D/2} dz \int_{-D/2}^{D/2} dz' \rho_{-\mathbf{q}}(z - z_m) V_{\mathbf{q}}(z, z') \rho_{\mathbf{q}}(z' - z_n).$$

The solution of Eq. (A2) can be obtained by a matrix inversion,

$$\bar{\phi}^m(\mathbf{q}, \omega) = \sum_l (\delta_{ml} + e^2 q^2 \chi_L(\mathbf{q}, \omega) \bar{V}_{\mathbf{q}}^{ml})^{-1} \bar{\phi}_{\text{ext}}^l(\mathbf{q}, \omega), \quad (\text{A4})$$

and the screened Coulomb interaction given in Eq. (10) in the main text is obtained by choosing  $\rho_{\text{ext}}(\mathbf{q}, z) = \delta(z - z_n)$ .

TABLE I. Material parameters for MoS<sub>2</sub>, WS<sub>2</sub>, MoSe<sub>2</sub>, and WSe<sub>2</sub> based on DFT calculations [19,24].

Material	$s \cdot \tau$	$\Delta_{s\tau}$ (eV)	$\lambda_C$ (Å)	$\alpha^{[0]}$	$a_0$ (Å)	$r_0$ (Å)	$\epsilon_{\parallel}^B$	$\epsilon_{\perp}$	$D$ (Å)	$\epsilon_{\parallel}$
MoS <sub>2</sub>	+	1,585	4,432	4.11	1.078	11.62	8.29	3.92	6.2	4.54
	−	1,735	4,049		0.985					
WS <sub>2</sub>	+	1,575	5,562	3.29	1.691	10.89	7.95	5.14	6.2	4.83
	−	2,005	4,369		1.328					
MoSe <sub>2</sub>	+	1,380	4,513	4.63	0.975	13.12	9.05	6.07	6.5	5.01
	−	1,560	3,993		0.862					
WSe <sub>2</sub>	+	1,370	5,750	3.66	1.571	12.27	7.25	5.16	6.5	3.36
	−	1,830	4,305		1.176					

For a monolayer in the strict 2D limit, the solution simplifies to

$$\phi^{2D}(\mathbf{q}) = \frac{\phi_{\text{ext}}(\mathbf{q}, z = D/2)}{1 + e^2 q^2 \chi_L(\mathbf{q}, \omega) V_{\mathbf{q}}(D/2, D/2)}, \quad (\text{A5})$$

where  $\phi^{2D}$  is the screened external potential. This result generally depends on the slab thickness  $D$  and becomes independent of  $D$  only in the two limiting cases  $D \rightarrow 0$  and  $D \rightarrow \infty$ . The limit  $D \rightarrow 0$  corresponds to a monolayer on a substrate, whereas the limit  $D \rightarrow \infty$  corresponds to a monolayer embedded in a homogeneous anisotropic medium. Defining  $\epsilon_{\text{eff}}$  by  $\epsilon_{\text{eff}} = (\epsilon_S + 1)/2$  and  $\epsilon_{\text{eff}} = \sqrt{\epsilon_{\perp} \epsilon_{\parallel}}$ , respectively, the localized 2D polarization contributes to the longitudinal dielectric function according to  $\epsilon_{\text{RES}} = 1 + 2\pi e^2 q_{\parallel} \chi_L(\mathbf{q}, \omega) / \epsilon_{\text{eff}}$ . If the 2D susceptibility is independent of  $\mathbf{q}$  and  $\omega$ , this part again corresponds to the Keldysh potential, with a resonant contribution to the antiscreening length  $r_0 = 2\pi e^2 \chi_L / \epsilon_{\text{eff}}$ .

In the middle part of Fig. 14, we show the resulting total effective dielectric function of the middle layer of a suspended multilayer sample, where we treat the resonant contributions to the dielectric function in the long-wavelength limit. As can be recognized, if  $N$  is increased, the long-wavelength limit of the total dielectric function  $\epsilon(q = 0)$  approaches the bulk value  $\sqrt{\epsilon_{\parallel}^B \epsilon_{\perp}}$ , with an in-plane component corresponding to the (fully screened) DFT bulk value, whereas the monolayer dielectric function in the small  $q$  regime can again be approximated by a Keldysh potential with a total linear coefficient  $r_{\text{tot}} = r + 2r_0 / (\epsilon_S + 1)$ . However, whereas the non-resonant contribution does not exceed the bulk background value  $\sqrt{\epsilon_{\parallel} \epsilon_{\perp}}$ , the total dielectric function increases linearly, exceeding the DFT fully screened bulk value by far. This unphysical result follows from the strict 2D treatment of the carriers, and the invalidity of the long-wavelength limit for the polarization function in this regime. In the right part of Fig. 14, we show the total effective dielectric function including finite thickness effects by the Ohno potential. As can be recognized, the effective dielectric function for the middle layer increases linearly for small  $q$  values starting at  $\epsilon(q = 0) = 1$ . However, due to finite thickness effects, the dielectric function does not exceed the fully screened bulk limit  $\sqrt{\epsilon_{\parallel}^B \epsilon_{\perp}}$ , but reaches a

maximum value between the bulk background value  $\sqrt{\epsilon_{\parallel} \epsilon_{\perp}}$  and the fully screened DFT bulk limit  $\sqrt{\epsilon_{\parallel}^B \epsilon_{\perp}}$ . The  $q$  value at which the maximum is achieved decreases with increasing number of layers, nicely reproducing the bulk long-wavelength limit for large layer numbers.

Finally, we compare the effective dielectric function for the monolayer with two recent publications where the effective 2D dielectric function for a monolayer TMDC has been extracted from a first-principles supercell calculation, once using a dielectric model similar to ours [33,52], that accounts for finite thickness effects, and once using a truncated Coulomb potential [34]. Both approaches find a dielectric function starting at  $\epsilon(q = 0) = 1$ , and a maximum value in the region  $q \approx 0.3 \text{ \AA}^{-1}$ . At large  $q$  values, the dielectric function decreases to  $\epsilon(q \rightarrow \infty) = 1$  again, reflecting the lack of dielectric screening at small distances. Apparently, our model overestimates the effect of screening in the large  $q \gg 1/d$  limit. This is a consequence of using a *constant* background dielectric constant, which is inappropriate for large  $q$  values. Indeed, choosing a background dielectric constant  $\epsilon_{\parallel} = \epsilon_{\perp} = 1$  in our model and lumping the background contributions into a linear coefficient  $r_{\text{tot}} = r + r_0$  instead, the monolayer dielectric function is in good agreement with both Refs. [33,34,52]. On the other hand, our model system is in good agreement with the findings in Refs. [33,34,52,53] in the region  $q \lesssim 1/d$ , relevant for excitons in the Wannier limit, and produces the correct bulk limit if the number of layers is increased. In contrast, lumping the background contributions into the linear increase in the small  $q$  region produces a wrong bulk limit  $\kappa^L(q \rightarrow 0) = \sqrt{1 + 2r/L}$ , which can be applied to bulk ( $L = D$ ) as well as to a supercell calculation with supercell period  $L$ .

## APPENDIX B: MATERIAL PARAMETERS

In Table I, we summarize the relevant parameters used in our numerical calculations. For the monolayer properties, we adopt the values given in Ref. [19] (parameters for the MDF Hamiltonian) and for the dielectric properties, we use the parameters from Ref. [24], respectively.

[1] A. R. Beal, J. C. Knights, and W. Y. Liang, *J. Phys. C* **5**, 3540 (1972).

[2] J. Bordas and E. A. Davis, *Phys. Status Solidi B* **60**, 505 (1973).

[3] R. A. Neville and B. L. Evans, *Phys. Status Solidi B* **73**, 597 (1976).

[4] E. Fortin and F. Raga, *Phys. Rev. B* **11**, 905 (1975).

- [5] A. Anedda, E. Fortin, and F. Raga, *Can. J. Phys.* **57**, 368 (1979).
- [6] A. Anedda and E. Fortin, *J. Phys. Chem. Solids* **41**, 865 (1980).
- [7] A. Kuc, N. Zibouche, and T. Heine, *Phys. Rev. B* **83**, 245213 (2011).
- [8] W. S. Yun, S. W. Han, S. C. Hong, I. G. Kim, and J. D. Lee, *Phys. Rev. B* **85**, 033305 (2012).
- [9] T. Cheiwchanchamnangij and W. R. L. Lambrecht, *Phys. Rev. B* **85**, 205302 (2012).
- [10] E. Cappelluti, R. Roldán, J. A. Silva-Guillén, P. Ordejón, and F. Guinea, *Phys. Rev. B* **88**, 075409 (2013).
- [11] K. F. Mak, C. Lee, J. Hone, J. Shan, and T. F. Heinz, *Phys. Rev. Lett.* **105**, 136805 (2010).
- [12] H. Zeng, G.-B. Liu, J. Dai, Y. Yan, B. Zhu, R. He, L. Xie, S. Xu, X. Chen, W. Yao, and X. Cui, *Sci. Rep.* **3**, 1608 (2013).
- [13] A. Chernikov, T. C. Berkelbach, H. M. Hill, A. Rigosi, Y. Li, O. B. Aslan, D. R. Reichman, M. S. Hybertsen, and T. F. Heinz, *Phys. Rev. Lett.* **113**, 076802 (2014).
- [14] K. He, N. Kumar, L. Zhao, Z. Wang, K. F. Mak, H. Zhao, and J. Shan, *Phys. Rev. Lett.* **113**, 026803 (2014).
- [15] Z. Ye, T. Cao, O. K., H. Zhu, X. Yin, Y. Wang, S. G. Louie, and X. Zhang, *Nature (London)* **513**, 214 (2014).
- [16] X. C. Bairen Zhu and Xi Chen, *Sci. Rep.* **5**, 9218 (2015).
- [17] K. S. Novoselov, A. Mishchenko, A. Carvalho, and A. H. Castro Neto, *Science* **353**, aac9439 (2016).
- [18] R. Dong and I. Kuljanishvili, *J. Vac. Sci. Technol. B* **35**, 030803 (2017).
- [19] D. Xiao, G.-B. Liu, W. Feng, X. Xu, and W. Yao, *Phys. Rev. Lett.* **108**, 196802 (2012).
- [20] T. Stroucken and S. W. Koch, in *Optical Properties of Graphene*, edited by R. Binder (World Scientific, Singapore, 2017), Chap. 2, pp. 43–84.
- [21] M. Ye, D. Winslow, D. Zhang, R. Pandey, and Y. K. Yap, *Photonics* **2**, 288 (2015).
- [22] L. F. Mattheiss, *Phys. Rev. B* **8**, 3719 (1973).
- [23] A. S. Rodin and A. H. Castro Neto, *Phys. Rev. B* **88**, 195437 (2013).
- [24] R. K. Ghosh and S. Mahapatra, *IEEE J. Electron Devices Soc.* **1**, 175 (2013).
- [25] H. Haug and S. W. Koch, *Quantum Theory of the Optical and Electronic Properties of Semiconductors*, 5th ed. (World Scientific, Singapore, 2009).
- [26] T. Stroucken, J. H. Grönqvist, and S. W. Koch, *Phys. Rev. B* **84**, 205445 (2011).
- [27] T. Stroucken and S. W. Koch, *J. Phys.: Condens. Matter* **27**, 345003 (2015).
- [28] L. V. Keldysh, *JETP Lett.* **29**, 658 (1978); N. S. Rytova, *Proc. MSU, Phys.*, *Astron.* **3**, 30 (1967).
- [29] P. Cudazzo, I. V. Tokatly, and A. Rubio, *Phys. Rev. B* **84**, 085406 (2011).
- [30] O. Pulci, P. Gori, M. Marsili, V. Garbuio, R. D. Sole, and F. Bechstedt, *Europhys. Lett.* **98**, 37004 (2012).
- [31] T. C. Berkelbach, M. S. Hybertsen, and D. R. Reichman, *Phys. Rev. B* **88**, 045318 (2013).
- [32] F. Wu, F. Qu, and A. H. MacDonald, *Phys. Rev. B* **91**, 075310 (2015).
- [33] S. Latini, T. Olsen, and K. S. Thygesen, *Phys. Rev. B* **92**, 245123 (2015).
- [34] D. Y. Qiu, F. H. da Jornada, and S. G. Louie, *Phys. Rev. B* **93**, 235435 (2016).
- [35] H. P. Komsa and A. V. Krasheninnikov, *Phys. Rev. B* **86**, 241201 (2012).
- [36] H. Shi, H. Pan, Y. W. Zhang, and B. I. Yakobson, *Phys. Rev. B* **87**, 155304 (2013).
- [37] F. A. Rasmussen and K. S. Thygesen, *J. Phys. Chem. C* **119**, 13169 (2015).
- [38] J. Zhou, W.-Y. Shan, W. Yao, and D. Xiao, *Phys. Rev. Lett.* **115**, 166803 (2015).
- [39] M. M. Ugeda, A. J. Bradley, S.-F. Shi, F. H. da Jornada, Y. Zhang, D. Y. Qiu, W. Ruan, S.-K. Mo, Z. Hussain, Z.-X. Shen, F. Wang, S. G. Louie, and M. F. Crommie, *Nat. Mater.* **13**, 1091 (2014).
- [40] G. Wang, X. Marie, I. Gerber, T. Amand, D. Lagarde, L. Bouet, M. Vidal, A. Balocchi, and B. Urbaszek, *Phys. Rev. Lett.* **114**, 097403 (2015).
- [41] G. Kioseoglou, A. T. Hanbicki, M. Currie, A. L. Friedman, D. Gunlycke, and B. T. Jonker, *Appl. Phys. Lett.* **101**, 221907 (2012).
- [42] K. F. Mak, K. He, C. Lee, G. H. Lee, J. Hone, T. F. Heinz, and J. Shan, *Nat. Mater.* **12**, 207 (2013).
- [43] A. A. Mitioglu, K. Galkowski, A. Surrente, L. Klopotoski, D. Dumcenco, A. Kis, D. K. Maude, and P. Plochocka, *Phys. Rev. B* **93**, 165412 (2016).
- [44] F. Cadiz, C. Robert, G. Wang, W. Kong, X. Fan, M. Blei, D. Lagarde, M. Gay, M. Manca, T. Taniguchi, K. Watanabe, T. Amand, X. Marie, P. Renucci, S. Tongay, and B. Urbaszek, *2D Mater.* **3**, 045008 (2016).
- [45] A. R. Klots, A. K. M. Newaz, B. Wang, D. Prasai, H. Krzyzanowska, J. Lin, D. Caudel, N. J. Ghimire, J. Yan, B. L. Ivanov, K. A. Velizhanin, A. Burger, D. G. Mandrus, N. H. Tolk, S. T. Pantelides, and K. I. Bolotin, *Sci. Rep.* **4**, 6608 (2014).
- [46] C. Robert, M. Semina, F. C. M. Manca, E. Courtade, T. Taniguchi, K. Watanabe, H. Cai, S. Tongay, B. Lassagne, P. Renucci, T. Amand, X. Marie, M. Glazov, and B. Urbaszek, [arXiv:1712.01548](https://arxiv.org/abs/1712.01548).
- [47] J. S. Ross, S. Wu, H. Yu, N. J. Ghimire, A. M. Jones, G. Aivazian, J. Yan, D. G. Mandrus, D. Xiao, W. Yao, and X. Xu, *Nat. Commun.* **4**, 1474 (2013).
- [48] J. Horng, T. Stroucken, L. Zhang, E. Y. Paik, H. Deng, and S. W. Koch, [arXiv:1712.04485](https://arxiv.org/abs/1712.04485).
- [49] M. M. Glazov, L. E. Golub, G. Wang, X. Marie, T. Amand, and B. Urbaszek, *Phys. Rev. B* **95**, 035311 (2017).
- [50] N. Saigal, V. Sugunakar, and S. Ghosh, *Appl. Phys. Lett.* **108**, 132105 (2016).
- [51] A. Arora, M. Drüppel, R. Schmidt, T. Deilmann, R. Schneider, M. R. Molas, P. Marauhn, S. Michaelis de Vasconcellos, M. Potemski, M. Rohlfing, and R. Bratschitsch, *Nat. Commun.* **8**, 639 (2017).
- [52] K. Andersen, S. Latini, and K. S. Thygesen, *Nano Lett.* **15**, 4616 (2015).
- [53] M. Van der Donck, M. Zarenia, and F. M. Peeters, *Phys. Rev. B* **96**, 035131 (2017).



# Paper II

**L. Meckbach**, T. Stroucken, and S. W. Koch

“Giant excitation induced bandgap renormalization in TMDC monolayers”  
Appl. Phys. Lett. **112**, 061104 (2018) DOI: 10.1063/1.5017069



## Giant excitation induced bandgap renormalization in TMDC monolayers

L. Meckbach, T. Stroucken, and S. W. Koch

Citation: *Appl. Phys. Lett.* **112**, 061104 (2018); doi: 10.1063/1.5017069

View online: <https://doi.org/10.1063/1.5017069>

View Table of Contents: <http://aip.scitation.org/toc/apl/112/6>

Published by the [American Institute of Physics](#)

---

### Articles you may be interested in

[The interplay between excitons and trions in a monolayer of MoSe<sub>2</sub>](#)

*Applied Physics Letters* **112**, 031107 (2018); 10.1063/1.5019177

[Broadband nonlinear optical response of monolayer MoSe<sub>2</sub> under ultrafast excitation](#)

*Applied Physics Letters* **112**, 031108 (2018); 10.1063/1.5010060

[Design of photonic crystal surface emitting lasers with indium-tin-oxide top claddings](#)

*Applied Physics Letters* **112**, 061105 (2018); 10.1063/1.5016442

[Strongly bound excitons in monolayer PtS<sub>2</sub> and PtSe<sub>2</sub>](#)

*Applied Physics Letters* **112**, 043101 (2018); 10.1063/1.5010881

[Band edge states, intrinsic defects, and dopants in monolayer HfS<sub>2</sub> and SnS<sub>2</sub>](#)

*Applied Physics Letters* **112**, 062105 (2018); 10.1063/1.5008959

[Exciton diffusion in WSe<sub>2</sub> monolayers embedded in a van der Waals heterostructure](#)

*Applied Physics Letters* **112**, 152106 (2018); 10.1063/1.5026478

---



**Sensors, Controllers, Monitors**

from the world leader in cryogenic thermometry



## Giant excitation induced bandgap renormalization in TMDC monolayers

L. Meckbach, T. Stroucken,<sup>a)</sup> and S. W. Koch

Department of Physics and Material Sciences Center, Philipps University Marburg, Renthof 5,  
D-35032 Marburg, Germany

(Received 24 November 2017; accepted 24 January 2018; published online 6 February 2018)

Optical absorption and gain spectra in MoS<sub>2</sub> monolayers with thermal carrier distributions are calculated from the combined gap and Dirac-Bloch equations. It is shown that the excited carriers lead to a bandgap renormalization as large as 800 meV for a suspended monolayer MoS<sub>2</sub>. Above the critical density, optical gain is obtained over an approx. 400 meV broad spectral range above the gap. Whereas the absorption spectra in the low density regime are very sensitive to the dielectric environment, the spectra become purely intrinsic at elevated carrier densities. *Published by AIP Publishing.* <https://doi.org/10.1063/1.5017069>

Transition metal dichalcogenide (TMDC) monolayers have attracted great attention, not least because of potential applications in electronic and optical devices. Unlike their bulk counterparts, monolayers of semiconducting TMDCs display a direct gap in the visible range,<sup>1–6</sup> exhibiting a pronounced light matter coupling and strong excitonic effects.<sup>7–10</sup> Excitonic resonances absorbing as much as 10% of the incoming light have been observed at room temperature and dominate the emission properties of TMDC monolayers at low excitation levels. Because of this strong light matter coupling, TMDCs have been proposed as promising candidates for the thinnest possible gain materials, especially attractive for nanolasers.

One of the key properties for operation and design of nano-electronic devices is the fundamental bandgap or optical gap. Due to Coulombic renormalizations, the gap depends on the excitation conditions.<sup>11</sup> In a conventional semiconductor where screening is strong, these Coulomb renormalizations of the bandgap are typically in the meV range and purely intrinsic. In contrast, in TMDCs where screening of the Coulomb interaction is weak and strongly influenced by the immediate dielectric surrounding, both the bandgap renormalization and exciton binding are comparatively large and depend sensitive on the dielectric environment. Indeed, a renormalization of the quasi-particle gap as large as 500 meV after excitation with an intense pump pulse has been reported for WS<sub>2</sub> bilayers on a quartz substrate.<sup>12</sup>

In this letter, we present a theoretical analysis of the influence of excited carriers on the bandgap renormalization and optical response of TMDC monolayers. To this end, we extend our recently developed scheme<sup>13</sup> that combines a dielectric model for the Coulomb interaction potential, gap equations for the renormalized ground state, and the Dirac-Bloch equations (DBE)<sup>13,14</sup> to determine the optical response and include initially present carrier densities, as can result, e.g., from doping or excitation with a prepulse and subsequent thermalization. This approach is based on an effective four-band Hamiltonian that models the electronic and optical properties in the vicinity of the fundamental gap at the

K-points of the Brillouin zone. Similar to the *GW*-Bethe Salpeter equation (*GW*-BSE) approach, the gap equations provide corrections to the non-interacting band structure as obtained by density functional theory (DFT), and a subsequent solution of the DBE gives access to the dynamical optical response, including excitonic features. Regarding the ground-state optical properties, this approach has proven to accurately reproduce both experimental<sup>7,8,15,16</sup> and well converged *ab initio* *GW*-BSE<sup>17–20</sup> results.

In the presence of initial carrier distributions, the gap equations determining the interacting quasi-particle dispersion for each spin and valley index combination  $s, \tau$  are given by

$$\tilde{\Delta}_{s\tau\mathbf{k}} = \Delta_{s\tau} + \frac{1}{2} \sum_{\mathbf{k}'} V_{|\mathbf{k}-\mathbf{k}'|}^S \frac{\tilde{\Delta}_{s\tau\mathbf{k}'}}{\varepsilon_{s\tau\mathbf{k}'}} (1 - f_{s\tau\mathbf{k}'}^e - f_{s\tau\mathbf{k}'}^h), \quad (1)$$

$$\tilde{v}_{s\tau\mathbf{k}} = v_F + \frac{1}{2} \sum_{\mathbf{k}'} V_{|\mathbf{k}-\mathbf{k}'|}^S \frac{k'}{k} \frac{\tilde{v}_{s\tau\mathbf{k}'}}{\varepsilon_{s\tau\mathbf{k}'}} e^{i\tau(\theta_{\mathbf{k}} - \theta_{\mathbf{k}'})} (1 - f_{s\tau\mathbf{k}'}^e - f_{s\tau\mathbf{k}'}^h), \quad (2)$$

from which the quasi-particle dispersion is obtained via  $\varepsilon_{s\tau\mathbf{k}}^{e/h} = \pm \frac{1}{2} \sqrt{\tilde{\Delta}_{s\tau\mathbf{k}}^2 + (2\hbar\tilde{v}_{s\tau\mathbf{k}}k)^2}$ . The non-interacting gap  $\Delta_{s\tau}$  and Fermi-velocity  $v_F$  are obtained by fitting the non-interacting dispersion to the upper spin-split valence bands and lowest conduction bands of the DFT band structure.<sup>21</sup> The gap equations contain the screened Coulomb interaction  $V_{\mathbf{q}}^S(\omega) = V_0(\mathbf{q})/\epsilon(\mathbf{q}, \omega)$  with a screened Coulomb potential

$$V_{\mathbf{q}}^S(\omega) = \epsilon(\omega, \mathbf{q})^{-1} V_0(\mathbf{q}) = [1 - V_0(\mathbf{q})\Pi(\omega, \mathbf{q})]^{-1} V_0(\mathbf{q})$$

$$\Pi(\omega, \mathbf{q}) = \Pi_0(\omega, \mathbf{q}) + \sum_{\alpha\alpha', \mathbf{k}} |W_{\alpha\alpha'}(\mathbf{k}, \mathbf{q})|^2$$

$$\times \frac{f_{\alpha, \mathbf{k}-\mathbf{q}} - f_{\alpha', \mathbf{k}}}{\hbar(\omega + i\delta) - (\varepsilon_{\alpha', \mathbf{k}} - \varepsilon_{\alpha, \mathbf{k}-\mathbf{q}})},$$

where  $\alpha$  combines the spin, valley, and band index,  $\Pi_0(\omega, \mathbf{q})$  is the ground state polarization function, and  $W_{\alpha\alpha'}(\mathbf{k}, \mathbf{q})$  is the overlap matrix element between the renormalized bands. The “bare” Coulomb interaction potential  $V_0(\mathbf{q})$  contains screening of the dielectric environment and the background screening of the TMDC monolayer resulting from remote

<sup>a)</sup> Author to whom correspondence should be addressed: tineke.stroucken@physik.uni-marburg.de

bands and is obtained as a solution of Poisson's equation.<sup>13</sup> Furthermore, we include a form factor that accounts for the finite extension of the monolayer in the growth direction.<sup>13</sup> For vanishing carrier densities, the gap equations give the bandgap renormalization of the interacting ground state. Assuming the system to be in a thermal equilibrium state with given temperature and chemical potential, the gap equations and the screened Coulomb interaction are solved self-consistently with the initial electron and hole distributions  $f_{\alpha\mathbf{k}}(\mu_\alpha, T) = [1 + e^{\beta(\epsilon_{\alpha\mathbf{k}} - \mu_\alpha)}]^{-1}$ .

Once we have determined the bandgap renormalization, we compute the optical response from the DBE. Assuming excitation with a weak optical field, the carrier distributions are unaffected by the optical probe-field and we can solve the linearized equation of motion for the induced interband polarization

$$i\hbar \frac{d}{dt} P_{s\tau\mathbf{k}} = 2\epsilon_{s\tau\mathbf{k}} P_{s\tau\mathbf{k}} - (1 - f_{s\tau\mathbf{k}}^e - f_{s\tau\mathbf{k}}^h) \Omega_{s\tau\mathbf{k}} - i\hbar \left. \frac{d}{dt} P_{s\tau\mathbf{k}} \right|_{\text{coll}}, \quad (3)$$

where

$$\Omega_{s\tau\mathbf{k}} = \sum_{\mathbf{k}'} V_{|\mathbf{k}-\mathbf{k}'|}^S [W_{cv\nu\nu}(\mathbf{k}, \mathbf{k}') P_{s\tau\mathbf{k}'} + W_{cv'c\nu}(\mathbf{k}, \mathbf{k}') P_{s\tau\mathbf{k}'}^* - 2W_{cv\nu\nu}(\mathbf{k}, \mathbf{k}') f_{s\tau\mathbf{k}'}] + \tau\sqrt{2} \frac{eV_F}{c} \left( v_k^2 e^{-2i\tau\theta_k} A^\tau - u_k^2 A^{-\tau} \right), \quad (4)$$

with  $u_{s\tau\mathbf{k}} = \sqrt{(\epsilon_{s\tau\mathbf{k}} + \tilde{\Delta}_{s\tau\mathbf{k}}/2)/2\epsilon_{s\tau\mathbf{k}}}$  and  $v_{s\tau\mathbf{k}} = \sqrt{(\epsilon_{s\tau\mathbf{k}} - \tilde{\Delta}_{s\tau\mathbf{k}}/2)/2\epsilon_{s\tau\mathbf{k}}}$  is the generalized Rabi frequency. From the interband polarization  $P_{s\tau\mathbf{k}}$ , we obtain the linear susceptibility via  $\chi^\tau(\omega) = \sqrt{2} eV_F \frac{c}{\omega^2} \frac{\delta}{\delta A^\tau} \sum_{s\tau\mathbf{k}} \tau' (u_{s\tau\mathbf{k}}^2 P_{s\tau\mathbf{k}} - v_{s\tau\mathbf{k}}^2 e^{2i\tau'\theta_k} P_{s\tau\mathbf{k}}^*)$  and the optical absorption/gain via  $\alpha(\omega) = -4\pi \frac{\omega}{c} \text{Im}[\chi(\omega)] / |(n_S + 1)/2 - 2\pi i \frac{\omega}{c} \chi(\omega)|^2$  where  $n_S$  is the refractive index of the substrate.

In the left part of Fig. 1, we show the resulting optical spectra obtained for MoS<sub>2</sub> at  $T=300$  K for several carrier densities  $n = \frac{1}{\mathcal{A}} \sum_{\alpha\mathbf{k}} f_{\alpha\mathbf{k}}(\mu_\alpha, T)$ , where we have chosen the chemical potentials such that we have equal electron and

hole carrier densities in the A- and B-bands. The spectra were obtained by solving Eq. (3) where the collision terms were treated by a phenomenological dephasing rate of  $\hbar\gamma = 10$  meV. The full lines show the spectra for a suspended monolayer and the dashed lines for a monolayer on a SiO<sub>2</sub> substrate, where we used a static dielectric constant  $\epsilon_S = 3.9$  and refractive index  $n_S = 1.46$  at the optical frequency, the overall absorption/gain on a SiO<sub>2</sub> substrate is reduced by a factor of approximately  $(n_S + 1)/2$ . As can be recognized, the bandgap and exciton binding for the monolayer on the substrate at low carrier densities is significantly below that of the suspended monolayer, whereas the influence of the substrate on the resonance positions diminishes at moderate till elevated carrier densities. The decreasing influence of the dielectric environment results from screening of the long range part of the Coulomb interaction by the carriers, the part that experiences screening by the surrounding. Increasing the carrier density leads to a bleaching of the exciton resonances and a simultaneous decrease of the bandgap. As a net result, the lowest exciton resonance displays a red shift of roughly 10 meV, until it vanishes completely at the Mott-density. Above the critical density where the absorption turns into gain, the spectra display a flat gain above the renormalized gap over a spectra range as large as 400 meV. In the right part of Fig. 1, we show the gain spectra for suspended MoS<sub>2</sub>, where we vary the B-band density for a fixed A-band density of  $n_A = 5.0 \times 10^{13} \text{ cm}^{-2}$  above the critical density. Whereas for equal A- and B-densities excitonic resonances are clearly observable for densities only slightly below the Mott-density, strong plasma screening of the A-populations leads to an ionization of the B e-h pairs, even for densities far below the critical density of the B-bands. In this density regime, we observe a free carrier absorption above the B-band edge and a simultaneous gain in the region between the A- and B-gaps. Increasing the B-band density beyond the critical density too, we obtain gain from both bands, resulting in the very broad spectral gain region of ca. 400 meV.

In the left panel of Fig. 2, we plot the bandgap and position of the lowest lying 1s excitons as a function of the total carrier density  $n = \frac{1}{\mathcal{A}} \sum_{\alpha\mathbf{k}} f_{\alpha\mathbf{k}}(\mu_\alpha, T)$  for  $T=300$  K for the

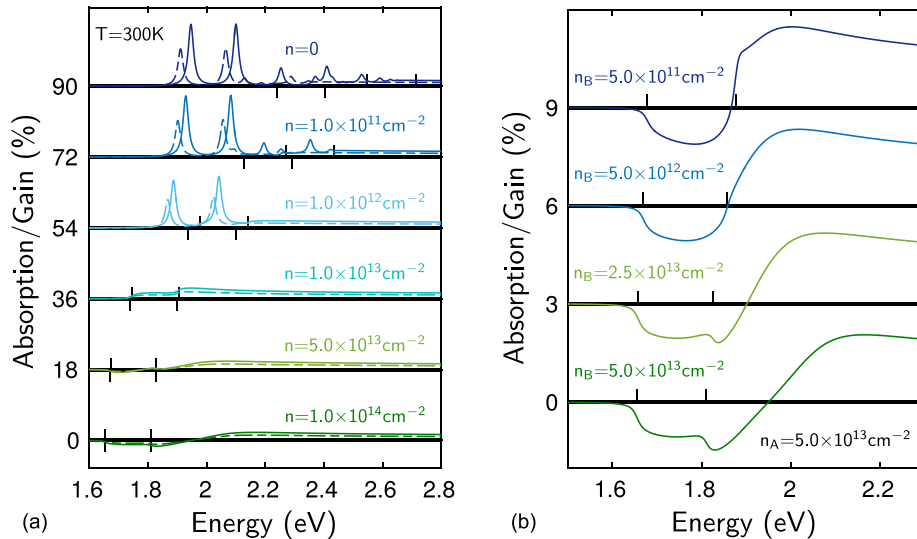


FIG. 1. Absorption/gain spectra for MoS<sub>2</sub> at  $T=300$  K for different carrier densities. Left: Equal electron and hole densities in the A- and B-bands. Right: Variation of the B-band density for a fixed A-band density of  $n_A = 5.0 \times 10^{13} \text{ cm}^{-2}$ . The full lines show the spectra for a suspended monolayer and the dashed lines for a monolayer on a SiO<sub>2</sub> substrate. The black lines indicate the position of the bandgap for the A- and B-excitons, respectively.

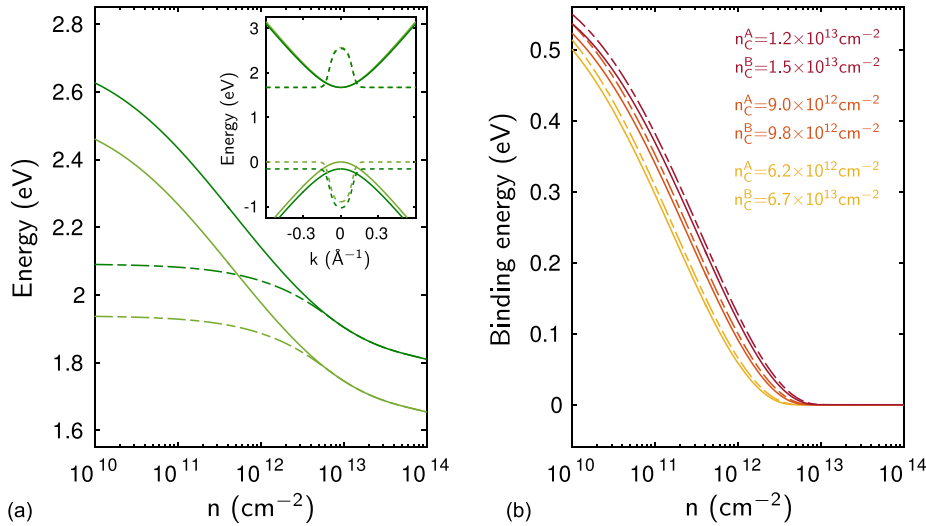


FIG. 2. Left: Renormalized bandgap (solid lines) and 1s exciton resonance energy (dashed lines) as a function of total carrier density for the A- (light green) and B (dark green) excitons of MoS<sub>2</sub> at  $T = 300$  K. The inset schematically shows the occupation of the A- and B-bands as a function of  $k$  for equal carrier densities in the A- and B-bands. Right: Exciton binding energy of the lowest A (solid lines) and B (dashed lines) exciton as a function of carrier density for  $T = 200, 300,$  and  $400$  K, respectively. The numbers refer to the critical density at which the lowest exciton merges with the continuum states.

example of the A-exciton of suspended MoS<sub>2</sub>. The inset schematically shows the occupation of the A- and B-bands as a function of  $k$  for equal carrier densities in the A- and B-bands. Taking the zero density bandgap as a reference, we observe a huge bandgap reduction with an increasing carrier density of almost 800 meV and a simultaneous shift of the 1s-exciton binding energy. There are two physically distinct mechanisms contributing to the bandgap reduction, namely, screening and phase space filling. By solving the gap equations with the screened Coulomb interaction but neglecting the terms proportional to the carrier distributions, we find that the dominant mechanism is the plasma screening, whereas in the density regime where phase space filling comes important, the screened Coulomb interaction is so weak that the renormalized gap approaches the non-interacting values of 1.585 eV and 1.735 eV for the A- and B-gaps, respectively. In the low density regime  $n \lesssim 10^{12} \text{ cm}^{-2}$ , we observe an almost cancellation in the band shrinkage and reduction of the exciton binding, leading to a small net-shift of the exciton resonance position. Similar behaviour occurs if screening by the dielectric environment is increased.

In the right panel of Fig. 2, we show the binding energy of the lowest A-exciton for  $T = 200, 300,$  and  $400$  K, respectively. As can be recognized, the critical density for ionization increases with increasing temperature. For the equal A and B-band carrier densities, similar results are obtained for the binding of the B-exciton with slightly larger critical densities. The larger critical density for the B-excitons can be explained by the smaller exciton radius of the B-type excitons. From the real space wave functions in the low density limit, we obtain an exciton Bohr radius  $a_B \equiv \langle 1s|r|1s \rangle$  of  $a_B^A = 9.257 \text{ \AA}$  and  $a_B^B = 8.896 \text{ \AA}$  for the A- and B-exciton, respectively, from which we obtain  $a_B n_c^{-1/2} = 0.23$  for both exciton species. These values are close to the Mott-criterion  $a_B n_c^{-1/2} \approx 0.25$ .

Figure 3 shows how the gain spectra at a fixed density of  $n = 5.0 \times 10^{13} \text{ cm}^{-2}$  vary with temperature. Although the gain is reduced by a factor of roughly 2 if the temperature is increased from 200 to 400 K, a significant gain is still observed at room temperature and beyond.

In conclusion, we find a bandgap renormalization as large as 800 meV for a suspended MoS<sub>2</sub> monolayer in the presence of excited carriers. These results are in good agreement with earlier theoretical findings based on the combined DBE and *GW*-approach.<sup>22</sup> For a monolayer on a typical substrate, the bandgap reduction is reduced to approx. 600 meV due to screening of the Coulomb interaction by the environment. Along with the bandgap shrinkage, the exciton binding is reduced. In the low density regime, the reduction in exciton binding and band-edge shrinkage almost cancel. Above the critical density, we predict a flat gain spectrum over a range as large as roughly 400 meV. In this regime, the effect of the substrate becomes negligible and the system becomes purely intrinsic. Similar results are expected for other TMDC materials. Our predictions are based on solutions of the gap equations and DBE for the optical excitations and in good agreement with recent experimental observations.<sup>12</sup>

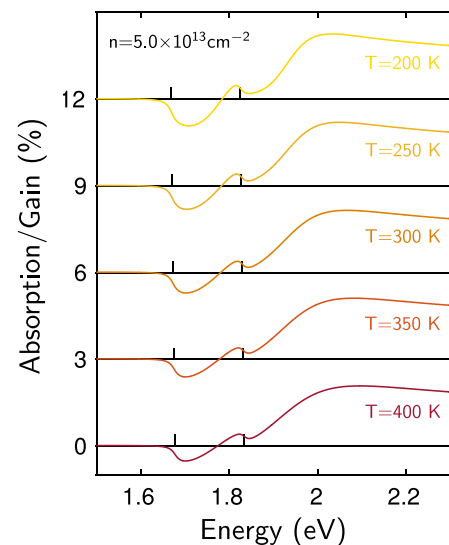


FIG. 3. Absorption/gain spectra for MoS<sub>2</sub> for a carrier density of  $n = 5.0 \times 10^{13} \text{ cm}^{-2}$  at different temperatures. Electron and hole densities in the A- and B-bands have been chosen to be equal.

This work is a project of the Collaborative Research Center SFB 1083 funded by the Deutsche Forschungsgemeinschaft.

- <sup>1</sup>A. Kuc, N. Zibouche, and T. Heine, *Phys. Rev. B* **83**, 245213 (2011).
- <sup>2</sup>W. S. Yun, S. W. Han, S. C. Hong, I. G. Kim, and J. D. Lee, *Phys. Rev. B* **85**, 033305 (2012).
- <sup>3</sup>T. Cheiwchanchamnangij and W. R. L. Lambrecht, *Phys. Rev. B* **85**, 205302 (2012).
- <sup>4</sup>E. Cappelluti, R. Roldán, J. A. Silva-Guillén, P. Ordejón, and F. Guinea, *Phys. Rev. B* **88**, 075409 (2013).
- <sup>5</sup>K. F. Mak, C. Lee, J. Hone, J. Shan, and T. F. Heinz, *Phys. Rev. Lett.* **105**, 136805 (2010).
- <sup>6</sup>H. Zeng, G.-B. Liu, J. Dai, Y. Yan, B. Zhu, R. He, L. Xie, S. Xu, X. Chen, W. Yao, and X. Cui, *Sci. Rep.* **3**, 1608 (2013).
- <sup>7</sup>A. Chernikov, T. C. Berkelbach, H. M. Hill, A. Rigosi, Y. Li, and O. B. Aslan, *Phys. Rev. Lett.* **113**, 076802 (2014).
- <sup>8</sup>K. He, N. Kumar, L. Zhao, Z. Wang, K. F. Mak, H. Zhao, and J. Shan, *Phys. Rev. Lett.* **113**, 026803 (2014).
- <sup>9</sup>Z. Ye, T. Cao, K. O'Brien, H. Zhu, X. Yin, Y. Wang, S. G. Louie, and X. Zhang, *Nature* **513**, 214 (2014).
- <sup>10</sup>B. Zhu, X. Chen, and X. Cui, *Sci. Rep.* **5**, 9218 (2015).
- <sup>11</sup>H. Haug and S. W. Koch, *Quantum Theory of the Optical and Electronic Properties of Semiconductors*, 5th ed. (World Scientific Publishing, Singapore, 2009).
- <sup>12</sup>A. Chernikov, C. Ruppert, H. M. Hill, A. F. Rigosi, and T. F. Heinz, *Nat. Photonics* **9**, 466–470 (2015).
- <sup>13</sup>L. Meckbach, T. Stroucken, and S. W. Koch, *Phys. Rev. B* **97**, 035425 (2018).
- <sup>14</sup>T. Stroucken and S. W. Koch, in *Optical Properties of Graphene*, edited by R. Binder (World Scientific Publishing, Singapore, 2017), Chap. 2, pp. 43–84.
- <sup>15</sup>M. M. Ugeda, A. J. Bradley, S.-F. Shi, F. H. da Jornada, Y. Zhang, D. Y. Qiu, W. Ruan, S.-K. Mo, Z. Hussain, Z.-X. Shen, F. Wang, S. G. Louie, and M. F. Crommie, *Nat. Mater.* **13**, 1091 (2014).
- <sup>16</sup>G. Wang, X. Marie, I. Gerber, T. Amand, D. Lagarde, L. Bouet, M. Vidal, A. Balocchi, and B. Urbaszek, *Phys. Rev. Lett.* **114**, 097403 (2015).
- <sup>17</sup>H. P. Komsa and A. V. Krasheninnikov, *Phys. Rev. B* **86**, 241201 (2012).
- <sup>18</sup>H. Shi, H. Pan, Y. W. Zhang, and B. I. Yakobson, *Phys. Rev. B* **87**, 155304 (2013).
- <sup>19</sup>F. A. Rasmussen and K. S. Thygesen, *J. Phys. Chem. C* **119**, 13169 (2015).
- <sup>20</sup>D. Y. Qiu, F. H. da Jornada, and S. G. Louie, *Phys. Rev. B* **93**, 235435 (2016).
- <sup>21</sup>D. Xiao, G.-B. Liu, W. Feng, X. Xu, and W. Yao, *Phys. Rev. Lett.* **108**, 196802 (2012).
- <sup>22</sup>A. Steinhoff, M. Rösner, F. Jahnke, T. O. Wehling, and C. Gies, *Nano Lett.* **14**, 3743 (2014).



# Paper III

**L. Meckbach**, U. Huttner, L. C. Bannow, T. Stroucken, and S. W. Koch

“Interlayer excitons in transition-metal dichalcogenide heterostructures  
with type-II band alignment”

J. Phys.: Condens. Matter **30**, 374002 (2018) **DOI:** 10.1088/1361-648X/aad984

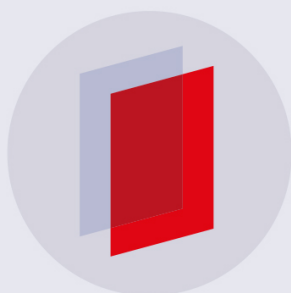


PAPER

## Interlayer excitons in transition-metal dichalcogenide heterostructures with type-II band alignment

To cite this article: L Meckbach *et al* 2018 *J. Phys.: Condens. Matter* **30** 374002

View the [article online](#) for updates and enhancements.



**IOP | ebooks**<sup>TM</sup>

Bringing you innovative digital publishing with leading voices to create your essential collection of books in STEM research.

Start exploring the collection - download the first chapter of every title for free.

# Interlayer excitons in transition-metal dichalcogenide heterostructures with type-II band alignment

L Meckbach<sup>✉</sup>, U Huttner, L C Bannow<sup>✉</sup>, T Stroucken<sup>✉</sup> and S W Koch

Department of Physics and Material Sciences Center, Philipps University Marburg, Renthof 5, D-35032 Marburg, Germany

E-mail: [tineke.stroucken@physik.uni-marburg.de](mailto:tineke.stroucken@physik.uni-marburg.de)

Received 2 May 2018, revised 6 August 2018

Accepted for publication 10 August 2018

Published 24 August 2018



## Abstract

Combining *ab initio* density functional theory with the Dirac–Bloch and gap equations, excitonic properties of transition-metal dichalcogenide hetero-bilayers with type-II band alignment are computed. The existence of interlayer excitons is predicted, whose binding energies are as large as 350 meV, only roughly 100 meV less than those of the coexisting intralayer excitons. The oscillator strength of the interlayer excitons reaches a few percent of the intralayer exciton resonances and their radiative lifetime is two orders of magnitude larger than that of the intralayer excitons.

Keywords: TMDCs, interlayer excitons, van-der-Waals heterostructures

(Some figures may appear in colour only in the online journal)

## 1. Introduction

Due to their reduced dimensionality, layered transition-metal dichalcogenide crystals (TMDCs) exhibit remarkable electronic and optical properties. Unlike their bulk counterparts, monolayers (MLs) of semiconducting TMDCs display a direct gap at the *K*-points of their respective Brillouin zone with a transition energy in the visible to near-infrared range of the electromagnetic spectrum [1–7]. The optical properties of TMDC MLs are dominated by strongly bound excitons that exist even at room temperature and absorb as much as 10% of the incoming light. Therefore, these MLs constitute a promising platform for fundamental material physics studies of two-dimensional (2D) systems as well as potential applications in opto-electronics and valleytronics [8–10].

Recently, TMDC-based heterostructures have attracted great interest [11, 12]. The availability of different materials with a similar lattice structure but different band gaps combined with recent advances in stacking technology allows for the engineering of the overall electronic and optical properties to a wide extent [13–18]. In particular, TMDC hetero-junctions with a type-II band alignment have been demonstrated

to host interlayer excitons where electrons and holes are confined in different layers [19–22].

Interlayer excitons are characterized by a long radiative lifetime, making them particularly interesting for the development of excitonic devices and the potential observation of exotic phenomena, such as spontaneous coherence and Bose–Einstein condensation. Due to their permanent out-of-plane dipole moment, they can be manipulated by an external gate voltage, thus creating the possibility to tune the exciton resonance and coupling strength within a given range [20, 23, 24]. Furthermore, a rapid charge transfer within 50 fs after optical excitation has been observed in type-II heterostructures [25, 26]. The coexistence of strongly absorbing intralayer and interlayer excitons with tunable radiative lifetime together with a rapid charge transfer not only enables optical pumping of the interlayer transition, but also holds potential for applications, e.g. in solar cells.

A systematic design and engineering of the electronic and excitonic properties of TMDC systems, including interlayer excitons, requires a predictive microscopic theory that systematically describes the fundamental structural properties as well as the strong Coulomb interaction effects among the

electronic excitations. In this paper, we theoretically investigate interlayer excitons in two different model systems with type-II band alignment, namely a  $\text{WSe}_2/\text{MoS}_2$  and a  $\text{WSe}_2/\text{MoSe}_2$  hetero-bilayer (H-BL). To this end, we combine our recently developed theoretical framework to compute the band gap renormalization and excitonic states [27] with *ab initio* density functional theory (DFT) band structure calculations. In a first step, we determine the *ab initio* band structure (including the band alignment), the optical dipole-transition elements and dielectric screening from DFT. The band parameters and dipole moments serve as input for an effective four-band Hamiltonian, for which we use the massive Dirac–Fermion (MDF) model. The screening parameters are used to determine the Coulomb interaction potential. From the MDF model Hamiltonian we derive the gap equations (GE) and the Dirac–Bloch equations (DBE). The solution of the GE yields the renormalized band gap and the DBE gives access to the excitonic states and their oscillator strengths.

The paper is organized as follows: in section 2, we present the details of the DFT calculations and the resulting DFT band structures. We analyze the contributions of the respective layers to the relevant bands, which allows us to identify the type-II band alignment and confirm previous findings [13, 16]. In section 3, we discuss the effective four-band model Hamiltonian and the resulting GE and DBE. In section 4, we show examples of our numerical results for the H-BL absorption spectra, exciton resonance energies, and lifetimes. Finally, in section 5, we discuss our results.

## 2. TMDC heterostructures

We investigate semiconducting TMDC H-BLs, which consist of two TMDC MLs stacked on top of each other [11]. In isolated TMDC MLs, optical transitions dominantly occur at the band gap minima in the vicinity of the  $K$ - and  $K'$ -points [1, 2]. If two TMDCs with different lattice constants are stacked on top of each other with an arbitrary twist angle between them, the individual  $K$ -points of each layer have a different crystal momentum [15, 21, 28]. Consequently, interlayer transitions between both materials have a non-vanishing momentum mismatch [28], making those transitions inefficient. In contrast, orientation matched H-BLs enable efficient radiative interlayer recombination [19].

Therefore, following [13, 14, 16], we investigate H-BLs where both layers are set to have the same in-plane lattice constant. We consider AA'-stacking, which is the stacking found in the bulk form of most TMDCs. A schematic of the H-BL geometry is shown in figure 1. In the AA'-stacking, the chalcogen atoms of one layer are on top of the transition-metal atom in the other layer and vice versa, with zero twist angle between the layers. The influence of a nonzero twist angle has been analyzed in [28], and observed experimentally in [20, 29].

In our investigation, we analyze a  $\text{WSe}_2/\text{MoS}_2$  H-BL and a  $\text{WSe}_2/\text{MoSe}_2$  H-BL as model systems. As  $\text{WSe}_2$  and  $\text{MoS}_2$  MLs have slightly different lattice constants of about 3.8% [30], the lattice constant changes to an equilibrium value when

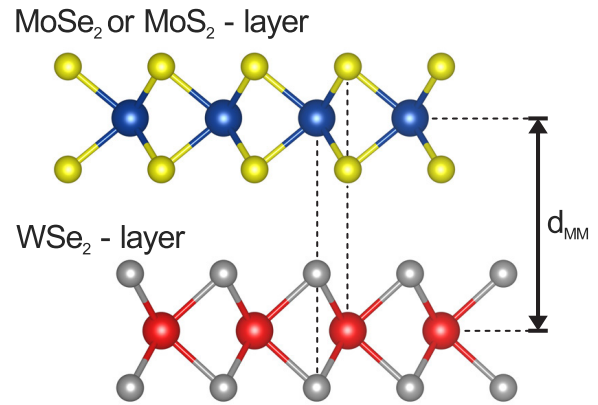


**Figure 1.** Crystal structure of the studied TMDC H-BLs: A  $\text{MoSe}_2$  or  $\text{MoS}_2$  ML is stacked on top of a  $\text{WSe}_2$  ML in AA'-stacking, where the chalcogen atoms sulfur (yellow) or selenium (grey) of the one layer are placed on top of a transition-metal atom tungsten (red) or molybdenum (blue) in the other layer. The interlayer spacing  $d_{\text{MM}}$  is determined by *ab initio* simulations.

the H-BL is formed. Therefore, the  $\text{WSe}_2/\text{MoS}_2$  H-BL is a strained system where both layers have a tensile / compressive strain of about 2% compared to the free standing ML [16]. The MLs of  $\text{WSe}_2$  and  $\text{MoSe}_2$  on the other hand have a very similar lattice constant. Therefore, the  $\text{WSe}_2/\text{MoSe}_2$  H-BL naturally has only minimal strain and is used as a prototypical system of a heterostructure, also in several experiments [19, 20, 22].

The influence of lateral strain on TMDCs usually results in a change of the band gap and has been studied in [31–33]. Unstrained TMDC H-BLs, on the other hand, where each layer retains its ML lattice constant are investigated in [15]. In this case, the incommensurate crystal lattices of both MLs form a Moire-Pattern where the stacking changes locally. Nevertheless, it is found that the overall valence band maximum is obtained from regions where approximately AA'-stacking is retained [18]. Consequently, using the lattice matched artificial structure is sufficient to obtain insights into interlayer excitons, while massively reducing the numerical effort.

### 2.1. Details of DFT computations

In order to study the excitonic properties of TMDC H-BLs, the electronic properties of the materials in the vicinity of the two nonequivalent  $K$ -points are required. Therefore, the band dispersion of the relevant bands closest to the band gap as well as the magnitude of the optical transition dipole-matrix elements between them are computed in an *ab initio* approach via DFT [34].

We use the DFT implementation Vienna *Ab initio* Simulation Package (VASP) [35–38]. VASP is a plane-wave code which utilizes the projector augmented-wave method [39, 40] such that only the relevant valence electrons are fully treated. The generalized-gradient approximation as parametrized in the Perdew–Burke–Ernzerhof (PBE) functional [41] is applied and spin-orbit interaction [42] is included. In general, the PBE functional captures the main features of

TMDC band structures very well [32]. The van-der-Waals interaction between individual MLs is incorporated by Grimme's dispersion correction method (PBE-D3) as implemented in VASP [43, 44].

Our computations use a  $15 \times 15 \times 3$ ,  $\Gamma$  centered Monkhorst–Pack [45]  $k$ -point mesh in  $x$ -,  $y$ -, and  $z$ -direction, respectively, to sample the complete Brillouin zone. The cutoff energy of the plane-wave expansion is set to 750 eV. For a H-BL structure in AA'-stacking, the unit cell contains six atoms. In order to prevent an interaction between the periodic repetition of the supercell, a vacuum region of 20 Å is added to the unit cell in  $z$ -direction. We have checked convergence with respect to the size of the vacuum region as well as the number of  $k$ -points.

The H-BL are constructed by taking the mean of the in-plane lattice constants of both ML materials, as well as the layer separation of the respective materials in their bulk form as starting values. Subsequently, the atom positions and the unit cell volume and shape are relaxed until all remaining forces between atoms are smaller than  $2.5 \text{ meV } \text{Å}^{-1}$ . For the calculation of the electronic properties, the energies are converged to  $10^{-9}$  eV. The optical transition dipole-matrix elements are accessible as an intermediate result in the calculation of the linear optical properties as described in [46] and the contributions of different atoms to a state are evaluated from the *spd* site-projected wave function character.

## 2.2. Ab initio band structures

To gain first insights into the electronic properties of the H-BLs, figure 2 shows the band dispersion of the  $\text{WSe}_2/\text{MoSe}_2$  (a) and  $\text{WSe}_2/\text{MoSe}_2$  H-BL (b) as obtained via DFT (grey lines). The  $\text{WSe}_2/\text{MoSe}_2$  H-BL is a direct gap semiconductor as expected from previous studies [13, 16], while the  $\text{WSe}_2/\text{MoSe}_2$  H-BL is slightly indirect [13].

Comparing the band structure of the  $\text{WSe}_2/\text{MoSe}_2$  H-BL with the band dispersion of the individual MLs of  $\text{WSe}_2$  (red-dashed line) and  $\text{MoSe}_2$  (blue-dashed line) in figure 2(a), it becomes evident that the electronic structure of the H-BL around the  $K$ - and  $K'$ -points is in very good approximation defined by the superposition of the two MLs' bands [14, 15, 17]. While both, the valence and the conduction bands of the two layers are well separated in energy at the  $K$ -points, the mutual band alignment is such that the resulting fundamental band gap in the H-BL is strongly reduced in comparison to the individual MLs. Furthermore, the highest valence band and the lowest conduction band combine contributions from different layers. Hence, the fundamental lowest-energy transition is an interlayer transition. As expected, the valence bands of both MLs show a strong spin-splitting due to the spin-orbit interaction [47], which is also present in the H-BL system. Consequently, the  $\text{WSe}_2/\text{MoSe}_2$  H-BL is a direct band gap semiconductor with type-II band alignment [13, 16, 29].

Approaching the  $\Gamma$ -point, the band structure of the H-BL starts to differ from the bands of the isolated MLs, giving evidence of a strong interaction between the layers [18]. Note that the band structure of the isolated MLs was computed for

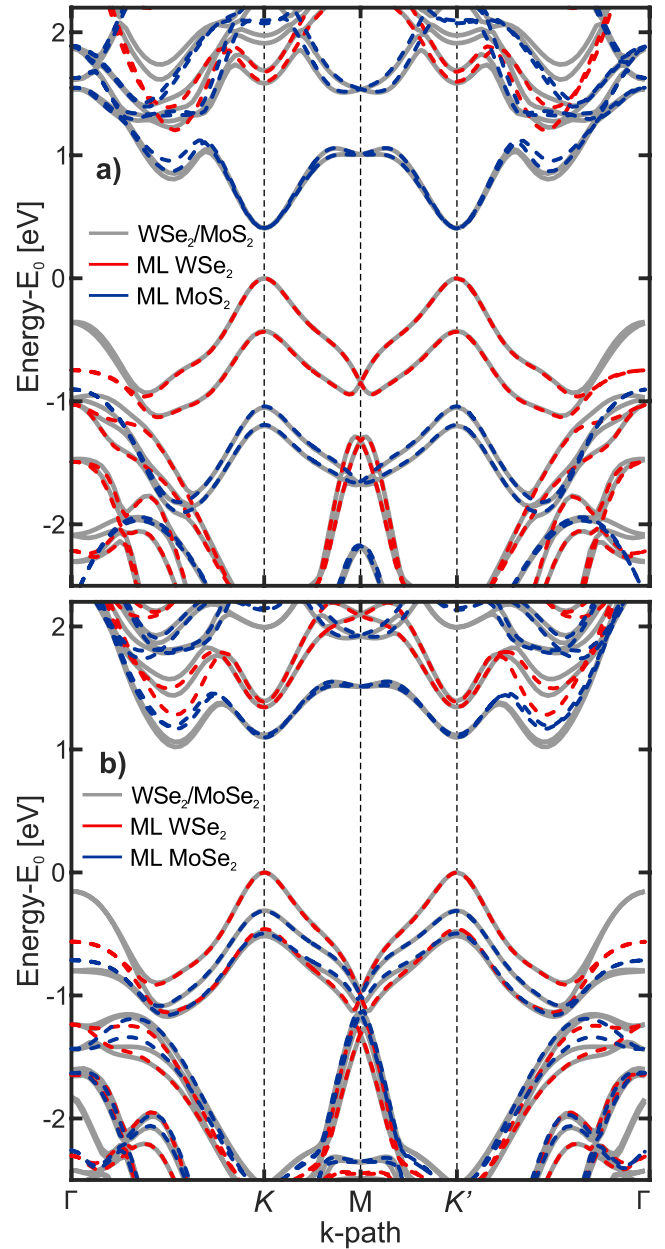


**Figure 2.** Band structure of (a)  $\text{WSe}_2/\text{MoSe}_2$  and (b)  $\text{WSe}_2/\text{MoSe}_2$  H-BLs in comparison to the constituent MLs: Band dispersion along the path  $\Gamma$ - $K$ - $M$ - $K'$ - $\Gamma$  of the H-BL (grey curve) in comparison to the band dispersion of the respective MLs (red and blue dashed lines). In case of the strained  $\text{WSe}_2/\text{MoSe}_2$  H-BL, the band structure of the MLs has been computed for the equilibrium lattice constant of the H-BL. As the overall band offset is not known from the ML computations, the band dispersion of the MLs has been shifted in energy, such that the uppermost valence band (lowest conduction band) coincides with the H-BL at the  $K$ -point. The vertical dashed lines mark the high symmetry points  $K$ ,  $K'$  and  $M$ .

the equilibrium in-plane lattice constant taken from the H-BL to allow for a comparison with the H-BL bands. As the overall band offset is not known from the ML computations, the band dispersion of the MLs has been shifted in energy, such that the uppermost valence band of the  $\text{WSe}_2$  ML and the lowest conduction band of the  $\text{MoSe}_2$  ML coincide with the corresponding H-BL band at the  $K$ -point.

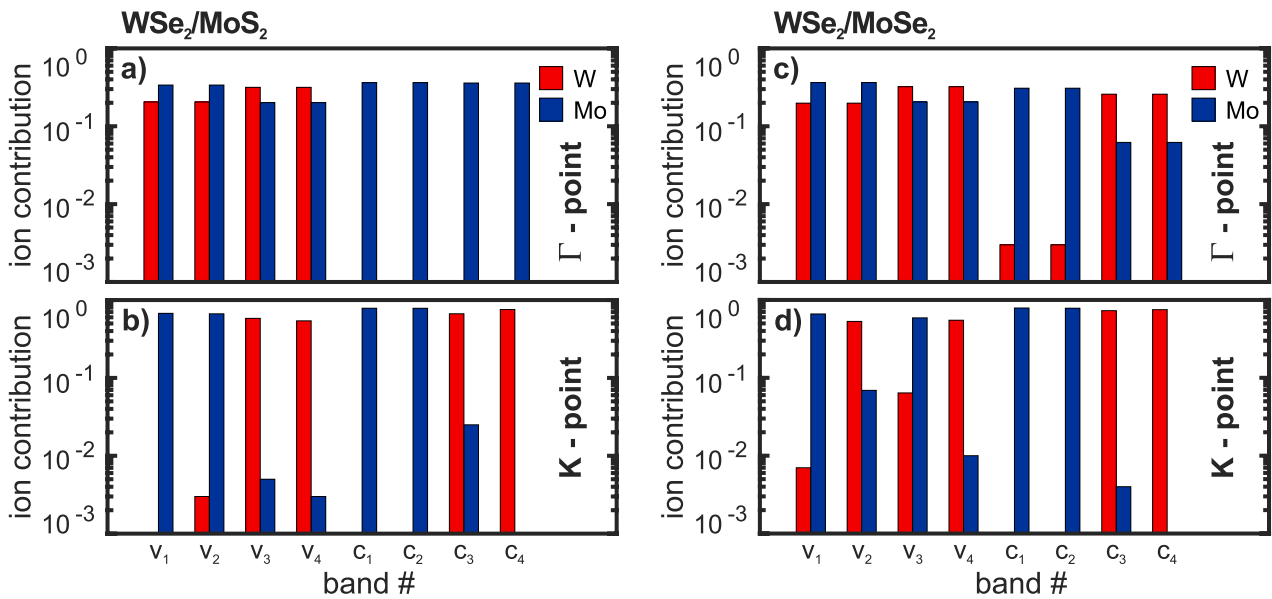


**Figure 3.** Relative ion contributions: relative contributions of tungsten (red) and molybdenum (blue) atoms to the first four valence and conduction bands at the  $\Gamma$ -point (top frames) and the  $K$ -point (bottom frames) for  $\text{WSe}_2/\text{MoS}_2$  (left frames) and  $\text{WSe}_2/\text{MoSe}_2$  H-BLs (right frames) on a logarithmic scale. The contributions of the sulfur and selenium atoms are not shown.

Also in the case of the  $\text{WSe}_2/\text{MoSe}_2$  H-BL in figure 2(b), the band structure around the  $K$ -point is well approximated by the ML band dispersion [22]. In contrast to the  $\text{WSe}_2/\text{MoS}_2$  H-BL, the band hetero-offset is much smaller such that the valence bands of both MLs are energetically close and partly overlap. Nevertheless, the highest valence band and the lowest conduction bands incorporate contributions from different layers, and the fundamental transition is an interlayer transition between  $\text{WSe}_2$  and  $\text{MoSe}_2$  layers [22]. Because of the smaller band hetero-offset, the overall band gap is not as strongly reduced as in the  $\text{WSe}_2/\text{MoS}_2$  H-BL case. Interestingly, going away from the  $K$ -points, the valence bands strongly interact, thus reducing the valence band energy such that the H-BL has a slightly indirect character in  $k$ -space.

Note that our computations show a slightly indirect band gap for the  $\text{WSe}_2$  ML, which is in agreement with recent *ab initio* computations and experiments [48–50]. Consequently, both material systems have type-II band alignment where the fundamental transition is of interlayer nature.

### 2.3. Relative ion contributions

In order to identify the inter- and intralayer nature of the optical transitions, we analyze which of the layers contribute to the involved bands. To this end, figure 3 presents the relative contributions of the tungsten atoms (representing the  $\text{WSe}_2$  layer) and molybdenum atoms (representing the  $\text{MoSe}_2$  or  $\text{MoS}_2$  layer) to the first four valence ( $v_1 - v_4$ ) and conduction bands ( $c_1 - c_4$ ) at the  $K$ - and the  $\Gamma$ -point. Here, only the contributions of the tungsten and molybdenum atoms are shown for clarity, while analyzing the contributions of the sulfur and selenium atoms leads to identical conclusions.

At the  $\Gamma$ -point of the  $\text{WSe}_2/\text{MoS}_2$  H-BL, (see figure 3(a)), both layers contribute to the valence band states  $v_1 - v_4$  with a comparable magnitude, which confirms the strong mixing

of the valence bands seen in the band structure plots. At the  $K$ -point, in contrast, (see figure 3(b)) the valence bands are almost exclusively created by only one of the layers. The two highest valence bands dominantly stem from  $\text{WSe}_2$  while the lower two bands are mainly created by  $\text{MoS}_2$  contributions, respectively. In addition, the three highest valence bands  $v_2 - v_4$  also have contributions from the other layer. However, those are smaller than 1%. Nevertheless, such a mixing of layers is a requirement to observe interlayer transitions. Only if the wave functions of both layers have sufficient overlap, transitions between them become possible. The same observation holds true for the conduction bands. Those are almost exclusively created by either the  $\text{WSe}_2$  or  $\text{MoS}_2$  layers, with the exception of the  $c_3$  conduction band. It is dominantly created by the  $\text{WSe}_2$  layer, but also has about 3% contributions from  $\text{MoS}_2$ . Consequently, as the interaction between the layers is rather weak, also the optical dipole-matrix elements are expected to be small. Indeed, we find in our computations that the magnitude of the dipole-matrix elements between the highest valence bands,  $v_3$  and  $v_4$ , to the lowest conduction bands,  $c_1$  and  $c_2$ , which describe the interlayer transitions, is only about 13% of the strongest intralayer transition.

Furthermore, in the  $\text{WSe}_2/\text{MoSe}_2$  H-BL (in figures 3(c) and (d)) the valence and conduction bands show a strong layer mixing at the  $\Gamma$ -point. At the  $K$ -point, each of the layers dominantly contributes to two of the valence bands and two of the conduction bands. In contrast to the  $\text{WSe}_2/\text{MoS}_2$  H-BL, the intermixing here is much stronger, especially for valence bands  $v_2$  and  $v_3$ , which have contributions stemming from the respective other layer of up to 13%. Therefore, we expect the interlayer dipole-matrix elements to be stronger in this case. Moreover, as the valence bands are energetically closer than in the case of  $\text{WSe}_2/\text{MoS}_2$ , the transitions from the lower lying valence bands  $v_1$  and  $v_2$  to the conduction bands  $c_3$  and  $c_4$  play a role.

Indeed, the magnitude of the corresponding dipole-matrix element of the interlayer transitions from  $v_2$  to  $c_1$  ( $v_3$  to  $c_3$ ) is about 23% (26%) of the strongest interlayer transitions. This is approximately twice as large as the fundamental interlayer transition from  $v_4$  to  $c_2$ .

### 3. Optical and excitonic spectra

To compute the optical and excitonic spectra, we use the equations of motion (EOM) approach. Here, one derives the EOM for a set of dynamical variables that are relevant in an optical experiment. For the bilayer configuration considered here, the relevant quantities are the intra- and interlayer inter-band polarizations that couple directly to the optical field, and the respective occupation probabilities of the involved bands. For the bilayer configuration, the EOM are derived from an effective four band Hamiltonian that is based on the single-particle band structure and dipole-matrix elements derived from our DFT calculations. Since DFT-based band structure calculations usually underestimate the optical band gap, we compute the gap renormalization self-consistently via the gap equations [27, 51–53].

#### 3.1. H-BL model Hamiltonian

In this section, we present the model Hamiltonian that is used in the EOM approach to determine the band gap renormalization and excitonic spectra. For each spin component, we include the two highest valence and two lowest conduction bands near the  $K$ -points of the joint Brillouin zone, yielding an effective four band model. According to the analysis presented in section 2.3, the near  $K$ -point valence and conduction bands can in good approximation be attributed to a given layer. Based on this observation, we assign the quantum number  $\{n, \lambda\}$ , where  $n = 1, 2$  refers to the layer, and  $\lambda = c, v$  to their respective valence and conduction bands. Treating the H-BL as two electronically independent layers, the Hamiltonian is given by

$$\hat{H} = \sum_n \hat{H}_0^n + \frac{1}{2} \sum_{nm} \sum_{\mathbf{q}} V_{\mathbf{q}}^{nm} \hat{\rho}_{\mathbf{q}}^n \hat{\rho}_{-\mathbf{q}}^m + \hat{H}_I.$$

Here, the first term describes the free-particle part of the isolated layers, the second term the Coulomb interaction,  $\hat{\rho}_{\mathbf{q}}^n$  denotes the charge density of layer  $n$ , and  $\hat{H}_I$  contains the light-matter (LM) interaction, respectively.

For the free-particle part of the individual layers, we employ the MDF model [54]:

$$\hat{H}_0^n = \sum_{\mathbf{k}} \hat{\Psi}_{n\mathbf{k}}^\dagger \begin{pmatrix} E_{F,n} + \frac{\Delta_{nm}}{2} & \hbar v_{F,n} k e^{i\tau_n \theta_{\mathbf{k}}} \\ \hbar v_{F,n} k e^{-i\tau_n \theta_{\mathbf{k}}} & E_{F,n} - \frac{\Delta_{nm}}{2} \end{pmatrix} \hat{\Psi}_{n\mathbf{k}}. \quad (1)$$

Here,  $\Delta_{nm} = E_n^c - E_n^v$  and  $v_{F,n}$  are the intralayer transition energy and Fermi-velocity in layer  $n$ , respectively. To ensure the correct band alignment, we explicitly include the Fermi levels  $E_{F,n} = (E_n^c + E_n^v)/2$  of the  $n$ th layer. Furthermore,  $\tau_n$  is the valley index of the  $n$ th layer. For the naturally AA'-stacked

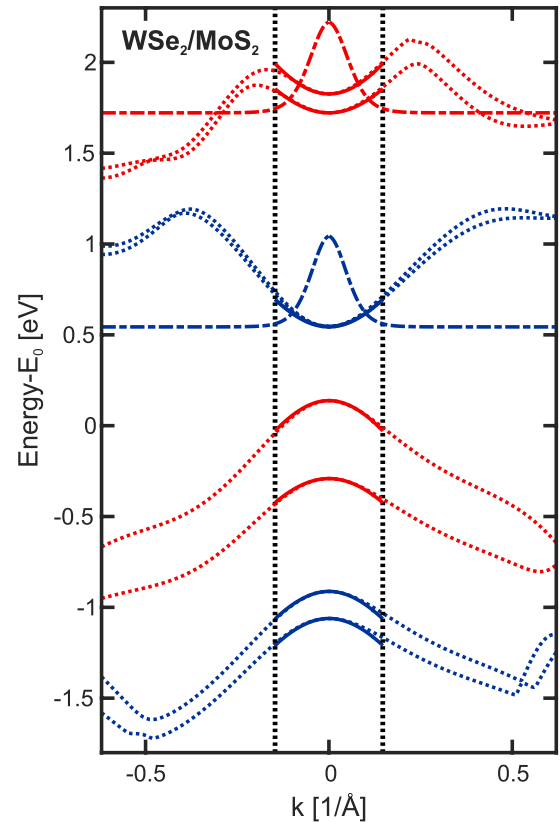


**Figure 4.** The single-particle band structure (dotted lines) of the WSe<sub>2</sub>/MoS<sub>2</sub> H-BL is approximated by the relativistic dispersion (solid lines) within the area marked by the vertical black dotted lines. The Mo dominated bands are plotted in blue whereas the W dominated bands are plotted in red, respectively. The probability densities of the respective intralayer excitonic ground states are shown in dashed-dotted lines.

bilayers considered here, adjacent layers are related by the parity transformation, leading to a locking of the valley indices in different layers  $\tau_1 = -\tau_2$ . Diagonalization of the MDF Hamiltonian within different layers gives the relativistic band dispersion

$$E_{nk}^{c/v} = E_{F,n} \pm \epsilon_{nk}, \quad (2)$$

with  $\epsilon_{nk} = \sqrt{(\Delta_{nm}/2)^2 + (\hbar v_{F,n} k)^2}$ . The explicit values for the transition energies  $\Delta_{nm}$ , Fermi levels  $E_{F,n}$  and Fermi-velocities  $v_{F,n}$  are obtained by fitting the relativistic quasi-particle dispersion to the DFT band structure presented in the previous section.

The resulting approximated band structure of the WSe<sub>2</sub>/MoS<sub>2</sub> H-BL (solid lines) is shown in figure 4 together with the DFT bands (dotted lines) and the  $k$ -space wave function of the exciton ground state (dashed-dotted lines). The bands referring to the MoS<sub>2</sub> layer are plotted in blue whereas the bands of the WSe<sub>2</sub> layer are plotted in red. The fitting procedure provides an excellent approximation to the DFT band structure within the  $k$ -space region, where the probability density of the excitonic ground state is largest, marked by the black-dotted lines. As the wave functions of the excited exciton states are even narrower in  $k$ -space, the relativistic approximation of the

bands is expected to yield an accurate description not only of the excitonic ground state, but also of the excited states of the H-BL system.

Expanding the field operators in terms of conduction and valence band operators of the respective layers yields the Coulomb interaction part of the Hamiltonian. It is given by

$$\hat{H}_C = \frac{1}{2} \sum_{\mathbf{k}, \mathbf{k}', \mathbf{q}} \sum_{n, m} \sum_{\lambda, \lambda', \mu, \mu'} V_{\mathbf{q}}^{nm} \langle n\lambda\mathbf{k} - \mathbf{q} | n\lambda'\mathbf{k}' \rangle \times \langle m\mu\mathbf{k}' + \mathbf{q} | m\mu'\mathbf{k}' \rangle \hat{a}_{n\lambda, \mathbf{k} - \mathbf{q}}^\dagger \hat{a}_{m\mu, \mathbf{k}' + \mathbf{q}}^\dagger \hat{a}_{m\mu', \mathbf{k}'} \hat{a}_{n\lambda', \mathbf{k}} \quad (3)$$

where  $\hat{a}_{n\lambda, \mathbf{k}}^{(\dagger)}$  creates (annihilates) an electron with momentum  $\mathbf{k}$  in band  $\{n, \lambda\}$  and  $\langle n\lambda\mathbf{k} - \mathbf{q} | n\lambda'\mathbf{k}' \rangle$  is the overlap matrix element. Within the effective four-band model, screening of the explicitly treated bands is included dynamically, whereas screening of all other bands and the dielectric environment is contained in the ‘bare’ Coulomb matrix element  $V_{\mathbf{q}}^{nm}$ . Following [27], the ‘bare’ Coulomb matrix elements are obtained as solution of Poisson’s equation for the anisotropic environment, composed of the substrate, capping layers, and non-resonant contributions of the TMDC bilayer. Furthermore, we include an effective thickness parameter  $d$  to account for the finite extension of the atomic orbitals [27]. The effective thickness parameter is chosen for each layer separately and determined by fitting a single spectral feature of a monolayer consisting of the same material to an experimentally well-known value, as described in [27]. The finite effective layer thickness leads to a regularization of the Coulomb potential at  $r = 0$ , mainly affecting the strongly bound intralayer excitons and band gap renormalization. For the interlayer excitons with an interlayer spacing  $D > d$ , its influence is rather small.

Employing the minimal substitution, an expansion of the field operators yields the LM interaction Hamiltonian:

$$\hat{H}_I = -\frac{e}{m_0 c} \sum_{n, m} \sum_{\lambda, \lambda'} \sum_{\mathbf{k}} \mathbf{p}_{\lambda, \lambda'}^{nm}(\mathbf{k}) \cdot \mathbf{A}(t) \hat{a}_{n\lambda, \mathbf{k}}^\dagger \hat{a}_{m, \lambda', \mathbf{k}} \quad (4)$$

where  $\mathbf{A}(t)$  describes the vector potential of the optical field at the position of the bilayer, and  $\mathbf{p}_{\lambda, \lambda'}^{nm}(\mathbf{k})$  is the matrix element of the momentum operator. The momentum matrix elements are related to the DFT dipole-matrix elements  $\mathbf{d}_{\lambda, \lambda'}^{nm}(\mathbf{k}) = e \langle n\lambda\mathbf{k} | \nabla_{\mathbf{k}} | m\lambda'\mathbf{k} \rangle$  via

$$\frac{e\hbar}{m_0} \mathbf{p}_{\lambda, \lambda'}^{nm}(\mathbf{k}) = e \nabla_{\mathbf{k}} E_{\lambda\mathbf{k}}^n \delta_{nm} \delta_{\lambda, \lambda'} + (E_{\lambda'\mathbf{k}}^m - E_{\lambda\mathbf{k}}^n) \mathbf{d}_{\lambda, \lambda'}^{nm}(\mathbf{k}). \quad (5)$$

It is worth noting that the intralayer momentum matrix elements can alternatively be computed directly from the model Hamiltonian (1), yielding the relation  $\hbar v_{F, n} = \Delta_{nm} |\mathbf{d}_{cv}^{nm}(\mathbf{k} = 0)| / (e\sqrt{2})$  for the Fermi velocities. As we have verified, the values for the Fermi velocities of 3.62 eV Å for MoS<sub>2</sub> and 3.90 eV Å for WSe<sub>2</sub>, obtained from this relation, are in perfect agreement with the values resulting from the fit of the band dispersion, thus further validating our model Hamiltonian.

### 3.2. Gap equations

Since DFT-based band structure calculations usually underestimate the optical band gap, in a first step, we compute the gap renormalization self-consistently via the GE. These GE are a set of coupled integral equations for the renormalized band gap and the Fermi-velocity and can be derived as static solution of the equations of motion in the absence of an external field [27, 51–53]. They are non-perturbative and can be derived on the same level of approximation as the EOM for the excitation dynamics.

Using the screened Hartree–Fock approximation, the GE are given by

$$\tilde{\Delta}_{m\mathbf{k}} = \Delta_{m\mathbf{k}} + \frac{1}{2} \sum_{\mathbf{k}'} V_{S|\mathbf{k}-\mathbf{k}'|}^{mn} \frac{\tilde{\Delta}_{m\mathbf{k}'}}{\varepsilon_{n\mathbf{k}'}} \quad (6)$$

$$\tilde{v}_{F, n, \mathbf{k}} = v_{F, n} + \frac{1}{2} \sum_{\mathbf{k}'} V_{S|\mathbf{k}-\mathbf{k}'|}^{mn} \frac{k'}{k} \frac{\tilde{v}_{F, n, \mathbf{k}'}}{\varepsilon_{n\mathbf{k}'}} e^{i\tau_n(\theta_{\mathbf{k}} - \theta_{\mathbf{k}'})} \quad (7)$$

with  $\varepsilon_{n\mathbf{k}} = \sqrt{(\tilde{\Delta}_{m\mathbf{k}}/2)^2 + (\hbar\tilde{v}_{F, n, \mathbf{k}})^2}$ , yielding the renormalized band dispersions

$$\tilde{E}_{n\mathbf{k}}^{c/v} = E_{F, n} \pm \varepsilon_{n\mathbf{k}}.$$

The GE contain the screened Coulomb interaction

$$V_{S\mathbf{q}}^{mm'}(\omega) = \sum_{m''} \left[ 1 - V_{\mathbf{q}}^{mm''} \Pi^{m''}(\omega, \mathbf{q}) \right]^{-1} V_{\mathbf{q}}^{m''m'} \quad (8)$$

where  $\Pi^n(\omega, \mathbf{q})$  is the ground-state polarization function of the  $n$ th layer. For the ground-state polarization function, we use the long-wavelength limit of the static RPA polarization function obtained within the MDF model Hamiltonian [55]

$$\Pi^n(0, \mathbf{q}) = -\frac{1}{6\pi} \frac{q^2}{\Delta_{m\mathbf{k}}}$$

and sum over all spin-valley combinations.

### 3.3. Dirac–Bloch equations

To determine the excitation dynamics of our H-BL systems, we transform the Hamiltonian into the electron–hole picture using the renormalized band structure and eigenstates. As dynamical variables, we use the interband transition amplitudes and occupation numbers of the renormalized bands

$$P_{\mathbf{k}}^{mn} = \langle \hat{a}_{m\nu, \mathbf{k}}^\dagger \hat{a}_{nc, \mathbf{k}} \rangle, \quad (9)$$

$$f_{\mathbf{k}}^n = 1 - \langle \hat{a}_{n\nu, \mathbf{k}}^\dagger \hat{a}_{n\nu, \mathbf{k}} \rangle = \langle \hat{a}_{nc, \mathbf{k}}^\dagger \hat{a}_{nc, \mathbf{k}} \rangle. \quad (10)$$

Here, the transition amplitudes  $P_{\mathbf{k}}^{mn}$  correspond to interlayer transitions for  $m \neq n$  and to intralayer transitions for  $m = n$ , respectively.

In the low excitation regime ( $f_{\mathbf{k}}^n = 0$ ) the resulting Heisenberg EOM for the interband transition amplitudes at the screened Hartree–Fock level are given by the Dirac–Bloch equations [27, 53]

$$i\hbar \frac{d}{dt} P_{\mathbf{k}}^{mn} = (\tilde{E}_{n\mathbf{k}}^c - \tilde{E}_{m\mathbf{k}}^\nu) P_{\mathbf{k}}^{mn} - \Omega_{\mathbf{k}}^{mn} - i\hbar \left. \frac{d}{dt} P_{\mathbf{k}}^{mn} \right|_{\text{coll}}, \quad (11)$$

with the renormalized band dispersions  $\tilde{E}_{n\mathbf{k}}^c$  and  $\tilde{E}_{m\mathbf{k}}^\nu$ . Similar to the GE, the generalized Rabi frequency

$$\Omega_{\mathbf{k}}^{mn} = \sum_{\mathbf{k}'} V_{S|\mathbf{k}-\mathbf{k}'|}^{nm} (W_{cv\nu}^{nm}(\mathbf{k}, \mathbf{k}') P_{\mathbf{k}'}^{mn} + W_{cvc\nu}^{nm}(\mathbf{k}, \mathbf{k}') P_{\mathbf{k}'}^{nm*}) + \frac{e}{m_0 c} \mathbf{p}_{c\nu}^{nm}(\mathbf{k}) \cdot \mathbf{A}(t) \quad (12)$$

contains the screened Coulomb interaction potential. Furthermore,  $W_{\lambda\lambda',\mu\mu'}^{nm}(\mathbf{k}, \mathbf{k}') = \langle n\lambda\mathbf{k} | n\lambda'\mathbf{k}' \rangle \langle m\mu\mathbf{k}' | m\mu'\mathbf{k} \rangle$  denote the overlap matrix elements within the renormalized bands.

From the interband polarization  $P_{\mathbf{k}}^{mn}$ , we obtain the linear susceptibility via

$$\chi(\omega) = \frac{ec}{m_0 \omega^2} \frac{\delta}{\delta \mathbf{A}(\omega)} \sum_{m,n,\mathbf{k}} \mathbf{p}_{c\nu}^{nm}(\mathbf{k}) P_{\mathbf{k}}^{mn}(\omega), \quad (13)$$

where  $\mathbf{A}(\omega)$  and  $P_{\mathbf{k}}^{mn}(\omega)$  denote the frequency components of the vector potential and the microscopic polarization, respectively. The linear optical susceptibility can be expressed with the aid of the Elliot formula

$$\chi(\omega) = -\frac{e^2}{m_0^2 \omega^2} \sum_{m,n} \sum_{\mu} \left( \frac{\mathcal{F}_{\mu}^{mn}}{\hbar(\omega + i\gamma) - E_{\mu}^{mn}} - \frac{\mathcal{F}_{\mu}^{mn}}{\hbar(\omega + i\gamma) + E_{\mu}^{mn}} \right). \quad (14)$$

It has resonances at the eigenvalues of the Dirac–Wannier equation for the respective intra- and interlayer excitons,

$$(\tilde{E}_{n\mathbf{k}}^c - \tilde{E}_{m\mathbf{k}}^\nu) \psi_{\mu}^{mn}(\mathbf{k}) - \sum_{\mathbf{k}'} V_{S|\mathbf{k}-\mathbf{k}'|}^{nm} [W_{cvc\nu}^{nm}(\mathbf{k}, \mathbf{k}') \psi_{\mu}^{mn}(\mathbf{k}') + W_{cv\nu}^{nm}(\mathbf{k}, \mathbf{k}') \psi_{\mu}^{nm*}(\mathbf{k}')] = E_{\mu}^{mn} \psi_{\mu}^{mn}(\mathbf{k}), \quad (15)$$

and  $\mathcal{F}_{\mu}^{mn} = |\sum_{\mathbf{k}} \mathbf{p}_{c\nu}^{nm}(\mathbf{k}) \psi_{\mu}^{mn}(\mathbf{k})|^2$  is a measure for the oscillator strength of the transition.

Whereas bright exciton states require a finite (nonzero) oscillator strength, interlayer excitons do exist even if the oscillator strength vanishes, in which case they correspond to dark excitons.

We compute the absorption spectrum of the bilayer configuration via

$$\alpha(\omega) = \frac{4\pi n_T \frac{\omega}{c} \text{Im}[\chi(\omega)]}{|(n_T + n_B)/2 - 2\pi i \frac{\omega}{c} \chi(\omega)|^2}, \quad (16)$$

where  $n_T$  and  $n_B$  are the refractive indices of the top and bottom dielectric materials supporting the TMDC H-BL. The denominator in equation (16) accounts for the interaction of the optically induced polarization with its own radiation field, which leads to a finite radiative lifetime. The radiative decay rate of a given exciton transition is computed from its oscillator strength via [56, 57]  $\Gamma_{\mu}^{mn} = \frac{4\pi}{n_T + n_B} \frac{e^2}{\hbar c} \frac{\mathcal{F}_{\mu}^{mn}}{m_0^2 \omega_{\mu}^{mn}}$ .

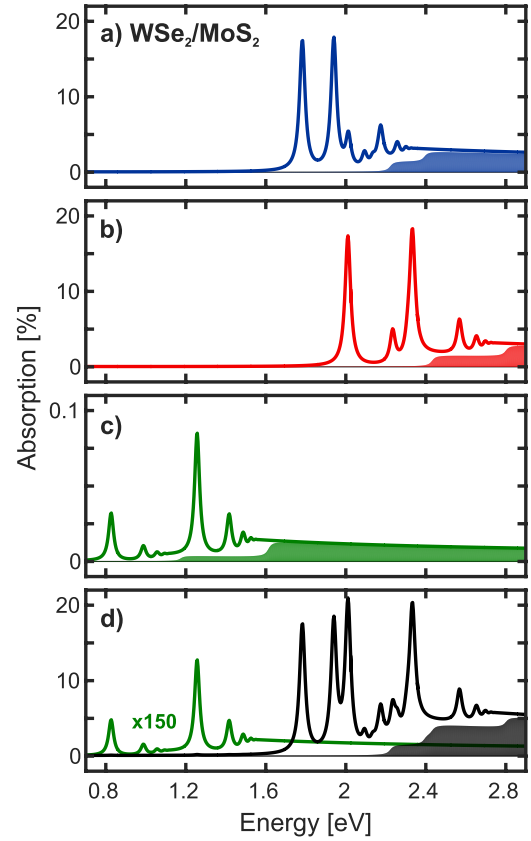


**Figure 5.** Absorption spectrum of the WSe<sub>2</sub>/MoS<sub>2</sub> H-BL: Contributions of intralayer transitions between Mo (a) and W (b) dominated bands to the absorption spectrum (solid line). (c) Contributions of interlayer transitions (green solid line) to the absorption spectrum. (d) Full absorption spectrum of the WSe<sub>2</sub>/MoS<sub>2</sub> H-BL in (black solid line). The contribution of the lowest interlayer transition is magnified by a factor of 150 (green solid line). The shaded areas show the respective free-particle transitions.

## 4. Results

In this section, we present the linear optical absorption spectra of the H-BLs WSe<sub>2</sub>/MoS<sub>2</sub> and WSe<sub>2</sub>/MoSe<sub>2</sub>, calculated with the aid of the combined gap equation and DBE approach. For our calculations we use a phenomenological dephasing of 15 meV.

The absorption spectrum of a suspended WSe<sub>2</sub>/MoS<sub>2</sub> H-BL is shown in figure 5 in comparison to the distinct inter- and intralayer contributions. In figure 5(a), we show the intralayer absorption of the MoS<sub>2</sub> dominated layer (blue solid line) and in figure 5(b) correspondingly for the WSe<sub>2</sub> dominated layer (red solid line). The shaded areas represent the respective free-particle absorption spectra without excitonic effects. From the onset of the free-particle transitions one recognizes the interacting gaps resulting from the GE, which are 770 and 750 meV above the noninteracting DFT gaps of 1.46 and 1.69 eV for MoS<sub>2</sub> and WSe<sub>2</sub>, respectively. Energetically below the onset of the continuum states, one clearly recognizes the resonances corresponding to bound intralayer excitons.

For the WSe<sub>2</sub>/MoS<sub>2</sub> H-BL, the ground state of the MoS<sub>2</sub> intralayer exciton is found at 1.73 eV and that of the WSe<sub>2</sub>

layer at 2.01 eV, respectively. These values deviate significantly from the exciton ground states of the respective MLs that are found experimentally at approximately 1.9 and 1.75 eV, respectively. The origin for these deviations is the tensile/compressive strain in the constituent layers, leading to a shift of the DFT band gap as compared to the unstrained MLs. From the energetic separation of the exciton resonances and renormalized gap, we obtain binding energies of 440 meV for the WSe<sub>2</sub> and 460 meV for the MoS<sub>2</sub> intralayer excitons, respectively. Furthermore, we extract the respective intrinsic radiative lifetimes from the oscillator strength of the excitonic transitions. For the intralayer excitons in the MoS<sub>2</sub> layers, we find  $T_{\text{rad}} = 0.412$  ps and  $T_{\text{rad}} = 0.406$  ps for the lowest A- and B-exciton, respectively, and almost identical values  $T_{\text{rad}} = 0.411$  ps and  $T_{\text{rad}} = 0.415$  ps for the WSe<sub>2</sub> layers.

In figure 5(c), we show the interlayer contributions to the WSe<sub>2</sub>/MoS<sub>2</sub> H-BL absorption spectrum, corresponding to transitions from the WSe<sub>2</sub> valence to the MoS<sub>2</sub> conduction bands. Again, the free-particle transitions are shown as a shaded area, allowing us to deduce the renormalized energy gaps of 1.18 eV and 1.62 eV for the interlayer A- and B-exciton series, respectively. The interlayer spectrum exhibits discrete bright resonances corresponding to the bound interlayer excitons, with a resonance energy of 0.83 eV and 1.26 eV for the lowest A- and B- interlayer excitons, respectively. Thus, the resulting binding energies of interlayer excitons of a suspended WSe<sub>2</sub>/MoS<sub>2</sub> H-BL are around 350 meV, only roughly 25% less than the intralayer binding energy. In contrast, the oscillator strength of the interlayer exciton is two orders of magnitude smaller than that of the intralayer excitons, leading to an absorption of a fraction of a percent per bilayer. The small oscillator strengths of the interlayer transitions imply long radiative lifetimes, exceeding those of the intralayer excitons by almost three orders of magnitude. Explicitly, we find  $T_{\text{rad}} = 108.1$  ps and  $T_{\text{rad}} = 277.1$  ps for the two lowest interlayer excitons.

Finally, in figure 5(d), we show the total absorption spectrum including all intra- and interlayer contributions (black lines). For better visibility, the green lines show the interlayer contributions with a magnification factor of 150.

Similar results are obtained for the suspended WSe<sub>2</sub>/MoSe<sub>2</sub> H-BL presented in figure 6, where (a) and (b) represent the respective intralayer contributions, whereas the interlayer contributions and total absorption spectrum are shown in (c) and (d). The lowest lying A-exciton intralayer resonances of both layers are almost degenerate and occur around 1.7 eV. These should be compared with the respective ML resonances that are found around 1.64 eV and 1.75 eV for MoSe<sub>2</sub> and WSe<sub>2</sub> MLs, respectively, the precise values depending on the dielectric environment. As compared to the WSe<sub>2</sub>/MoS<sub>2</sub> H-BLs, these deviations are significantly smaller, reflecting the small strain in the bilayer where the constituting monolayers have similar lattice constants. For the radiative lifetimes of the WSe<sub>2</sub>/MoSe<sub>2</sub> H-BL intralayer excitons, we find again that the A- and B-excitons of the individual layers have almost identical radiative lifetimes. In fact, we obtain 0.492 ps and 0.482 ps for the MoSe<sub>2</sub> layer and 0.437 ps and 0.453 ps for the WSe<sub>2</sub> layer. However, for the almost degenerate states,

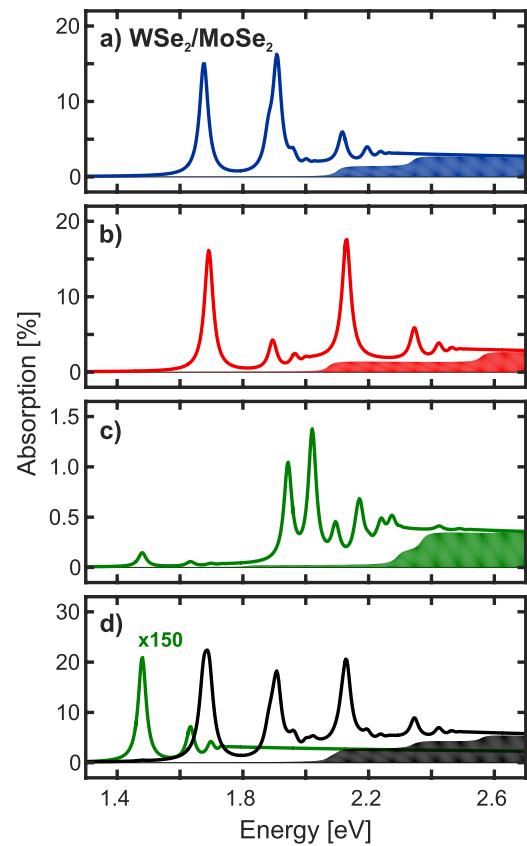


**Figure 6.** Absorption spectrum of the WSe<sub>2</sub>/MoSe<sub>2</sub> H-BL: Contributions of intralayer transitions between Mo (a) and W (b) dominated bands to the absorption spectrum (solid line). (c) Contributions of interlayer transitions (green solid line) to the absorption spectrum. (d) Full absorption spectrum of the WSe<sub>2</sub>/MoSe<sub>2</sub> H-BL in (black solid line). The contribution of the lowest interlayer transition is magnified by a factor of 150 (green solid line). The shaded areas show the respective free particle transitions.

the lifetimes are further reduced by radiative coupling effects [56, 57].

Analyzing the corresponding interlayer transitions in figure 6(c), the fundamental exciton transition can be observed at 1.48 eV, which corresponds to a transition from the upper spin-split valence band in the WSe<sub>2</sub> layer, to the conduction band of the MoSe<sub>2</sub> layer and has a binding energy of ca. 330 meV. The radiative lifetime of this transition is 63 ps, two orders of magnitude larger than the intralayer exciton lifetime. Additionally, we find bright interlayer exciton resonances, both corresponding to transitions from the lower spin-split valence band in the W-dominated layer to the Mo-dominated layer conduction band, as well as transitions from the MoSe<sub>2</sub> layer to the WSe<sub>2</sub> layer. The latter transitions are energetically above the lowest lying intralayer excitons and dominate the interlayer absorption due to their larger dipole-matrix elements. Nevertheless, a direct observation of these excitons in an absorption measurement is unlikely as they interfere with the much brighter intralayer excitons. In figure 6(d), we show the full absorption spectrum including all intra- and interlayer contributions. Again, the green line shows the magnified interlayer contributions with a magnification factor of 150.

## 5. Summary and discussion

In summary, we performed fully microscopic computations of the resonance positions and radiative lifetimes of intra- and interlayer excitons in two different TMDC based heterostructures. In a first step, we computed the *ab initio* band structure and dipole-matrix elements via DFT using the PBE functional and including spin-orbit interaction. A subsequent analysis of the relative ion contributions reveals a type-II band alignment for both investigated structures, a WSe<sub>2</sub>/MoS<sub>2</sub> and a WSe<sub>2</sub>/MoSe<sub>2</sub> H-BL. Subsequently, the DFT band dispersion and dipole-matrix elements were used as input parameters for an effective four band Hamiltonian. From the effective four-band Hamiltonian, we derived and numerically solved the GE to compute the band gap renormalization, and the DBE to determine the exciton states.

Our calculations predict the coexistence of intra- and interlayer excitons. We find that the binding energy of the interlayer excitons is only about 25% less than that of the intralayer excitons, yielding a binding energy of around 350 meV for the fundamental interlayer exciton transition for the investigated suspended H-BLs. This very large binding energy promises a high stability of the respective excitons with regards to temperature, doping or substrate screening. The coupling strength of the interlayer excitons to the optical field is roughly two orders of magnitude smaller than that of the intralayer excitons, yielding a correspondingly enhanced radiative lifetime of several tens of picoseconds. Despite the strongly decreased oscillator strength, the interlayer excitons remain optically active, enabling convenient optical access, whereas the long radiative lifetime of several tens of picoseconds opens new prospects for the investigation of excitonic devices in the non-equilibrium regime.

It is tempting to compare our predictions with available experimental data. However, we explicitly note that any comparison should be taken with care since the key quantities, i.e. the band gap, exciton binding, and exciton radiative lifetime all depend on the precise conditions like strain, substrate screening and temperature. As we have seen in our calculations, tensile/compressive strain strongly influences the noninteracting gap and therewith the absolute resonance positions. In particular, the WSe<sub>2</sub>/MoS<sub>2</sub> heterostructure suffers from strong lattice mismatch between the constituent layers. Hence, we refrain from comparing our results for the strained WSe<sub>2</sub>/MoS<sub>2</sub> H-BLs with those of [29], where photoluminescence was observed on bilayers created by exfoliation that are essentially unstrained.

Another important factor influencing the exciton resonance positions is substrate screening by the dielectric environment. As is known from TMDC MLs, substrate screening leads to a simultaneous reduction of the band gap renormalization and exciton binding energy, such that the absolute position of the lowest lying exciton is only weakly affected by the dielectric environment. As a general trend, increasing the substrate screening leads to a red shift of a few meV of the lowest lying A- and B-resonances. Therefore, we can compare our predictions with experimental observations on WSe<sub>2</sub>/MoSe<sub>2</sub>

H-BLs supported by different substrates, keeping in mind that quantitative agreement can only be expected within an accuracy of roughly 10 meV resulting from screening effects, and another roughly 10 meV resulting from lattice mismatch induced strain. Indeed, within this accuracy range, the predicted resonance positions of 1.7 eV for the intralayer excitons and 1.48 eV for the interlayer exciton are in good agreement with the intralayer resonance positions of 1.65 eV and 1.75 eV and interlayer resonance at 1.4 eV observed on mechanically exfoliated SiO<sub>2</sub> supported samples in [20], and of 1.7 eV and 1.4 eV on nominally identical samples in [19]. Also, the values of 1.65 eV and 1.56 eV for the intralayer excitons and 1.37 eV for the respective interlayer exciton reported by [22] for graphite supported samples capped with an additional graphene layer are consistent with our predictions.

For the exciton lifetime, our calculations predict a radiative lifetime of approximately 0.4 ps for the intralayer transitions at zero temperature. The interlayer exciton lifetime in WSe<sub>2</sub>/MoSe<sub>2</sub> is found to be approximately 63 ps, two orders of magnitudes larger. Our predictions for the radiative lifetime of the intralayer excitons is in very good agreement with the values found in [58] from the Bethe–Salpeter-equation, whereas our predictions for the interlayer exciton lifetime is more than a factor five larger. The radiative lifetime increases linearly with temperature, typically increasing the lifetime from the picosecond to the nanosecond range while increasing the temperature to room temperature [58]. Therefore, the computed values at zero temperature cannot be directly compared to finite temperature lifetimes. Nevertheless, the calculated ratio of the inter- and intralayer exciton lifetimes is in reasonable agreement with experimental observations [20], where the interlayer exciton lifetime was found to be one order of magnitude larger than typical ML exciton lifetimes.

## Acknowledgments

This work was supported by the Deutsche Forschungsgemeinschaft through grant number KI 917/2-2, grant number KI 917/3-1, via the Collaborative Research Center 1083 (DFG:SFB1083) and the GRK 1782 ‘Functionalization of Semiconductors’. Computing resources from the HRZ Marburg are acknowledged. The schematics of the H-BL structure shown in figure 1 was created with the VESTA software [59].

## ORCID iDs

L Meckbach  <https://orcid.org/0000-0001-9563-2147>

L C Bannow  <https://orcid.org/0000-0002-1379-6242>

T Stroucken  <https://orcid.org/0000-0002-0546-7289>

## References

- [1] Mak K F, Lee C, Hone J, Shan J and Heinz T F 2010 *Phys. Rev. Lett.* **105** 136805
- [2] Splendiani A, Sun L, Zhang Y, Li T, Kim J, Chim C Y, Galli G and Wang F 2010 *Nano Lett.* **10** 1271

- [3] Zhang C, Wang H, Chan W, Manolatu C and Rana F 2014 *Phys. Rev. B* **89** 205436
- [4] Ding Y, Wang Y, Ni J, Shi L, Shi S and Tang W 2011 *Phys. B: Phys. Condens. Matter* **406** 2254
- [5] Qiu D Y, Da Jornada F H and Louie S G 2013 *Phys. Rev. Lett.* **111** 216805
- [6] Novoselov K S, Mishchenko A, Carvalho A and Castro Neto A H 2016 *Science* **353** 6298
- [7] Cheiwchanchamnangij T and Lambrecht W R L 2012 *Phys. Rev. B* **85** 205302
- [8] Wang Q H, Kalantar-Zadeh K, Kis A, Coleman J N and Strano M S 2012 *Nat. Nanotechnol.* **7** 699
- [9] Zeng H, Dai J, Yao W, Xiao D and Cui X 2012 *Nat. Nanotechnol.* **7** 490
- [10] Xia F, Wang H, Xiao D, Dubey M and Ramasubramaniam A 2014 *Nat. Photon.* **8** 899
- [11] Geim A K and Grigorieva I V 2013 *Nature* **499** 419
- [12] Jariwala D, Marks T J and Hersam M C 2016 *Nat. Mater.* **16** 170
- [13] Terrones H, López-Urías F and Terrones M 2013 *Sci. Rep.* **3** 1549
- [14] Kośmider K and Fernández-Rossier J 2013 *Phys. Rev. B* **87** 075451
- [15] Komsa H P and Krasheninnikov A V 2013 *Phys. Rev. B* **88** 085318
- [16] Amin B, Kaloni T P, Schreckenbach G and Freund M S 2016 *Appl. Phys. Lett.* **108** 063105
- [17] Latini S, Winther K T, Olsen T and Thygesen K S 2017 *Nano Lett.* **17** 938
- [18] Kang J, Li J, Li S S, Xia J B and Wang L W 2013 *Nano Lett.* **13** 5485
- [19] Nagler P *et al* 2017 *Nat. Commun.* **8** 1551
- [20] Rivera P *et al* 2015 *Nat. Commun.* **6** 6242
- [21] Rivera P, Seyler K L, Yu H, Schaibley J R, Yan J, Mandrus D G, Yao W and Xu X 2016 *Science* **351** 688
- [22] Wilson N R *et al* 2017 *Sci. Adv.* **3** e1601832
- [23] Ross J S *et al* 2017 *Nano Lett.* **17** 638
- [24] Ciarrocchi A, Unuchek D, Avsar A, Watanabe K, Taniguchi T and Kis A 2018 arXiv:1803.06405 [cond-mat.mes-hall]
- [25] Hong X, Kim J, Shi S F, Zhang Y, Jin C, Sun Y, Tongay S, Wu J, Zhang Y and Wang F 2014 *Nat. Nanotechnol.* **9** 682
- [26] Ceballos F, Bellus M Z, Chiu H Y and Zhao H 2014 *ACS Nano* **8** 12717
- [27] Meckbach L, Stroucken T and Koch S W 2018 *Phys. Rev. B* **97** 035425
- [28] Yu H, Wang Y, Tong Q, Xu X and Yao W 2015 *Phys. Rev. Lett.* **115** 187002
- [29] Fang H *et al* 2014 *Proc. Natl Acad. Sci.* **111** 6198
- [30] Kormányos A, Burkard G, Gmitra M, Fabian J, Zólyomi V, Drummond N D and Fal V 2015 *2D Mater.* **2** 022001
- [31] Yun W S, Han S W, Hong S C, Kim I G and Lee J D 2012 *Phys. Rev. B* **85** 033305
- [32] Le D, Barinov A, Preciado E, Isarraraz M, Tanabe I, Komesu T, Troha C, Bartels L, Rahman T S and Dowben P A 2015 *J. Phys.: Condens. Matter* **27** 182201
- [33] Feierabend M, Morlet A, Berghäuser G and Malic E 2017 *Phys. Rev. B* **96** 045425
- [34] Kohn W and Sham L J 1965 *Phys. Rev.* **140** A1133
- [35] Kresse G and Hafner J 1993 *Phys. Rev. B* **47** 558
- [36] Kresse G and Hafner J 1994 *Phys. Rev. B* **49** 14251
- [37] Kresse G and Furthmüller J 1996 *Phys. Rev. B* **54** 11169
- [38] Kresse G and Furthmüller J 1996 *Comput. Mater. Sci.* **6** 15
- [39] Blöchl P E 1994 *Phys. Rev. B* **50** 17953
- [40] Kresse G and Joubert D 1999 *Phys. Rev. B* **59** 1758
- [41] Perdew J P, Burke K and Ernzerhof M 1996 *Phys. Rev. Lett.* **77** 3865
- [42] Steiner S, Khmelevskiy S, Marsmann M and Kresse G 2016 *Phys. Rev. B* **93** 224425
- [43] Grimme S, Antony J, Ehrlich S and Krieg H 2010 *J. Chem. Phys.* **132** 154104
- [44] Grimme S, Ehrlich S and Goerigk L 2011 *J. Comput. Chem.* **32** 1456
- [45] Monkhorst H J and Pack J D 1976 *Phys. Rev. B* **13** 5188
- [46] Gajdoš M, Hummer K, Kresse G, Furthmüller J and Bechstedt F 2006 *Phys. Rev. B* **73** 045112
- [47] Zhu Z Y, Cheng Y C and Schwingenschlögl U 2011 *Phys. Rev. B* **84** 153402
- [48] Ramasubramaniam A 2012 *Phys. Rev. B* **86** 115409
- [49] Zhang C, Chen Y, Johnson A, Li M Y, Li L J, Mende P C, Feenstra R M and Shih C K 2015 *Nano Lett.* **15** 6494
- [50] Hsu W T *et al* 2017 *Nat. Commun.* **8** 929
- [51] Stroucken T, Grönqvist J H and Koch S W 2011 *Phys. Rev. B* **84** 205445
- [52] Stroucken T, Grönqvist J H and Koch S W 2013 *Phys. Rev. B* **87** 245428
- [53] Stroucken T and Koch S W 2017 *Optical Properties of Graphene* ed R Binder (Singapore: World Scientific) ch 2, pp 43–84
- [54] Xiao D, Liu G B, Feng W, Xu X and Yao W 2012 *Phys. Rev. Lett.* **108** 196802
- [55] Rodin A S and Castro Neto A H 2013 *Phys. Rev. B* **88** 195437
- [56] Stroucken T, Knorr A, Thomas P and Koch S W 1996 *Phys. Rev. B* **53** 2026
- [57] Stevens C E, Stroucken T, Stier A V, Paul J, Zhang H, Dey P, Crooker S A, Koch S W and Karaickaj D 2018 *Optica* **5** 749
- [58] Palummo M, Bernardi M and Grossman J C 2015 *Nano Lett.* **15** 2794
- [59] Momma K and Izumi F 2011 *J. Appl. Cryst.* **44** 1272



# Paper IV

**L. Meckbach**, J. Hader, U. Huttner, J. Neuhaus, J. T. Steiner, T. Stroucken,  
J. V. Moloney, and S. W. Koch

“Ultrafast band-gap renormalization and build-up of optical gain  
in monolayer MoTe<sub>2</sub>”

Phys. Rev. B **101**, 075401 (2020) **DOI:** 10.1103/PhysRevB.101.075401



**Ultrafast band-gap renormalization and build-up of optical gain in monolayer MoTe<sub>2</sub>**L. Meckbach,<sup>1</sup> J. Hader,<sup>2</sup> U. Huttner,<sup>1</sup> J. Neuhaus,<sup>1</sup> J. T. Steiner,<sup>1</sup> T. Stroucken<sup>⊗,1,\*</sup>, J. V. Moloney,<sup>2</sup> and S. W. Koch<sup>1</sup><sup>1</sup>*Department of Physics and Material Sciences Center, Philipps University Marburg, Renthof 5, D-35032 Marburg, Germany*<sup>2</sup>*Wyant College of Optical Sciences, University of Arizona, 1630 East University Boulevard, Tucson, Arizona 85721, USA*

(Received 18 November 2019; revised manuscript received 14 January 2020; accepted 22 January 2020; published 3 February 2020)

The dynamics of band-gap renormalization and gain build-up in monolayer MoTe<sub>2</sub>-H is investigated by evaluating the nonequilibrium Dirac-Bloch equations with the incoherent carrier-carrier and carrier-phonon scattering treated via quantum-Boltzmann type scattering equations. For the case where an approximately 300-fs-long high-intensity optical pulse generates charge-carrier densities in the gain regime, the strong Coulomb coupling leads to a relaxation of excited carriers on a few-femtosecond timescale. The pump-pulse generation of excited carriers induces a large band-gap renormalization during the timescale of the pulse. Efficient phonon coupling leads to a subsequent carrier thermalization within a few picoseconds, which defines the timescale for the optical gain build-up energetically close to the low-density exciton resonance.

DOI: [10.1103/PhysRevB.101.075401](https://doi.org/10.1103/PhysRevB.101.075401)**I. INTRODUCTION**

Monolayers (MLs) of transition-metal dichalcogenides (TMDCs) hold great promise as active material in next-generation optoelectronic devices. Unlike their bulk counterparts, MLs of many semiconducting TMDCs exhibit a direct gap with transition energies in the visible to near-infrared regime [1–7]. As compared to conventional semiconductors, they provide strong light-matter coupling and many-body effects due to carrier confinement and weak intrinsic screening of the Coulomb interaction. At low excitation levels, the electron-hole attraction leads to the formation of excitons with large binding energies that absorb as much as 10–20% of the incoming light for a single layer [8–11]. Because of this strong light-matter interaction, TMDC-based photonic devices promise high efficiency and have the potential for saturable absorbers, nanoemitters or nanolasers with the smallest possible amount of optically active material. Indeed, room temperature lasing has been reported for different TMDC materials for comparatively low pump intensities and emission frequencies centering around the respective A exciton resonances [12–14].

One of the key properties for operation and design of nanophotonic devices is the quasiparticle or optical band gap. Due to Coulombic renormalizations, the quasiparticle gap is modified by the presence of excited carriers and depends on the precise excitation conditions. In a conventional semiconductor where screening is strong, these band-gap renormalizations are typically in the meV range. In contrast, in TMDCs excitation-induced band-gap shrinkages of several hundred meV have been reported in experimental [15,16] and theoretical [17,18] investigations. The injection of external charge carriers has been proposed as a possibility to dynamically control the optical gap on a femtosecond timescale [15,16]. Furthermore, carrier-carrier and carrier-phonon scattering lead to

excitation-induced dephasing and the build-up of screening, thus dynamically modifying the exciton binding and peak gain positions. In particular, for laser applications precise predictions for the peak gain are desirable to design optical cavities correspondingly.

In this paper, we use the example of MoTe<sub>2</sub>-H to perform a microscopic calculation of the carrier dynamics and optical gain development after nonresonant optical excitation. Among semiconducting TMDC materials, MoTe<sub>2</sub>-H provides the most favourable conditions to achieve optical plasma gain. Whereas in W-based TMDCs the fundamental gap corresponds to spin-forbidden, dark transitions, in MoTe<sub>2</sub>-H, for each spin component, the fundamental gap is undoubtedly direct with a relatively large spin splitting and offset between the side and global minima in the conduction band. Without such an offset substantial amounts of electrons can leak quickly from the K/K'-points to the side valley. This reduces the carrier inversion at the global band minima and reduces or even prevents optical gain.

A well-established scheme to deduce the carrier dynamics and its influence on the optical spectra is to probe the optical response of the system at different delay times after excitation with a strong optical pump pulse. To simulate such a scenario, we extend our recently developed Dirac-Bloch equation (DBE) scheme [18–21] beyond the linear low-excitation and quasiequilibrium regime. In particular, we include incoherent interactions due to electron-electron and electron-phonon scattering to study the carrier dynamics and to determine the dephasing of the optical polarizations and the resulting broadening of optical spectra self-consistently.

**II. METHODS**

To compute the carrier dynamics and its influence on the optical spectra, we use a hybrid density functional theory (DFT) and equation of motion (EOM) approach. In a first step, we determine the relevant material parameters, i.e.,

\*tineke.stroucken@physik.uni-marburg.de

TABLE I. Material parameters for MoTe<sub>2</sub>-H, i.e., the conduction-band (valence-band) valley minima (maxima)  $\epsilon_K^c$  and  $\epsilon_\Sigma^c$  ( $\epsilon_K^v$ ), effective masses  $m_K^*$  and  $m_\Sigma^*$ , dipole-matrix elements  $d_K^\pm$ , as well as the dielectric constants  $\epsilon_\parallel^B$ ,  $\epsilon_\perp$  and out-of-plane lattice constant  $D$  ( $c/2$ ), based on our DFT calculations. For the  $K'$  and  $\Lambda$  valleys, the spin components are interchanged.

Spin	$\epsilon_K^c$ [eV]	$\epsilon_K^v$ [eV]	$\epsilon_\Sigma^c$ [eV]	$m_K^*$ [ $m_0$ ]	$m_\Sigma^*$ [ $m_0$ ]	$d_K^\pm$ [eÅ]	$\epsilon_\parallel^B$	$\epsilon_\perp$	$D$ ( $c/2$ ) [Å]
↑	1.017	0.0	1.114	0.607	0.407	3.51	20.30	10.90	6.99
↓	1.052	-0.214	1.099	0.728	0.428	2.88			

the band structure, dipole-matrix elements, as well as the dielectric constants of bulk MoTe<sub>2</sub>-H, via density functional theory. To compute the carrier dynamics and evolution of the optical spectra on a dense  $\mathbf{k}$ -grid, we use an effective four-band Hamiltonian that is based on the single-particle band structure and dipole-matrix elements derived from our DFT calculations to describe the regions of the Brillouin zone that are actually populated. Subsequently, we derive the EOM for interband polarizations that couple directly to the optical field, and the respective occupation probabilities of the involved bands. Since DFT-based band structure calculations usually underestimate the quasiparticle gap, we compute the ground-state band-gap renormalization self-consistently from the gap equations.

### A. DFT calculations

The relevant material parameters are calculated via density functional theory (DFT) [22] using the Vienna *ab initio* simulation package (VASP) [23–26] and listed in Table I. All computations employ the generalized-gradient-approximation via the Perdew-Burke-Ernzerhof (PBE) functional [27], including the spin-orbit interaction [28]. The unit cell describing a MoTe<sub>2</sub>-H ML contains three atoms in total, while a vacuum region of 20 Å around the ML is sufficient to prevent unphysical interactions with its periodic copies. The unit cell of bulk MoTe<sub>2</sub>-H in the common 2H form, used in the computations of the bulk dielectric constant, consists of two MLs and contains six atoms. The Van-der-Waals interaction between neighboring layers is modeled via Grimme’s dispersion correction method (PBE-D3) [29,30]. In both cases, bulk and ML, a full relaxation of atomic positions and the unit cell shape and size is performed until all inter-atomic forces are smaller than  $2.5 \times 10^{-3}$  eV/Å. The reciprocal space is sampled by a  $15 \times 15 \times 3$  Monkhorst-Pack [31]  $k$ -mesh in the case of the ML and  $10 \times 10 \times 10$  in the bulk case. The cutoff energy of the plane wave expansion is set to 750 eV for the structural relaxations and the MLs properties, while a value of 500 eV is used in the bulk case. The self-consistency cycle of the electronic minimization is repeated until an energy convergence criterion of  $10^{-8}$  eV is reached.

The resulting ML band structure is shown in Fig. 1 and exhibits direct gaps at the  $K$  and  $K'$  points of the Brillouin zone with a noninteracting gap of  $\Delta_A = 1.017$  eV and  $\Delta_B = 1.266$  eV for the A ( $K_\uparrow/K'_\downarrow$ ) and B ( $K_\downarrow/K'_\uparrow$ ) bands. As in other TMDC materials, the atomic orbitals predominantly contributing to the valence and conduction bands at the  $K$  and  $K'$  point are the  $d$ -type Mo-orbitals with equal parity. Furthermore, the conduction bands display a spin splitting of  $-35$  meV and side valleys at the  $\Sigma/\Lambda$  points, that are

97 meV ( $\Sigma_\uparrow/\Lambda_\downarrow$ ) and 82 meV ( $\Lambda_\uparrow/\Sigma_\downarrow$ ) above the respective  $K/K'$ -valley minima. These values are on the lower end of the range of published values that have been obtained using different functionals for the exchange correlation potential or GW corrections [32–34] and sufficiently large to prevent an excitation-induced transition from a direct to indirect band gap [35,36].

The interband dipole-matrix elements are accessed via the linear optics routine in VASP as described in Ref. [37] and include contributions associated with a geometric phase. Furthermore, we compute the macroscopic static dielectric tensor of bulk MoTe<sub>2</sub>-H using density functional perturbation theory as described in Refs. [37,38], following Ref. [39].

### B. DFT-based model Hamiltonian

To model the DFT band structure presented in the previous section, we include the two spin-split valence and conduction bands to obtain an effective four-band Hamiltonian. As the different valleys are separated by large barriers, intervalley scattering is expected to be significantly slower than intravalley scattering and, on the ultrashort timescale, the valley index can be considered to be approximately conserved. Hence, we

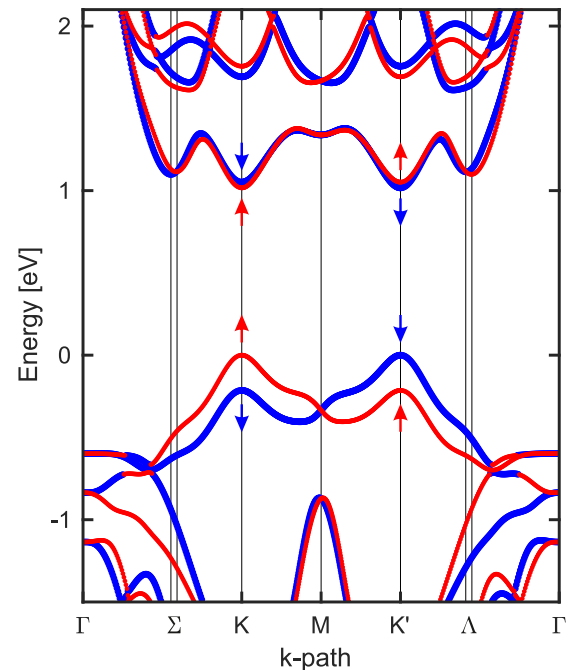


FIG. 1. DFT band structure of a MoTe<sub>2</sub>-H ML. Bands with spin-up are depicted in red, bands with spin-down in blue.

TABLE II. Resulting MDF model parameters for MoTe<sub>2</sub>-H.

Band	$\Delta$ [eV]	$\hbar v_F$ [eVÅ]	$E_F$ [eV]
A	1.017	2.526	0.509
B	1.266	2.574	0.419

write the single particle part of the Hamiltonian as

$$H_0 = \sum_{\alpha\mathbf{k}} \epsilon_{\alpha\mathbf{k}} c_{\alpha\mathbf{k}}^\dagger c_{\alpha\mathbf{k}},$$

where  $\alpha$  combines the spin, valley, and band index. Using the  $\mathbf{p} \cdot \mathbf{A}$  gauge, the light matter interaction is given by

$$H_{\text{LM}} = \frac{e}{m_0 c} \sum_{\alpha\alpha'\mathbf{k}} \mathbf{A} \cdot \mathbf{p}_{\alpha\alpha'\mathbf{k}} c_{\alpha\mathbf{k}}^\dagger c_{\alpha'\mathbf{k}},$$

where the interband momentum matrix elements are related to the DFT dipole matrix elements via  $\frac{e\hbar}{m_0} \mathbf{p}_{\alpha\alpha'\mathbf{k}} = (\epsilon_{\alpha'\mathbf{k}} - \epsilon_{\alpha\mathbf{k}}) \mathbf{d}_{\alpha\alpha'}$ . Whereas the side valleys at  $\Sigma/\Lambda$  are modeled within the effective mass approximation, we treat the  $K$  and  $K'$  valleys utilizing the widely used massive Dirac-Fermion (MDF) model Hamiltonian [40] to account for the geometric phase contained in the dipole matrix elements. The MDF Hamiltonian has the relativistic dispersion

$$\epsilon_{i\mathbf{k}}^{c/v} = E_{F,i} \pm \frac{1}{2} \sqrt{\Delta_i^2 + (2\hbar v_{F,i} k)^2}, \quad (1)$$

where  $i = s\tau$  combines the spin and valley index,  $\Delta_i$ ,  $v_{F,i}$ , and  $E_{F,i}$  are the spin- and valley-dependent gap, Fermi velocity and Fermi level, respectively. Whereas the spin- and valley-dependent band gaps are directly taken from our DFT calculations, the Fermi-velocities of the A and B bands are determined to reproduce the DFT band structure around the  $K/K'$  points and listed in Table II. Within the MDF model, the nonvanishing dipole moments at the Dirac points are solely associated with the geometric phase or pseudospin. They are related to the Fermi velocity via  $d_i^\pm = e\sqrt{2}\hbar v_{F,i}/\Delta_i$  and agree within less than 5% with the DFT dipole matrix elements. The approximated band structure is shown together with the DFT bands and the equilibrium carrier distributions at the delay time  $\tau = 2.5$  ps in Fig. 2.

The Coulomb interaction Hamiltonian

$$H_C = \frac{1}{2} \sum_{\mathbf{q} \neq 0} \sum_{\alpha\alpha'\beta\beta'\mathbf{k}\mathbf{k}'} V_{\mathbf{q};\mathbf{k}';\mathbf{k}}^{\alpha\beta\beta'\alpha'} c_{\alpha\mathbf{k}-\mathbf{q}}^\dagger c_{\beta\mathbf{k}'+\mathbf{q}}^\dagger c_{\beta'\mathbf{k}'} c_{\alpha'\mathbf{k}}$$

contains the quasi-2D Coulomb matrix elements

$$V_{\mathbf{q};\mathbf{k}';\mathbf{k}}^{\alpha\beta\beta'\alpha'} = \int_{ec} d^3r \int_{ec} d^3r' u_{\alpha\mathbf{k}-\mathbf{q}}^*(\mathbf{r}) u_{\beta\mathbf{k}'+\mathbf{q}}^*(\mathbf{r}') \times V_{\mathbf{q}}(z - z') u_{\beta'\mathbf{k}'}(\mathbf{r}') u_{\alpha'\mathbf{k}}(\mathbf{r})$$

that are computed using the DFT wave functions. The Coulomb interaction potential  $V_{\mathbf{q}}(z - z')$  for the unexcited ML is determined from Poisson's equation according to Ref. [20]. Here, we use the parameters  $\epsilon_{\parallel}$  and  $\epsilon_{\perp}$  for the in- and out-of-plane dielectric constants based on bulk DFT calculations of MoTe<sub>2</sub>-H. From the previously stated bulk in-plane dielectric constant  $\epsilon_{\parallel}^B$  we obtained the nonresonant 2D contribution  $\epsilon_{\parallel} = 15.32$  as described in Ref. [20]. The so determined “bare” Coulomb interaction potential contains screening contributions from the dielectric environment and all remote bands,

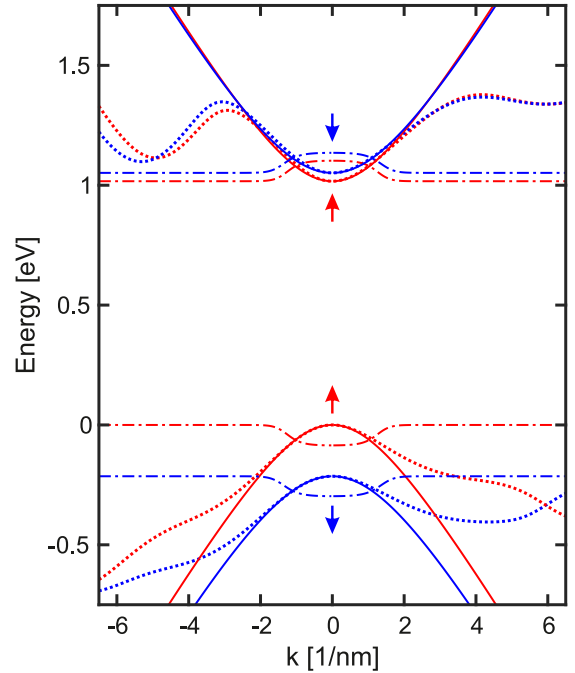


FIG. 2. Comparison of the relevant DFT bands (dotted) with the approximated unrenormalized relativistic band dispersion (solid). Arrows indicate the spin of the correspondingly colored bands. The dashed-dotted lines show the equilibrium carrier distributions (2.5 ps after excitation) for the excitation conditions discussed in the text. For the distributions the baseline is taken to be the edge of the corresponding band and the maximum values are set to be the corresponding chemical potentials.

as well as the ground-state screening contributions from the valence and conduction bands.

The interaction with longitudinal optical (LO) phonons, which has been shown to be the most effective phonon-coupling contribution in monolayer MoTe<sub>2</sub>-H [41], is contained in the Fröhlich Hamiltonian

$$H_{e-\text{LO}} = \sum_{\alpha\mathbf{k},\mathbf{q}} g_{\mathbf{q}}^0 c_{\alpha,\mathbf{k}+\mathbf{q}}^\dagger c_{\alpha,\mathbf{k}} (b_{\mathbf{q}} + b_{-\mathbf{q}}^\dagger).$$

For the “bare” Fröhlich-interaction matrix element  $g_{\mathbf{q}}^0$ , we use the explicit expression based on the analytical model of Sohier *et al.* [41] that, similarly to the “bare” Coulomb interaction, already contains background screening contributions from the remote bands and dielectric environment.

### C. Dirac-Bloch Equations

To evaluate the material response after optical excitation, we compute the microscopic interband polarizations  $P_{i\mathbf{k}} = \langle c_{i\mathbf{k}}^\dagger c_{i\mathbf{k}} \rangle$  and occupation probabilities  $f_{i\mathbf{k}}^\lambda = \langle c_{i\mathbf{k}}^\dagger c_{i\mathbf{k}} \rangle$  ( $\lambda = c, v$ ) from the Dirac Bloch equations (DBE)

$$i\hbar \frac{d}{dt} P_{i\mathbf{k}} = (\Sigma_{i\mathbf{k}}^c - \Sigma_{i\mathbf{k}}^v) P_{i\mathbf{k}} + (f_{i\mathbf{k}}^v - f_{i\mathbf{k}}^c) \Omega_{i\mathbf{k}} + i\hbar \frac{d}{dt} P_{i\mathbf{k}} \Big|_{\text{corr.}}, \quad (2)$$

$$i\hbar \frac{d}{dt} f_{i\mathbf{k}}^{c/v} = \pm 2i\Im[P_{i\mathbf{k}} \Omega_{i\mathbf{k}}^*] + i\hbar \frac{d}{dt} f_{i\mathbf{k}}^{c/v} \Big|_{\text{corr.}}. \quad (3)$$

Here,

$$\Sigma_{ik}^c = \epsilon_{ick} - \sum_{k'} [V_{k-k';k';k}^{cccc} - V_{k-k';k';k}^{cvev}] f_{ik'}^c + \sum_{k'} [V_{k-k';k';k}^{cvcc} P_{ik'} + c.c.], \quad (4)$$

$$\Sigma_{ik}^v = \epsilon_{ivk} - \sum_{k'} [V_{k-k';k';k}^{vvvv} - V_{k-k';k';k}^{vvcv}] f_{ik'}^v + \sum_{k'} [V_{k-k';k';k}^{vvvc} P_{ik'} + c.c.], \quad (5)$$

$$\Omega_{ik} = \frac{e}{m_0 c} \mathbf{A} \cdot \mathbf{p}_{icvk} - \sum_{k'} V_{k-k';k';k}^{cvvv} (f_{ik'}^v - f_{ik'}^c) - \sum_{k'} [V_{k-k';k';k}^{cvvc} P_{ik'} + V_{k-k';k';k}^{ccvv} P_{ik'}^*] \quad (6)$$

contain the Hartree-Fock contributions to the single particle energy renormalizations  $\Sigma_{ik}^{c/v}$  and the renormalization to the Rabi energy  $\Omega_{ik}$ , while all many-body correlations that arise from the two-particle Coulomb interaction and carrier-phonon scattering are contained within  $\frac{d}{dt} P_{ik}|_{\text{corr.}}$  and  $\frac{d}{dt} f_{ik}^{c/v}|_{\text{corr.}}$ , respectively.

The DBE are formally equivalent to the semiconductor Bloch equations (SBE), but the expression for the renormalized Rabi and single particle energies differ by the Coulomb matrix elements of the type  $V_{k-k';k';k}^{cvvv}$  and  $V_{k-k';k';k}^{ccvv}$  referring to Auger- and pair creation/annihilation processes, where at least one of the particles changes its band index. Within the MDF model Hamiltonian, these Coulomb matrix elements contain the geometric phase and induce a coupling between a dark static interband polarization and the carrier populations. Consequently, the initial condition  $f_{ik}^c = 1 - f_{ik}^v = P_{ik} = 0$  does not correspond to a stationary solution of the DBE in the absence of an external field and hence, does not specify the system's ground state.

To determine the ground-state band renormalization, which is the initial state before the pump pulse arrives, we require a stationary solution of the Dirac-Bloch equations in the absence of an external field as described in Refs. [19,20,42]. This leads to the gap equations

$$\tilde{\Delta}_{ik} = \Delta_i + \frac{1}{2} \sum_{k'} V_{|k-k'|} \frac{\tilde{\Delta}_{ik'}}{\tilde{\epsilon}_{ik'}}, \quad (7)$$

$$\tilde{v}_{ik} = v_{F,i} + \frac{1}{2} \sum_{k'} V_{|k-k'|} \frac{k'}{k} \frac{\tilde{v}_{ik'}}{\tilde{\epsilon}_{ik'}} \cos(\theta_k - \theta_{k'}), \quad (8)$$

from which the ground-state quasiparticle dispersion is obtained via  $\tilde{\epsilon}_{ik}^{e/h} = \frac{1}{2} \sqrt{\tilde{\Delta}_{ik}^2 + (2\hbar\tilde{v}_{ik})^2}$ . Similar to the Coulomb matrix elements  $V_{\mathbf{q};\mathbf{k};\mathbf{k}}^{\alpha\beta\beta'\alpha'}$ , the ‘‘bare’’ quasi-2D Coulomb interaction entering Eqs. (7) and (8) already contains the previously mentioned background and ground-state screening contributions. The solution of the gap equations yields a rigid shift of the single-particle dispersion with an interacting gap  $\tilde{\Delta}_{ik}$  that depends on the dielectric environment. For a suspended ML, we find a ground-state band renormalization of 549 meV for the A band, that shrinks by 70 meV for a SiO<sub>2</sub>-supported MoTe<sub>2</sub>-H ML.

In the low density limit, where correlation effects can be neglected, we find the transition energies for the lowest 1s-

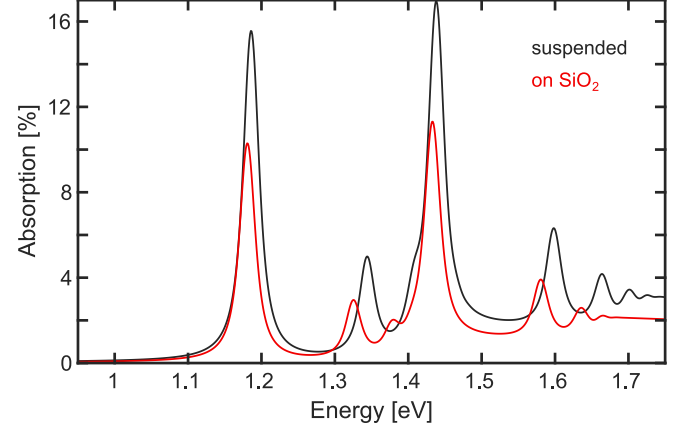


FIG. 3. Linear absorption spectra of a suspended (black) and SiO<sub>2</sub>-supported (red) ML MoTe<sub>2</sub>-H. Here, we used a phenomenological dephasing rate of  $\hbar\gamma = 10$  meV. To match the experimentally observed data, the spectra have been shifted by  $-0.044$  eV.

exciton resonance at 1.230 and 1.225 eV, for the suspended and SiO<sub>2</sub> supported MoTe<sub>2</sub>-H ML, respectively, which is slightly above the experimentally observed low-temperature resonance energy of about 1.18 eV for the SiO<sub>2</sub>-supported ML [43]. To allow for a direct comparison between the predicted excitation-induced modifications of the optical spectra with the experiment, we correct the bare DFT computed band gap and shift all spectra by  $-0.044$  eV. The resulting linear absorption spectra for a freely suspended and quartz-supported MoTe<sub>2</sub>-H ML are shown in Fig. 3 using a phenomenological dephasing rate of  $\hbar\gamma = 10$  meV.

#### D. Many-body correlations

Incoherent processes that lead to the dephasing of the microscopic polarizations and to the carrier relaxation dynamics are contained within  $\frac{d}{dt} P_{ik}|_{\text{corr.}}$  and  $\frac{d}{dt} f_{ik}^{c/v}|_{\text{corr.}}$ , respectively. Using the notation  $P_{\mathbf{k}}^{\alpha\alpha'} = \langle c_{\alpha\mathbf{k}}^\dagger c_{\alpha'\mathbf{k}} \rangle$ ,  $f_{\mathbf{k}}^{\alpha} = P_{\mathbf{k}}^{\alpha\alpha}$  for the single-particle expectation values, the Coulomb interaction leads to a contribution

$$i\hbar \frac{d}{dt} P_{\mathbf{k}}^{\alpha\alpha'} \Big|_{\text{corr.}}^{\text{el.}} = \sum_{\mathbf{q} \neq 0} [\Delta I_{\mathbf{q};\mathbf{k}}^{\alpha\alpha'} - (\Delta I_{\mathbf{q};\mathbf{k}}^{\alpha'\alpha})^*], \quad (9)$$

where

$$I_{\mathbf{q};\mathbf{k}}^{\alpha\alpha'} = \sum_{\beta\gamma\gamma'} \sum_{\mathbf{k}'} V_{-\mathbf{q};\mathbf{k}';\mathbf{k}-\mathbf{q}}^{\alpha'\gamma\gamma'\beta} C_{\mathbf{q};\mathbf{k};\mathbf{k}}^{\alpha\gamma\gamma'\beta}$$

are the density-assisted transition/occupation probabilities that contain the two-particle expectation values  $C_{\mathbf{q};\mathbf{k};\mathbf{k}}^{\alpha\gamma\gamma'\beta} = \langle c_{\alpha\mathbf{k}}^\dagger c_{\gamma\mathbf{k}-\mathbf{q}}^\dagger c_{\gamma'\mathbf{k}'} c_{\beta\mathbf{k}-\mathbf{q}} \rangle$ . In general, the two-particle expectation values can be divided into a Hartree-Fock (singlet) part and a correlated part according to

$$C_{\mathbf{q};\mathbf{k};\mathbf{k}}^{\alpha\gamma\gamma'\beta} = C_{\mathbf{q};\mathbf{k};\mathbf{k}}^{\alpha\gamma\gamma'\beta}|_S + \Delta C_{\mathbf{q};\mathbf{k};\mathbf{k}}^{\alpha\gamma\gamma'\beta},$$

and it is easily verified that the Hartree-Fock contributions to the renormalized single particle energies and Rabi-energy given in Eqs. (4)–(6) correspond to the singlet part  $I_{\mathbf{q};\mathbf{k}}^{\alpha\alpha'}|_S$ .

Physically,  $I_{\mathbf{q};\mathbf{k}}^{\alpha\alpha'}$  describes Coulomb mediated transitions from all initial states  $\beta\mathbf{k} - \mathbf{q}$  to the final state  $\alpha\mathbf{k}$  via the

intermediate states  $\gamma\mathbf{k}' - \mathbf{q}$ ,  $\gamma'\mathbf{k}'$  with the Coulomb matrix elements  $V_{-\mathbf{q};\mathbf{k};\mathbf{k}-\mathbf{q}}^{\alpha'\gamma\gamma'\beta}$ . As mentioned above, the Coulomb matrix elements with  $\beta \neq \alpha'$  and/or  $\gamma \neq \gamma'$  correspond to Auger recombinations and pair creation/annihilation processes. Whereas these processes give a small contribution to the static ground-state renormalization of the valence bands contained in the singlet parts, they are strongly nonresonant for the optically induced density dependent modifications contained in the correlated part. As verified numerically, the timescales for Auger recombinations and pair creation/annihilation processes are four to five orders of magnitude longer than those of intraband scattering processes and will be neglected in the following. Additionally neglecting the weak orbital and  $\mathbf{k}$ ,  $\mathbf{k}'$ -dependence of the Coulomb matrix elements, the expression for the density-assisted transition/occupation probabilities simplifies to

$$I_{\mathbf{q};\mathbf{k}}^{\alpha\alpha'} = \tilde{V}_{\mathbf{q}} \langle c_{\alpha\mathbf{k}}^\dagger \rho_{\mathbf{q}} c_{\alpha'\mathbf{k}-\mathbf{q}} \rangle,$$

where  $\tilde{V}_{\mathbf{q}}$  is a quasi-2D Coulomb matrix element that again contains ground-state and background screening contributions only and  $\rho_{\mathbf{q}} = \sum_{\beta\mathbf{k}'} c_{\beta\mathbf{k}'-\mathbf{q}}^\dagger c_{\beta\mathbf{k}'}$  is the density operator.

To derive an approximation for the correlated part of the density-assisted transition amplitudes, we employ a second-order cluster expansion where we derive the EOM for the relevant two-particle correlations and factorize the occurring three-particle expectation values into singlet and doublet contributions [44]. Within this approximation, the singlet factorizations act as source terms for the two-particle correlations, whereas the doublet contributions lead to a renormalization of the single-particle energies, excitonic correlations, biexcitons, and screening of the Coulomb interaction in the Hartree-Fock contributions. Assuming screening to be the dominant correlation effect at elevated densities, we write the EOM for the relevant two-particle correlations as

$$\begin{aligned} i\hbar \frac{d}{dt} \Delta C_{\mathbf{q};\mathbf{k};\mathbf{k}}^{\alpha\beta\beta\alpha'} &= (\Delta \Sigma_{\mathbf{q};\mathbf{k};\mathbf{k}}^{\alpha\beta\beta\alpha'} - i\hbar\gamma_T) \Delta C_{\mathbf{q};\mathbf{k};\mathbf{k}}^{\alpha\beta\beta\alpha'} \\ &+ (f_{\mathbf{k}'-\mathbf{q}}^\beta - f_{\mathbf{k}'}^\beta) I_{\mathbf{q};\mathbf{k}}^{\alpha\alpha'} + S_{\mathbf{q};\mathbf{k};\mathbf{k}}^{\alpha\beta\beta\alpha'} \\ &+ \text{remaining doublets}, \end{aligned} \quad (10)$$

where we explicitly quoted only the doublet correlations that lead to the build-up of screening,  $\Delta \Sigma_{\mathbf{q};\mathbf{k};\mathbf{k}}^{\alpha\beta\beta\alpha'} = \Sigma_{\alpha'\mathbf{k}-\mathbf{q}} + \Sigma_{\beta\mathbf{k}'} - \Sigma_{\beta\mathbf{k}'-\mathbf{q}} - \Sigma_{\alpha\mathbf{k}}$ , and included a phenomenological dephasing of the triplets  $\gamma_T$ . Note that in Eq. (10), the density assisted transition probabilities  $I_{\mathbf{q};\mathbf{k}}^{\alpha\alpha'}$  contain both the singlet and correlated part and the remaining singlet sources are contained in  $S_{\mathbf{q};\mathbf{k};\mathbf{k}}^{\alpha\beta\beta\alpha'}$ . Using the shorthand notation  $\bar{f}_{\mathbf{k}}^\beta = 1 - f_{\mathbf{k}}^\beta$ , the singlet sources are explicitly given by

$$\begin{aligned} S_{\mathbf{q};\mathbf{k};\mathbf{k}}^{\alpha\beta\beta\alpha'} &= \tilde{V}_{\mathbf{q}} (P_{\mathbf{k}}^{\alpha\alpha'} f_{\mathbf{k}'-\mathbf{q}}^\beta \bar{f}_{\mathbf{k}'}^\beta - P_{\mathbf{k}-\mathbf{q}}^{\alpha\alpha'} \bar{f}_{\mathbf{k}'-\mathbf{q}}^\beta f_{\mathbf{k}'}^\beta) \\ &+ \tilde{V}_{\mathbf{k}-\mathbf{k}'} P_{\mathbf{k}}^{\alpha\beta} \sum_{\gamma} P_{\mathbf{k}'-\mathbf{q}}^{\beta\gamma} (P_{\mathbf{k}-\mathbf{q}}^{\gamma\alpha'} - \delta_{\gamma\alpha'}) \\ &- \tilde{V}_{\mathbf{k}-\mathbf{k}'} P_{\mathbf{k}'}^{\alpha\beta} \sum_{\gamma} P_{\mathbf{k}-\mathbf{q}}^{\gamma\alpha'} (P_{\mathbf{k}'-\mathbf{q}}^{\beta\gamma} - \delta_{\gamma\beta}) \\ &+ \tilde{V}_{\mathbf{k}-\mathbf{k}'} (P_{\mathbf{k}'-\mathbf{q}}^{\beta\alpha'} - P_{\mathbf{k}-\mathbf{q}}^{\beta\alpha'}) \sum_{\gamma} P_{\mathbf{k}}^{\alpha\gamma} P_{\mathbf{k}'}^{\gamma\beta} \end{aligned} \quad (11)$$

and treated on the level of a second Born approximation.

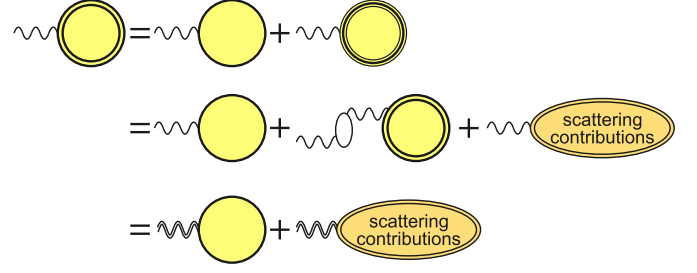


FIG. 4. Diagrammatic representation of the density assisted transition/occupation probabilities. The full density assisted transition amplitudes are represented by twofold contoured circles whereas the singlet and correlated parts are represented by simple and threefold contoured circles, respectively. Similarly, simple and doubly contoured wiggles represent the “bare” and screened Coulomb interaction, respectively. The upper line corresponds to the division into the singlet (Hartree-Fock) and correlated part and the second and third lines represent the first and second line of Eq. (12).

If one assumes quasistatic single-particle distributions  $f_{\mathbf{k}}^\beta$  and neglects the remaining doublet contributions, then one can analytically solve Eq. (10) in frequency space [44]. A subsequent summation over  $\beta$  and  $\mathbf{k}'$  yields the closed expression

$$\begin{aligned} I_{\mathbf{q};\mathbf{k}}^{\alpha\alpha'}(\omega) &= I_{\mathbf{q};\mathbf{k}}^{\alpha\alpha'}(\omega)|_S + \tilde{V}_{\mathbf{q}} \Pi_{\mathbf{q};\mathbf{k}}^{\alpha\alpha'}(\omega + i\gamma_T) I_{\mathbf{q};\mathbf{k}}^{\alpha\alpha'}(\omega) \\ &+ \tilde{V}_{\mathbf{q}} T_{\mathbf{q};\mathbf{k}}^{\alpha\alpha'}(\omega) \\ &= W_{\mathbf{q};\mathbf{k}}^{\alpha\alpha'}(\omega + i\gamma_T) \sum_{\beta\mathbf{k}'} C_{\mathbf{q};\mathbf{k};\mathbf{k}}^{\alpha\beta\beta\alpha'}(\omega)|_S \\ &+ W_{\mathbf{q};\mathbf{k}}^{\alpha\alpha'}(\omega + i\gamma_T) T_{\mathbf{q};\mathbf{k}}^{\alpha\alpha'}(\omega), \end{aligned} \quad (12)$$

where the screened Coulomb matrix element  $W_{\mathbf{q};\mathbf{k}}^{\alpha\alpha'}$  is given by Dyson's equation

$$W_{\mathbf{q};\mathbf{k}}^{\alpha\alpha'}(\omega) = \tilde{V}_{\mathbf{q}} + \tilde{V}_{\mathbf{q}} \Pi_{\mathbf{q};\mathbf{k}}^{\alpha\alpha'}(\omega) W_{\mathbf{q};\mathbf{k}}^{\alpha\alpha'}(\omega)$$

and

$$\begin{aligned} \Pi_{\mathbf{q};\mathbf{k}}^{\alpha\alpha'}(\omega) &= \Pi_{\mathbf{q}}(\omega) + (\Sigma_{\alpha\mathbf{k}} - \Sigma_{\alpha'\mathbf{k}-\mathbf{q}})/\hbar, \\ \Pi_{\mathbf{q}}(\omega) &= \sum_{\beta\mathbf{k}'} \frac{f_{\mathbf{k}'-\mathbf{q}}^\beta - f_{\mathbf{k}'}^\beta}{\hbar\omega + \Sigma_{\beta\mathbf{k}'-\mathbf{q}} - \Sigma_{\beta\mathbf{k}'}} \end{aligned}$$

is the standard Lindhard polarization function. Furthermore, we define

$$T_{\mathbf{q};\mathbf{k}}^{\alpha\alpha'}(\omega) = \sum_{\beta\mathbf{k}'} \frac{S_{\mathbf{q};\mathbf{k};\mathbf{k}}^{\alpha\beta\beta\alpha'}(\omega)}{\hbar\omega - \Delta \Sigma_{\mathbf{q};\mathbf{k};\mathbf{k}}^{\alpha\beta\beta\alpha'} + i\hbar\gamma_T}.$$

Hence, the doublet contributions explicitly written in Eq. (10) lead to screening of the Coulomb potential both in the Hartree-Fock and scattering contributions, as shown schematically in Fig. 4. Note that at this level of approximation, the energy denominators in the scattering integrals and Lindhard polarization function still contain the unscreened Hartree-Fock renormalizations. However, it can be shown that screening in these contributions is introduced by the inclusion of the next level cluster expansion [44] and we will replace all unscreened energy renormalizations  $\Sigma_{\mathbf{k}}^\alpha$  by their screened counterparts  $\tilde{\Sigma}_{\mathbf{k}}^\alpha$  in the following.

If one would neglect the remaining scattering integrals contained in  $\sum_{\mathbf{q}} W_{\mathbf{q};\mathbf{k}}^{\alpha\alpha'} T_{\mathbf{q};\mathbf{k}}^{\alpha\alpha'}$ , then one would thus arrive at the level of the screened Hartree-Fock approximation where all the Coulomb matrix elements in Eqs. (4)–(6) are replaced by their screened counterparts. The remaining scattering contributions predominantly lead to carrier relaxation and excitation-induced dephasing of the coherent interband polarization. They contain only small additional renormalizations of the single-particle dispersion. Hence, the screened Hartree-Fock renormalizations of the single-particle energies provide a useful measure for the band-gap renormalization in the presence of excited carriers. In particular, in a fully incoherent quasistatic equilibrium situation, a steady state solution of the screened DBE equations yields the density-dependent gap equations

$$\tilde{\Delta}_{i\mathbf{k}} = \Delta_i + \frac{1}{2} \sum_{\mathbf{k}'} W_{|\mathbf{k}-\mathbf{k}'|} \frac{\tilde{\Delta}_{i\mathbf{k}'}}{\tilde{\epsilon}_{i\mathbf{k}'}} (f_{i\mathbf{k}'}^v - f_{i\mathbf{k}'}^c), \quad (13)$$

$$\tilde{v}_{i\mathbf{k}} = v_{F,i} + \frac{1}{2} \sum_{\mathbf{k}'} W_{|\mathbf{k}-\mathbf{k}'|} \frac{k'}{k} \frac{\tilde{v}_{i\mathbf{k}'}}{\tilde{\epsilon}_{i\mathbf{k}'}} \cos(\theta_{\mathbf{k}} - \theta_{\mathbf{k}'}) (f_{i\mathbf{k}'}^v - f_{i\mathbf{k}'}^c), \quad (14)$$

where  $W_{\mathbf{q}}$  is the statically screened Coulomb interaction.

Equation (12) together with Eq. (11) provides an efficient scheme to compute the Coulomb correlations numerically. As a consequence of the strong Coulomb interaction in TMDCs and the large associated exciton binding, it is important to properly include the full frequency dependence of the screened interband matrix elements  $W_{\mathbf{q};\mathbf{k}}^{\text{vc}}$  which enter the scattering contributions of the microscopic polarizations and lead to memory effects beyond the Markov approximation.

In addition to the Coulomb correlations, the inclusion of the Fröhlich Hamiltonian introduces the scattering of excited charge carriers within their bands by the absorption or emission of LO phonons. These are evaluated on the level of quantum-kinetic theory in second Born approximation. Our analysis shows that, similarly as for the Coulombic scattering rates, it is sufficient to treat the phonon scattering rates of the quasistatic carrier distribution functions within the Markov approximation, whereas it is crucial to maintain the full frequency dependency for the polarization-phonon scattering rates. The resulting phononic contributions to the electron and polarization scattering rates are given by

$$\begin{aligned} \left. \frac{d}{dt} f_{s\mathbf{k}}^c \right|_{\text{corr.}}^{\text{ph.}} &= \frac{2\pi}{\hbar} \sum_{\mathbf{q}} g_{\mathbf{q}}^0 g_{\mathbf{q};\mathbf{k}+\mathbf{q}}^{\text{cc}} \mathcal{D}_{\eta} (\tilde{\Sigma}_{s\mathbf{k}+\mathbf{q}}^c - \tilde{\Sigma}_{s\mathbf{k}}^c - \hbar\omega_{\mathbf{q}}) [(n_{\mathbf{q}}+1) f_{s\mathbf{k}+\mathbf{q}}^c \tilde{f}_{s\mathbf{k}}^c - n_{\mathbf{q}} f_{s\mathbf{k}}^c \tilde{f}_{s\mathbf{k}+\mathbf{q}}^c] \\ &+ \frac{2\pi}{\hbar} \sum_{\mathbf{q}} g_{\mathbf{q}}^0 g_{\mathbf{q};\mathbf{k}}^{\text{cc}} \mathcal{D}_{\eta} (\tilde{\Sigma}_{s\mathbf{k}-\mathbf{q}}^c - \tilde{\Sigma}_{s\mathbf{k}}^c + \hbar\omega_{\mathbf{q}}) [n_{\mathbf{q}} f_{s\mathbf{k}-\mathbf{q}}^c \tilde{f}_{s\mathbf{k}}^c - (1+n_{\mathbf{q}}) f_{s\mathbf{k}}^c \tilde{f}_{s\mathbf{k}-\mathbf{q}}^c], \end{aligned} \quad (15)$$

$$i\hbar \left. \frac{d}{dt} P_{s\mathbf{k}} \right|_{\text{corr.}}^{\text{ph.}} = i\hbar \left. \frac{d}{dt} P_{s\mathbf{k}} \right|_{\text{corr.}}^{\text{c,ph.}} + i\hbar \left. \frac{d}{dt} P_{s\mathbf{k}} \right|_{\text{corr.}}^{\text{v,ph.}}, \quad (16)$$

$$\begin{aligned} i\hbar \left. \frac{d}{dt} P_{s\mathbf{k}} \right|_{\text{corr.}}^{\text{c,ph.}} &= \mathcal{F} \left[ \sum_{\mathbf{q}} g_{\mathbf{q}}^0 g_{\mathbf{q};\mathbf{k}}^{\text{vc}} \left\{ \frac{\tilde{f}_{s\mathbf{k}-\mathbf{q}}^c n_{\mathbf{q}} + f_{s\mathbf{k}-\mathbf{q}}^c (1+n_{\mathbf{q}})}{\hbar(\omega + \omega_{\mathbf{q}}) + \tilde{\Sigma}_{s\mathbf{k}}^c - \tilde{\Sigma}_{s\mathbf{k}-\mathbf{q}}^c + i\eta} + \frac{\tilde{f}_{s\mathbf{k}-\mathbf{q}}^c (1+n_{\mathbf{q}}) + f_{s\mathbf{k}-\mathbf{q}}^c n_{\mathbf{q}}}{\hbar(\omega - \omega_{\mathbf{q}}) + \tilde{\Sigma}_{s\mathbf{k}}^c - \tilde{\Sigma}_{s\mathbf{k}-\mathbf{q}}^c + i\eta} \right\} P_{s\mathbf{k}} \right. \\ &\left. - \sum_{\mathbf{q}} g_{\mathbf{q}}^0 g_{\mathbf{q};\mathbf{k}+\mathbf{q}}^{\text{vc}} \left\{ \frac{\tilde{f}_{s\mathbf{k}}^c n_{\mathbf{q}} + f_{s\mathbf{k}}^c (1+n_{\mathbf{q}})}{\hbar(\omega + \omega_{\mathbf{q}}) + \tilde{\Sigma}_{s\mathbf{k}+\mathbf{q}}^c - \tilde{\Sigma}_{s\mathbf{k}}^c + i\eta} + \frac{\tilde{f}_{s\mathbf{k}}^c (1+n_{\mathbf{q}}) + f_{s\mathbf{k}}^c n_{\mathbf{q}}}{\hbar(\omega - \omega_{\mathbf{q}}) + \tilde{\Sigma}_{s\mathbf{k}+\mathbf{q}}^c - \tilde{\Sigma}_{s\mathbf{k}}^c + i\eta} \right\} P_{s\mathbf{k}+\mathbf{q}} \right], \end{aligned} \quad (17)$$

$$\begin{aligned} i\hbar \left. \frac{d}{dt} P_{s\mathbf{k}} \right|_{\text{corr.}}^{\text{v,ph.}} &= \mathcal{F} \left[ \sum_{\mathbf{q}} g_{\mathbf{q}}^0 g_{\mathbf{q};\mathbf{k}+\mathbf{q}}^{\text{vc}} \left\{ \frac{f_{s\mathbf{k}+\mathbf{q}}^v n_{\mathbf{q}} + \tilde{f}_{s\mathbf{k}+\mathbf{q}}^v (1+n_{\mathbf{q}})}{\hbar(\omega + \omega_{\mathbf{q}}) + \tilde{\Sigma}_{s\mathbf{k}+\mathbf{q}}^v - \tilde{\Sigma}_{s\mathbf{k}}^c + i\eta} + \frac{f_{s\mathbf{k}+\mathbf{q}}^v (1+n_{\mathbf{q}}) + \tilde{f}_{s\mathbf{k}+\mathbf{q}}^v n_{\mathbf{q}}}{\hbar(\omega - \omega_{\mathbf{q}}) + \tilde{\Sigma}_{s\mathbf{k}+\mathbf{q}}^v - \tilde{\Sigma}_{s\mathbf{k}}^c + i\eta} \right\} P_{s\mathbf{k}} \right. \\ &\left. - \sum_{\mathbf{q}} g_{\mathbf{q}}^0 g_{\mathbf{q};\mathbf{k}}^{\text{vc}} \left\{ \frac{f_{s\mathbf{k}}^v n_{\mathbf{q}} + \tilde{f}_{s\mathbf{k}}^v (1+n_{\mathbf{q}})}{\hbar(\omega + \omega_{\mathbf{q}}) + \tilde{\Sigma}_{s\mathbf{k}}^v - \tilde{\Sigma}_{s\mathbf{k}-\mathbf{q}}^c + i\eta} + \frac{f_{s\mathbf{k}}^v (1+n_{\mathbf{q}}) + \tilde{f}_{s\mathbf{k}}^v n_{\mathbf{q}}}{\hbar(\omega - \omega_{\mathbf{q}}) + \tilde{\Sigma}_{s\mathbf{k}}^v - \tilde{\Sigma}_{s\mathbf{k}-\mathbf{q}}^c + i\eta} \right\} P_{s\mathbf{k}-\mathbf{q}} \right], \end{aligned} \quad (18)$$

and a similar equation holds for the valence-band distribution functions. Here,  $\pi \mathcal{D}_{\eta}(x) = \frac{\eta}{x^2 + \eta^2}$  denotes the numerical energy-conserving function,  $n_{\mathbf{q}}$  is the phonon occupation number,  $\hbar\omega_{\mathbf{q}} = 27.72$  meV [41] is the corresponding LO-phonon energy, and  $\mathcal{F}[f]$  denotes the Fourier transform of function  $f$ . The inclusion of the screened Fröhlich interaction  $g_{\mathbf{q};\mathbf{k}}^{\alpha\alpha'}(\omega) = g_{\mathbf{q}}^0 + g_{\mathbf{q}}^0 \Pi_{\mathbf{q};\mathbf{k}}^{\alpha\alpha'}(\omega) g_{\mathbf{q};\mathbf{k}}^{\alpha\alpha'}(\omega)$  accounts for screening contributions arising from the excited charge carriers in addition to the background screening contributions of the remote bands and dielectric environment already included in  $g_{\mathbf{q}}^0$ . Thus, Coulomb and phonon-coupling matrix elements are treated on the same level of approximation.

### III. NUMERICAL RESULTS

In this section, we present the results of our numerical analysis of the excitation dynamics and gain build-up in monolayer MoTe<sub>2</sub>-H. As physical conditions, we assume a pump-probe scenario, where we consider a room-temperature ML of MoTe<sub>2</sub>-H, which has been placed on a quartz substrate and is excited by a high-intensity linear-polarized optical pump pulse ( $E_0 \sim 1.25$  MV/cm). The central pump frequency is chosen to be slightly above the interacting B-band gap and the pump pulse has a full width at half maximum (FWHM) of 333 fs corresponding to a photon density of  $1.8 \times 10^{15}$  cm<sup>-2</sup>

(a pump fluence of  $520 \mu\text{J}/\text{cm}^2$ ). For these excitation conditions, it is ensured that virtually all carriers are created in the  $K$  and  $K'$  valleys.

For the pump simulations, we solve the Dirac-Bloch Eqs. (2) and (3) in the time domain. The optically induced interband polarizations lead to the generation of excited charge carriers and the subsequent carrier relaxation dynamics is computed from the carrier-carrier and carrier-phonon scattering contributions, Eqs. (9)–(12) for  $\alpha = \alpha'$  and Eq. (15), respectively. For the carrier dynamics, the numerically most important effect of the many-body correlations of the interband polarizations is the replacement of the “bare” Coulomb potential by its screened counterpart in the Hartree-Fock contributions, whereas the detailed excitation-induced dephasing of the interband polarizations play only a minor role. As verified numerically, it is sufficient to compute the carrier dynamics within the Markov approximation and the excitation-induced band-gap renormalization is determined from the density dependent gap Eqs. (13) and (14). They yield the renormalized single-particle bands wherein the excited carriers relax on the level of screened Hartree-Fock approximation. We then define the excitation-induced band-gap renormalization as the density-dependent change of the gaps between the spin-split renormalized single-particle bands relative to the respective gaps in the low-density limit.

For the probe pulse and for equilibrium configurations, we solve Eq. (2) in frequency domain via a matrix-inversion scheme, where the carrier distribution functions are quasistatic and we restrict ourselves to the terms linear in  $P_{\mathbf{sk}}$  in the singlet sources. However, to predict the correct line shapes of the optical spectra, it turns out to be crucial to include the detailed and fully dynamical many-body correlations of the interband polarizations, Eqs. (9)–(12) for  $\alpha/\alpha' = v/c$  and Eq. (16)–(18).

### A. Carrier dynamics and band-gap renormalization

In Fig. 5(a), we plot the excitation and subsequent relaxation dynamics of the A-band electron distribution function  $f_{A,\mathbf{k}}^e(t) = f_{A,\mathbf{k}}^c(t)$  in the vicinity of the  $K/K'$  points. Since conduction and valence bands with the same spin and valley indices have identical effective masses within the MDF model, the evolution of the hole distribution function  $f_{A,\mathbf{k}}^h(t) = \bar{f}_{A,-\mathbf{k}}^v(t)$  is identical to that of the electrons. The excitation dynamics of the B-band distribution functions are similar and not shown here.

Due to the strong Coulomb interaction, carrier-carrier scattering is extremely efficient and drives the carrier distributions into hot quasiequilibrium distributions within a few femtoseconds. Here, the carrier temperature reaches  $T = 2350 \text{ K}$  10 fs after the pump maximum has interacted with the sample. This ultrafast carrier-carrier scattering quickly redistributes the pump injected carriers to energies near the band gap and away from the excitation energy, thus almost completely preventing the accumulation of carriers at the excitation energy and effectively removing the associated Pauli-blocking of the absorption during the excitation process. The result is a highly efficient generation of excited charge carriers which is limited only by the absorption coefficient of the unexcited layer. After the pump pulse has passed, we find a total carrier density

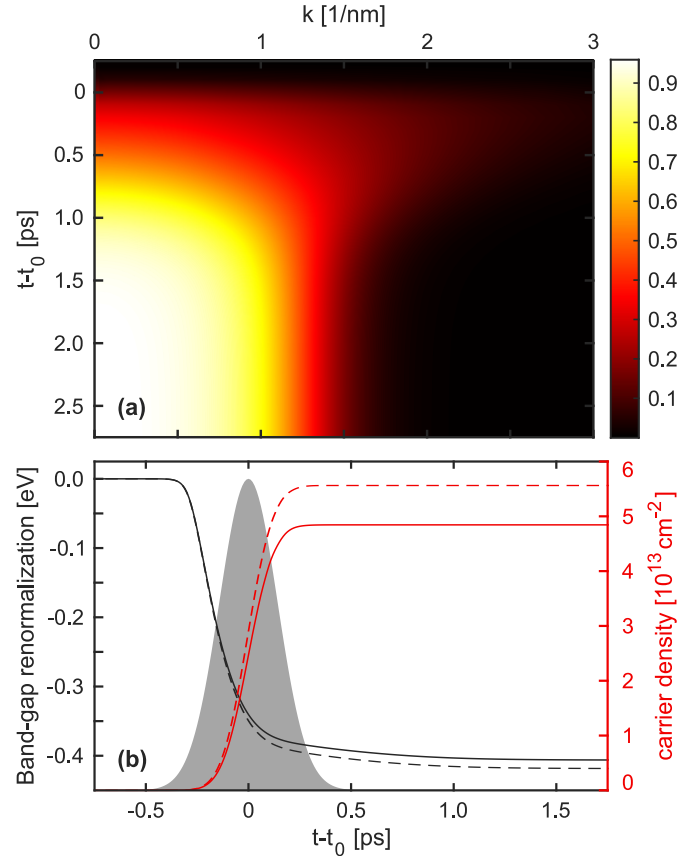


FIG. 5. (a) Dynamics of the A-band electron distribution in the vicinity of the  $K/K'$  points after excitation with a 333 fs pump pulse with peak amplitude of  $1.25 \text{ MV}/\text{cm}$  at  $t = t_0$ . (b) Time evolution of the excitation-induced band-gap renormalization (black) and the density of excited charge carriers (red). The solid lines correspond to the A-band properties, whereas the dashed lines show the B-band properties. The gray shaded area indicates the envelope of the optical pump pulse.

of  $1.040 \times 10^{14} \text{ cm}^{-2}$ , or equivalently,  $5.20 \times 10^{13} \text{ cm}^{-2}$  generated electron hole-pairs, corresponding to an absorption of about 2.9% of the incoming photons. Due to the Coulomb enhancement of the above band-edge absorption, this value is slightly larger than the universal low-density continuum absorption of  $\pi\alpha = 2.3\%$  for noninteracting Dirac Fermions.

The initial ultrafast relaxation into hot quasiequilibrium distributions is followed by a phonon-induced thermalization that takes about 2.5 ps until a quasiequilibrium at the temperature of the phonon bath (300 K) is reached. At  $\tau = 0.1 \text{ ps}$  and  $\tau = 1 \text{ ps}$ , we find intermediate temperatures of  $T = 2175 \text{ K}$  and  $T = 555 \text{ K}$ , respectively. This relaxation time is about twice as fast as in conventional semiconductors and based on the efficient phonon coupling in ML  $\text{MoTe}_2\text{-H}$  [41].

The time evolution of the excitation-induced band-gap renormalization (black) and the total carrier density with given spin and valley index  $n_i(t) = \frac{1}{\mathcal{A}} \sum_{\alpha,\mathbf{k}} f_{i\mathbf{k}}^\alpha(t)$  (red) is shown in Fig. 5(b). With solid lines, we depict the respective A-band properties, whereas the B-band properties are plotted using dashed lines. The gray shaded area shows the envelope of the Gaussian shaped optical pump pulse centered around  $t_0$ . Due to the initially nearly resonant excitation with the B-band

gap, the final amount of charge carriers in the B bands ( $n_B = 5.56 \times 10^{13} \text{ cm}^{-2}$ ) is slightly higher than in the A bands ( $n_A = 4.84 \times 10^{13} \text{ cm}^{-2}$ ). Note that due to the opposite spin, there are no relaxation processes between the B and the A bands on the timescales of interest here.

As can be recognized in Fig. 5(b), the build-up of populations during the excitation process is accompanied by an almost instantaneous large shrinkage of the band gap, followed by a much slower further reduction. The band-edge shrinkage results from combined screening and phase-space-filling effects. As in conventional two-dimensional semiconductors, the screening wave number is proportional to the carrier occupation at  $k = 0$ . Due to the ultrafast Coulomb scattering, the major contribution to screening develops within the timescale of the pump pulse with a correspondent reduction of the band gap of about 389 meV within the first 0.4 ps. Once the amount of excited charge carriers has saturated, the band edge can only be further reduced by phase-space filling. This leads to an additional reduction of about 17 meV on the timescale of the thermalization, yielding the total excitation-induced band-gap renormalizations of 406 meV (A gap) and 419 meV (B gap), respectively, for the investigated excitation conditions. These results are in good agreement with our previous findings in the equilibrium regime [18] and reported experimental observations [15,16] on similar systems.

### B. Evolution of optical spectra and build-up of optical gain

In Fig. 6, we present the time evolution of optical absorption/gain spectra computed as linear response to an ultrashort, low-intensity probe pulse for different delay times  $\tau = t - t_0$ . To cover the wide relevant energy range of several hundred meV, we choose a temporal width of 10 fs for the probe pulse. The use of such an ultrashort probe pulse also provides the necessary time resolution to study the evolution of the optical response during the excitation process, which is shown in Fig. 6(a). Here, the pump-probe delay increases from  $\tau = -0.30$  ps to  $\tau = -0.05$  ps in 0.05 ps steps. For comparison, the linear absorption spectrum of the unexcited ML is depicted in black. We notice an initial increase of the excited carrier density leading to dephasing, excitation-induced band-edge shrinkage, and reduction of the exciton binding energy. As a consequence of compensating effects, we observe practically no shift of the exciton resonance position under the given excitation conditions. Excitation-induced dephasing increases the 1-s-exciton linewidth from 2.3 meV at a delay time  $\tau = -0.25$  ps to 42.2 meV at  $\tau = -0.15$  ps. Note, that we include an additional dephasing constant of 10 meV for the microscopic polarizations to assure convergence in the zero-density limit. At  $\tau = -0.05$  ps and a density of about  $3.36 \times 10^{13} \text{ cm}^{-2}$  the exciton resonance is completely bleached out, marking the Mott-density.

In Fig. 6(b), we show the optical absorption in the thermalization regime. Here, pump-probe delays increase from  $\tau = 0.5$  ps to  $\tau = 1.5$  ps in 0.2 ps steps. The inset displays snapshots of the corresponding A-band electron distribution functions. In this time regime, no additional excited charge carriers are generated, but thermalization relaxes the existing carriers into quasiequilibrium at the lattice temperature (300 K). As a consequence of the high barriers between

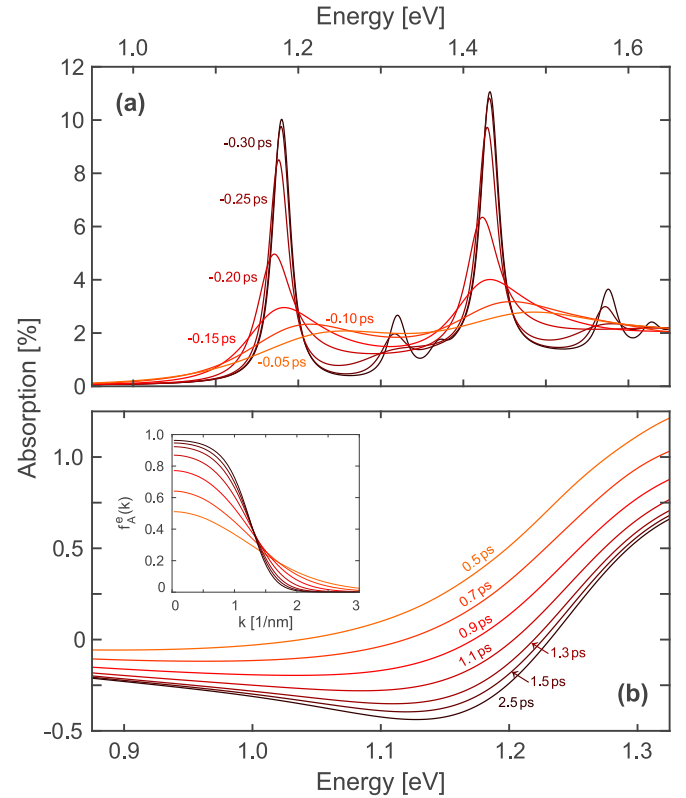


FIG. 6. Optical absorption spectra at distinct pump-probe delays. (a) Excitation regime. Pump-probe delays increase from  $\tau = -0.30$  ps to  $\tau = -0.05$  ps in 0.05 ps steps. The black solid line represents the low-density limit before the excitation. (b) Thermalization regime. Pump-probe delays increase from  $\tau = 0.5$  ps to  $\tau = 1.5$  ps in 0.2 ps steps. The absorption spectrum in the quasiequilibrium limit ( $\tau \geq 2.5$  ps) is shown in black. The corresponding A-band distribution functions are depicted in the inset.

the  $K/K'$  and  $\Sigma/\Lambda$  valleys, no significant percentage of the excited carriers can reach the side valleys on the fast carrier relaxation timescale. Therefore, the total carrier densities in the  $K/K'$  valleys is practically conserved. The absorption spectrum for quasiequilibrium conditions is depicted in black in Fig. 6(b). With decreasing temperature of the quasiequilibrium distributions, the occupation probabilities near the band-gap increase. About 0.5 ps after the pump pulse, inversion with  $(1 - f_{ik}^e - f_{ik}^h) < 0$  is reached and optical gain (negative absorption) appears in the spectrum. Inversion and gain increase with increasing cooling of the carriers. After about 2.5 ps thermal equilibrium is reached, where we observe broad A-band optical gain with a peak energy of 1.13 eV, slightly below the low density A-exciton resonance. Note that while the inclusion of the carrier-phonon scattering is crucial for the thermalization of the carriers, linewidths and energy renormalizations within the optical spectra are dominated by polarization-carrier rather than polarization-phonon scattering contributions. The maximum gain approaches a value of 0.5% amplification of the incoming light, which is clearly below the theoretical upper limit of  $\pi\alpha/2 = 1.15\%$  for the free carrier, single-band case. Therefore, continuum absorption of the A band overcompensates the gain of the B band at higher

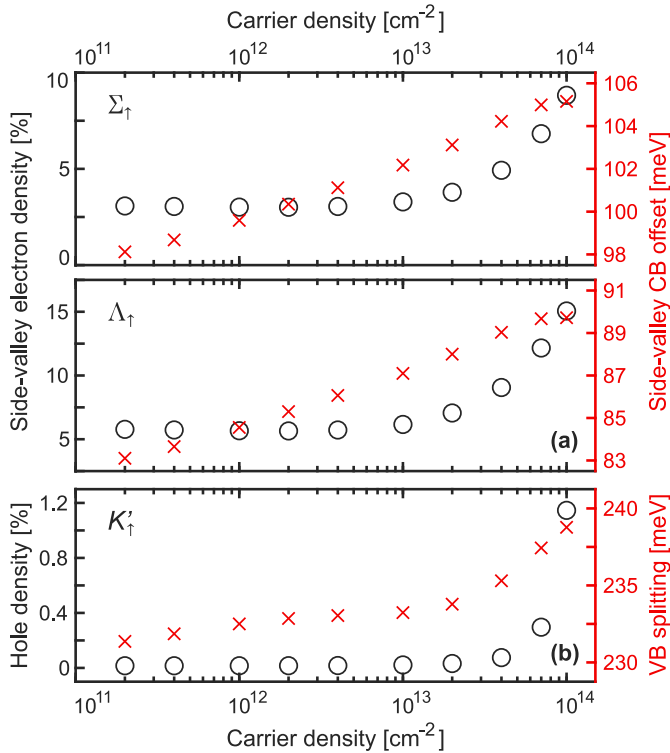


FIG. 7. (a)  $\Sigma_{\uparrow}$  (top) and  $\Lambda_{\uparrow}$  (bottom) side-valley electron densities (left axis, black circles) and  $\Sigma_{\uparrow}$  (top) and  $\Lambda_{\uparrow}$  (bottom) conduction-band offsets (right axis, red crosses) in dependence of the total amount of excited charge carriers. (b) Similarly, charge-carrier dependence of the  $K'_{\uparrow}$  hole density (left axis, black circles) and  $K_{\uparrow}/K'_{\uparrow}$  valence-band splitting (right axis, red crosses). The respective spin-up electron (hole) densities are stated as fraction of the total spin-up electron (hole) density.

energies yielding a net absorption in the frequency range of the B exciton.

### C. Influence of the side valleys

The full DFT band structure displays six side minima in the conduction band located at the  $\Sigma/\Lambda$  points of the Brillouin zone. For the previously considered excitation conditions, carrier equilibration leads to a net electron drain from the  $K/K'$  to the  $\Sigma/\Lambda$  valleys as well as a hole drift between the  $K$  and  $K'$  valleys. To compute this side-valley drain and hole drift and its influence on the optical gain spectra, we consider an equilibrium situation where all electrons and holes have relaxed to a common chemical potentials. The side valleys are treated within the effective mass approximation and the influence of their populations is considered self-consistently including their contribution to screening and excitation-induced renormalizations.

The electron drain to the side valleys critically depends on the offset between the side valleys and the conduction band minima at the  $K/K'$  points, which in turn are modified by the carrier occupations in each valley. In Fig. 7(a), we depict the  $\Sigma_{\uparrow}$  (top) and  $\Lambda_{\uparrow}$  (bottom) side-valley electron densities (black circles) as well as the corresponding conduction-band offsets (red crosses) in dependence of the total density of excited charge carriers. Increasing the total carrier density

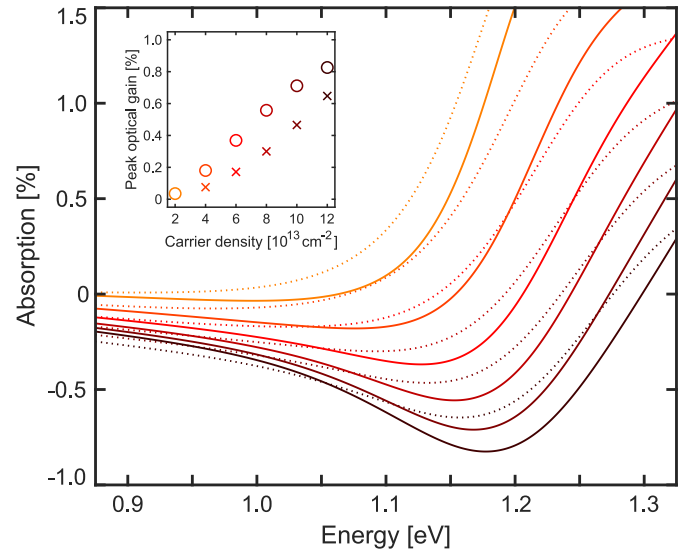


FIG. 8. Optical absorption spectra before and after equilibration of the carriers between the different valleys. The solid lines show the optical spectra after equilibration, the dotted lines before equilibration, where all carriers are located in the  $K$  and  $K'$  valleys. The inset shows the peak optical gain for the corresponding charge-carrier densities after (before) equilibration in circles (crosses).

from  $2 \times 10^{11} \text{ cm}^{-2}$  to  $10^{14} \text{ cm}^{-2}$ , the  $\Sigma_{\uparrow}$  ( $\Lambda_{\uparrow}$ ) conduction-band offset increases by 7.0 meV (6.6 meV), while the fraction of  $\Sigma_{\uparrow}$  ( $\Lambda_{\uparrow}$ ) electrons increases from about 3.1% (5.8%) in the low-density regime to about 8.8% (15.1%) in the regime investigated by the pump-probe simulations. The larger electron drain towards the  $\Lambda_{\uparrow}$  valleys arises from the smaller side-valley offset, that increases from 82 meV (DFT value) to 89.7 meV for the highest investigated carrier density. For the  $\Sigma_{\uparrow}$  valleys, the band offset increases from 97 meV (DFT value) to 105.2 meV.

In addition to the electron drain, intervalley scattering leads to a drift of the hole density between the  $K$  and  $K'$  valleys. In our calculations, the influence of this is taken into account in a similar manner as the side-valley drain, i.e., by considering an equilibrium situation with a common chemical potential for the holes in different valleys. In Fig. 7(b), we plot the charge-carrier dependence of the fractional  $K'_{\uparrow}$  hole density (black circles) and the corresponding  $K_{\uparrow}/K'_{\uparrow}$  valence-band splitting (red crosses). Because of the large valence-band splitting in the low-density limit, almost all the holes from the  $K'_{\uparrow}$  valley have drifted to the energetically favorable  $K_{\uparrow}$  valley after equilibration. Only for carrier densities as high as  $10^{14} \text{ cm}^{-2}$ , the  $K'_{\uparrow}$  valley is occupied with at least 1% of the spin-up holes. Thus, the increasing valence-band splitting with increasing carrier density is exclusively introduced by the dominant occupation of holes in the  $K_{\uparrow}$  valley. For the shown carrier densities, the valence-band splitting increases by 7.4 meV from 231.4 to 238.8 meV.

Finally, we present the resulting optical absorption spectra after equilibration within the entire Brillouin zone for elevated charge-carrier densities in Fig. 8. The carrier densities increase from orange ( $2.0 \times 10^{13} \text{ cm}^{-2}$ ) to black ( $1.2 \times 10^{14} \text{ cm}^{-2}$ ). The solid (dotted) lines show the optical spectra after (before) equilibration. The inset depicts the peak optical

gain for the corresponding charge-carrier densities. Prior to equilibration, all carriers are assumed to be located in the  $K$  and  $K'$  valleys. As pointed out before, equilibration not only leads to electron drain to the side valleys, but also to hole drift between the  $K$  and  $K'$  valleys. Both processes have counteracting effects on the optical spectra. While the electron drain to the side-valleys leads to a loss of optically recombining electrons, the hole drift between the  $K$  and  $K'$  valleys increases the amount of optically recombining holes. Because of the large  $K_{\uparrow}/K'_{\uparrow}$  ( $K'_{\downarrow}/K_{\downarrow}$ ) valence-band splitting about 99% of the holes contribute to A-band population inversion after equilibration, compared to the nearly 50% before equilibration. This overcompensates the effect of electron drain—between 10.8% and 26.9% of the electrons for the stated carrier densities—to the side valleys. Consequently, enhanced peak optical gain is observed in equilibrium. In particular, for carrier densities of  $0.8/1.0/1.2 \times 10^{14} \text{ cm}^{-2}$  peak optical gain increases by 86/53/28% due to equilibration. For a carrier density as high as  $1.2 \times 10^{14} \text{ cm}^{-2}$ , we observe peak optical gain occurring slightly below the low-density A-exciton resonance with a magnitude of 0.83% of the incoming light. Normalized to the layer thickness of  $D = 6.99 \text{ \AA}$  (see Table I), this corresponds to a peak gain of about  $10^5 \text{ cm}^{-1}$ , which should be compared to the gain maximum of  $5000 \text{ cm}^{-1}$  in typical III/V semiconductors under realistic excitation conditions [45].

#### IV. DISCUSSION

In summary, we investigated the carrier dynamics in ML  $\text{MoTe}_2$ -H after excitation with a strong optical pump pulse slightly above the interacting B-band gap. Our investigations cover two distinct time regimes. In the excitation regime, i.e., during the optical pulse, generation of photo-induced charge carriers is accompanied by an almost instantaneous band-gap renormalization of about 410 meV in our case, that exceeds the exciton binding energy of the unexcited crystal. In the low-density regime, the band-gap renormalization is almost exactly canceled by the weakening of the excitonic

binding such that the exciton resonance displays a negligible spectral shift. The initial fast carrier relaxation is followed by a much slower thermalization of the hot carriers. Due to efficient phonon coupling, the thermalization occurs within a few picoseconds, whereas it is typically of the order of tens of picoseconds in conventional III–V quantum well systems. For the chosen pump-pulse intensity, thermalization finally leads to population inversion. Here, we observe the transition from plasma absorption to broadband optical gain. The maximum of the A-band optical gain occurs slightly below the low-density A-exciton resonance and its magnitude approaches 0.5% of the incoming light.

On the longer timescale, equilibration of the excited carriers among different valleys is expected with a simultaneous electron drain from the  $K/K'$  to the side valleys at the  $\Sigma/\Delta$  points of the Brillouin zone. Although the electron drain leads to an efficiency drop of several percent in the gain regime, there is no evidence for an excitation-dependent roll-over from a direct to an indirect band gap, as has been predicted theoretically for similar material systems [35,36]. Instead, we find that the drop due to the electron drain is overcompensated by a hole drift between the  $K$  and  $K'$  valleys, leading to a net increase of the optical gain up to several 10%.

Our results are in general agreement with experimentally observed excitation-induced band-gap shrinkage of similar TMDC systems [15,16] and confirms the possibility of ultrafast band-gap modulation by the injection of carriers. Furthermore, our results identify conditions for achieving plasma gain in ML  $\text{MoTe}_2$ -H and the short relaxation times enable high repetition rates for possible applications in pulsed laser operation.

#### ACKNOWLEDGMENTS

The Marburg work of this project was funded by the DFG via the Collaborative Research Center SFB 1083. The Arizona work was supported by the Air Force Office of Scientific Research under Award No. FA9550-17-1-0246. We thank T. Sohler for correspondence concerning the 2D Fröhlich interaction in TMDC MLs.

- 
- [1] K. F. Mak, C. Lee, J. Hone, J. Shan, and T. F. Heinz, *Phys. Rev. Lett.* **105**, 136805 (2010).
  - [2] A. Splendiani, L. Sun, Y. Zhang, T. Li, J. Kim, C. Y. Chim, G. Galli, and F. Wang, *Nano Lett.* **10**, 1271 (2010).
  - [3] C. Zhang, H. Wang, W. Chan, C. Manolatu, and F. Rana, *Phys. Rev. B* **89**, 205436 (2014).
  - [4] Y. Ding, Y. Wang, J. Ni, L. Shi, S. Shi, and W. Tang, *Physica B: Phys. Condens. Matter* **406**, 2254 (2011).
  - [5] D. Y. Qiu, F. H. da Jornada, and S. G. Louie, *Phys. Rev. Lett.* **111**, 216805 (2013).
  - [6] K. S. Novoselov, A. Mishchenko, A. Carvalho, and A. H. Castro Neto, *Science* **353**, aac9439 (2016).
  - [7] T. Cheiwchanchamnangij and W. R. L. Lambrecht, *Phys. Rev. B* **85**, 205302 (2012).
  - [8] A. Chernikov, T. C. Berkelbach, H. M. Hill, A. Rigosi, Y. Li, O. B. Aslan, D. R. Reichman, M. S. Hybertsen, and T. F. Heinz, *Phys. Rev. Lett.* **113**, 076802 (2014).
  - [9] K. He, N. Kumar, L. Zhao, Z. Wang, K. F. Mak, H. Zhao, and J. Shan, *Phys. Rev. Lett.* **113**, 026803 (2014).
  - [10] Z. Ye, T. Cao, O. K., H. Zhu, X. Yin, Y. Wang, S. G. Louie, and X. Zhang, *Nature* **513**, 214 (2014).
  - [11] B. Zhu, X. Chen, and X. Cui, *Sci. Rep.* **5**, 9218 (2015).
  - [12] O. Salehzadeh, M. Djavid, N. H. Tran, I. Shih, and Z. Mi, *Nano Lett.* **15**, 5302 (2015).
  - [13] Y. Ye, Z. J. Wong, X. Lu, X. Ni, H. Zhu, X. Chen, Y. Wang, and X. Zhang, *Nat. Photon.* **9**, 733 (2015).
  - [14] Y. Li, J. Zhang, D. Huang, H. Sun, F. Fan, J. Feng, Z. Wang, and C. Z. Ning, *Nat. Nanotech.* **12**, 987 (2017).
  - [15] A. Chernikov, C. Ruppert, H. M. Hill, A. F. Rigosi, and T. F. Heinz, *Nat. Photon.* **9**, 466 (2015).
  - [16] S. Ulstrup, A. G. Čabo, J. A. Miwa, J. M. Riley, S. S. Grønborg, J. C. Johannsen, C. Cacho, O. Alexander, R. T. Chapman, E. Springate, M. Bianchi, M. Dendzik, J. V. Lauritsen, P. D. C. King, and P. Hofmann, *ACS Nano* **10**, 6315 (2016).

- [17] A. Steinhoff, M. Rösner, F. Jahnke, T. O. Wehling, and C. Gies, *Nano Lett.* **14**, 3743 (2014).
- [18] L. Meckbach, T. Stroucken, and S. W. Koch, *Appl. Phys. Lett.* **112**, 061104 (2018).
- [19] T. Stroucken and S. W. Koch, in *Optical Properties of Graphene*, edited by R. Binder (World Scientific Publishing, Singapore, 2017), Chap. 2, pp. 43–84.
- [20] L. Meckbach, T. Stroucken, and S. W. Koch, *Phys. Rev. B* **97**, 035425 (2018).
- [21] L. Meckbach, U. Huttner, L. Bannow, T. Stroucken, and S. W. Koch, *J. Phys.: Condens. Matter* **30**, 374002 (2018).
- [22] W. Kohn and L. J. Sham, *Phys. Rev.* **140**, A1133 (1965).
- [23] G. Kresse and J. Hafner, *Phys. Rev. B* **47**, 558 (1993).
- [24] G. Kresse and J. Hafner, *Phys. Rev. B* **49**, 14251 (1994).
- [25] G. Kresse and J. Furthmüller, *Phys. Rev. B* **54**, 11169 (1996).
- [26] G. Kresse and J. Furthmüller, *Comp. Mater. Sci.* **6**, 15 (1996).
- [27] J. P. Perdew, K. Burke, and M. Ernzerhof, *Phys. Rev. Lett.* **77**, 3865 (1996).
- [28] S. Steiner, S. Khmelevskiy, M. Marsmann, and G. Kresse, *Phys. Rev. B* **93**, 224425 (2016).
- [29] S. Grimme, J. Antony, S. Ehrlich, and H. Krieg, *J. Chem. Phys.* **132**, 154104 (2010).
- [30] S. Grimme, S. Ehrlich, and L. Goerigk, *J. Comput. Chem.* **32**, 1456 (2011).
- [31] H. J. Monkhorst and J. D. Pack, *Phys. Rev. B* **13**, 5188 (1976).
- [32] A. Molina-Sánchez, K. Hummer, and L. Wirtz, *Surf. Sci. Rep.* **70**, 554 (2015).
- [33] A. Kormányos, G. Burkard, M. Gmitra, J. Fabian, V. Zólyomi, N. D. Drummond, and V. Fal’ko, *2D Materials* **2**, 022001 (2015).
- [34] D. Novko, [arXiv:1907.04766](https://arxiv.org/abs/1907.04766) [cond-mat.mtrl-sci].
- [35] D. Erben, A. Steinhoff, C. Gies, G. Schönhoff, T. O. Wehling, and F. Jahnke, *Phys. Rev. B* **98**, 035434 (2018).
- [36] F. Lohof, A. Steinhoff, M. Florian, M. Lorke, D. Erben, F. Jahnke, and C. Gies, *Nano Lett.* **19**, 210 (2019).
- [37] M. Gajdoš, K. Hummer, G. Kresse, J. Furthmüller, and F. Bechstedt, *Phys. Rev. B* **73**, 045112 (2006).
- [38] S. Baroni and R. Resta, *Phys. Rev. B* **33**, 7017 (1986).
- [39] A. Laturia, M. L. Van de Put, and W. G. Vandenberghe, *npj 2D Mater. Appl.* **2**, 6 (2018).
- [40] D. Xiao, G.-B. Liu, W. Feng, X. Xu, and W. Yao, *Phys. Rev. Lett.* **108**, 196802 (2012).
- [41] T. Sohler, M. Calandra, and F. Mauri, *Phys. Rev. B* **94**, 085415 (2016).
- [42] T. Stroucken, J. H. Grönqvist, and S. W. Koch, *Phys. Rev. B* **84**, 205445 (2011).
- [43] C. Robert, R. Picard, D. Lagarde, G. Wang, J. P. Echeverry, F. Cadiz, P. Renucci, A. Högele, T. Amand, X. Marie, I. C. Gerber, and B. Urbaszek, *Phys. Rev. B* **94**, 155425 (2016).
- [44] M. Kira and S.W. Koch, *Progr. Quant. Electron.* **30**, 155 (2006).
- [45] See <http://www.nlcstr.com/publications.htm> and <http://www.nlcstr.com/examples0.htm> for examples.





## Wissenschaftlicher Werdegang

Name	Lars Meckbach
Geburtsdatum	28. September 1990
Geburtsort	Marburg (Lahn)
06/2010	Erlangung der Allgemeinen Hochschulreife am Gymnasium Philippinum Marburg
10/2011 bis 03/2015	Studium der Physik (Bachelorstudiengang) an der Philipps-Universität Marburg
06/2014 bis 09/2014	Bachelorarbeit zum Thema: “FIB-Tomographie metallischer Tropfen auf Ga(AsBi)” bei Prof. Dr. Kerstin Volz im “Struktur- und Technologieforschungslabor”
04/2015 bis 05/2017	Studium der Physik (Masterstudiengang) an der Philipps-Universität Marburg
12/2016 bis 05/2017	Masterarbeit zum Thema: “Exzitonische Eigenschaften von TMDCs” bei Prof. Dr. Stephan W. Koch in der Arbeitsgruppe “Theoretische Halbleiterphysik”
10/2014 bis 09/2015	Wissenschaftliche Hilfskraft im “Struktur- und Technologieforschungslabor” bei Prof. Dr. Kerstin Volz an der Philipps-Universität Marburg
seit 06/2017	Wissenschaftlicher Mitarbeiter und Doktorand in der Arbeitsgruppe “Theoretische Halbleiterphysik” bei Prof. Dr. Stephan W. Koch an der Philipps-Universität Marburg
02/2018 bis 03/2018 und 02/2019 bis 03/2019	Forschungsaufenthalte am “College of Optical Sciences” bei Prof. Dr. Jerome V. Moloney an der University of Arizona in Tucson, AZ, USA